Radiative-transfer modelling of the circumstellar environments of pre-main-sequence stars

Claire Frances Esau

Submitted by Claire F. Esau to the University of Exeter as a thesis for the degree of Doctor of Philosophy in Physics, December 2015.

I certify that all material in this thesis which is not my own work has been identified and that no material has previously been submitted and approved for the award of a degree by this or any other University.

Signed: . . . . . .

Claire Frances Esau

Date: . . . . . .

Abstract

Circumstellar discs of pre-main sequence stars undergo different processes depending on the nature of the circumstellar environment, which is governed by stellar mass. I have performed numerical simulations of the circumstellar regions of classical T Tauri stars (CTTs) and Herbig Ae (HAe) stars using the radiative transfer code TORUS in order to test the paradigm of magnetospheric accretion in CTTs, and to ascertain the nature of the material in the inner regions of HAe discs.

The process of magnetospheric accretion (MA) involves disc material attaching to stellar magnetic field lines and impacting the photosphere, producing accretion shocks. When the magnetic field is inclined to the star, disc warps form which periodically occult the photosphere. With specific reference to the CTTs AA Tau I perform three-dimensional MA models to study this variability. By comparing synthetic photometry with observational data I show that the geometry of the system can be constrained. I go on to study Balmer line profiles in the context of MA and disc wind outflows. I present three-dimensional models of a system comprising the star, magnetosphere, disc, and disc wind, producing synthetic line profiles and images. Using these profiles I perform time-series fitting to observational data and demonstrate that the mass accretion rate, mass loss rate, and magnetosphere temperature can be constrained. I show that there is a degeneracy between wind temperature and wind acceleration which require alternative methods to constrain further. While an outflow model alternative to a sole disc wind may produce better fits to observations, MA models reproduce various observational features well.

Finally I test the hypothesis that refractory grains produce the innermost emission in HAe discs. Focussing on the HAe stars MWC 275 and AB Aur, I perform radiative equilibrium modelling to create synthetic images of these objects from which interferometric visibility profiles are produced. I show that the temperatures at which these refractory grains are required to survive are too high to be physically plausible. I also find that silicate dust is shielded when sufficiently high mass fractions of refractory grains are used, enabling the silicates to survive interior to the classical sublimation radius. While refractory dust may provide a significant contribution to the emission observed in these inner regions, this alone is not sufficient.

Contents

List of Figures

List of Tables

Declaration

This thesis contains work that has been published. Chapters 3 and 4 are based on a paper published in Monthly Notices of the Royal Astronomical Society (MNRAS), volume 443, issue 2, pages 1022-1043. I am first author on this paper and my co-authors have provided a supervisory role (TJH) and have provided the data used in the paper (JB). Chapter 2 summarises the functionality of the TORUS radiative transfer code which has been developed by TJH and NHS, and forms the basis of the models I have executed.

Acknowledgements

Firstly, my thanks to my supervisor, Tim Harries, who gave me the opportunity to work with the most immense piece of code that I have ever encountered. I spent perhaps too long in the early days sat in my office feeling overwhelmed by the learning curve ahead of me, but I have come out immeasurably more confident in my own abilities. Thank you to all in the Astronomy group who have given me fond memories of my time in this beautiful part of the country, from bike rides along the Exe to beach barbecues.

I cannot thank my soon-to-be husband, Lee Summers, enough for his help with everything, particularly while I was writing up - shopping, cooking, proof-reading, keeping me focussed on my less motivated days, and looking after me and the house in general. I'd also like to thank the furry and feathered friends that have brightened my days, in particular over the last three years; the baby seagulls that graced our balcony in Paignton, and our Marty, the most charismatic and comical little hamster we could have hoped for.

Many thanks of course go to my parents for their support throughout my PhD, as well as to my brother, sister, and extended family. There are people who have not only helped me through my time as a PhD student but have perhaps unknowingly led me to pursue a career in astrophysics, without whom I'd be doing goodness-knows-what. My greatest thanks go to my grandfather, Peter Wood, who sadly passed away shortly before my thesis submission. The astronomy books you gave me as a child gave me a sense of familiarity with the subject that led me to where I am today.

It certainly doesn't feel like I have spent nearly a third of my life as a student of astrophysics. I think that is testament not only to those who have made these 8 years as an undergraduate and a postgraduate so enjoyable, but also to the fascinating field in which I am able to say I have made a contribution. Fingers crossed I will continue to do so!

Claire Esau
Exeter, U.K.
21st December 2015

Dedicated to

the memory of

Peter James Wood

Chapter 1

Introduction

The study of star formation and the evolution of circumstellar environments is appealing not just in professional astronomy but also in popular science. General interest in this area can be inspired by broad questions such as *"How did the first stars form?"* and *"Where did the Earth come from?"* as well as by the incredibly eye-catching images of star forming regions in the Galaxy that we are now able to achieve through high-resolution imaging. While this thesis focuses on the dynamical interactions between pre-main sequence stars and their circumstellar environments, a brief outline of star formation is given in order to explain the origins of these objects. This is by no means a full explanation; there are many areas in star formation that are not yet understood, such as the roles of turbulence and magnetic fields in star forming regions, the effect that outflows from massive stars have on the surrounding material, and the origin of the initial mass function (the apparently universal distribution of stellar masses), to name a few. A brief description of star formation and early stellar evolution is given in Sections 1.1 and 1.2 respectively, followed by the observational characteristics of Classical T Tauri stars (Section 1.3.1) and Herbig Ae/Be stars (Section 1.3.2). Models of the process of magnetospheric accretion are discussed in Section 1.4 followed by a description of the types of outflows observed in Section 1.5. Finally, the aims of this thesis are presented in Section 1.6 along with an outline of the following chapters.

Table 1.1: Physical properties of molecular clouds. Table adapted from Stahler & Palla (2004)

Cloud Type	$n_{\rm H}$ ($\rm cm^{-3}$)	Linear Size (pc)	Mass ($\rm M_\odot$)
Giant Molecular Clouds	100	50	10^5
Clumps	10^3	2	10^4
Cores	10^4	0.1	10

1.1 Star formation

Most stars form in clusters within giant molecular clouds (GMCs). These are cool (~10s K) dense ($\bar{n_{\rm H}}$ ~100s $\rm cm^{-3}$, e.g. Williams et al. 2000) turbulent regions in the interstellar medium (ISM) primarily composed of molecular hydrogen. There is also a significant amount of dust in these clouds, contributing ~1% of the cloud's mass (Goldsmith et al. 1997). The presence of significant amounts of dust means observations are restricted to the radio portion of the spectrum. However, since H_2 is not excited at low temperatures and thus does not emit in the radio, observers rely on less abundant molecules such as CO and its isotopes for molecular cloud observations. GMCs typically have masses of ~10^4–10^6 $\rm M_\odot$ and linear sizes of several 10s pc. These regions are not uniformly dense; they have complex structures consisting of numerous clumps and filaments with densities of $n_{\rm H} \sim 10^3 - 10^4$ $\rm cm^{-3}$ and masses of ~100 $\rm M_\odot$ (see reviews by Blitz 1993; Mac Low & Klessen 2004; Bergin & Tafalla 2007). Further fragmentation of these clumps produces even denser cores ($n_{\rm H} \sim 10^4 - 10^5$ $\rm cm^{-3}$), which are the sites of localised star formation. A summary of the main properties of GMCs, clumps, and cores is given in Table 1.1.

The condition for fragmentation is described by the Jeans mass (Jeans 1902), $M_{\rm J}$, given by

$$M_{\rm J} = \left(\frac{5kT}{G\mu m_{\rm H}}\right)^{3/2} \left(\frac{3}{4\pi\rho}\right)^{1/2}, \tag{1.1}$$

where k_B is the Boltzmann constant, G is the gravitational constant, μ is the mean molecular weight, $m_{\rm H}$ is the mass of a hydrogen atom. The Jeans mass is the maximum mass

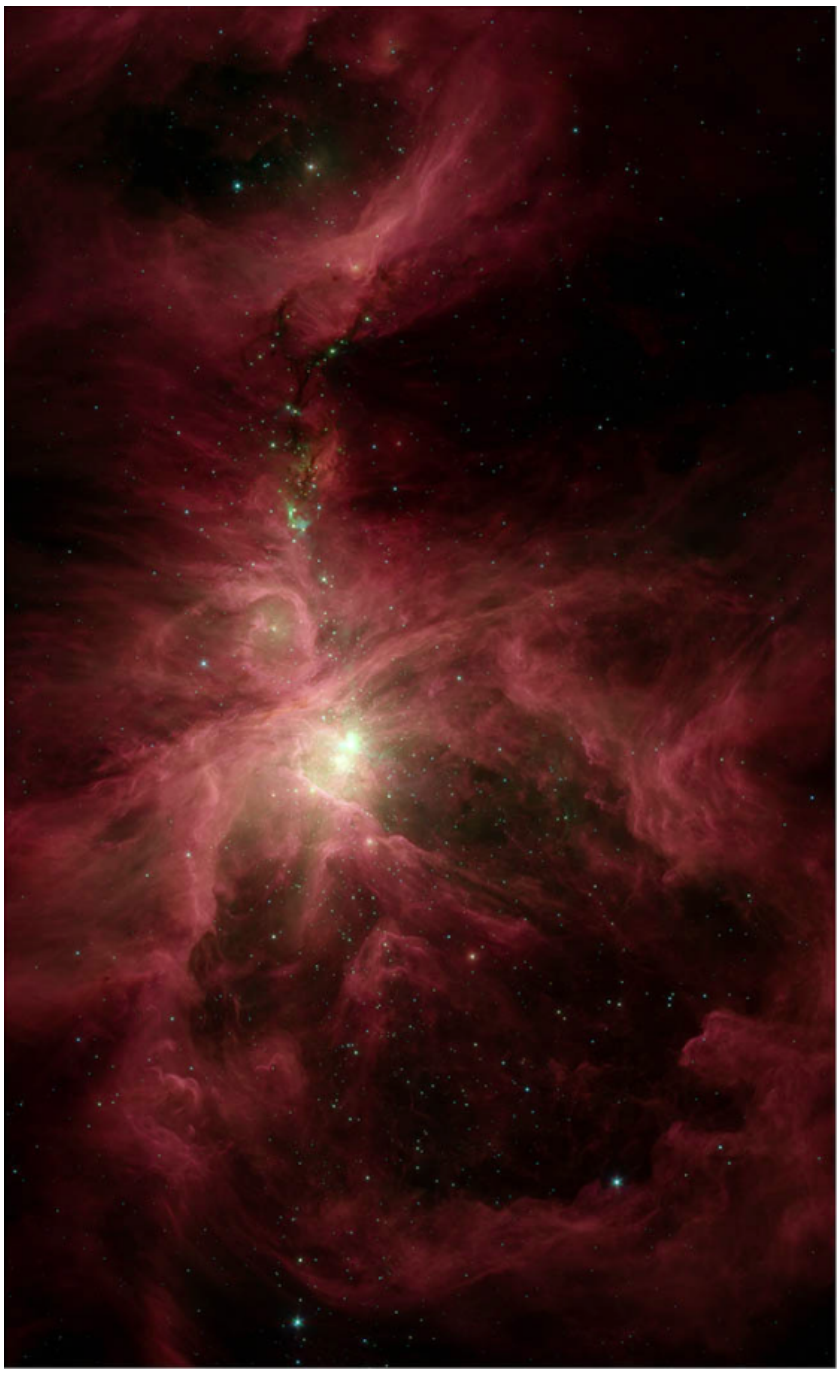

Figure 1.1: An infrared image of the Orion nebula, the nearest massive star forming region to Earth, from NASA's Spitzer Space Telescope. The turbulent nature of the gas and dust in this region is very clear. The majority of the image, in red, shows dust in the region which is illuminated by young stars forming in the nebula. The slight flecks of green and blue show hot gas and dust, and starlight, respectively. *Image Credit: NASA, JPL-Caltech, S.T. Megeath (Univ. Toledo)*

at which a cloud (or local region within a cloud) of given temperature T and density ρ is gravitationally stable against thermal pressure, assuming the material is distributed homogeneously throughout a sphere. It is clear from this relation that the higher the density of the material, the lower the mass required for further fragmentation. Initial perturbations in a region can be caused by internal turbulence or external factors; whatever the origin of the perturbation, if $M_{\rm J}$ decreases sufficiently so that it falls below the mass of the region, then the thermal pressure is no longer sufficient to support the gas and gravitational collapse occurs. Eventually the collapsed region becomes sufficiently dense that the thermal emission from dust at the centre of the core is no longer able to radiate away sufficiently quickly. While in theory a dense region would decrease the sound speed, reducing $M_{\rm J}$ and enabling further collapse, subsequent fragmentation is prevented due to the the considerable thermal pressure of the gas (e.g. Boss 1988). This is the "opacity limit" for fragmentation (e.g. Low & Lynden-Bell 1976), and it is at this point that an isothermal description for the collapse is no longer valid; the central region heats up and the process becomes adiabatic. It is at this stage that protostars may form, as the process of material accretion and increasing temperature continues. Cores are defined as either protostellar or starless depending on whether or not there is evidence for the presence of a protostar (e.g. di Francesco et al. 2007). Detection of an internal infrared (IR) or centimetre radio source, for instance, is indicative of higher densities of material than in the surrounding core, and thus signifies the presence of a 'point mass' source, i.e. a protostar. The presence of bipolar outflows from within these cores provides further evidence (for reviews on the physical properties of cores, see di Francesco et al. 2007; Ward-Thompson et al. 2007, and references therein).

1.2 Early stellar evolution

The early stages of stellar evolution are frequently described using a morphological classification scheme first coined by Lada (1987), in which young stellar objects are divided into classes (I, II or III in increasing order of age) based on the shape of their spectral

energy distribution (SED). Class I objects are protostars which are characterised by a positive slope in the infrared portion of their SED, peaking in the far-IR or sub-mm. This excess of infrared emission in comparison to the blackbody SED of a stellar photosphere is due to the fact that these protostars are still deeply embedded in circumstellar dust, rendering them unobservable at wavelengths shorter than the infrared. Class II and III sources represent the period of stellar evolution where the majority of core material has accreted onto the star and they have become observable at optical wavelengths. Their SEDs peak around near-IR wavelengths. Class II sources still exhibit an infrared excess in their SEDs due to the presence of a dusty circumstellar disc, although this excess is much less than that of the Class I SED. The intensity of the IR excess decreases longward of about 2 microns, and photospheric emission becomes dominant at shorter wavelengths. The power law slope of the SED is a result of the temperature gradient in the optically thick circumstellar disc. Concentric dusty annuli in the disc effectively radiate as blackbodies at different temperatures whose individual SEDs produce the slope of the infrared portion when superimposed. The SEDs of Class III sources fall far more steeply at long wavelengths compared to the Class II stage, providing a much closer match to the shape expected from a stellar blackbody, implying the optically thick circumstellar disc has now dispersed. Example energy distributions are shown in Figure 1.2.

This sequence was extended by André et al. (1993) who argued that Class I sources may be more evolved than true protostars. Class 0 was introduced to distinguish between extremely young protostars and the slightly older, observationally different Class I objects, which are around 10^5 years old by the time the surrounding gas and dust has dispersed sufficiently for optical observations. The only way to penetrate the optically thick dust surrounding Class 0 and I objects is by observing them at infrared and longer wavelengths. Class 0 objects are embedded so deeply in circumstellar material that they are unobservable even at infrared wavelengths. They are, however, strong submillimeter sources, and their SEDs are very similar to a single temperature 10–30 K blackbody spectrum, indicative of cold gas and dust. It is during this phase that the majority of material

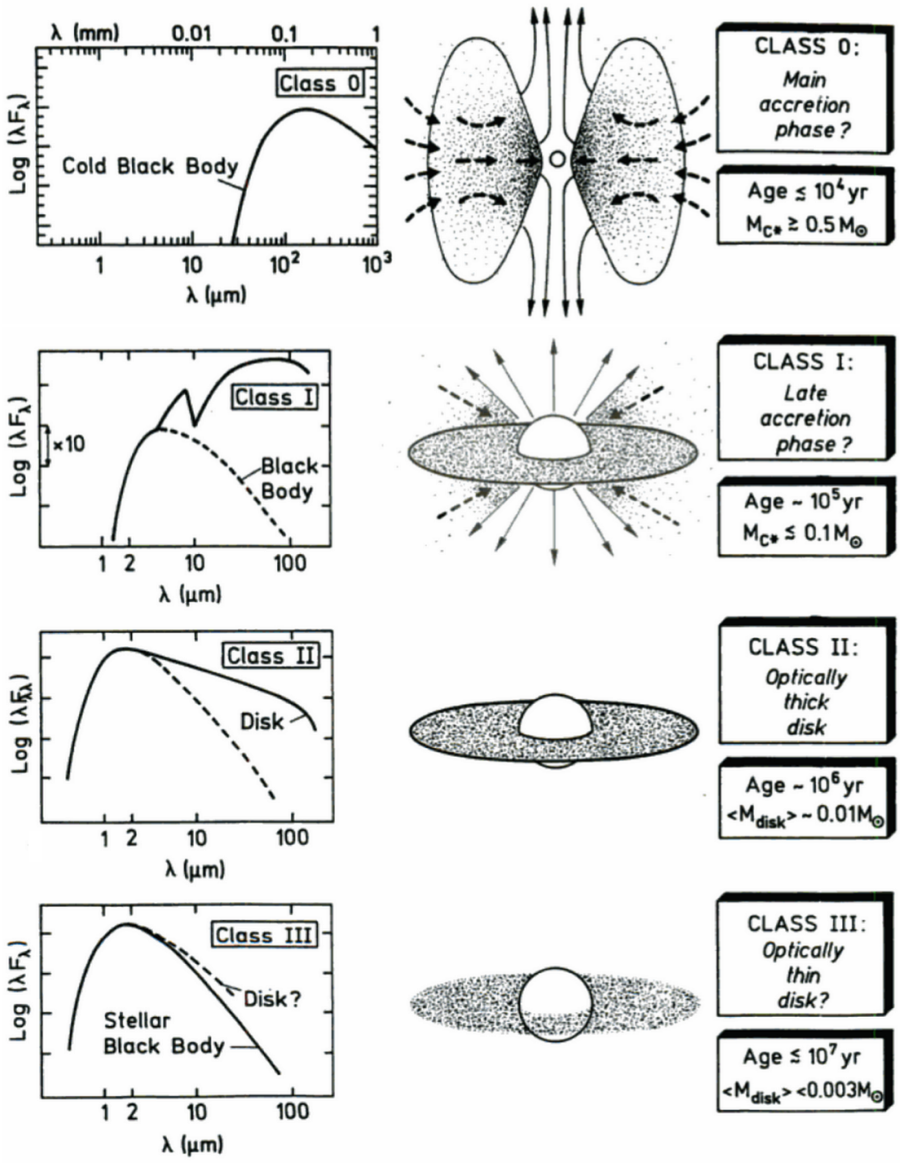

Figure 1.2: The evolutionary sequence of young stellar objects and their corresponding SEDs. Reproduced from André (1994).

is accreted, with the mass of core material exceeding the mass of the central protostar, entering the Class I phase when the mass of the protostar exceeds that of the surrounding core material. Since Class 0 and I stars are so heavily embedded, with the mass of core material exceeding that of the central star, they are often referred to as 'protostars', with the emerged Class II and III objects known as 'pre-main sequence' (PMS) stars. Protostars and PMS stars are also often grouped together under the catch-all term 'young stellar object', or YSO. While classification criteria are defined by distinct differences in the observed spectral energy distributions, star formation is a continuous process and the classification of YSOs using SEDs is not always simple. Instead, discrete parameterisation has been achieved by using the bolometric temperature $T_{\rm bol}$ (Myers & Ladd 1993), defined as the temperature of a blackbody which has the same mean frequency as the observed SED (not to be confused with the *effective* temperature, $T_{\rm eff}$, which is the temperature of a blackbody with the same radius and energy flux as a given star). Chen et al. (1995) found that Class 0 objects have $T_{\rm bol} < 70$ K, Class I have $T_{\rm bol}$ in the range of 60–650 K, Class II in the range of 650–2880 K, and Class III in excess of 2880 K. Class II and III stars are also known as classical and weak-lined T Tauri stars, respectively. Classical T Tauri stars (CTTS) exhibit strong Hα emission lines in their spectra, whereas the Hα lines of weak-lined T Tauri stars (WTTS), as the name suggests, are weaker. Traditionally these objects are classed depending on the equivalent with of the Hα line, where an equivalent width of $\gtrsim 10$ Å signifies a CTTS (e.g. Herbig & Bell 1988; Strom et al. 1989). White & Basri (2003) suggested using the Doppler width at 10 per cent of the peak flux as an alternative, finding that this yielded correct classification more often than using the alternative equivalent width method. They found that CTTS could be defined as having 10 per cent widths greater than 270 km s^{-1}, and WTTS having 10 per cent widths of less than this value.

This description of YSO evolution is applicable to objects that will have a main sequence mass of $M < 2$ M$_\odot$. The most massive stars, with $M > 8$ M$_\odot$, have no PMS phase, having joined the main sequence before they become optically visible, i.e. before

they reach the Class II stage (Palla & Stahler 1993; Beech & Mitalas 1994). Intermediate mass YSOs, with masses between ~2–8 $M_{\odot}$, are known as Herbig Ae/Be stars (HAeBes) (e.g. Thé et al. 1994; Malfait et al. 1998; Sloan et al. 2005). First designated as a separate class of PMS star by Herbig (1960), HAeBes are higher-mass counterparts of CTTS, with the former also showing excess IR emission in their SEDs and Balmer line emission in their spectra. While they cover the same period of evolution as CTTS and display similar observational characteristics, a separate designation is warranted since the physics of the stellar interior between these two types of object differs. The cores of CTTS are convective; the inner regions have a sufficiently high opacity for the transport of energy by convection to dominate over that by radiation. Since HAeBe stars are much more massive, the average opacity throughout the star is lower and the stellar core is radiative rather than convective. This has the knock-on effect that the pre-main-sequence tracks of HAeBes on the Hertzsprung-Russell (HR) diagram differ from those of CTTS. HAeBes follow a horizontal radiative track (where the temperature increases with only a small change in luminosity) for the majority of the star's contraction towards the main sequence (MS) (Henyey et al. 1955; Palla & Stahler 1993), whereas T Tauri stars initially follow a vertical convective track, with decreasing luminosity while remaining at a roughly constant temperature, before commencing along the radiative track towards the MS (Hayashi 1961; Cohen & Kuhi 1979)

1.3 Observations

1.3.1 Classical T Tauri stars

The first suggestion that T Tauri stars should be classified as a unique group was noted by Alfred Joy in 1941 during a study of variable stars, in which T Tauri itself was recognised as part of "a small but important group which deserves more attention than it has yet received" (Joy 1942). This was shortly followed with the publication of a set of criteria describing observational characteristics which were found to be unique to a small subset

of variable stars, of which T Tauri was the prototype. Namely TTS were characterised as being low-luminosity objects of spectral type F5–G5 with strong emission lines, showing irregular light variations of about 3 mag, and being associated with nebulosity (Joy 1945). In a further spectroscopic study soon after, Joy found that examination of short-wavelength absorption lines was not possible since the spectra of many CTTS showed the presence of "an unknown hot source which produces an overlying continuous spectrum, strong in the violet region" (Joy 1949). This so-called 'veiling' results in partial filling in or even complete removal of absorption lines present in the UV and optical region (see e.g. Bertout 1989). Another observation worth noting here is that CTTS were found to have much broader absorption lines than those found in main sequence stars of corresponding spectral type, implying that CTTS are faster rotators (Herbig 1952).

The following few years saw a great deal of progress in explaining these observations; CTTS were found to be newly formed stars undergoing contraction which would end up as main sequence stars of an earlier spectral type than that observed during the CTTS phase. This process of contraction reconciled the rotational velocity problem since the conservation of angular momentum would cause the star to spin up as a consequence of its decreasing radius, resulting in good agreement between observational evidence and theoretical calculations of the expected rotation rate for a star of a given mass. It was first proposed that CTTS were undergoing gravitational contraction by Armenian-Soviet astrophysicist Viktor Ambartsumian in 1947, although this idea did not gain serious recognition in the West until the mid 1950s (e.g. Herbig 1957). Around this time Herbig also redefined T Tauri stars purely spectroscopically based on specific emission lines that are present in their spectra (e.g. Herbig 1962, and references therein), removing Joy's criteria of variability and association with nebulae as primary defining features. This was revised again two decades later since certain spectral lines specified in Herbig's definition were not visible in some TTS, and were not necessarily always visible even in TTS that had displayed them previously due to the intrinsic variability of these objects. Thus, the final explicit working definition returned to Joy's mention of association with regions of ob-

scuration, as well as the presence of hydrogen Balmer lines and Ca II lines in emission, with the Hα line having an equivalent width of at least 5 Å, and finally with a spectral type later than F (Bastian et al. 1983).

Aside from evidence pointing towards contraction towards the main sequence, the youth of CTTS is evident due to their frequent association with young objects, such as the short-lived OB associations and HAeBes (e.g. Walker 1956; Herbig 1962; Strom et al. 1975). CTTS were also found early on to lie above the main sequence on the HR diagram (e.g. Herbig 1952; Walker 1956). Evolutionary tracks computed by Henyey et al. (1955) and Hayashi (1961) confirmed that CTTS contract towards the MS as they age, and by comparing CTTS positions with these evolutionary tracks CTTS are found to be under 10^7 years old (e.g. D'Antona & Mazzitelli 1994). There are strong lithium absorption lines found in CTTS spectra implying their youth; lithium is destroyed in stellar interiors, but has not had sufficient time to become significantly depleted in TTS. The rate of lithium depletion is increased by convective mixing, in which lithium-rich material flows inward towards the centre of the star where it is burned, and lithium-poor material is dredged upwards (e.g. Bildsten et al. 1997; White & Hillenbrand 2005). This effect is strongest for stars with mass below ~0.6 $M_\odot$, where a convective core is maintained throughout main sequence contraction. The onset of a radiative core at around this limit restricts the lithium mixing such that depletion timescales are longer. Bonsack & Greenstein (1960) found that lithium in CTTS was about 100 times more abundant that the solar value, and correlation between stellar age and lithium abundance was confirmed by Duncan (1981) and Soderblom (1983). While broadly the lithium content of a star can be used to estimate stellar age, there is also evidence for a correlation between lithium abundance and stellar rotation rate. Faster rotators have been found to be systematically more lithium rich than stars that are slower rotators but similar in other respects. It has recently been shown that this correlation exists for pre-main sequence stars as young as 5 Myr old across temperatures which correspond to a mass range of 0.5–1.2 $M_\odot$ (Bouvier et al. 2016). Since young stars accrete material that contains lithium, lithium can still be observed in stars

during its destruction phase. Therefore while the presence of lithium implies stellar youth, there are various processes that contribute both to maintaining the lithium abundance as well as its destruction.

Photometric variability is a key property of CTTS. Generally studies have found that variations in lightcurves are unpredictable and irregular both in time (with variations found to occur over anything between minutes and decades) and magnitude (with variations of several magnitudes having been observed across many wavebands) (e.g. Joy 1945; Mendoza 1968; Appenzeller & Mundt 1989), although a small number were found early on to have a degree of cyclic behaviour with periods of about a week (Herbig 1962, and references therein). The primary source of this variation for CTTS, for both periodic and aperiodic variations, has been attributed to hot spots on the stellar surface (e.g. Bouvier & Bertout 1989; Vrba et al. 1989) producing occasional periodic variability that is similar to the rotation periods of these stars (but not exactly the same; photometric periods are unstable and have been found to vary by a day or two on timescales of a few weeks, e.g. Simon et al. 1990; Bouvier et al. 1995). As well as photometric variations, emission lines have also been found to vary in intensity. Vrba et al. (1993) found a strong correlation between photometric variability and the equivalent width of Hα, implying that the same mechanism is responsible for both of these phenomena. While other studies have also found periodic line profile variations to be similar to the stellar rotation period (e.g. Johns & Basri 1995; Johns-Krull & Hatzes 1997), there have also been results showing no such periodicity, instead finding more stochastic spectroscopic variability (e.g. Johns-Krull & Basri 1997; Smith et al. 1999), as observed in the photometry. Hot spots are formed as a direct result of accretion of circumstellar material, where periodic variations are due to mass accreting at a constant rate and aperiodicity in both photometric and spectroscopic observations is due to variable rates of accretion (e.g. Bertout et al. 1988; Bouvier & Bertout 1989; Vrba et al. 1993). Evidence for infall is found in spectral lines, with many CTTS showing inverse P Cygni (IPC) profiles, in which a redshifted absorption component is present in the central emission line profile (e.g. Walker 1972; Appenzeller & Wolf

1977; Edwards et al. 1994). These absorption components appear at up to 400 km s^{-1} indicating that the infalling material is travelling at free-fall velocities.

Broad classical P Cygni profiles, in which the absorption component occurs on the blue side of the emission line, signify high-velocity outflows (e.g. Kuhi 1964; Edwards 1979; Mundt 1984). Blueshifted forbidden lines are also found to be present (Appenzeller et al. 1984; Edwards et al. 1987), allowing the outermost regions of the outflow to be probed where the gas density is sufficiently low for these lines to form. As with mass infall, strong periodicity has sometimes been detected in these outflow signatures, but outflows are not always present in observations. Mass loss rates have been found to correlate with mass infall rates, suggesting that outflows are powered by accretion (Cabrit et al. 1990; Edwards et al. 1993; Hartigan et al. 1995; Johns & Basri 1995). Outflows appear to have a biconical form rather than that of a spherical envelope; observed line profiles are not well-matched by models with spherical outflows, with bipolar winds giving much better fits (Appenzeller et al. 1984; Edwards et al. 1987). More direct evidence for winds with a bipolar geometry has been found in molecular flows emanating from circumstellar regions, signifying both high and low collimation (see review by Lada 1985). High-velocity jets of ionised gas have also been directly observed in optical (e.g. Strom et al. 1986) and radio (e.g. Cohen et al. 1982; Mundt & Fried 1983) continuum observations of T Tauri stars. A more thorough discussion of the different types of outflows observed is given in Section 1.5.

As mentioned previously in Section 1.2, CTTS are surrounded by an optically thick circumstellar disc which is observed as an IR excess. This was first observed by Mendoza (1968) who found that the IR excess was too large to be explained by interstellar extinction and hypothesised the presence of a circumstellar dust cloud which absorbs optical radiation and reradiates it in the IR. Thermal emission from circumstellar dust was confirmed to be the source of this excess by Cohen & Kuhi (1979). Circumstellar disc structures were proposed in favour of a circumstellar dust shell by Cohen & Schmidt (1981) and Rydgren et al. (1982) with direct observations of extended disc-like structures following

soon after (e.g. Beckwith et al. 1984; Grasdalen et al. 1984). Bertout et al. (1988) found strong evidence that these were *accretion* discs, with continuum observations fitted well by an accretion disc model where the source of the UV excess often observed in CTTS is a boundary layer at which point the Keplerian circumstellar disc meets the slowly-rotating photosphere, liberating the required energy through shear between these two surfaces. However, they also found that photometric observations from one star, DF Tau, could not be reproduced by the axisymmetric accretion of the boundary layer model and instead found observations were fitted much better by a single hot spot on the photosphere. They suggested magnetically controlled accretion as an alternative, in which material is accreted along a dipolar magnetic field and accretion energy is released in shocks from material impacting the photosphere, producing hot spots at the magnetosphere poles.

While the suggestion of magnetospheric accretion by Bertout et al. enabled explanations for numerous observational problems (for instance the origin of stellar hot spots and the high velocities of infalling material), at this time only measurements of surface magnetic activity had been achieved (e.g. Montmerle et al. 1983; Bertout 1989; Basri et al. 1992). The presence of large circumstellar magnetic fields around CTTS was not confirmed by direct measurements until a few years later (e.g. Guenther et al. 1999; Johns-Krull et al. 1999a), although significant magnetic fields had previously been successfully measured in WTTS (Basri et al. 1992). One method of detecting magnetic fields is Zeeman broadening, in which splitting of spectral lines due to the Zeeman effect is not discrete but contributes to an overall broadening of the line, although this is less effective for extremely young stars where it is not possible to separate the Zeeman broadening from the Doppler broadening produced by these fast rotators. Alternatively, polarisation measurements can be used. Zeeman-sensitive lines undergo circular polarisation in the presence of magnetic fields, with the shift between these lines proportional to the size of the magnetic field. Each of these consequences of the Zeeman effect, i.e. polarisation and broadening, have successfully been used by Johns-Krull et al. (1999a,b) to measure the magnetic field strength of the CTTS BP Tau, with each method finding a magnetic field

strength of ~ 2.1 kG; sufficiently strong to disrupt a circumstellar disc.

In summary, the observational properties of CTTS include variability, UV veiling, an infrared excess, both emission and broad absorption lines (including strong lithium lines), and both regular and inverse P Cygni profiles. These observations point to CTTS being young stellar objects undergoing contraction as they approach the main sequence. They are surrounded by an optically thick dusty disc from which they accrete matter, as well as undergoing mass loss through outflows on various scales. Photometric variability has been shown to be similar to the stellar rotation period but more stochastic behaviour has also been observed. Frequent correlation between infall and outflow signatures implies that these two processes are directly related. These objects have also been found to harbour strong magnetic fields capable of disrupting accretion discs, increasing the credibility of the magnetospheric accretion paradigm.

1.3.2 Herbig Ae/Be stars

While Herbig Ae and Be stars are often grouped together as one class, they are actually quite distinct in that HAes are higher-mass analogues of CTTS whereas the more massive HBes remain fairly obscured by circumstellar gas and dust until they reach the MS (here we define HBes to be of spectral type B5 or earlier in keeping with the categorisation used by Natta et al. (2001), with HAes comprising of later spectral types). HAeBes are much more luminous than CTTS but are also less common since the number of high mass stars in general is smaller than the number of low mass stars, and the contraction timescale towards the main sequence for high mass stars is shorter (for HAes) or virtually non-existent (HBes). First studied by Herbig (1960) in an effort to identify the progenitors of higher-mass stars using similar indicators as for CTTS, HAeBe characteristics were defined as A-type or earlier with emission lines (hence the ‘e’ in HAeBes), associated with an obscured region, and illuminating nearby nebulosity. These criteria have since been relaxed, with late F-type stars also considered as part of the HAeBe class as well as candidates which are not associated with obscured regions, although there is now more emphasis on

the requirement to have an IR excess in their spectra (Thé et al. 1994; Malfait et al. 1998). They were found by Strom et al. (1972) to lie on or above the zero-age main sequence confirming the PMS nature of these objects. Their irregular variability (Herbig 1960), spectroscopic similarity to CTTS in both their emission spectra and presence of P Cygni profiles (Strom et al. 1972), and the presence of IR excess signifying a dusty circumstellar region (Strom et al. 1972) also point to a young evolutionary status. Millimeter and sub-millimeter observations have since confirmed the presence of circumstellar discs, rather than dusty shells, around many HAeBes (e.g. Mannings & Sargent 1997; Cesaroni et al. 1997; Natta et al. 2001; Hernández et al. 2005; Beltrán et al. 2014), although detections of circumstellar discs become more difficult for early-type stars due to less time spent unobscured in the pre-main sequence phase and shorter disc lifetimes.Estimated disc fractions for TTS and HAeBe stars are shown in Figure 1.3. There is clearly a significant reduction in disc frequency around HAeBes, with disc fractions of just ∼2–5% for HAeBes in stellar groups with an age of ∼ 3 Myr. Conversely, disc frequencies for low-mass stars of this age are at ∼50%, dropping to ∼ 15% at 5 Myr.

As with CTTS, there is strong evidence for infalling material in HAeBe observations. Hillenbrand et al. (1992) were able to fit SEDs with an optically thick accretion disc containing an optically thin inner disc region. Lada & Adams (1992) also found an inner hole was required in order to match JHK colour-colour diagrams, specifically with an inner disc temperature of 2000–3000 K, near the dust sublimation temperature. However, the models computed by Hillenbrand et al. required large accretion rates of $\sim 10^{-6}$ $M_\odot$ yr^{-1}, which were shown by Hartmann et al. (1993) to require optically thick inner regions, rendering the optically thin inner geometry incompatible. In a study of HAe disc properties, Natta et al. (2001) reconciled this problem with a 'puffed-up' disc geometry. In this model the disc is truncated at around the dust sublimation radius, leaving the inner rim of the disc exposed to stellar radiation. The resulting increase in temperature relative to the disc midplane causes the inner wall to puff up, intercepting a significant fraction of stellar radiation which is then emitted from the disc predominantly in the near-

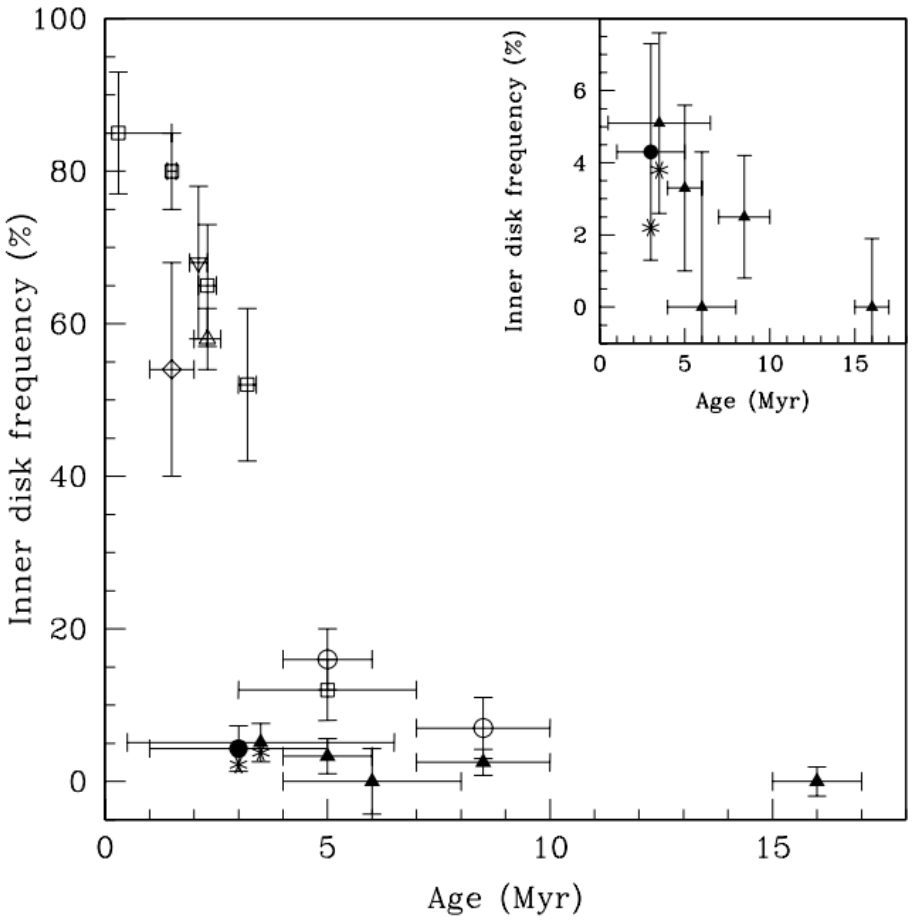

Figure 1.3: Disc fractions around low- and intermediate-mass stars in various stellar groups as a function of age. Open symbols represent low-mass stars and solid symbols represent intermediate-mass stars. The youngest low-mass stars plotted here have disc fractions of up to $\sim$ 90%, dropping to $\sim$ 15% by 5 Myr. No such decrease is present in intermediate-mass stars, with disc fractions of $\sim$ 5% at 3 Myr, declining towards 0% at 15 Myr. Reproduced from Hernández et al. (2005).

IR. This model was extended by Dullemond et al. (2001) who considered the effect of the shadow cast over the disc from the puffed up inner rim. They found that in some cases the shadow cast is sufficient to cover the entire disc, significantly cooling the disc as a result. HAeBe SEDs show a 10 μm silicate feature with varying strength between stars; disc shadowing significantly reduces the strength of the feature, even eliminating it in some cases, providing a possible explanation as to why this feature was found to be absent from some spectra in a study by Meeus et al. (2001).

In the last few years evidence for magnetospheric accretion has been found from line profile modelling. Muzerolle et al. (2004) found that observed Balmer and sodium line profiles were well fitted by profiles computed from magnetospheric accretion models. However, unlike the case for CTTS, the magnetospheres of HAeBes are significantly further in towards the star than the sublimation radius present in HAeBe discs, and thus the dust disc does not reach the magnetosphere. This leads to the possibility of an optically thin inner gaseous portion of the disc from which material accretes. Magnetic field measurements of HAeBe stars have yielded only low field strengths of order $\lesssim$ 100s G (e.g. Donati et al. 1997; Wade et al. 2005, 2007; Catala et al. 2007; Hubrig et al. 2009).

Evidence for HAeBe outflows is well-established (e.g. Finkenzeller & Mundt 1984; Skinner et al. 1993), with magnetic origins often proposed (Praderie et al. 1986; Catala et al. 1999). Outflow signatures differ slightly from those of CTTS in that the line profiles of the former are much more symmetric than in the latter (Böhm & Catala 1994). Less symmetric blue-shifted HAeBe profiles appear to be associated with more heavily embedded objects (Corcoran & Ray 1997). Corcoran & Ray interpreted these results as an evolutionary sequence of a two-component outflow, with highly-collimated jets giving rise to strongly blue-shifted lines for the youngest objects. The lower blueshifted velocities observed in more evolved objects indicate that jets are no longer present, with just a low-velocity disc wind remaining which itself disappears over time.

1.4 Magnetospheric accretion

Circumstellar accretion discs were observationally identified by Bertout et al. (1988), but their presence had been suggested theoretically many years earlier from pioneering work by Lynden-Bell & Pringle (1974). This model consists of a thin boundary layer between the accretion disc and the star. As mentioned in Section 1.3.1, while this model simultaneously explains observational results such as the IR and UV excesses while also allowing for stellar outflows along the rotation axis, there are numerous problems. The high velocities of the absorption feature in IPC profiles show material is travelling ballistically, whereas infall velocities in the boundary layer model would be no more than a few km s^{-1}. Beckwith et al. (1990) found that NIR emission from observations of CTTS was smaller than expected for a disc extending to the stellar surface, leading them to conclude that the inner region of the disc must be clear of material. Finally, CTTS are observed to rotate at an order of magnitude below their break-up velocity, whereas the equatorial accretion of the boundary layer model would result in enough inward angular momentum transfer to spin up the star to about half its break-up velocity (Hartmann & Stauffer 1989). All of these problems can be solved with the magnetospheric accretion model.

First developed by Ghosh & Lamb (1979) in their investigation of accreting magnetised neutron stars, the stellar magnetic field is assumed to be dipolar and nearly aligned with the stellar rotation axis, with magnetic field lines threading the circumstellar disc. In the innermost parts of the disc the stellar radiation is intense enough to ionise a significant fraction of the disc material, allowing the material to couple to the magnetic field. At distances of a few stellar radii from the star, the magnetic field threading the disc is sufficiently strong for the magnetic pressure to overcome the ram pressure of the accreting material. At this point material preferentially travels in a poloidal direction up the field lines, rather than continuing its inward path towards the star, causing the disc to become truncated at a few stellar radii. Circumstellar material attaches to these field lines, travels along them, and falls onto the stellar surface. At the point of the corotation radius, $R_{\rm co}$,

the angular velocity of the star, $\Omega_\star$, is equal to the Keplerian velocity of the disc:

$$R_{\rm co} = \left(\frac{GM_\star}{\Omega_\star^2}\right)^{1/3}, \tag{1.2}$$

where $M_\star$ is the mass of the star. The braking torque of the field lines outside the corotation radius of the disc balances the spin-up torque of the material accreting from within the corotation radius, preventing the star from spinning up, effectively locking the stellar rotation period to the disc rotation period at the truncation radius. In order for material to accrete, the magnetospheric truncation radius must be less than the corotation radius; otherwise, disc material with a smaller angular velocity than that of the star will be attaching to the field lines and will undergo a centrifugal force causing the material to be flung away from the star. The magnetic field would also cause the star to brake, effectively moving $R_{\rm co}$ further in. This model was applied to CTTS by Königl (1991) in order to explain the low rotation rates of these stars. Results showed that steady state accretion requires a $\sim$ 1 kG field, in agreement with observational magnetic field measurements, and that the observed UV excess can be accounted for by accretion shocks at the magnetosphere poles on the stellar surface, as suggested by Bertout et al. (1988). Camenzind (1990) found that for a 1 kG field and an accretion rate of 10^{-7} $M_\odot$ yr^{-1}, the disc will be truncated at a few stellar radii, consistent with the findings of Beckwith et al. (1990) that SEDs are best fitted when the inner disc radius falls in the range of 0.05–0.3 AU. The high infall velocities inferred from IPC profiles are also naturally explained by this model since material will fall ballistically onto the stellar surface, providing sufficiently high velocities (Calvet & Hartmann 1992). Rotation periods of CTTS were modelled by Collier Cameron & Campbell (1993) who included the PMS contraction phase in their angular momentum calculations as well as the disc interaction. They found that for a magnetic field of a few hundred gauss and an accretion rate of a few 10^{-8} $M_\odot$ yr^{-1}, a star is able to maintain an equilibrium rotation period of between 2 and 10 days, which is consistent with the CTTS rotation rates observed.

While a magnetospheric accretion model (see Figure 1.4) was able to provide good

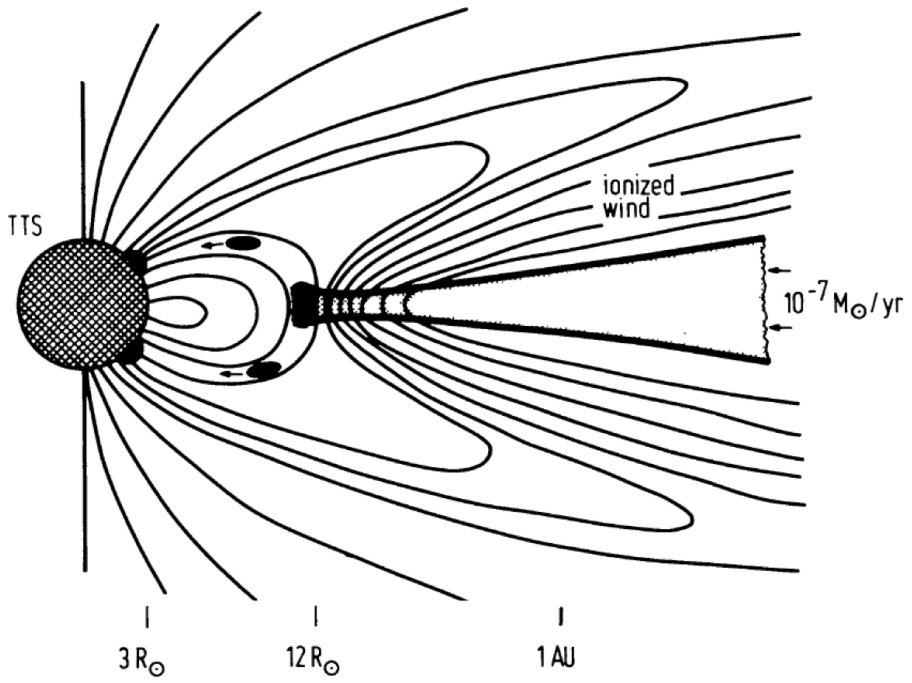

Figure 1.4: The configuration of a magnetic field aligned with the stellar rotation axis. Closed field lines truncate the disc and provide a pathway for disc material to accrete onto the star. Hot spots, shown here as black areas on the stellar surface, are produced at the point where closed field lines threading the circumstellar disc join the star, causing high-velocity material to impact the stellar surface. Open stellar and disc field lines provide sources of outflows. Reproduced from Camenzind (1990).

fits to SEDs for DR Tau by Kenyon et al. (1994), they found that it was unable to explain variations in their optical/NIR light curves. By tilting the magnetic axis relative to the rotational axis, the hot spot produced is no longer a symmetric ring around the rotation axis but rather a bright ring at the magnetospheric pole that sweeps in and out of view with stellar rotation. Bouvier et al. (1995) also suggested that periodic variations in CTTS could be due to an inclined dipolar field. Mahdavi & Kenyon (1998) ran a series of models investigating the effect that different dipole offset angles and different inclinations of the star with respect to the observer would have on photometric variations, where a stellar inclination of 0° is for a star viewed pole-on and a dipole offset angle of 0° is for a magnetosphere aligned with the stellar rotation axis. They found that stars viewed nearly pole-on require a significant dipole offset, greater than 50°, in order for any photometric variability to be observed. Bouvier et al. (1999) used this inclined dipole model to explain

photometric observations of the CTTS AA Tau. The observed light curve for AA Tau is fairly unique, attributed to AA Tau's inclination by Bouvier et al.; it is over 70°, i.e. nearly edge-on, causing photospheric occultations to be more conspicuous than in other CTTS that may also experience this phenomenon. Circumstellar material may load onto the field lines either above or below the disc since field lines are closed. For the case of an inclined dipole, field lines threading the disc will be shorter on one side of the disc than the other for some angles of azimuth. Material is more easily loaded onto the shorter field lines, resulting in a vertical non-axisymmetric thickening of the disc, or disc warp. Rotation of the star then results in periodic occultations by the warp. Photometric observations of HH 30, which is a system containing a central YSO surrounded by an edge-on circumstellar disc and bipolar jets, have shown variability in both space- and ground-based observations (e.g. Burrows et al. 1996; Wood et al. 2000). Using *HST* images Burrows et al. drew the conclusion that brightness variations observed in the surrounding reflection nebulae of HH 30 were due to variations in the central light source rather than due to density perturbations in the nebulous material. This variability was also detected in *HST* images at various wavelengths by Stapelfeldt et al. (1999) and Cotera et al. (2001), who each found that models with a single hotspot produced in the magnetospheric accretion process could fit the observations. The same conclusion was drawn by Wood et al. (2000), comparing their models with ground-based *VRI* photometric observations.

Morphologies of line profiles for different objects have also been found to vary, with stellar inclination angle and dipole offset being attributed to the cause of these variations. In early line profile studies Hartmann et al. (1994) found that strong asymmetry in the profile is to be expected from low inclination angles, with greater emission on the red side of the profile, since the blue contribution from the stream on the far side of the star is occulted by the disc. Higher inclination angles, when the line of sight intercepts the circumstellar disc, produces more centrally-peaked profiles since the lower-velocity material near the disc surface is travelling perpendicular to the line of sight. Line profile shapes are significantly affected by outflows, the effects of which are discussed further

in Section 1.5. The full range of profile morphologies is so diverse that Reipurth et al. (1996) produced an atlas of Hα profiles, defining four main classes of profile morphology dependent on the strength of the secondary emission peak relative to the primary, with additional subclasses depending on whether the secondary peak appears on the blue or red side of the primary. A total of seven profile morphologies were defined. This classification sequence was studied further by Kurosawa et al. (2006) who found that every type of profile morphology was reproducible by varying the stellar inclination, accretion rate and outflow rate across their models.

When taken together, photometric and spectroscopic results often show similar variable behaviour. For instance, in a further study by Bouvier et al. (2003) on the variability of AA Tau it was found that the periodic photometric and spectroscopic variability coincided, with the with weaker continuum excess veiling and weaker line fluxes in general occurring during quieter photometric periods. The discussion so far has established that periodic and spectroscopic variability is as a result of hot spots and, in the case of AA Tau at least, a disc warp intercepting the line of sight with stellar rotation. Changes in variable behaviour thus imply that something has caused the way in which the magnetosphere interacts with the star and disc to change. Bouvier et al. suggested that this is an example of magnetic field lines twisting and opening, preventing material from accreting, then reconnecting in the original dipolar geometry allowing accretion to proceed. Evidence for twisted field lines has been reported for the CTTS SU Aur by Oliveira et al. (2000), who found that the variability observed in certain spectral lines was time-lagged with respect to other lines. They proposed that this time lagging was due to a twisted magnetic field causing the lines form in the part of the accretion funnel closer to the disc to be azimuthally shifted from lines that form further along the funnel towards the star. This process was proposed to occur quasi-periodically by Aly & Kuijpers (1990) in their study of flaring neutron stars. Since the disc undergoes differential rotation about $R_{\rm co}$ and the footprints of the field lines are anchored in the disc, the field lines will be dragged by the rotating disc and will experience a toroidal flux. The increased pressure along

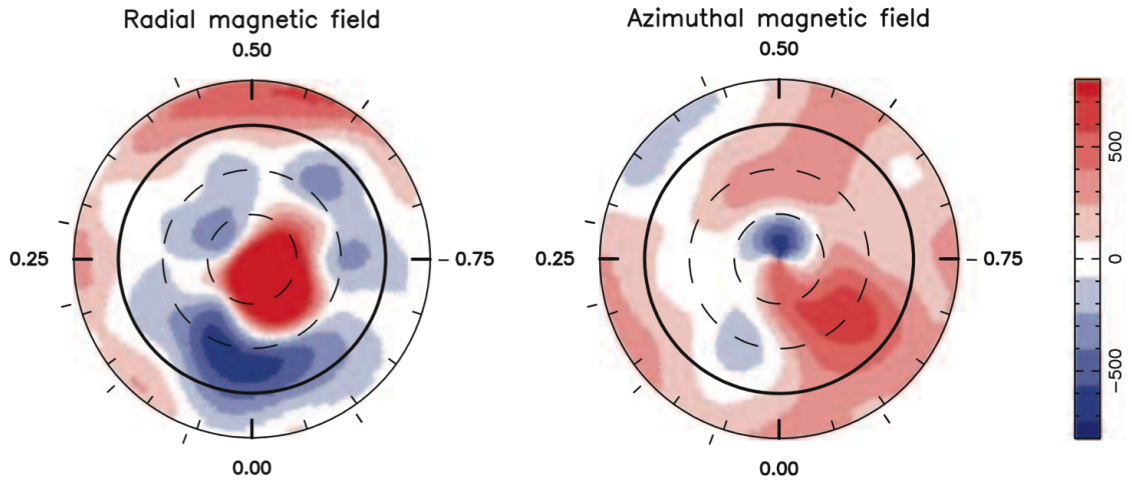

Figure 1.5: Topology of CTTS V2129 Oph reconstructed from ZDI measurements. Radial field components are shown on the left and azimuthal components on the right. Field fluxes are labelled in G. Reproduced from Donati et al. (2007).

these toroidal components causes the field lines to expand away from the star and break. Magnetohydrodynamic (MHD) simulations of this phenomenon in YSOs have found that they are likely to undergo field line expansion and reconnection events on timescales of the order of a few rotation periods (e.g. Goodson & Winglee 1999; Uzdensky et al. 2002; Romanova et al. 2002). The resulting disruption to the accretion process causes the hot spots to die down as well as the inner disc warp, in the case of at least AA Tau, explaining the lack of variation in photometry and spectroscopy. In addition to these relatively short-term quieter periods, variability appears to change over timescales of years (e.g. Bouvier et al. 2007), suggesting long-term variability in the portion of the magnetic field that interacts with the disc on timescales of ~years. To avoid confusion, periodic variability due to stellar rotation will be referred to as rotational variability, and changes to the dynamics of the star-disc-magnetosphere system such as expanding magnetic field lines or changes in mass accretion rate will be referred to as intrinsic variability.

In order to test the assumption of the magnetic field being a large-scale dipole, results from polarisation measurements can be used to infer details about the magnetic field topology. The process of Zeeman-Doppler imaging (ZDI) involves measuring the Doppler shifts of Zeeman-sensitive lines with stellar rotation. The overall field struc-

ture is obtained by mapping the positions of magnetic spots on the stellar surface, where spot positions are found using radial velocity measurements of the star, as with standard Doppler imaging. The orientation of the field lines is found using circular polarisation measurements, which vary in amplitude or shape depending on the orientation of the field to the observer (Donati & Brown 1997). The first field map of a CTTS using this method was published by Donati et al. (2007) (see Figure 1.4). While many models assume a dipolar magnetic field for simplicity, ZDI results have shown that this is not necessarily true. However, Valenti & Johns-Krull (2004) found that while the coronal field structure is more complicated, a dipolar field is likely to dominate at the inner edge of the accretion disc.

1.4.1 Advances in numerical models

While the analytical model of Königl (1991) was sufficient to demonstrate how the magnetospheric accretion phenomenon could apply to YSOs, significant improvements have been made over the last two decades in order to understand the physical processes that are behind the wealth of observational results acquired for these objects. There are two primary techniques in modelling magnetospheric accretion: magnetohydrodynamic (MHD), and radiative transfer (RT). Advances in these techniques are summarised here.

MHD modelling

Magnetohydrodynamic methods are concerned with modelling the dynamics of fluid systems in the presence of a magnetic field. The first significant improvement in modelling the interaction between stellar magnetic fields and circumstellar discs was made by Shu et al. (1994), who considered not only spin-down, magnetospheric accretion, and disc truncation, as in previous models, but also introduced winds and outflows. In this picture, the circumstellar disc is conductive and shielding currents prevent the magnetic field from intersecting the disc at any point except for at a range of radii about $R_{\rm co}$. At around this point the field lines are connected to the star, but just outside of this the field lines bow

away from the star. Here, the magnetic pressure is sufficiently weak for the ram pressure of the gas to open these bowed field lines, resulting in an outflow. Since the disc is mostly devoid of any magnetic field interaction, except in the innermost regions, the outflow is only generated in this region, known as an *X-wind*.

Outflow mechanisms were studied further by Miller & Stone (1997). They employed the ZEUS-2D (Stone & Norman 1992) MHD code to model three different magnetic field topologies: a disc which is threaded throughout by a simple dipole field, as in the Ghosh & Lamb model; a shielded disc allowing field penetration only in the innermost regions of the disc, as in the Shu et al. model; and a stellar dipole field threading the disc with an additional vertical disc field. The path of accretion varied, from equatorial accretion for a quickly rotating star with a pure dipole geometry to polar accretion for a uniform axial disc field in addition to the dipole. Each of these setups produced channelled winds, which formed from reconnection events in the two single poloidal field models and from the disc surface along open field lines in the axial field plus dipole model.

A further MHD model was presented by Goodson et al. (1997) with the focus on modelling the launching of stellar jets. The resulting mechanism was time-dependent, producing episodic mass loss as field lines inflate then reconnect. However, like the Miller & Stone model, simulations were run over just a few stellar rotations. The first high-resolution model was presented by Goodson et al. (1999), enabling a study of the structure within jets. The earlier low-resolution work of Goodson et al. showed that the magnetic loops which form from differential rotation expand and drive plasma either in a highly-collimated jet away from the magnetic poles or in a lower-velocity disc wind, depending on whether the outflow is emanating from field lines that are connected to the star or to the disc. Their later work showed that these jets contain high-density condensations of plasma, or 'knots', due to the episodic nature of these outflows, which is consistent with observations. This work demonstrated the link between magnetic field expansion and jet formation. Goodson et al. suggested improvements that should be made in order to test the model with CTTS variability; particularly the inclusion of radiative transfer capabilities in

order to simulate line and continuum emission as a function of time, providing theoretical comparisons to spectroscopic observations of jet-forming regions.

Disc accretion was studied in the context of MHD by Romanova et al. (2002), who developed a model to investigate accretion onto rotating stars with a dipolar magnetic field aligned with the rotation axis. These models successfully demonstrated the truncation of the circumstellar disc and formation of funnel flows at the magnetosphere radius. This work was extended by Romanova et al. (2003, 2004) to incorporate magnetospheric accretion onto inclined dipoles. In the first of these studies, non-axisymmetric accretion was found to become notable at dipole offsets as small as θ ~2–5° and to consist of a roughly dipolar flow for $\theta \lesssim 30°$, with more complicated flow geometries for higher dipole offset angles. The second of these studies focussed on photospheric hotspots, investigating physics properties such as temperature, density, and velocity in the hotspots. This work demonstrated that these parameters increase in value towards the centre of the hotspots, such that lower temperatures and densities yield larger hotspots and *vice versa*. Light curves were also calculated as part of this study, and were found to take a roughly sinusoidal form for stellar magnetic field offsets of $\theta \lesssim 45°$ and inclinations of $i \lesssim 60°$.

MHD models enable the physical study of large-scale fluid systems, in this case disc material, funnel flows, and stellar photospheres, and the mutual interaction between these components. However, in order to make sense of these systems in the context of observational astronomy, radiative transfer models are required to simulate the radiation emitted from these sources. The results of these simulations may then be compared directly with observations.

RT modelling

The radiative transfer (RT) model of Hartmann et al. (1994) was sufficient for a basic analysis of line morphology, as mentioned earlier, for initial tests of the magnetospheric accretion paradigm. While results were sufficient to demonstrate that it was possible for emission lines to form in the accretion streams, the two-level atom used restricted

Hartmann et al. to the Balmer lines of hydrogen. This model was modified by Muzerolle et al. (1998) who removed the previous two-level approximation and instead used a multi-level hydrogen atom in statistical equilibrium. Since the emission line widths observed in these profiles are so broad, calculations were performed under the Sobolev approximation (Sobolev 1957); in order to calculate the level populations of a particular atomic species the radiation field intensity must be calculated. The presence of large velocity gradients allows a simplification of this problem since atoms emitting a specific line transition are able to interact only with other atoms which have a similar velocity. When Doppler broadening dominates over natural line widths, the atoms that are able to interact with one another occupy very thin volumes, allowing the assumption to be made that only the local radiation need be considered. The Sobolev approximation only holds for large velocity gradients, where the larger the velocity gradient, the better the approximation holds. Line profile calculations were further improved by Muzerolle et al. (2001) who included line damping. Since the Sobolev method relies on the dominance of Doppler broadening, it prevents other broadening mechanisms from being treated. Line profile calculations instead required a ray-by-ray calculation, in which intensities are calculated for a number of rays travelling parallel to the line of sight and integrated to find the total emergent flux at a particular frequency. The inclusion of damping provided much better fits with observations, particularly in the more optically thick lines such as Hα, since line width dependence was no longer restricted to the infall velocity of the gas, enabling much higher velocity wings.

The code used for the work presented in this thesis is the three-dimensional Monte Carlo radiative transfer code TORUS (Harries 2000). In order to resolve length scales across many orders of magnitude, for instance in this case from accretion spots to the outer disc, the adaptive mesh refinement (AMR) grid is utilised (Harries et al. 2004) enabling high-resolution calculations where required without being computationally expensive in low-density regions. A description of the numerical methods employed in TORUS is given in Chapter 2. Hydrogen emission line profiles have previously been computed using TORUS in

magnetospheric accretion studies for non-axisymmetric accretion (e.g. Symington et al. 2005). Hybrid models consisting of both accretion and a disc wind were presented by Kurosawa et al. (2006) in their study of Hα formation, with the result that numerous profile morphologies were able to be reproduced. Observations by Edwards et al. (2003) demonstrated how the He I λ10830 line is a useful probe of winds in CTTS. This was followed by a more thorough study (Edwards et al. 2006) with new measurements demonstrating how sensitive this line is to inner winds. Torus was thus extended by Kurosawa et al. (2011) to compute helium ions in addition to the hydrogen atoms in previous models, enabling an even more detailed study of both winds and accretion flows to be undertaken.

1.5 Outflows

Evidence of outflows from YSOs is evident on a number of scales. The primary types of outflow observed are stellar winds, disc winds, and jets. The disc wind paradigm was first suggested by Blandford & Payne (1982) in the context of black hole accretion discs. For a wind to launch along field lines, the field must not exceed an angle of 60° to the disc. The first evidence for a connection between disc accretion and outflows in YSOs was provided by Cabrit et al. (1990), who found that forbidden line luminosity and IR luminosity were correlated. Since there was no correlation between the line luminosity and the photospheric luminosity, Cabrit et al. concluded that the strength of the observed outflows was powered by discs rather than stars. Disc winds can be formed either from uniform threading of the disc by the magnetic field, or by the X-wind model of Shu et al. (1994), discussed in the previous section.

Jets are fast-flowing disc winds which are highly collimated towards the rotation axis, and appear to emanate from closer to the star than the slower disc winds (e.g. Hamann 1994; Appenzeller et al. 2005). In a study of CTTS and HAeBes, Hamann found opening angles of $\lesssim 20°$ for the highest-velocity line profiles, consistent with the strong collimation of jets. Hamann also found that high- and low-velocity outflow signatures tend to appear at the same time, indicating a common origin. The effects of jets

on the circumstellar environment are often observable as Herbig-Haro objects; regions of molecular gas, sometimes with a companion object on the opposite pole, that have been impacted by partially ionised high-velocity material moving away from the central stellar source.

Stellar winds flow along the open magnetic field lines that are anchored into the photosphere. These winds have been proposed as an alternative method of removing stellar angular momentum to explain low rotation rates, as an alternative to disc-locking (e.g. Matt & Pudritz 2005b). The argument is that there is sufficient gravitational potential energy released during accretion for these stellar field lines to open, resulting in a system that has considerably more open field lines than the generally assumed closed system, whose field lines only tend to open periodically during reconnection periods.

1.5.1 Hybrid infall and outflow models

The significant contributions of outflows to observational results makes the inclusion of outflows in accretion models absolutely necessary in order to fully explain observations. While the source of outflows in the magnetospheric accretion paradigm has long been considered conceptually (e.g. Shu et al. 1994), the fist hybrid models combining accretion and outflows in line profile studies were computed over a decade later by Alencar et al. (2005). Previous accretion-only models by Muzerolle et al. (2001) demonstrated that computed line profiles were able to fit observations very well with the exception of narrow blueshifted absorption seen in the profile of DR Tau. Using the Blandford & Payne model of an axisymmetric steady disc wind flow, Alencar et al. found that wind features were best fitted by a collimated ($\sim 30^{\circ}$) disc wind emanating from the inner disc radius, where extended disc winds at more than a few stellar radii from the corotation radius providing poor fits.

The dependence of line profile morphology on various parameters was studied by Kurosawa et al. (2006). The line profile classification scheme of Reipurth et al. (1996) defines symmetric profiles as type I, double peaked profiles where the secondary peak

exceeds half of the maximum of the primary as type II, double peaked profiles where the secondary peak is less than half of the strength of the primary as type III, and emission profiles with superimposed blue- or redshifted absorption, i.e. P Cygni or IPC profiles. For profiles where the secondary peak falls blueward of the primary peak a subcategory B is assigned, with subcategory R if the secondary peak lies on the red side. The profiles that Kurosawa et al. (2006) calculated in accordance with this scheme are given in Figure 1.6. While each of the profiles were achievable, they were not all produced from the initial grid of parameters, with less frequent morphologies requiring very specific conditions. The profiles that particularly require a disc wind are types IV-B, the classical P Cygni profile, and III-B, with a weak secondary blue peak. The type IV-B profile was difficult to reproduce since the extent of the absorption component was beyond the emission line wing, preventing sufficient velocities from being reached with the disc wind model. Presumably a highly collimated jet or a stellar wind is necessary to reach such high absorption velocities. Type II-B profiles, with a strong secondary blueward peak, may or may not require a disc wind, depending on the stellar inclination.

Outflows are all the more important to consider in models since not only do they appear in these accreting systems, but there is evidence of outflows being powered by the accretion process itself (e.g. Cabrit et al. 1990; Hartigan et al. 1995). An MHD investigation carried out by Romanova et al. (2009) found that outflows sharing some characteristics the X-wind configuration of Shu et al. (1994) occurred at the disc-magnetosphere boundaries of both slowly- and rapidly-rotating stars, with the addition of an axial jet contribution in the latter. These winds were found to take the form of a thin conical shell away from the disc, and were also found to be long-lasting, stable phenomena.

In an extension of this work, Kurosawa & Romanova (2012) added magnetospheric accretion flows in order accurately to model the hydrogen and helium line profiles that would be formed in systems with this conical wind. Radiative transfer models were used to produce line profiles over a range of inclinations, luminosities, and temperatures using this geometry, finding that a conical shell wind can make a significant contribution to the

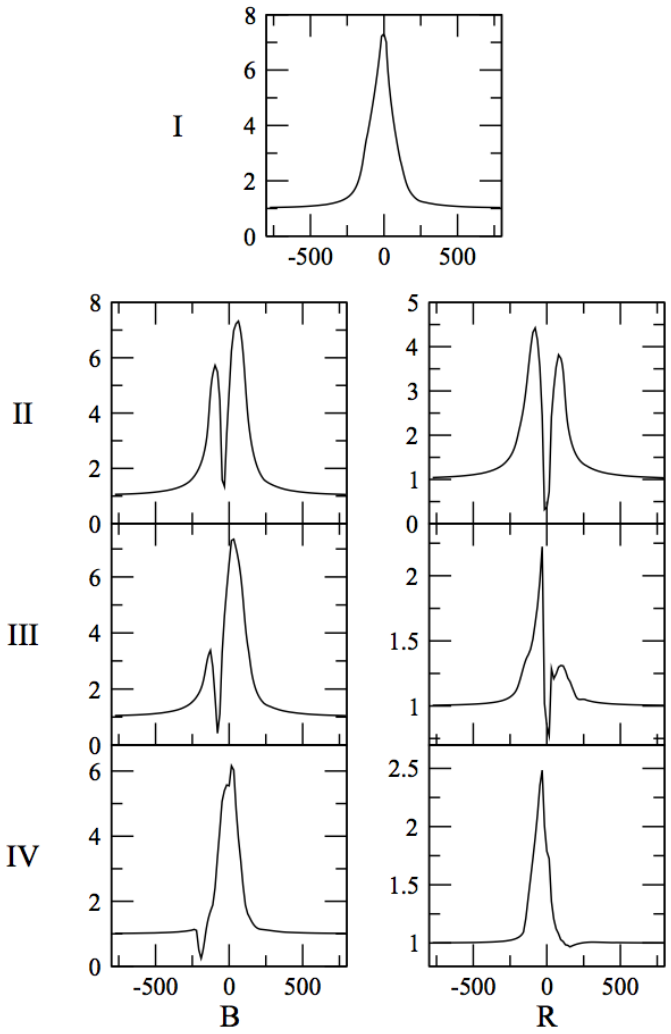

Figure 1.6: Synthetic Hα profiles demonstrating the profile classification scheme of Reipurth et al. (1996). By changing parameters such as accretion rate, mass loss rate, inclination angle and accretion flow temperature. Reproduced from Kurosawa et al. (2006).

hydrogen line profiles modelled but less to to the helium lines. The implementation of a stellar wind was suggested as a further avenue for study in order to test the effects that this alternative outflow would have on these line profiles.

1.6 Thesis aims

The focus of this thesis is on using radiative transfer modelling to examine the inner discs of CTTS and HAeBes; in particular, the dynamic interaction between the stellar magnetic field and the inner regions of the circumstellar disc in CTTS, and the likelihood of the survival of dust in the inner regions of HAeBe circumstellar discs. Observational data from numerous sources using various techniques, including photometry, spectroscopy, and interferometry, have been compiled in order to test the results of these simulations.

In Chapter 2 I present an overview of the theory of radiative transfer and describe the radiative transfer model TORUS. In Chapter 3 I present the results of photometric modelling of the CTTS AA Tau in the context of a magnetically-induced disc warp periodically obscuring the photosphere. This subject is continued in Chapter 4, in which I present the results of spectroscopic modelling of hydrogen lines in order to test line formation in magnetic accretion streams and a disc wind. In Chapter 5 the focus is moved to the inner discs of HAeBes. After an introduction to the technique of interferometry and visibility modelling, I examine the possibility of refractory dust grains surviving in the inner regions of circumstellar discs where silicate grains are not able to survive. This is achieved using SEDs to determine the disc geometry and visibilities from interferometric observations to test the sublimation temperatures required in order for dust to survive these temperatures, enabling observations to be reproduced. In Chapter 6 I present a general summary of the results obtained in this thesis and draw concluding remarks on these findings. Finally, I present possible directions for further research based on these findings.

Chapter 2

Numerical Method

In this chapter I describe the TORUS radiative transfer code used to compute the models presented in this thesis, as well as the physical processes that are considered in the code.

Qualitatively, radiative transfer is a fairly simple concept. Photons from a source traverse a medium of given opacity whose constituent gas and dust may absorb or scatter the incoming photons. However, quantitatively it is a complex problem; gas and dust may emit photons and the rate at which they do so can be altered by incident photons. The microphysics involved and the recursive nature of the radiative transfer phenomenon require intricate methods to be employed in order to self-consistently solve the equation of radiative transfer in astrophysical objects. The images and spectra that we obtain from observations of these objects can be strongly affected by the properties of the photons emitted or absorbed in the region of interest, such as photon energies and emission or absorption rates. It is therefore of importance that we understand the process of radiative transfer quantitatively so that accurate models can be developed, enabling these observations to be correctly interpreted.

2.1 The equation of radiative transfer

Electromagnetic radiation undergoes various interactions when propagating through a medium. Emission, absorption and scattering processes cause the intensity of a beam

of radiation to vary as it traverses a given path. The specific intensity of a radiation field, I_ν, is defined mathematically as the energy $\mathrm{d}E_\nu$ transported per unit time $\mathrm{d}t$ as the radiation passes through a surface area $\mathrm{d}A$ inclined at an angle θ to the normal of the surface within a solid angle $\mathrm{d}\Omega$ and in the frequency range ν to $\nu + \mathrm{d}\nu$,

$$I_\nu = \frac{\mathrm{d}E_\nu}{\cos\theta\, \mathrm{d}A\, \mathrm{d}\Omega\, \mathrm{d}\nu\, \mathrm{d}t}. \tag{2.1}$$

A quantitative description of how I_ν varies along a distant element $\mathrm{d}s$ as a result of emission and absorption processes is given by the equation of radiative transfer,

$$\frac{\mathrm{d}I_\nu}{\mathrm{d}s} = -\kappa_\nu I_\nu + j_\nu, \tag{2.2}$$

where κ_ν is the local absorption coefficient, or opacity, which is dependent on the number density of absorbing atoms along the path of the beam and their quantum mechanical state, and j_ν is the emission coefficient.

Alternatively, the equation of radiative transfer can be written in the more simple form

$$\frac{\mathrm{d}I_\nu}{\mathrm{d}\tau_\nu} = -I_\nu + S_\nu. \tag{2.3}$$

Here, S_ν is the source function, defined as the ratio of the emission coefficient to the absorption coefficient. τ_ν is the optical depth, describing the amount of absorption occurring over a given distance, where

$$\tau_\nu = \int \kappa_\nu \mathrm{d}s. \tag{2.4}$$

The differential form of the intensity distribution can be solved by multiplying it through by the factor of $e^{\tau'}$ and integrating across $0 \leq \tau' \leq \tau$, yielding

$$I_\nu(\tau) = I_\nu(0)\, e^{-\tau_\nu} + \int_0^{\tau_\nu} e^{-(\tau_\nu - \tau'_\nu)} S_\nu(\tau'_\nu)\, \mathrm{d}\tau'_\nu. \tag{2.5}$$

Another useful measure of intensity is J_ν, the mean intensity, which is the average of the specific intensity integrated over all solid angles, i.e.

$$J_\nu = \frac{1}{4\pi} \int I_\nu \mathrm{d}\Omega, \tag{2.6}$$

and is used to calculate the specific intensity at any given point. For isotropic radiation, the specific intensity is equal to J_ν.

When considering line transfer, the absorption and emission coefficients can be written as functions of the transition rates between energy levels. One of three different radiative transitions may occur: spontaneous emission, stimulated emission, or absorption. Spontaneous emission describes a transition from an upper to a lower energy level by emission of a photon which occurs with no external influence. The emission coefficient in this case can be written as

$$j_\nu = \frac{h\nu_0}{4\pi} n_u A_{ul} \phi(\nu), \tag{2.7}$$

where n_u is the number of photons in the upper energy level of the transition, $\phi(\nu)$ is the line profile function and ν_0 is the central frequency of the profile distribution. A_{ul} is the transition probability for spontaneous emission from an upper energy level u to a lower energy level l per unit time, also known as the Einstein A-coefficient. The line profile function is normalised such that $\int_0^\infty \phi(\nu)\, d\nu = 1$, and so is effectively a probability distribution describing the likelihood of a photon with a frequency around ν_0 being emitted by the atom. The absorption coefficient takes a similar form, although a correction must be included for stimulated emission; both absorption and stimulated emission are affected by the radiation field, as opposed to spontaneous emission which is an isolated process. The absorption coefficient is therefore written as

$$\kappa_\nu = \frac{h\nu_0}{4\pi} \left(n_l B_{lu} - n_u B_{ul}\right) \phi(\nu), \tag{2.8}$$

where B_{lu} and B_{ul} are the Einstein B-coefficients for absorption and stimulated emission,

respectively.

In addition to these radiative processes, collisional excitation and de-excitation may occur. These collisional rates are represented by the coefficients C_{lu} and C_{ul}, respectively, and are proportional to the electron number density n_e and also dependent on temperature.

The above radiative and collisional coefficients can be used to calculate the relative populations between two energy levels. The principle of statistical equilibrium states that the number of transitions into a given level is equal to the number of transitions out of that level at all times, i.e. the change in the population of a level with time $\mathrm{d}n/\mathrm{d}t = 0$. In full, this can be written as the equation of statistical equilibrium,

$$n_i\left[\sum_{i\neq j} C_{ij} + \sum_{i\neq j} B_{ij}J_\nu + \sum_{i>j} A_{ij}\right] = \sum_{i\neq j} n_j C_{ji} + \sum_{i\neq j} n_j B_{ji} J_\nu + \sum_{i<j} n_j A_{ji}, \tag{2.9}$$

where the left-hand terms give the excitation and de-excitation rates out of level i, and the right-hand terms give the excitation and de-excitation rates into i from some other level j.

2.1.1 Local thermodynamic equilibrium

For matter to be in thermal equilibrium, collisions between particles dominate over radiative processes and every constituent particle is at the same temperature. The radiation field is isotropic, i.e. $I_\nu = J_\nu$. Since the radiation field is only dependent on temperature, its form is given by the Planck function for a thermally radiating blackbody, B_ν, where

$$B_\nu(T) = \frac{2h\nu_{ul}^3}{c^2}\frac{1}{e^{h\nu/kT} - 1}. \tag{2.10}$$

The assumption of *local* thermodynamic equilibrium (LTE) is valid when temperature gradients in a medium are sufficiently small such that thermal equilibrium can be assumed in the vicinity of the region of interest.

Each electron transition occurs as per the principle of detailed balance, in which each electron excitation process from $n = l$ to $n = u$ is exactly balanced by an inverse

de-excitation process from u to l. The number of states n_u in energy level u relative to the number of states n_l in a lower energy level l is given by the Boltzmann distribution,

$$\frac{n_u}{n_l} = \frac{g_u}{g_l} e^{-\chi_{ul}/k_B T}, \tag{2.11}$$

where T is the temperature of the gas, k_B is the Boltzmann constant, and $\chi_{ul} = (E_u - E_l)$, where E_u and E_l are the energies of states u and l respectively. The g_n factors are the statistical weights of levels u and l; more than one quantum state can have the same energy, so g_n is used to give the number of different states that have energy E_n. For hydrogen $g_n = 2n^2$, where the factor of 2 comes from spin states $\pm 1/2$. The Boltzmann distribution can be extended to the case of ionised states, where the population ratio between continuum states n_k, a lower ionisation level, and n_{k+}, a higher ionisation level, is given by the Saha equation,

$$\frac{n_{k+}}{n_k} = \frac{1}{n_e} \frac{Z_{k+}}{Z_k} \frac{(2\pi m_e k_B T)^{3/2}}{h^3} e^{-\chi_k/k_B T}, \tag{2.12}$$

where $\chi_k = (E_{k+} - E_k)$, and Z_n is the partition function of the n^{th} level, or the number of ways that an atom can arrange its electrons with the same energy. This is defined mathematically as

$$Z = g_1 + \sum_{i=2}^{\infty} g_i e^{-\chi_i/k_B T}. \tag{2.13}$$

LTE is a good assumption in dense regions where collisional processes dominate over radiative processes, such as in stellar interiors. In regions where LTE does not hold, interactions between the radiation field and constituent particles become important and calculations become much more complicated.

2.1.2 Non-local thermodynamic equilibrium

In more tenuous atmospheres, when radiative processes become important, the assumption that atomic populations can be calculated from the Boltzmann distribution is no

longer valid. Optically thin gases do not act as blackbodies; radiative processes dominate and so the level populations are dependent on the radiation field. It can no longer be assumed that levels are determined only by the temperature of the medium. Instead, level populations are dependent on the location within the medium and the detailed atomic processes for excitation and ionisation must be considered by solving the equations of statistical equilibrium. It is clear from equation 2.9 that in order to calculate the level populations, the mean intensity of the radiation field must be known. However, the mean intensity is calculated from the specific intensity at all points within the medium, and this in turn is dependent on the source function, which itself is dependent on the emission and absorption coefficients, which are dependent on the level populations. This problem must therefore be solved iteratively, and to do so is not trivial; the time and resources required to accurately model non-LTE systems are substantial, and the computational code itself is complex.

For moving media, the problem of solving the equation of radiative transfer in non-LTE can be greatly simplified by employing the Sobolev approximation (Sobolev 1957; see also Rybicki & Hummer 1978), as noted in Section 1.4.1 (see 'RT modelling'). Also known as the large velocity gradient approximation, it exploits the fact that a Doppler-shifted line profile will not interact with other material in the medium if there is a significant velocity gradient present. This effectively decouples line interactions between two points in a medium, since the central peak of a line profile will be shifted to a different frequency from that produced by the same transition occurring in a region of different velocity. Its validity thus improves with increasing velocity gradients, and the approximation is particularly useful when modelling rapid outflows such as stellar winds.

The Doppler width of a line is given by

$$\Delta\nu_D = \frac{\nu_0}{c}\sqrt{\frac{2kT}{m}}, \tag{2.14}$$

where the factor of $\sqrt{2kT/m}$ gives the thermal velocity, v_{th}. Under the Sobolev approximation, photon interactions need only be considered locally (or for two distinct regions in

the medium that are moving with comparable velocity), meaning that once a photon has escaped from its immediate surroundings it is able to escape the medium without undergoing further scattering or absorption. For two points in a medium between which there is a velocity difference of $\Delta\upsilon$, the corresponding shift in frequency is

$$\Delta\nu = \frac{\nu_0}{c}\Delta\upsilon. \tag{2.15}$$

The distance over which the velocity difference is sufficiently large for a spectral line to be shifted by an amount equal to the Doppler width of the line is quantified by the Sobolev length L, where

$$L = \upsilon_{th} / \left|\frac{d\upsilon}{ds}\right|. \tag{2.16}$$

For the Sobolev approximation to be valid, conditions in the gas must not change significantly over L. Once a photon has travelled this length, it is able to escape the local region. If the photon then encounters a new region whose velocity is comparable to the point of emission, the photon will once again undergo interactions with the local material until it travels another Sobolev length. This vastly reduces the number of regions in a medium along the line of sight within which a photon interacts with its surroundings, significantly simplifying the calculation as a result.

In the following sections I describe the TORUS radiative transfer code that has been used for the computations presented in this thesis, from the initial grid set-up to the subroutines that are of particular importance in these models.

2.2 The TORUS radiative transfer code

TORUS (Harries 2000) is a three-dimensional Monte Carlo radiative transfer code. The code employs the adaptive mesh refinement (AMR) technique when refining the simulation space. Since the regions modelled here vary over several orders of magnitude in space and density, a regular homogeneously split grid would either not provide sufficient

resolution to accurately model the denser regions of interest, or would be so computationally expensive that models would not be able to run (or at least would take up significant amounts of time and resources). The AMR method enables high resolution to be achieved where increased sampling is required, while retaining low resolution in large, less-dense regions. In the case of a three-dimensional Cartesian grid, the initial state of the grid consists of one cubic cell, or *parent* cell, encompassing the simulation space. This cell is then linearly halved in each of the cube's three dimensions, producing eight smaller *child* cells. These cells, or *octals* in the three-dimensional case, can be repeatedly sub-divided until sufficient resolution is achieved for that region, resulting in a grid which is stored with an overall octal-tree structure, or *octree*. The two-dimensional analogue of this is known as a *quadtree*. Both of these structures are demonstrated in Figure 2.1 Alternatively a cylindrical grid may be used, in which case the parent cell is split across height, radius, and azimuth in the three-dimensional case, or just height and radius in the case of a two-dimensional model.

The amount by which a region is split is dependent on some physical parameter of the material within the cell, for example density or velocity. In the case of density, the mass encompassed within an octal is calculated by sampling the density at numerous points and multiplying this average density by the volume of the octal. The octal is then split recursively until the mass of material contained falls below a maximum value which may be defined by the user. In order to prevent the grid from exceeding the amount of memory available, a maximum cell depth is also defined (keyword `maxcelldepth`), where a cell of size 2^{-N} times that of the grid will cease to be split (where $1 \leq N \leq$ `maxcelldepth`). Each cell is checked and split until the mass of material within the cell falls below the maximum mass, as long as the depth of the mesh refinement is less than `maxcelldepth`. TORUS performs the maximum mass test by default, although there are more subtle methods of splitting the grid depending on the geometry of the object being modelled. Splitting specific to the disc wind and magnetosphere in the T Tauri geometry is summarised in Section 3.5.1.

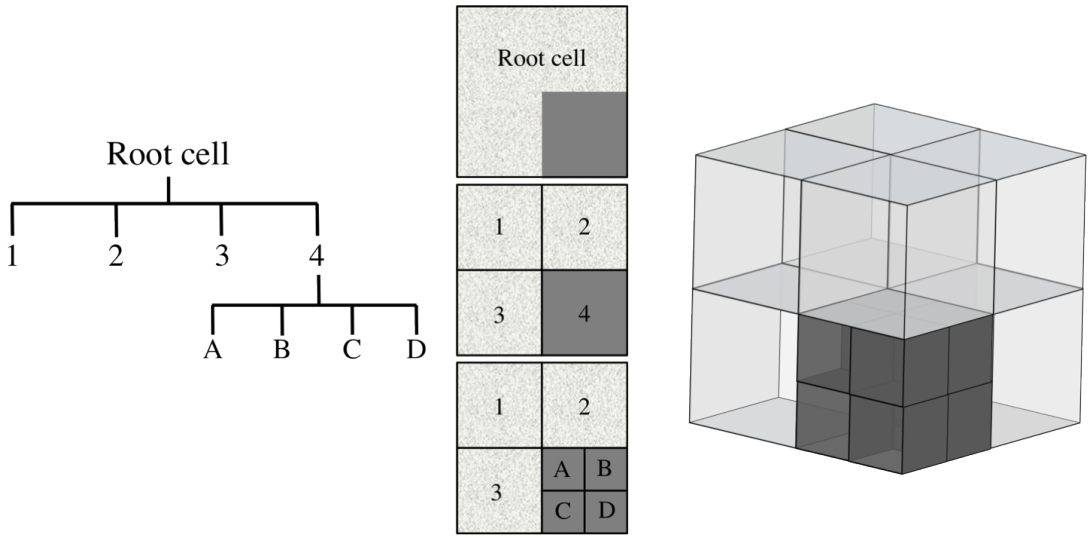

Figure 2.1: An example the structure of a basic quadtree (left) with the corresponding two-dimensional grid (centre). The grid contains material of given density with a density enhancement in the bottom right. Initially the grid is composed of one single root cell. This is split into four subcells (1, 2, 3, and 4). A second split then takes place to better resolve the density enhancement, producing an additional four cells in the bottom right region (A, B, C, and D). The equivalent three-dimensional octree is shown on the right, with eight cells produced in the initial octal, followed by one further octal in the enhanced density region.

In solving the radiative transfer it is important that there is sufficient grid resolution to adequately resolve rapid changes in emissivity and opacity. In order to ensure that the grid has been sufficiently resolved for optimal sampling I performed convergence tests by increasing the maximum resolution of the grid until the line profiles of a fiducial model no longer changed. I found that the profiles converged when a maximum AMR depth of 15 was reached in the most dense areas of the grid. For a grid size of 15×10^{12} cm, this is equivalent to a linear resolution of 7×10^{-3} $R_{\odot}$.

There are six main parts to TORUS: reading in the inputs of the model; setting up the required microphysics (which involves reading in atomic data such as atom mass, charge, collisional and radiative rates, etc.); creating the AMR grid; adding the photon sources (an individual PMS star in this case); performing the radiative transfer and statistical equilibrium calculations; and producing the required outputs. The remainder of this chapter will describe these stages in more detail.

2.2.1 Grid setup

Before the AMR process can take place, the geometry of the system must be added to the single-cell grid. A number of different system geometries are hardwired into TORUS, resulting in a very flexible code covering numerous scales from individual stars, to clusters, to entire galaxies. The geometries used in the models presented in this thesis are the `ttauri` and `shakara` cases, for the CTT and HAeBe studies respectively. The setup described here is in the context of the `ttauri` case; departures from this geometry when employing the `shakara` case will be specified in Chapter 5, although in general the `ttauri` geometry allows for inflow and outflow from the protostar, whereas the `shakara` geometry just consists of a circumstellar disc.

The physical properties of the components of a particular geometry are defined in a parameters file, along with the grid properties, the physics to be included (e.g. whether or not the material is in LTE, the number of atoms included in the model, etc.), and the desired outputs. Once the geometric structures have been added to the grid, such as the accretion disc and disc wind, the refinement process can begin (this is described only briefly here; see Symington 2006 for a detailed discussion on the implementation of AMR in TORUS).

The initial stage of grid creation sees the top-level parent cell, or *octree root*, initialised, and physical attributes such as density, temperature, velocity, and position are calculated for the octal. The subroutine `splitGrid` is then called, recursively splitting cells (or technically adding new child cells with higher levels of refinement) as per the criteria described above. With each split, various physical parameters of the new cell are calculated in a similar fashion to the initial octree root calculations. For certain geometries, it is possible for variations in density over several orders of magnitude to occur over very small length scales, resulting in very refined regions of the grid being produced adjacent to significantly larger cells. There is the capability in TORUS to insert intermediate-sized cells between such regions, effectively smoothing the grid, improving the accuracy of calculations that require the interpolation of data from neighbouring cells. Once the

final grid has been constructed, the photon sources can be added and the radiative transfer calculations can begin.

2.2.2 Source setup

The user-defined input parameters relating to the photon source cover the number of photon sources in the model (just the one for each of the models described in this thesis), the model atmosphere used to describe the continuum flux of the source, the position of the source in the grid, and physical parameters such as effective temperature, mass, and radius. Using these parameters, a sphere is then constructed from a number of individual surface area elements. The photospheric luminosity is calculated by summing the luminosities of each of these surface elements. The `ttauri` geometry also includes an additional hot source superimposed onto the photosphere caused by accretion hot spots. The normal of each of the surface area elements is tested to see whether the grid cells above each of these elements are in the accretion flow. Since the additional contribution of a hot spot can be small, of order 1 per cent, 10^6 surface area elements are produced to ensure that the additional contribution to the luminosity from the accretion spots are well-sampled. This also allows for arbitrary accretion patterns to be calculated correctly, with no assumptions needing to be made about the shape of these footprints. The kinetic power of each surface element that falls within the hot spots is calculated from the density and velocity of the inflowing material. Finally, the hot spot contribution to the luminosity is added under the assumption that the kinetic power is re-radiated as blackbody radiation. Combining this additional luminosity with the hot spot area also allows the hot spot temperature to be determined. The physical causes of these hot spots and accretion streams will be discussed in Chapter 3, along with the analytical function used to describe the hot spots.

2.2.3 Statistical equilibrium

As noted in Section 2.1.2, solving the equation of statistical equilibrium in non-LTE requires an iterative algorithm due to the inter-dependence of variables in the equations of statistical equilibrium and radiative transfer. Initially LTE level populations are assigned in order for an initial estimate of the radiation field to be made. The radiation field is sampled using a number of rays which propagate through the grid and, for each transition, finds the specific intensity along the path of the ray and the path length through the cell. These values are used to calculate the mean radiation field of the cell, from which non-LTE level populations are calculated. The equation of statistical equilibrium employed in TORUS is that of Klein & Castor (1978), who use

$$\begin{aligned}
&\sum_{i<j} [N_i(B_{ij}\bar{J}_{ij} + N_e C_{ij}) - N_j(A_{ji} + B_{ji}\bar{J}_{ij} + N_e C ji)] \\
&\quad + \sum_{i>j} [N_i(A_{ij} + B_{ij}\bar{J}_{ij} + N_e C ij) - N_j(B_{ji}\bar{J}_{ij} + N_e C_{ji})] \\
&\quad + N_j^*\Big[4\pi \int_{\nu_j}^{\infty} \frac{\sigma_j(\nu)}{h\nu}\Big(\frac{2h\nu^3}{c^2} + J_\nu\Big)\exp\Big(-\frac{h\nu}{k_B T}\Big)\mathrm{d}\nu + N_e C_{jk}\Big] \\
&\quad - N_j\Big(4\pi \int_{\nu_j}^{\infty} \frac{\sigma_j(\nu)}{h\nu} J_\nu \mathrm{d}\nu + N_e C_{jk}\Big) = 0,
\end{aligned} \tag{2.17}$$

where $\bar{J}_{ij}$ is the intensity of the line transition between levels i and j averaged over angle and integrated over the line profile, and σ_j is the photoionisation cross-section of the j^{th} level. The level populations calculated under LTE are expressed as N^*, with levels N calculated in non-LTE. The electron density is fixed by the equation $N_e = N(H^+)$, and the total hydrogen density is fixed by the mass density ρ using

$$\sum_{n=1}^{16} N_n + N(H^+) = \frac{\rho}{m_H}. \tag{2.18}$$

Equation 2.17 breaks down into the various excitation and de-excitation terms (cf. Equation 2.9) as follows: the first line gives the net transition rate into the j^{th} level from all lower levels i, calculating the absorption of radiation from lower levels plus collisional

excitation, from which spontaneous and stimulated emission and collisional de-excitation are subtracted; the second line gives the net transition rate into the j^{th} level from all upper levels i, where this time the absorption terms are subtracted from the emission terms; the third line gives the net recombination rate, where the exponent is effectively a correction factor for 'stimulated' recombination; and the final line gives the net ionisation rate. The mean radiation field is then recalculated using the estimate of the level populations obtained from the solution to equation 2.17. In TORUS this is achieved by setting up a linear matrix for all the rates required in Equation 2.17 and inverting it to find the level populations. These level populations are used to recalculate the radiation field, producing a new set of matrices which are then inverted, and so on. This iterative exchange between the radiation field calculation and the level population calculation continues until the radiation field and level populations converge on a consistent solution.

Since the Sobolev approximation states that photons that are emitted locally are likely to be absorbed only locally, the radiation field for transitions into and out of level j from lower levels, i.e. where $i < j$, can be simplified, since these transitions are dependent only on the local source function. $\bar{J}_{ij}$ can therefore be expressed as

$$\bar{J}_{ij} = \left(1 - \beta_{ij}\right) \frac{2h\nu_{ij}^3}{c^2} \left[\frac{g_j}{g_i}\frac{n_i}{n_j} - 1\right]^{-1} + \beta_{c,ij} I_{c,ij} \tag{2.19}$$

(see e.g. Castor 1970; Klein & Castor 1978), where β_{ij} and $\beta_{c,ij}$ are the escape probabilities of radiation formed in the local vicinity and from the stellar continuum around the line frequency, respectively. Similarly, $I_{c,ij}$ is the intensity of the continuum around this frequency. The escape probabilities are defined as

$$\beta_{ij} = \frac{1}{4\pi} \int \frac{1 - e^{-\tau_{ij}}}{\tau_{ij}} \mathrm{d}\Omega \tag{2.20}$$

and, for the continuum contribution integrated over the solid angle of the stellar photosphere Ω_*,

$$\beta_{c,ij} = \frac{1}{4\pi} \int_{\Omega_*} \frac{1 - e^{-\tau_{ij}}}{\tau_{ij}} \mathrm{d}\Omega \tag{2.21}$$

(see e.g. Rybicki & Hummer 1978). The optical depth from the line transition is

$$\tau_{ij} = \frac{\pi e^2}{m_e \nu_{ij}} g_{ij} f_{ij} \frac{\mathrm{d}s}{\mathrm{d}\upsilon} \left(\frac{n_i}{g_i} - \frac{n_j}{g_j} \right), \tag{2.22}$$

where f_{ij} is the oscillator strength, ds is some small displacement from the point of emission, and dv is the change in velocity of the emitting material over that distance.

For the models calculated under the `ttauri` geometry, the temperature of the gas is calculated from a user-defined input parameter. The equation of radiative equilibrium is not solved in this case since there is considerable uncertainty in the temperature structure of the magnetosphere. Instead, the model of Hartmann et al. (1994) is used in which a volumetric heating rate, proportional to r^{-3}, is assumed. The energy balance between this and the radiative cooling rate of Hartmann et al. (1982) is solved to establish the temperature distribution in the magnetosphere, with the maximum temperature in the magnetosphere defined manually and the temperature elsewhere falls off from this accordingly. The local cooling rate Λ is given by

$$\Lambda(T) = \frac{Q m_H^2}{\rho^2}, \tag{2.23}$$

where Q is the heating rate and ρ is the local density of material. The maximum temperature in the magnetosphere is a user-defined parameter, from which the maximum heating rate required to obtain this temperature is determined. The temperature structure of the magnetosphere is still a major area of uncertainty (e.g. Hartmann 2009). An attempt to self-consistently solve the thermal structure of the gas was presented by Martin (1996), finding that the primary heating mechanism was adiabatic compression due to the convergence of the field lines. The dominant cooling mechanisms were found to be bremsstrahlung radiation and line emission from Ca II and Mg II ions, in which radiative deexcitation from a bound state can lead to cooling. While this is strongly dependent on

the external radiation field strength, Martin (1996) demonstrated that for a given radiation field more cooling from these lines will occur in a hotter gas than a cooler gas. However, line profiles calculated by Muzerolle et al. (1998) using the thermal structure determined by Martin were found to be inconsistent with the stronger emission lines which are observed, implying the presence of a more significant heating source that was not considered in the work by Martin. While the Hartmann et al. (1994) temperature distribution is not calculated self-consistently, line profiles calculated under this model give much better agreement with observations; this is therefore the model that is adopted in this study.

The HAeBe study presented in Chapter 5 requires an accurate determination of the temperature structure of the disc. This requires a self-consistent calculation to be made under the assumption of radiative equilibrium. The method employed in TORUS uses the iterative scheme of Lucy (1999), which is described in the next section.

2.2.4 Dust physics and radiative equilibrium

The statistical equilibrium calculations described previously enable the level populations of various spectral lines to be determined. In the absence of broadening, line emission occurs at discrete wavelengths depending on the atomic properties of the gas. In dusty regions, radiant energy heats the dust which is comprised of grains of various cross sections. Consequently, the radiation emitted by the dust does so over a continuum, with larger grains contributing to emission at longer wavelengths.

Before the radiative equilibrium calculation can take place, the physical properties of the dust grains within the circumstellar disc are required, namely the maximum and minimum grain sizes, the fractional abundance of a particular grain relative to others, and the power law index of the grain size distribution function. Since the grains under consideration here are relatively large and are efficient absorbers, i.e. the complex part of the refractive index is important, Mie scattering dominates. Grain sizes and complex refractive indices are used to calculate the absorption and scattering cross-sections of the grains and the Mie scattering phase matrix of the grain. Once the dust has been distributed

throughout the disc, a call is made to the `lucyRadiativeEquilibrium` subroutine where the radiative equilibrium calculation commences.

This calculation uses photon 'packets' comprising of n photons. The frequency of a photon packet emitted from the photosphere is determined using a probability distribution in which the black body spectrum is split over N equal probability bins. The mid-probability points giving frequency ν_i are found from the equation

$$\frac{i - \frac{1}{2}}{N} = \int_0^{\nu_i} B_\nu \mathrm{d}\nu \Big/ \int_0^{\infty} B_\nu \mathrm{d}\nu, \tag{2.24}$$

where $i = 1, 2, ..., N$. For a randomly selected i, the new frequency of the emitted photon packet is set to the corresponding mid-probability point ν_i. After initial emission from the photosphere these photon packets are propagated through the grid, undergoing scattering events until they either escape the grid or are re-absorbed by the photosphere. Photon packets absorbed elsewhere in the medium are re-emitted instantaneously. The emissivity at some point in the disc is also given by a probability distribution, since the frequency of a photon packet at a random position and direction in the disc depends only on the emissivity spectrum at that point. The new frequency is assigned according to

$$\eta = \int_0^{\nu} j_\nu \mathrm{d}\nu \Big/ \int_0^{\infty} j_\nu \mathrm{d}\nu, \tag{2.25}$$

where $j_\nu = \kappa_\nu B_\nu$ and η is a random number such that $0 < \eta < 1$.

The optical depth of a subcell is also calculated using a randomly generated η, where

$$\tau = -\ln(1 - \eta). \tag{2.26}$$

The distance that a photon packet of energy ϵ_ν will travel before either being absorbed or leaving the computational domain is given by the path length l. This is dependent on τ and the density of material in the cell, ρ, where

$$\tau = (\kappa_\nu + \sigma_\nu)\,\rho l. \tag{2.27}$$

where σ_ν is the scattering cross-section. With the photon behaviour set up, attention can be moved to the transfer of heat towards radiative equilibrium.

The rate at which energy in a medium is absorbed is given by

$$\dot{A} = 4\pi \int_0^\infty \kappa_\nu J_\nu \mathrm{d}\nu. \tag{2.28}$$

Similarly, the rate at which the matter emits energy is

$$\dot{E} = 4\pi \int_0^\infty \kappa_\nu B_\nu \mathrm{d}\nu. \tag{2.29}$$

Since the disc material is assumed to be in LTE, the source function is taken to be described by the Planck function. Consequently, we can take $\dot{A} = \dot{E}$ when the medium is in radiative equilibrium.

$\dot{A}$ can be calculated independently of $\dot{E}$ by considering the path length l. For a given volume V, the energy density of the radiation field u can be found by integrating the mean intensity over all solid angles. The energy density of the radiation field at a given frequency is therefore

$$u = \frac{4\pi}{c} J_\nu \mathrm{d}\nu. \tag{2.30}$$

A photon travelling at speed c traverses a path length l between successive events in time δt. The energy density contribution at a particular frequency to a volume V_i from a packet traversing this path is $(\epsilon_\nu / V_i)\delta t / \Delta t$. Equation 2.30 can therefore be re-written in terms of J_ν as

$$J_\nu \mathrm{d}\nu = \frac{1}{4\pi} \frac{1}{\Delta t} \frac{1}{V_i} \sum_{d\nu} \epsilon_\nu l. \tag{2.31}$$

Combining this with equation 2.28 yields a new expression for the absorption rate,

$$\dot{A} = \frac{1}{\Delta t}\frac{1}{V_i}\sum \kappa_\nu \epsilon_\nu l. \tag{2.32}$$

To aid the calculation of $\dot{A}$, the factor of $\epsilon_0/\Delta t$ can be converted to more useful physical units by defining the luminosity of the stellar source to be proportional to the number of photons that escape the grid, n_∞, over time, i.e.

$$L_* = n_\infty \frac{\epsilon_0}{\Delta t}, \tag{2.33}$$

where ϵ_0 is the total energy of a given photon packet.

Equation 2.29 can be rewritten by integrating the Planck function B_ν and using the Planck-mean absorption coefficient $\bar{\kappa}_p$, producing $\dot{E} = 4\pi\bar{\kappa}_p B$. In radiative equilibrium, this is also equal to $\dot{A}$, i.e.

$$\dot{A} = 4\pi\bar{\kappa}_p B. \tag{2.34}$$

However, for material that is not in thermal equilibrium, the above equation will not hold since $\dot{A} \neq \dot{E}$ and so there is a net change in the energy density of the radiation field.

Since the integral of the Planck function is $B = \sigma T^4/\pi$, an expression in terms of temperature can be derived, where, in thermal equilibrium, the temperature of the dust is

$$T_d = \left(\frac{\dot{A}}{4\sigma\bar{\kappa}_p}\right)^{1/4}. \tag{2.35}$$

The dust population is added to the grid gradually so that it grows in from the outside. The alternative method of sublimating dust from the inner rim outwards is more computationally expensive since it involves removing the dust from the inner rim in very thin shells; the hot dust at the inner rim is very optically thick, shielding the dust immediately behind it which remains relatively cool. Setting the dust fraction to zero in all regions where the dust temperature is greater than the sublimation temperature and running equilibrium again would result in the newly unshielded dust reaching a very high temperature exceeding that of sublimation and so is also removed, revealing a new layer,

and so on. This process would eventually yield the correct solution but would take a considerable amount of time due to the small widths of the shells being removed. Instead, the first three iterations are calculated with a vanishingly low dust fraction of 10^{-20} so that the circumstellar region is completely optically thin. The following three iterations are run with a maximum optical depth of $\tau_{\rm max} = 0.01$. The optical depth for a given dust fraction f is given by

$$\tau = f\rho\kappa_\nu\Delta x, \tag{2.36}$$

where $f\rho$ gives the density of the dust in a cell of size Δx. Using this equation, the value of f required for $\tau = 0.01$ is calculated and, for all cells where the dust temperature is less than the sublimation temperature, the dust fraction in the cell is set to either the fraction calculated as described or the fraction set in the user-defined inputs, whichever is smaller. On completion of these iterations, the process follows again for another three iterations with $\tau = 0.1$, then three with $\tau = 1$, then three with $\tau = 10$, each time setting the dust fraction to the minimum of that required by the opacity or that defined by the user and removed dust whose temperature $T_{\rm dust}$ exceeds the sublimation temperature $T_{\rm sub}$. Finally, some unphysically large opacity value is used ($\tau = 10^{30}$ in this case) to ensure that the dust fraction has been set to the user-defined value in all regions where $T_{\rm dust} < T_{\rm sub}$ and zero elsewhere. This process is used for each individual dust population.

The first step of the radiative equilibrium calculation is to set the grid to a very low temperature, 20 K in this case. The general iterative process in the radiative equilibrium algorithm then proceeds as follows:

(i) A loop is performed over all photons simulated in one iteration, gathering information such as positions, energies, number of scatters, etc. It is here that the distance travelled in one iteration, l, is calculated;

(ii) The mean intensity of a subcell is calculated using equation 2.31;

(iii) $\dot{A}$ is found from equation 2.32;

iter	Mean dT [K]	Min dT [K]	Max dT [K]	% bad cells	Eta dust/*	Eta Total	Max dT/T	nMonte
1	1523.99	92.65	9990.00	0.00	0.00	15.85	0.9997	6332000
2	436.89	-3312.44	-21.46	0.00	0.00	2.45	1.9633	6332000
3	194.01	-1318.48	-7.34	0.00	0.00	0.96	0.6533	6332000
4	155.95	-783.30	-0.97	0.00	495.08	88866890.91	6.3797	6332000
5	71.92	-364.63	-0.21	0.00	137.07	24604459.57	2.7167	6332000
6	32.62	-181.83	195.10	0.00	79.56	14281797.06	1.5045	6332000
7	40.94	-656.73	336.54	0.00	281.78	50579661.32	76.6175	6332000
8	19.80	-278.71	154.58	0.00	153.67	27583277.81	64.4420	6332000
9	9.56	-139.81	75.01	0.00	118.27	21229175.99	42.5422	6332000
10	7.97	-624.42	431.21	0.00	181.87	32646501.15	25.5994	6332000
11	3.96	-306.33	139.53	0.00	167.59	30082745.09	24.6918	6332000
12	2.21	-640.09	107.09	0.00	160.49	28808049.48	142.5559	6332000
13	4.83	-696.66	869.95	0.04	276.73	49673743.08	25.6351	6332000
14	2.55	-714.54	118.75	0.03	257.10	46149973.39	24.7859	6332000
15	1.65	-220.67	56.86	0.02	253.52	45507234.35	35.2186	6332000
16	5.47	-755.69	903.16	0.04	218.82	39279080.16	24.3185	6332000
17	2.62	-644.05	117.71	0.04	207.81	37301445.84	64.0998	6332000
18	1.61	-269.93	62.25	0.03	205.59	36902845.65	23.8042	6332000
19	1.23	-65.48	32.25	0.02	204.97	36792974.74	38.1650	6332000

Figure 2.2: Convergence data for the radiative equilibrium calculations. The columns follow the order of iteration number; the mean, minimum, and maximum change in temperature from the previous iteration; the percentage of undersampled cells in the radiation field; the emissivity of the dust disc in stellar and cgs units; the fractional change in temperature between the current and previous iteration; and the number of photon packets used. The difference between the emissivity values in the final two iterations is less than one per cent, so the model has converged. Increases in emissivity are due to dust being added during these iterations.

(iv) The temperature of each subcell, T_{new}, is calculated using equation 2.35. The change in temperature is $\Delta T = T_{new} - T_{old}$. In the iteration that follows, T_{old} is overwritten with T_{new}.

(v) The luminosity of the dust, L_d, is found from $L_d = \int_V \dot{E} \mathrm{d}V$. This value for the total emission is compared with the value calculated in the previous iteration to test for convergence. If the difference between these two emissivities is less than one per cent then convergence has been reached.

An example of the temperature and emissivity values calculated after each iteration is shown in Figure 2.2 and the approach to thermal equilibrium over a subset of these iterations is shown in Figure 2.3.

2.2.5 Outputs

During execution, TORUS outputs a number of VTK (Visualization ToolKit) files in addition to any user-defined outputs. These files enable colour plots of various data for the

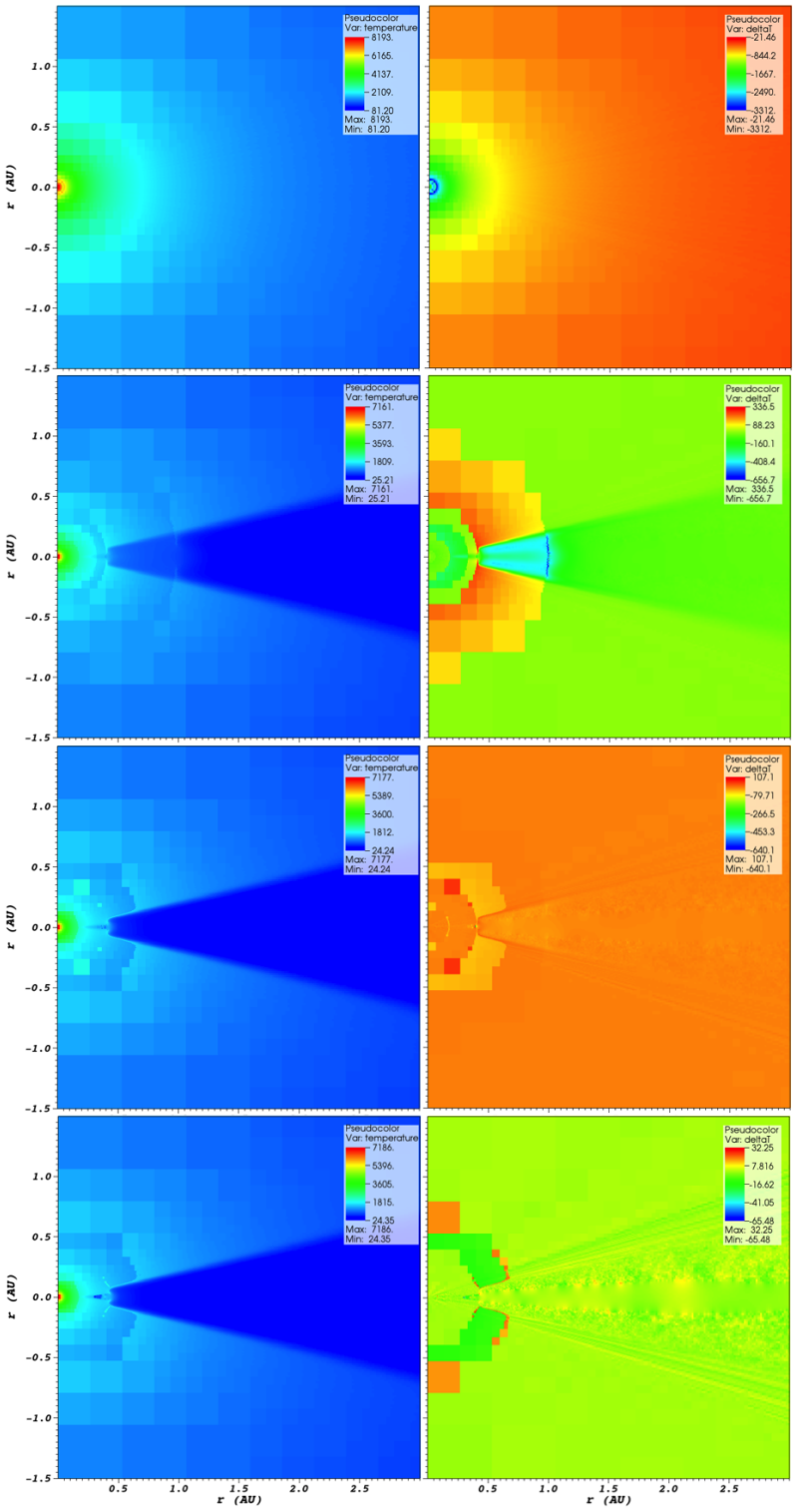

Figure 2.3: Temperature convergence using the Lucy (1999) algorithm. Left-hand panels show the temperature structure of the disc and right-hand panels show the corresponding change in temperature from the previous iteration. The legend on each plot shows the temperature scale with the maximum and minimum temperature (or change in temperature). The iterations presented in each row are the second, seventh, twelfth, and final nineteenth iteration, respectively. The legend on the bottom right panel shows how small the temperature change is between this final iteration compared with previous values.

grid output such as the density of material within cells, level populations, the density and temperature structure, etc., as well as the AMR splitting of the grid itself. This allows visualisation of the grid at various stages during run-time, such as after the AMR grid creation, as well as between any iterative processes, such as after each iteration towards thermal equilibrium. One such example is in Figure 2.3, showing T and ΔT plots from various `lucy.vtu` files.

A number of text files are also produced by default. These include `info_grid.dat`, which contains information such as the number of octals in the grid, the maximum AMR depth reached, the sizes of the largest and smallest cell, and the geometry of the grid; `tune.dat`, which contains the timing information of the simulation, such as the time between various iterations and the time the entire model took to run; and, in the case of thermal equilibrium calculations, `convergence_lucy.dat`, which includes the mean temperature change, the maximum and minimum temperatures in the grid, and the dust emissivity for each iteration (see Figure 2.2).

As well as these diagnostic files, there are a number of optional outputs that users can define before execution, such as photometric data, line profiles, SEDs, and datacubes. Images that are produced for the dust continuum models use a Monte Carlo imaging method. The temperature of the dust is calculated using the method described in Section 2.2.4. Using the luminosity of the star and the emissivity of the circumstellar dust, the probability of a photon being produced by the star as opposed to being produced by the dust is known. The images and SEDs are calculated using these probabilities. A photon is produced either at the stellar surface or in the dust itself and is propagated around the grid. A peel-off method (Yusef-Zadeh et al. 1984) is used to calculate the intensity observed from a specified direction. On the initial emission of a photon, an additional photon is emitted in the observer's direction, weighted by the probability p that the photon would have taken this trajectory. At each scattering or emission event an additional photon is produced, again weighted by the probability of it being scattered or emitted in the direction of the observer. It is also weighted by the optical depth along the photon's

path, such that the total weighting of the additional photon added to the SEDs and images is given by $pe^{-\tau}$. This method produces high signal-to-noise images efficiently since individual photon packets are able to contribute to the outputs more than once due to the weighting used, rather than having to propagate a greater number of packets in order to achieve the required sampling.

Datacubes are calculated in spectral line models using a ray tracing technique which is described in detail in the next section. Once the equation of radiative transfer has been solved and the source function has been found, a formal integral of the equation of radiative transfer is performed along the line of sight of the observer, giving the specific intensity at the end point of each ray. Datacubes can be constructed from these rays, allowing visualisation of a spatially two-dimensional image at a given wavelength across numerous velocity channels. These are saved as FITS files, which also enables line profile data to be examined at any point in the datacube space in any given velocity slice. Example datacube images are presented in Chapter 4.

Ray tracing and image production

Line profile calculation uses a ray tracing technique. Previously, when solving statistical equilibrium, the Sobolev approximation was used, enabling the definition of resonant zones where the radiation from the star can interact at line frequencies. This speeds the calculation up since the large velocity gradients allow a small length scale to be defined over which the gas conditions are assumed to be constant. One consequence of this method is that natural line broadening is ignored. Therefore, when calculating line profiles, the method of Sobolev with Exact Integration is used (Lamers et al. 1987). An integral of the equation of radiative transfer (Equation 2.5) is performed that includes the broadening; rather than allowing a line to interact only at specific points in the grid, the line is integrated from the observer's viewpoint over the entire grid in order to calculate the line profile.

However, there are subtle numerical issues associated with this method. The inte-

gral being performed covers many dimensions, being calculated over all space and over many different frequencies. In the case of modelling magnetospheric accretion and disc winds, many different size scales must be considered; there is the stellar disc, which requires enough sampling for the hotspots to be detected, the magnetosphere, and the disc wind. If the sampling precision is not sufficient enough to result in numerous rays hitting the hotspots then the line profile will not be correct, and too many rays will result in computational timescales that are too long to make running numerous models feasible. These issues are overcome by sampling the structures in an adaptive method. Rays are created in a cylindrical geometry, assigning a number of rays across a radius r and a number in azimuthal angle ϕ. Different numbers of rays are assigned to sample the photosphere, the magnetosphere, and the wind. Since the size scale of these structures differs so greatly, the photospheric rays are distributed linearly from the centre of the star to the radius, whereas the rays used to sample the magnetosphere and wind are distributed logarithmically. This is particularly necessary for the wind as it is such an extended feature.

The generation of images is done slightly differently. An image plane is set up with a given number of pixels in the x and y directions. The sampling described above is maintained, and one additional point is added in the centre of each pixel. The intensity of a given pixel is calculated as a function of solid angle. However, while the intensity across a given ray is known as described above, how much each ray contributes to the overall intensity of a pixel is not known; for instance, a number of uniformly spaced rays will produce a different pixel intensity than that achieved for a pixel in which all rays are located to one side. This is overcome by using a Voronoi tessellation, which consists of dividing each pixel up differently depending on the distribution of rays within them. Subdivisions within pixels are defined such that each subdivision contains one ray, and that ray is the closest one to any given point within the subdivision. An example of this geometry is shown in Figure 2.4. This allows the average pixel flux to be calculated more accurately in instances where the intensity distribution of the radiation in the area of the grid corresponding to a given pixel is not uniform. For instance, if the image is

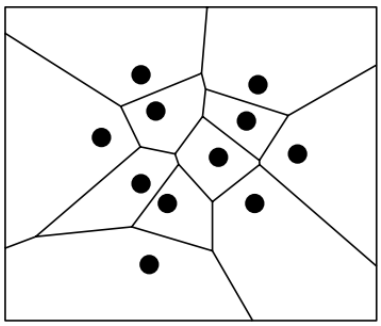

Figure 2.4: Pixels within images are divided up using the Voronoi tessellation method. The points in this figure are analogous to rays within a pixel. The inter-point boundaries are defined such that every source point is the closest source point to every position within the defined boundaries. Reproduced from de Berg et al. (2008).

constructed with an array of pixels in which one ray is fired down the centre of each pixel, it is possible to miss an object that is projected in an area smaller than one pixel, even if there is something very bright there. To avoid this, numerous rays are generated that sample the two-dimensional projection of the object as best as possible. The number of rays used is dependent on the size of the image; for a 200x200 pixel image, 180,000 rays are generated. This means that many rays can pass through one pixel of the image, and the aim is to appropriately weight the intensity of each of those rays. Rather than simply dividing the area of a pixel by the number of rays to find the average intensity of the pixel, each ray is weighted by the area calculated in the Voronoi tessellation. This prevents the pixel intensity from being over-estimated in instances where a high number density of rays happen to fall in a small but bright region of the pixel, and vice versa.

Line profiles calculated from datacubes should virtually match those produced by ray tracing, or may in some circumstances be better, since there are $n_{\rm pixels}$ more points. However, including the entirety of the wind in these images would require an incredibly high resolution in order to resolve the hotspots, so image sizes are defined such that only the magnetosphere and disc warp are encompassed. Line profiles calculated in this manner therefore do not include the whole system, and so in this instance cannot be used for analysis. A selection of images depicting the warp and inclined accretion flow is presented in Figure 2.5. These have been taken at various azimuthal angles, ϕ, showing an

unobscured star ($\phi = 0°$), a disc warp encroaching upon the photosphere ($\phi = 72°$), the warp at maximum photosphere occultation ($\phi = 180°$), and the warp beginning to pass back behind the star ($\phi = 252°$).

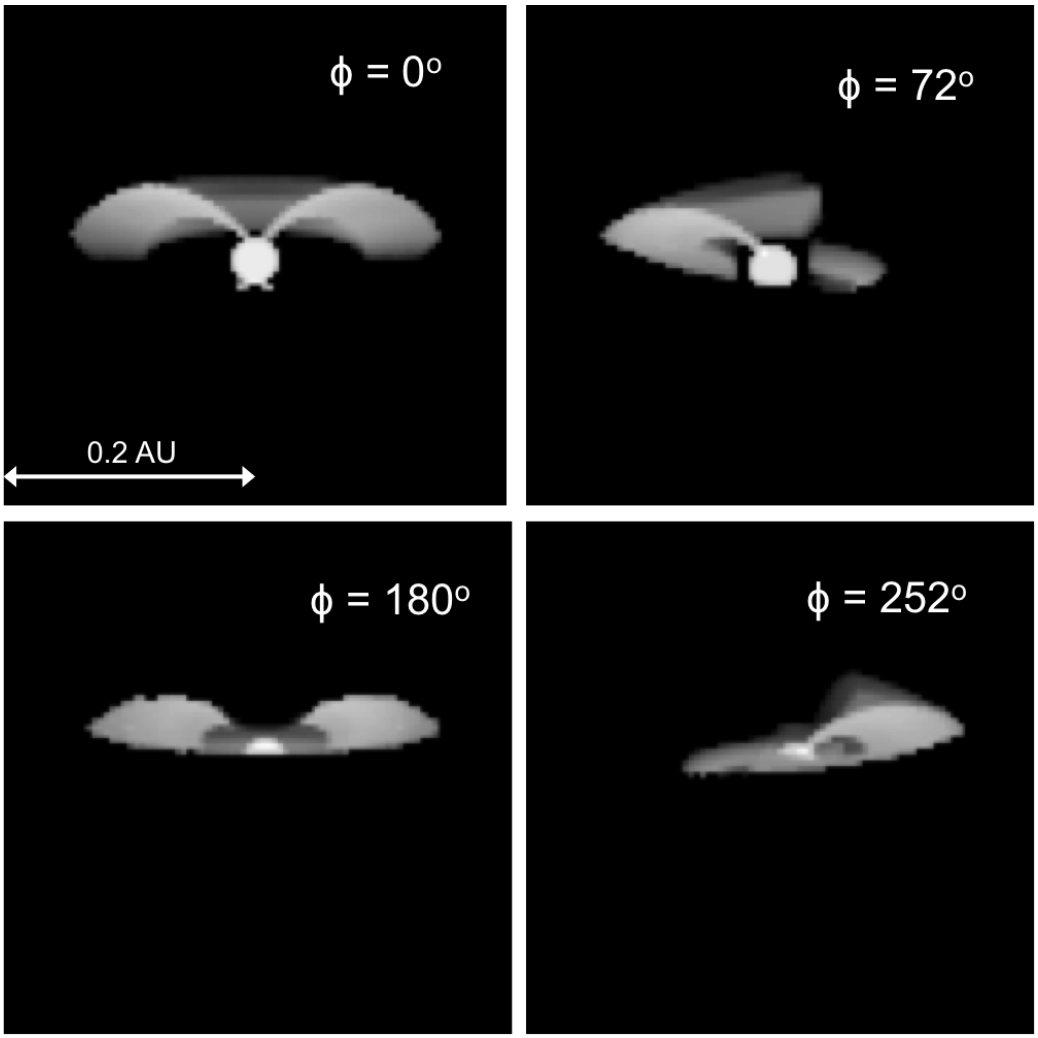

Figure 2.5: Example images in Hα showing the photosphere, inclined accretion flow, and disc warp. The top left shows the warp behind the photosphere, at azimuthal angle $\phi = 0°$, the top right shows the warp on the left of the star, with $\phi = 72°$, the bottom left shows the warp fully occulting the photosphere, with $\phi = 180°$, and the bottom right shows the warp retreating, with $\phi = 252°$.

Chapter 3

Photometric modelling of AA Tau

The work described in this chapter has been published in Esau, Harries & Bouvier, Monthly Notices of the Royal Astronomical Society, 443:1022 (2014).

3.1 Introduction

In was noted in the overview of classical T Tauri stars given in section 1.3.1 that a key feature of CTTS is their strong, occasionally periodic, photometric variability. The hypothesis that consequences of magnetospheric accretion are the cause of these variations is well studied (e.g. Kenyon et al. 1994; Bouvier et al. 1995; Mahdavi & Kenyon 1998). The aim of this chapter and the next is to test the observed photometric and spectroscopic variations using an object that has very well-constrained physical parameters. The CTTS AA Tau is a typical CTTS, with a mass of 0.85 $M_{\odot}$ and a radius of about 1.85 $R_{\odot}$ (Bouvier et al. 1999). It is an ideal candidate for magnetospheric accretion studies due to its high inclination angle of 75°, resulting in magnetically-produced disc warps intercepting the line of sight as the star rotates. Indeed, there have been many observation campaigns involving AA Tau, both photometric and spectroscopic (e.g. Bouvier et al. 1999, 2003, and the All Sky Automated Survey *ASAS*, e.g. Pojmanski et al. 2005). Photopolarimetric variability has been observed by Bouvier et al. (1999, 2003) and Menard2003, and modelled by O'Sullivan et al. (2005), with results demonstrating increased polarisation

during photometric minima which implies obscuration by dust. Spectropolarimetric observations have also been used to map the magnetic field of AA Tau at different epochs (Donati et al. 2010). AA Tau is a particularly well-constrained object geometrically and shows signatures of azimuthally varying accretion and outflows, both photometrically and spectroscopically, which are consistent with the paradigm of magnetospheric accretion. We are therefore able to use this star-disc-wind system to strongly test the paradigm of magnetospheric accretion in relation to CTTs in general.

In this chapter I investigate the well-documented photometric variations observed for AA Tau. The main aim here is to use a self-consistent geometric model of a magnetosphere and an optically thick disc warp to produce synthetic light for curves this star, testing the interpretation of Bouvier et al. (1999) that photometric variations are a direct consequence of the inner edge of the disc interacting with the magnetosphere (see Section 3.2. Models were run using the radiative transfer code TORUS (Harries 2000; Symington et al. 2005). Various synthetic light curves were produced by varying numerous parameters and the resulting data was compared with photometric observations in order to find the parameter set most consistent with observations. It is well-known that occultation events come and go, with epoch to epoch variations observed between occultations, so we collated as much photometric data as was publicly available to compare with the resulting synthetic light curves. We cannot expect a single parameter set to consistently fit all epochs since the magnetic field strength and geometry of AA Tau varies, causing the height and azimuthal position of the warp (and hence the depth of the occultation) to vary over time. We are therefore looking for a model which is broadly consistent with the typical deep occultation events observed to occur with an 8.22 day period.

Existing observational data from Bouvier et al. (1999, 2003, 2007, hereafter B99, B03, and B07 respectively), Pojmanski et al. (2005, hereafter *ASAS*), and Grankin et al. (2007, hereafter G07) are presented in section 3.2 with a discussion of the characteristics that signify the process of magnetospheric accretion. Known physical and geometric parameters of AA Tau are given in Section 3.4, with a discussion on which additional

parameters of the system are to be constrained by numerical models. A further brief description of TORUS is given in the context of modelling magnetospheric accretion in section 3.5, followed by a presentation of the synthetic photometry produced by the models in section 3.6. Finally, a comparison between these models and observational data is presented in section 3.7 along with a discussion of the additional constraints that have successfully been placed on the AA Tau system as a result of this work.

3.2 Observational photometry

Photometric observations of AA Tau show periodic dips in its light curve, which have been explained by azimuthally asymmetric accretion (e.g. B99, B03; O'Sullivan et al. 2005). The stellar magnetic field lifts material out of the circumstellar disc, channelling the disc material onto the photosphere. If the magnetosphere axis is misaligned with the rotation axis, the disc material will have a smaller potential to overcome by traversing field lines that provide a shorter path between the disc and the photosphere. This causes two waves of material to rise up in disc warps on opposite sides of the star with each warp obscuring part of the photosphere. Hotspots are produced near the magnetosphere poles due to the accreting material impacting the photosphere. These hotspots sweep in and out of view as the star rotates, separated by half a rotation period. Since the line-of-sight inclination of AA Tau is sufficiently high, the photosphere and hotspot in the observable hemisphere are only periodically visible. This causes photometric variations, where AA Tau appears fainter during occultation and brighter when the warp is behind the star relative to the line of sight. A graphic of this geometry is shown in Figure 3.1.

AA Tau's photometric period has been shown to vary from 8.2 to 8.6 d (e.g. Vrba et al. 1989; Bouvier et al. 1999; Artemenko et al. 2012). This general trend is supported by radial velocity measurements yielding a period of 8.29 d (Bouvier et al. 2003), although observations do show more complex variability occasionally, with multiple smaller amplitude dips having been observed by B03 and *ASAS*. Conversely, there have also been occurrences where no or very little photometric variability has been apparent over a num-

Claire F Esau

Image copyrighted.
Original source image can be found at:

http://www.scientific.pictures/-/galleries/astronomy/-/medias/d71be1a2-fa8b-11e2-bec1-519e42f345a7-image-of-classic-t-tauri-star

Third Party Copyright Marker

Figure 3.1: An artist's impression of a Classical T Tauri star with a similar inclination to AA Tau. There is a second disc warp obscured by the disc to the bottom right of the star. As the star rotates, the disc warp sweeps across the line of sight of the observer, causing photometric dips. *Image Credit: Russell Kightley Media. Retrieved from http://www.scientific.pictures/-/galleries/astronomy.*

ber of stellar rotation periods (e.g. observations by B03 in the months of August and September 1999; see Appendex A). The degree of photometric variability is expected to change with time as the geometry of the system itself will not remain uniform; the combination of differential rotation of the disc and solid-body rotation of the magnetic field causes the magnetic field lines to twist. This leads to *inflation* (Lovelace et al. 1995) in which magnetic field lines on either side of the corotation radius break and open up, resulting in no or very little accretion (see Section 1.4). Photometric variations from AA Tau during periods of steady accretion have been found to reach an amplitude of $\Delta V \sim 1.7$ mag. Since the photometric period is generally similar to the rotational period of AA Tau, a constraint is placed on the position of the inner edge of the disc, which is equal to the Keplerian corotation radius of 8.8 $R_\star$ for an 8.22 d period. While initially AA Tau's photometric behaviour was regarded as atypical of CTT photometry, light curves showing 'AA Tau-like' variations – that is, variations due to an occulting wall, rather than more periodic variations due solely to the hotspot or completely irregular variations – have been observed in ~28 per cent of CTTs (Alencar et al. 2010), from a sample of 83 CTTs.

B- and *V*-band photometric data from B99 were taken in November and December 1995, data from B03 were taken between August 1999 and January 2000, and data from B07 were taken between September 2004 and January 2005. Data from long-term surveys have also been obtained, with additional *B*, *V*, and *R*-band data from G07, taken between August 1987 and January 2004, and *V*-band data from *ASAS*, taken between December 2002 and November 2009. I have split the data from these surveys into numerous epochs for the photometric analysis, as shown in Table 3.1. While a number of these epochs do not have sufficient data for a detailed study on variations in the structure of AA Tau over individual rotations, they are still useful in determining the average nature of AA Tau's varying structure over time. All data are plotted for each waveband as a function of time in Appendix A, demonstrating both the long-term variation in photometry as well as the periods during which such variation is not observed. One clear source of variation in the data between different epochs is the photometric amplitude. It is obvious from Figure A.2 that the data from the first portion of the 1999 observing campaign does not produce well-defined photometric modulation, with variations of about 0.5 mag over a number of weeks, whereas previous observations during 1995 show a photometric amplitude of about 1.6 mag. A similar 'quiet' spell occurs in 2005 – 2006, with even less photometric variation. Conversely, data from 2007 – 2008 shows variations returning to about $\Delta V =$ 1.5 mag. Phased photometric data from the Bouvier et al. campaigns and a selection from G07 are shown in Figures 3.2 and 3.3, repsectively, where phase $\varphi = \{0, 1\}$ is out of occultation and $\varphi = 0.5$ is during occultation. The point of photometric minimum is generally clear after folding the data over the rotation period, with the exception being B03. As can be seen in Figure 3.2, there are two apparent instances of a photometric minimum. This is not an effect of phasing the data; for two rotation periods there are secondary minima apparent in the raw data which are separated by the 8.2 d period.

In addition to variations in amplitude, AA Tau also exhibits variations in brightness. Figure 3.4 shows the average out-of-occultation *V*-band magnitudes for each data set. Data falling at $\varphi < 0.15$ and $\varphi > 0.85$ were collated to find the average out-of-occultation

Table 3.1: Sources of photometric data along with the dates over which these observations were made and the filters used. The amount of data obtained in each case for each passband is also given.

Source	Filter	Dates of observations	No. of data points
Bouvier et al. (1999)		11/11/95 – 11/12/95	262 (*B*), 275 (*V*)
Bouvier et al. (2003)	*BV*	09/08/99 – 05/01/00	250 (*B*), 273 (*V*)
Bouvier et al. (2007)		11/09/04 – 25/01/05	99 (*B*), 115 (*V*)
		12/08/87 – 12/01/88	47 (*BVR*)
		04/09/88 – 25/12/88	24 (*BV*), 19 (*R*)
		02/08/89 – 26/12/89	59 (*BV*), 44 (*R*)
		31/08/90 – 08/01/91	46 (*BV*), 39 (*R*)
		03/09/91 – 11/11/91	31 (*BV*), 19 (*R*)
		23/08/92 – 27/11/92	30 (*BV*), 9 (*R*)
		19/08/92 – 14/10/93	33 (*BV*), 24 (*R*)
Grankin et al.	*BVR*	13/09/94 – 18/10/94	12 (*BVR*)
(2007)		20/08/95 – 30/10/95	21 (*BV*), 18 (*R*)
		28/08/97 – 03/10/97	10 (*BV*), 9 (*R*)
		18/09/98 – 20/10/98	24 (*BVR*)
		09/08/99 – 16/12/99	96 (*BVR*)
		01/09/00 – 23/10/00	14 (*BVR*)
		16/08/01 – 23/09/01	15 (*BVR*)
		13/09/02 – 30/11/02	58 (*BVR*)
		26/08/03 – 23/01/04	47 (*BVR*)
		13/12/02 – 13/03/03	55
		10/08/03 – 24/02/04	64
Pojmanski et al.	*V*	21/09/04 – 19/12/04	101
(2005)		17/08/05 – 02/01/06	44
		20/08/07 – 06/03/08	48
		13/09/08 – 28/02/09	36
		14/09/09 – 27/11/09	10

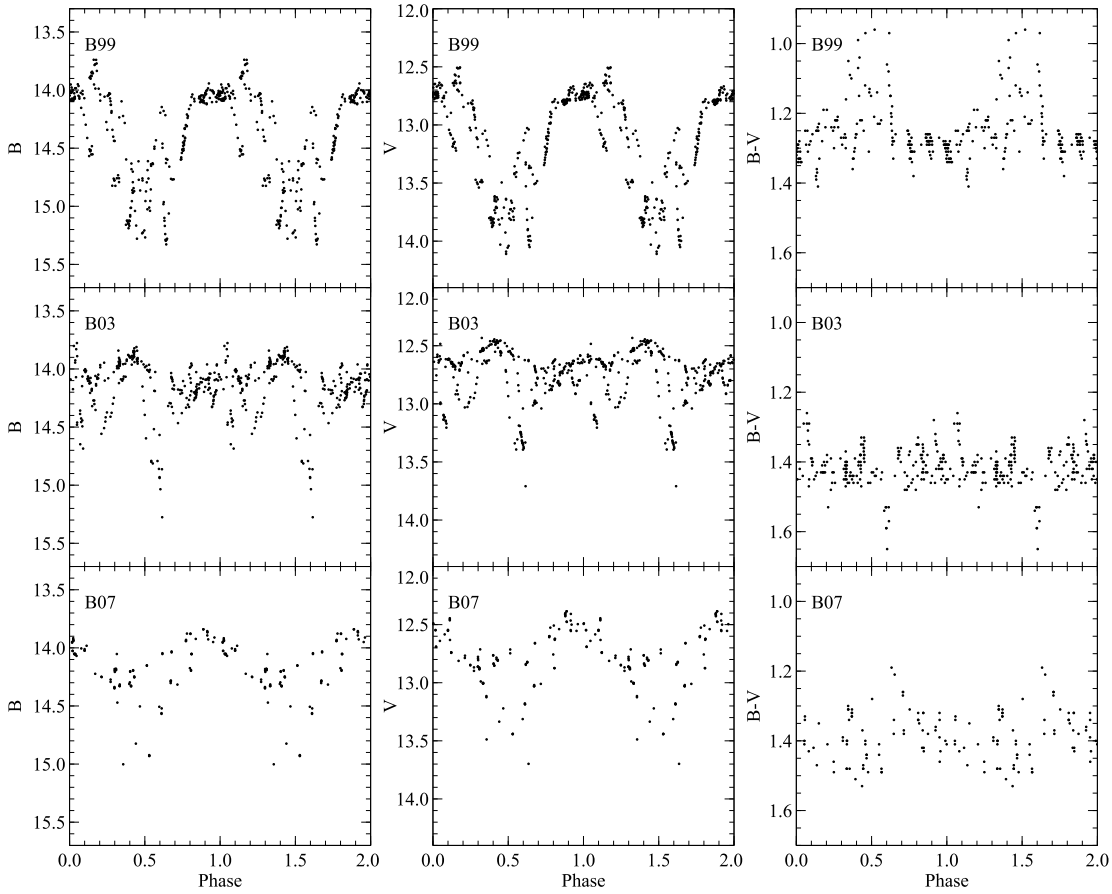

Figure 3.2: B and V photometry for AA Tau from B99, B03 and B07. $B - V$ colours for each data set are on the right. Observations are phased over a period of 8.22 days, where the system is out of occultation at phase $\varphi = 0$ and at maximum occultation at $\varphi = 0.5$. Data from B03 shows two apparent occultation events in one period. This is not an effect of phasing the data; this double trough is also apparent in the raw unphased data.

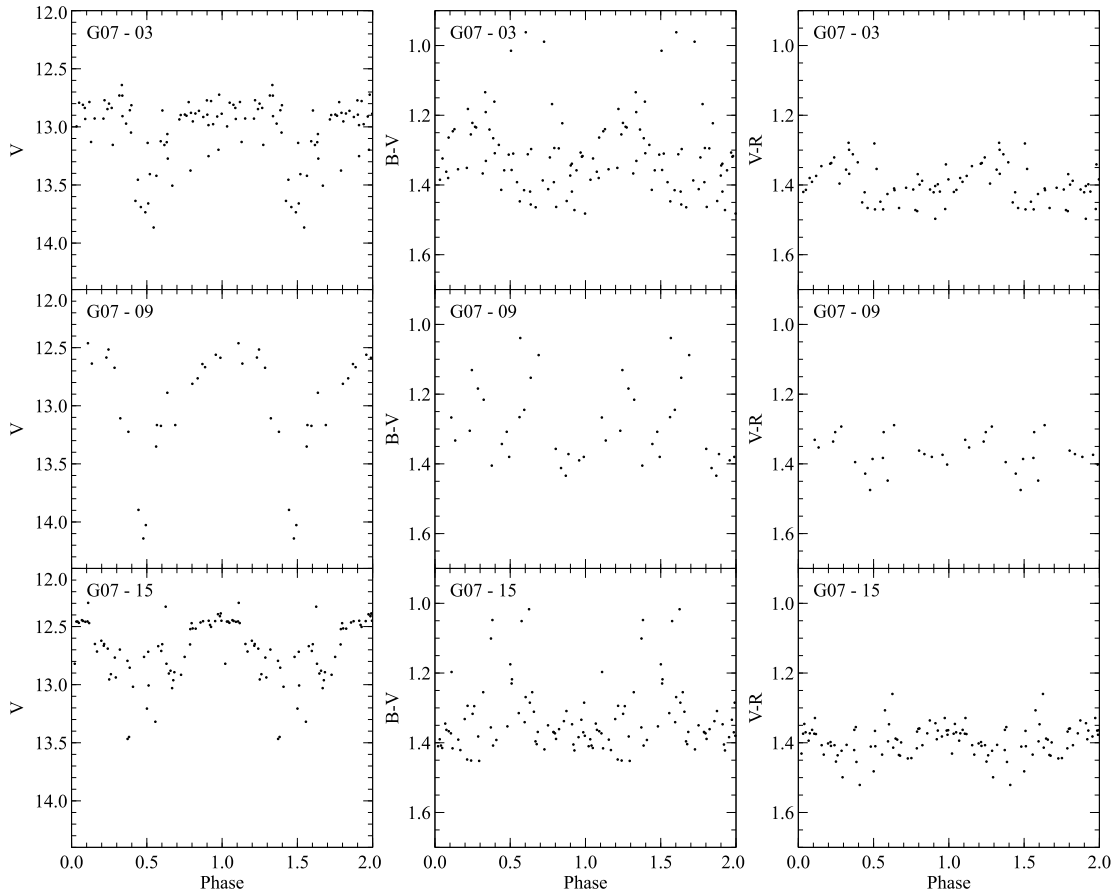

Figure 3.3: A selection of photometric results from G07. The left-hand column shows V-band photometry, with $B-V$ in the centre and $V-R$ on the right. The epochs presented are the third *(top)*, ninth *(middle)*, and fifteenth *(bottom)* as given in Table 3.1 (taken in the years 1989, 1995, and 2002, respectively). The redder end of the spectrum is clearly less sensitive to AA Tau's photometric variations, with significantly less variability in $V-R$ than in $B-V$.

magnitude during each epoch, along with the standard deviation of each data set. The global mean and standard deviation are given in Figure 3.4 by the blue line and light blue shaded region, respectively. The global mean lies at $V = 12.73$ while the full spread in data varies from a maximum brightness of $V = 12.33$ (G07, epoch 11) to a minimum brightness of $V = 13.69$ (*ASAS*, epoch 6) out of occultation. The range in individual data sets is denoted by red dashes.

Colour changes are evident in AA Tau's photometry. Phased $B - V$ colour plots are presented in Figure 3.2, along with phased B and V observations. The average $B-V$ colour out of occultation is seen to increase from ~1.25 in B99 to ~1.42 in B03. This reddening has been attributed to a lower accretion rate during the 1999 (B03) observing campaign, causing a reduction in the blue excess. The average colour excess remained in the region of 1.4 in the data from the 2004 observations, although there is more dispersion. The $B-V$ index clearly varies over the stellar rotation period. The average $B - V$ colour was found to decrease by about 0.4 mag during occultation in the 1995 observing campaign of B99, i.e. AA Tau appeared bluer when fainter. However, as with the variation in photometric amplitude at different epochs, $B - V$ behaviour also changes; there is no evidence of a correlation between colour and brightness in the later observations of B03 and B07, with both the bluest and reddest colours in the B07 data occurring during the photometric minimum (see the bottom right plot of Figure 3.2). Phased colour plots from G07 also show a wide behaviour in colour variability. These data do often show the system to be bluer when fainter, particularly during the years towards the end of the campaign (see e.g. bottom panel of Figure 3.3), but the reverse is also occasionally seen to be true. Equally, there are times when there is clearly a significant variation in colour with stellar rotation but there is too much dispersion to say with certainty whether there is any correlation between this colour change and overall brightness. However, one thing that is clear is that there is significantly less colour variation towards the redder end of the spectrum; there is very little variability found in $V - R$. Comparisons between $B - V$ and $V - R$ variability are shown in Figure 3.3.

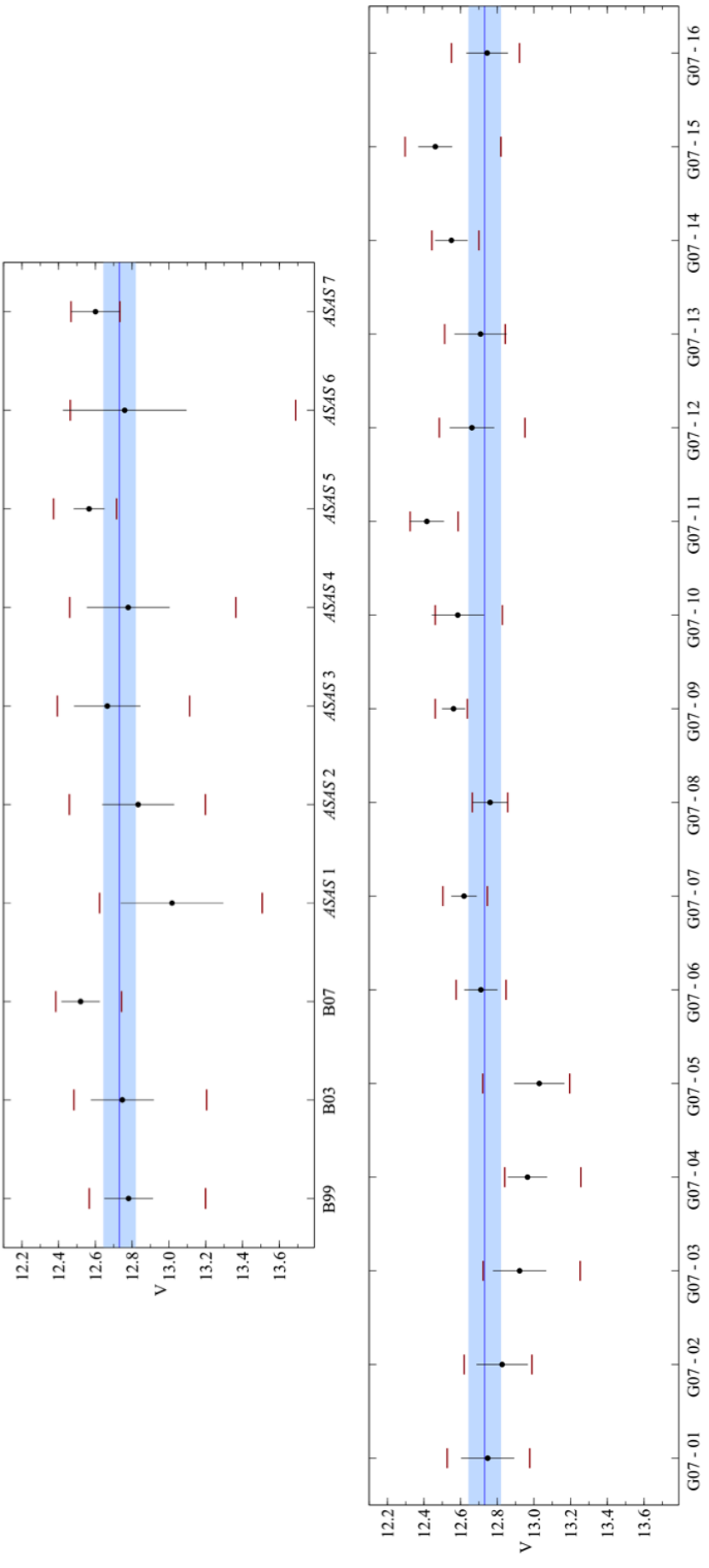

Figure 3.4: Average out-of-occultation magnitudes for each data set. The data points follow the order of B99, B03, B07, and *ASAS* 1 – 7 *(top)*, and each of the G07 epochs *(bottom)*. Red dashes show the range in each individual data set with the corresponding standard deviation given by the vertical error bars. The global mean is given by the blue line, with the global standard deviation given by the shaded blue region.

Recently AA Tau's photometry has changed significantly, with a decrease in the average brightness level by ∼2 mag occurring during 2011 (Bouvier et al. 2013). Observations taken in 2011 show no evidence of coherent photometric modulations, but by the end of 2012 an 8.2 d period is recovered, while remaining in this much fainter state. V-band magnitudes during this time range from $V \simeq 14$ to $V \simeq 16.5$, with an average brightness of $V \simeq 14.8$ and an amplitude of up to 0.9 mag. This has been attributed to a density perturbation in the disc, resulting in an increase in visual extinction from $A_V = 0.8$ mag (B99) to $A_V \geq 4$ mag with no evidence for any significant change in the mass accretion rate.

3.3 Geometry

The magnetosphere of AA Tau is modelled as a dipole field along which circumstellar material is assumed to be travelling ballistically. This flow is defined by the mass accretion rate $\dot{M}_{\rm acc}$, stellar mass $M_\star$, stellar radius $R_\star$, dipole offset θ, and inner and outer magnetosphere radii, $r_{\rm i}$ and $r_{\rm o}$ respectively. The dipole offset is the angle by which the dipole is tilted with respect to the axis of rotation, where $\theta = 0^\circ$ describes a system in which the magnetic field and stellar rotation axis are aligned. The system is also inclined to the observer by an angle i. The effects that i and θ have on the observed photometric variations of CTTS have been studied in detail by Mahdavi & Kenyon (1998). They also discuss the most likely path that accreting material will take. A tilted dipole results in some field lines providing a longer path to the stellar surface than others, with material in the accretion disc therefore potentially having to travel further depending on which field lines the material travels along. Material traversing the longer paths needs to gain potential energy as it climbs the line, whereas material travelling from the same position in the disc but along the opposite, shorter field line is able to simply fall onto the star. This is depicted in Figure 3.1, where material above the disc on the left of the image clearly has much more of a potential to overcome than were it to travel underneath the disc to the opposite magnetic pole of the star. Surface hotspots are defined geometrically where the

flow hits the stellar surface. We assume that all the kinetic energy from the accretion flow is liberated as thermal radiation. The temperature of these hotspots is calculated from the accretion luminosity and the area of the hotspots. Typically we have found that the hotspots cover about 2 per cent of the stellar surface.

Material is assumed to accrete from around the corotation radius, interior to which the disc is truncated by the magnetic field. $r_{\rm i}$ and $r_{\rm o}$ define the inner and outer radii at which closed magnetic field lines transport material from the disc to the star. In the models presented here, material is assumed to accrete only along energetically favourable field lines, resulting in an azimuthal variation in accretion spot luminosity. The resulting shocks from material impacting the stellar surface produce an accretion signature in the form of a thin elliptical arc near the magnetic pole in each hemisphere.

The photometric variations of AA Tau have been attributed to a warp in the circumstellar disc (B99), caused by the tilt of the magnetic dipole. This produces an optically thick occulting wall. The height of this inner disc wall was modelled by B99 as an azimuthally varying cosine function, where

$$h(\phi) = h_{\rm max} \left| \cos \frac{\pi \, (\phi - \phi_0)}{2} \right| \tag{3.1}$$

h is the height of the disc at azimuth angle ϕ, and ϕ_0 is the azimuth at which the disc height is at its maximum, $h_{\rm max}$. This relation has been shown roughly to fit observations. The photometric minima then correspond to the times at which the highest part of the disc wall occults the star. The occulting warp in our model is defined in a similar manner to B99, in that it is parameterised by the aspect ratio $h_{\rm max}/r_{\rm o}$. An illustrative model of the disc-star system is shown in Figure 3.5. We do not consider the outer disc structure since this will have a negligible effect on the both the photometry and the line profiles which are presented in the next chapter.

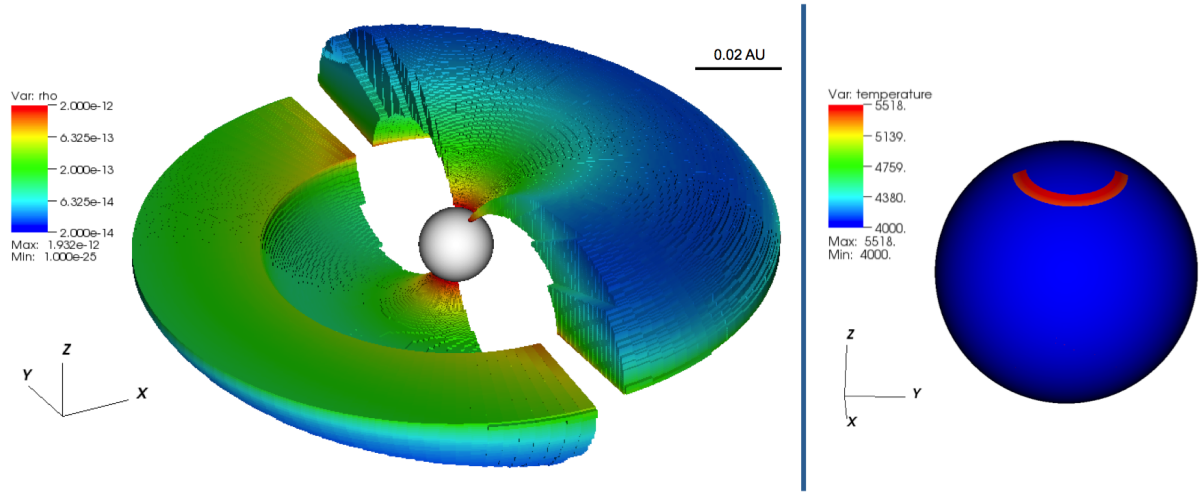

Figure 3.5: AA Tau, modelled with TORUS. The density structure of the magnetosphere is shown on the left with AA Tau shown centrally in white. The density of material covers two orders of magnitude, increasing from 2×10^{-14} g cm^{-3} (blue) to 2×10^{-12} g cm^{-3} (red). The temperature structure of AA Tau is shown on the right, with the hotspot clearly visible.

3.4 Stellar parameters

Numerous simulations were run for AA Tau over a range of parameter space. The stellar parameters used in the model are listed in Table 3.2 with the mass accretion rate ($\dot{M}_{\rm acc}$), dipole offset (θ), aspect ratio ($h_{\rm max}/r_{\rm o}$), and inner magnetosphere radius ($r_{\rm i}$), which were varied. Stellar parameters were taken from B99, determined as follows: $L_\star$ was calculated using the observed V-band magnitude of 12.5, when AA Tau is not obscured by the warp, with a bolometric correction of -0.87 ± 0.15 (Kenyon & Hartmann 1995). For a star at a distance of 140 pc, this yields a stellar luminosity of $L_\star/L_\odot = 0.8 \pm 0.1$. Assuming the standard effective temperature for a K7 dwarf, $T_{\rm eff} = 4030 \pm 30$ K, a stellar radius of $R_\star/R_\odot = 1.85 \pm 0.15$ was determined. The mass of $M_\star = 0.85$ M$_\odot$ was found from stellar evolution models. A high inclination angle i is apparent, since deep central absorption is present in Balmer emission lines. The source of this absorption is thought to be equatorial, lying at or above one stellar radius from the disk (Kwan 1997). The line of sight must intercept both this disk corona and the top of the accretion column in which the Balmer lines are formed in order to explain these observations. A value of $i = 75°$ has been

adopted, yielding a rotation period of 8.22 days using $v \sin i = 11$ km s^{-1} (B99), which is consistent with observations (e.g. Vrba et al. 1989).

A quadratic limb darkening law from Kopal (1950) has been adopted, given by

$$I_\mu / I_0 = 1 - a(1-\mu) - b(1-\mu)^2, \tag{3.2}$$

where μ is the cosine of the angle subtended by the normal to a given point on the stellar surface and the line of sight, I_μ is the intensity of the emergent radiation at angle $\cos^{-1}\mu$, and I_0 is the intensity of centrally emergent radiation, i.e. at $\mu = 1$. a and b are wavelength dependent linear and quadratic limb darkening coefficients respectively. The coefficients used in the model for B, V and R bands are given in Table 3.2, as well as the central wavelengths of each of these bands.

3.5 Modelling magnetospheric accretion

The radiative transfer code TORUS (Harries 2000; Symington et al. 2005; Kurosawa et al. 2006) uses the adaptive mesh refinement (AMR) technique to sample each region of the system being simulated (e.g. magnetosphere, accretion disc) with sufficient resolution, without being too computationally expensive. For 2D models the simulation space is 2D cylindrical and rotationally symmetric in azimuth. Splitting occurs across the cylinder radius r and height z to produce a grid of squares, where each square is the cross-section of a given annulus. 3D simulations use a 3D cylindrical coordinate system in which the top level of the AMR mesh is a cylinder that has a height equal to its radius. Child cells may be formed by either splitting the parent equally in both height, radius, and azimuthal extent (resulting in eight children), or by just splitting equally in height and radius (resulting in four children). In general the cells are truncated, cylindrical shells. The principal advantage of this method is that the grid need only be refined in regions where there are significant departures from rotational symmetry, thus minimising the global number of grid cells.

Table 3.2: Parameters for the grid of models. Stellar parameters i, $M_\star$, $R_\star$, $T_{\rm eff}$ and $r_{\rm o}$ are fixed, taken from B99. Effective wavelengths and limb darkening coefficients are from Howarth (2011). Model parameters $\dot{M}_{\rm acc}$, $h_{\rm max}/r_{\rm i}$ and θ have been fitted using the values listed here.

Parameter	Description	Value
i	Stellar inclination	75°
$M_\star$	Stellar mass	0.8 $M_\odot$
$R_\star$	Stellar radius	1.85 $R_\odot$
$T_{\rm eff}$	Effective temperature	4000 K
$\log g$	Surface gravity	3.8 (cgs)
$r_{\rm o}$	Outer magnetosphere radius	8.8 $R_\star$
$\lambda_{\rm eff}(B)$	Effective wavelength (B passband)	4576.4 Å
$\lambda_{\rm eff}(V)$	Effective wavelength (V passband)	5608.3 Å
$\lambda_{\rm eff}(R)$	Effective wavelength (R passband)	6562.8 Å
a_B	Limb darkening coefficient a (B-band)	1.054
b_B	Limb darkening coefficient b (B-band)	– 0.165
a_V	Limb darkening coefficient a (V-band)	0.830
b_V	Limb darkening coefficient b (V-band)	0.016
a_R	Limb darkening coefficient a (R-band)	0.660
b_R	Limb darkening coefficient b (R-band)	1.303
$\dot{M}_{\rm acc}$	Accretion rate	1×10^{-9}
	($M_\odot$ yr^{-1})	2×10^{-9}
		5×10^{-9}
		1×10^{-8}
$h_{\rm max}/r_{\rm o}$	Aspect ratio	0.29
		0.30
		0.31
		0.32
		0.33
		0.34
$r_{\rm i}$	Inner magnetosphere radius	5.2
	(R$\star$)	6.4
		7.6
θ	Dipole offset	10°
		20°
		30°
		40°

The main components considered in the photometric models are the photosphere and the magnetosphere. A disc wind is also included in the spectroscopy models, presented in Chapter 4. The method of general source set-up used in TORUS has previously been described in Section 2.2.2, in which the total continuum source is comprised of both a central star and photospheric hotspots. The stellar parameters for AA Tau used in this setup are given in the top portion of Table 3.2. The photospheric contribution is defined using the model atmosphere of Kurucz (1979) with $T_{\rm eff}$ and log g as given in Table 3.2. The hotspot contribution is given as a single-temperature blackbody, under the assumption that the kinetic energy of the infalling gas at the base of the stream is converted to thermal energy on impact with some temperature T.

The accretion flow model of Hartmann et al. (1994) model consists of a dipolar stellar magnetic field along which material from the circumstellar disc flows (see also Muzerolle et al. 2001). The circumstellar disc is truncated at the inner magnetosphere radius $r_{\rm i}$, with the disc disrupted up until the outer magnetosphere radius $r_{\rm o}$. The streamlines of the magnetic field are given by

$$r = r_{\rm m} \sin^2 \theta, \tag{3.3}$$

where $r_{\rm m}$ is the radial distance to the point in the circumstellar disc from where the material is flowing, i.e. $r_{\rm i} \leq r_{\rm m} \leq r_{\rm o}$, r is the radial distance to the material at some point in the accretion stream, and θ is the polar component of this position within the stream where $0 < \theta < \pi$ (cf. Ghosh et al. 1977).

While the Hartmann et al. model assumes an axisymmetric flow, the formation of a warp requires a dipole with an offset axis. The results presented here are calculated using the model of Mahdavi & Kenyon (1998) to calculate the shape of the accretion signature and the precise geometry of the flow. For spherical coordinates (r, θ, ϕ) in a frame where the stellar rotation axis is parallel to $\hat{\mathbf{z}}$, a second frame can be defined with coordinates (r', θ', ϕ') where the dipole axis is parallel to $\hat{\mathbf{z}}'$. The magnetic field line geometry given in equation 3.3 must be redefined in the frame of the mag-

netic dipole, and is now described by $r' = r_{\rm m}\sin^2\theta'$, with the transformation between frames given by $\cos\theta'\sin\theta' = \cos\phi\sin\theta\cos\beta - \cos\theta\sin\beta$; $\sin\phi'\sin\theta' = \sin\phi\sin\theta$; $\cos\theta' = \cos\phi\sin\theta\sin\beta - \cos\theta\cos\beta$; and $r' = r$.

The velocity of the gas at a given point along the field lines is calculated by assuming material is infalling ballistically from the initial rest point $r_{\rm m}$. Such a velocity field is given by

$$\upsilon_{\rm p} = \left[\frac{2{\rm G}M_\star}{R_\star}\left(\frac{R_\star}{r'} - \frac{R_\star}{r_{\rm m}}\right)\right]^{1/2}, \tag{3.4}$$

(Calvet & Hartmann 1992). Assuming that the infalling gas traverses a path parallel to the magnetic field lines, the poloidal velocity is found to be

$$\boldsymbol{\upsilon}_{\mathbf{p}} = -\upsilon_{\rm p}\left[\frac{3y^{1/2}(1-y)^{1/2}\hat{R} + (2-3y)\hat{z}}{(4-3y)^{1/2}}\right], \tag{3.5}$$

where $y = r'/r_{\rm m} = \sin^2\theta'$.

The density of material moving along the field lines is calculated by applying conservation of mass using the method of Hartmann et al. (1994). For two hotspots, the mass flux at the photosphere between two latitudes $\theta_{\rm i}$ and $\theta_{\rm o}$, corresponding to the inner and outer magnetosphere radii, is related to the density of material in the stream by

$$\dot{M} = 2\int_{\theta'_{\rm i}}^{\theta'_{\rm o}} 2\pi R_\star^2\,\sin\theta'\,{\rm d}\theta'\,\rho(R_\star)\,\upsilon_{\rm r}(R_\star). \tag{3.6}$$

The density of the material at some point r within the stream is given by

$$\rho = \frac{\dot{M}\,R_\star}{4\pi(R_\star/r'_{\rm i} - R_\star/r'_{\rm o})}\,\frac{r'^{-5/2}}{(2{\rm G}M_\star)^{1/2}}\,\frac{(4-3y)^{1/2}}{(1-y)^{1/2}}. \tag{3.7}$$

3.5.1 Splitting the AMR grid

One numerical subtlety is including splitting criteria that produce a grid which sufficiently resolves the regions of interest, without wasting computational time and memory splitting the grid unnecessarily elsewhere. The decision to split a cell is therefore not made using

some global criterion, but varies depending on the structure contained within the cell. For instance, when splitting the area of the grid which contains the magnetospheric accretion streams, the code first needs to ascertain whether or not inflowing material is present in the given cell. For large cells it is easy to miss the flow being present if it is contained in just a very small corner of the cell. To avoid missing these regions, 400 points are randomly selected within the cell and if the radial position of one of these points is found to coincide with a region of infalling material then the cell is set to contain inflowing material. The cell will be split if its size is larger than some given length scale. Azimuthal splitting will occur if the azimuthal extent of cell, which in three dimensions is a cylindrical slice, is greater than 7.5° ($\frac{1}{48}$ of the circumference). If a cell is found to contain solely the photosphere then it will not split.

The cells in which the warp falls are split according to the height of the disc warp in a given cell. For a cell to be split, it must lie over the outer outer magnetosphere boundary, where the disc warp is present. If the height of the portion of the warp that falls within the cell is less than the size of the cell then the cell is split. The maximum depth that the AMR grid is allowed to reach is defined in the user input parameters, and this splitting in accordance with the warp height is repeated until this depth is reached. This enables the resolution across the height of the warp to be as smooth as possible given the AMR depth restrictions.

The disc wind is distributed radially over a logarithmically spaced size scale from the inner edge of the wind to the outer edge. For cells contained within the wind zone, the distance from the inner edge of the wind to the central point in the cell is found. The location of the cell is used to determine how much it may be split; for cells within some characteristic distance of the inner disc wind, splitting will occur to a greater degree, such that there is a logarithmically increasing number of cells from the outside radius of the disc wind inwards. Examples of these splitting criteria are depicted in Figure 3.6.

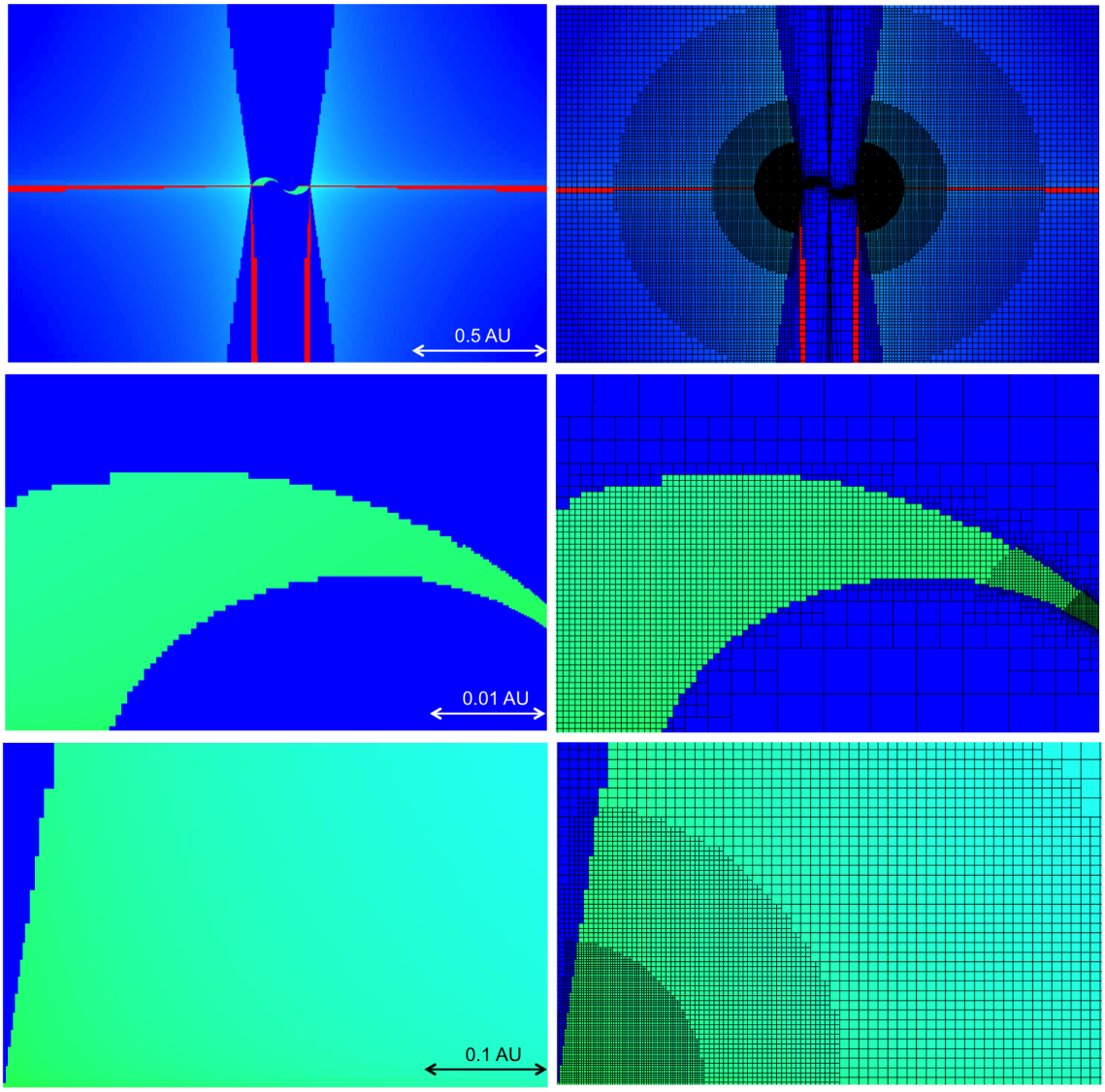

Figure 3.6: AMR splitting in various regions of the grid, shown without and with the overlying mesh in the left and right columns, respectively. The top panels show the grid in its entireity. The particularly well-refined regions are clearly shown to be the accretion streams and the very inner regions of the disc. The middle panels show the splitting of the accretion streams, with higher levels of refinement on the right-hand side of the stream, as it approaches the photosphere, when there is a larger gradient in height z. The bottom panels show a zoomed-in view of the inner regions of the disc wind, in which the highest levels of refinement are found towards the inner edge of the wind at the base. The amount of refinement reduces logarithmically as the distance from the innermost launching point increases.

3.6 Synthetic photometry

Photometric models are calculated by constructing a grid of rays and integrating a formal solution to the equation of radiative transfer along multiple lines of sight. The rays are chosen to sample the photosphere, the hotspots, and the disc wall with sufficient coverage for each component of the system.

The monochromatic flux F which is calculated by the model is converted to apparent magnitude m using

$$m = -2.5 \log\left(\frac{F}{F_0}\right), \tag{3.8}$$

where F_0 is a normalising flux, corresponding to $m = 0$, with $F_0 = 6.4{\times}10^{-9}$ erg s^{-1} cm^{-2} Å^{-1} for the B-band, $F_0 = 3.75 \times 10^{-9}$ erg s^{-1} cm^{-2} Å^{-1} for the V-band, and $F_0 = 1.8 \times 10^{-9}$ erg s^{-1} cm^{-2} Å^{-1} for the R-band (Cox 2000). The resulting photometry was folded over an 8.22 day period (Bouvier et al. 2007) and reddened by A_V =0.78 (B99), A_B =1.03, and $A_R = 0.584$, adopting reddening constants of $A_V/E_{B-V} = 3.1$ and $A_R/E_{B-V} = 2.32$ (Schultz & Wiemer 1975), for direct comparison with observations. The point of maximum occultation has been set to occur at a phase of 0.5, with no occultation at phase 0. Ideally a statistical analysis using a χ^2 minimalisation technique would have been performed to determine the best fitting parameters. However, due to the variability of AA Tau's photometry, we have taken a pragmatic approach in selecting a best fitting model by judging the level of agreement between models and observations over different epochs by eye.

B99 calculated an accretion luminosity of $L_{\rm spots} = 6.5 \times 10^{-2}$ L$_\odot$ using the blue excess determined from photometric observations, where

$$L_{\rm spots} = A_{\rm spots}\sigma T_{\rm spot}^4. \tag{3.9}$$

$A_{\rm spots}$ is the area of the stellar surface which is covered by the accretion spots, and $T_{\rm spot}$ is the spot temperature, found using the B-band flux of a spot measured from AA Tau's SED.

Table 3.3: The range of accretion luminosities calculated for different mass accretion rates.

$\dot{M}_{\rm acc}$ ($M_\odot$ yr^{-1})	$L_{\rm min}$ (10^{-2} $L_\odot$)	$L_{\rm max}$ (10^{-2} $L_\odot$)
1×10^{-8}	10.9	12.5
5×10^{-9}	5.5	6.1
2×10^{-9}	2.1	2.5
1×10^{-9}	1.1	1.2

The B99 accretion luminosity was used to determine the best mass accretion rate from the models presented here. The range of accretion luminosities calculated in different models for each accretion rate is given in Table 3.3. An accretion rate of $\dot{M}_{\rm acc} = 5 \times 10^{-9}$ $M_\odot$ yr^{-1} has been selected, being the accretion rate most consistent with the accretion luminosity from B99.

3.7 Results

It is clear that the AA Tau system varies considerably over time, so there will be a number of different parameter sets that provide the best fits to the data at different times. For this reason, we have averaged all of the available data and have compared this mean light curve with our models. We then compared the models that gave the best fit to this averaged data with individual observational data sets to determine the set of parameters that best describes the system over the longest period of time. The average B, V and R light curves are presented in Figure 3.7. B and V-band data are binned into 20 bins per phase, and R-band data are binned into 10 bins per phase. The solid line shows the mean magnitude in each bin along with the standard deviation. The median magnitude is given by the dashed line, and the shaded region gives the range in magnitudes in which the median 90 per cent of data falls, thus removing the more extreme outlying data points.

Comparison plots between the averaged observational data and a number of our models are presented in Appendix B. One obvious feature of our results is the offset between averaged observational data and modelled data in the V-band by about 0.2 mag. As mentioned in Section 3.2, the observed maximum brightness has been found to vary with

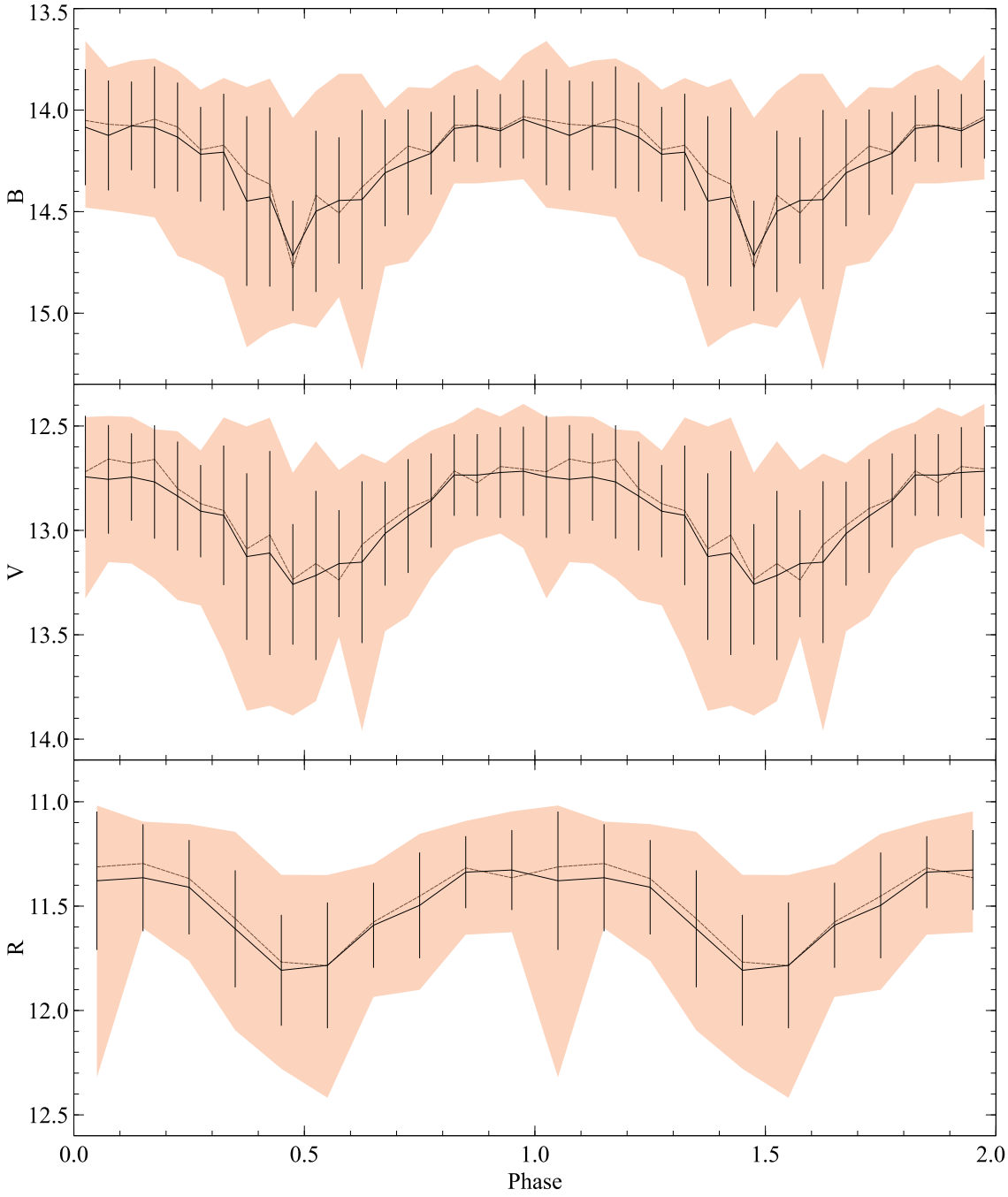

Figure 3.7: Average light curves for *B*-band *(top)*, *V*-band *(centre)*, and *R*-band *(bottom)* observations split across 20 bins per phase in *B* and *V* and 10 bins in *R*. The solid line shows the mean brightness in each bin and the dashed line shows the median. The standard deviation of each bin is shown by the error bars. The brightest 5 per cent and faintest 5 per cent of the data have been removed with the remaining 90 per cent shown in the shaded region.

time, with fluctuations around the $V \sim 12.4 - 13.0$ mag level over the last 25 years (see Figure 3.4). A number of our models yield a maximum brightness of $V \sim 12.5$ and are therefore consistent with the data sets showing brighter out-of-occultation magnitudes. From Figure 3.2, AA Tau is clearly bluer in 1995–96, which implies that this change in absolute brightness is not inherent to the star itself. Since V-band data from B99 is systematically fainter both during and out of occultation, the cause is also not likely to be a change in the warp structure. This points to an azimuthally symmetric density perturbation in the disc, obscuring the photosphere even when the warp is on the opposite side of the star. Since the only obscuring material included in the model presented here is the warp itself, it is reasonable to expect that the modelled data may systematically lie above the average V-band photometry since we calculate the maximum brightness for a given parameter set, providing good agreement with the brightest observations. Disappearance of this perturbation would cause the reduced brightness to increase in V back to the level calculated in the model. No significant change in the B-band photometry implies that the additional density perturbation is restricted to the plane of the disc, thus not obscuring the hotspot.

With the cause of the brightness variations in AA Tau being a warped disc, the height of the warp will strongly affect the observational results. It is therefore unsurprising that, from our models, the aspect ratio appears to be the parameter best constrained by observations. Synthetic light curves from a disc with $h_{\rm max}/r_{\rm o} \geq 0.33$ occult too much of the photosphere, producing photometric variations in that are far too deep in V to fit observations (see Fig B.4 – B.8). B-band models with $h_{\rm max}/r_{\rm o} = 0.32$ fit well at low dipole offsets but, while V-band models fit within the range of observational data, they still show excessive occultation when compared with the average observational results (Fig B.3). Further discussion is therefore restricted to $h_{\rm max}/r_{\rm o} = 0.29$, 0.30 and 0.31. B-band data are used to fit the dipole offset, since the data in this waveband are the most sensitive to the hotspot. The dipole offset angle translates to the position of the hotspot on the photosphere, with the hotspot moving closer to the line of sight as θ increases, for

stars highly inclined such as AA Tau. This has the effect that higher offset angles will cause an increase in the overall brightness in B. A dipole offset of 40° gives light curves which are too bright compared with observations, falling about 0.3 mag above the out-of-occultation magnitude, and also produces variations which are too shallow (Fig B.11, B.12). A 30° offset with a small inner magnetosphere radius, i.e. a magnetosphere with a broad radial distribution, does start to produce sufficient photometric variations and the out-of-occultation magnitude enters into the region of maximum error on the mean light curve, but the maximum brightness in V still falls above the brightest observational data (Fig B.9, B.10). The dipole offset is therefore restricted to 10° and 20°. The smallest magnetosphere size, with $r_{\rm i} = 7.6$ R$\star$, does not produce sufficient occultation in the B-band for any of the models with $h_{\rm max}/r_{\rm o} \leq 0.30$ (e.g. Fig B.10, dash-dot line). While the fit is much improved in B for $h_{\rm max}/r_{\rm o} = 0.31$ (Fig B.2), superior fits are given by the larger magnetospheres, with this smaller magnetosphere beginning to provide the best fit for $h_{\rm max}/r_{\rm o} = 0.32$. The inner magnetosphere radius is therefore restricted to $r_{\rm i} = 6.4$ and 5.2 R$_\star$, given the previous constraints placed on $h_{\rm max}/r_{\rm o}$ using V-band results.

Since the size of the magnetosphere has very little effect on V-band photometry, individual B-band datasets were used to determine the best fitting magnetosphere size. The ranges determined above were considered, with the exception of $r_{\rm i} = 6.4$ R$_\star$ where $\theta = 10°$ or 20° with $h_{\rm max}/r_{\rm o} = 0.29$ (Fig B.1, B.6), and where $\theta = 20°$ with $h_{\rm max}/r_{\rm o} = 0.30$ (Fig B.7), i.e. a smaller magnetosphere with a larger offset and smaller wall height, since there is not enough of an occultation to produce the required luminosity dip for these distinct parameter sets. The best B-band fits are given compared with all data from Bouvier et al. (1999, 2003, 2007) in Figure 3.8. B03 data are difficult to fit due to the unusual shape of the light curve with two minima present in one phase. B07 data could fit either magnetosphere size, with evidence for both shallower and deeper minima than found by the models, although the smaller magnetosphere size does not fit the $\theta = 20°$ model so well, with the resulting light curve being a touch shallow. Due to the large amplitude measured in B99, the larger magnetosphere size provides the best fit.

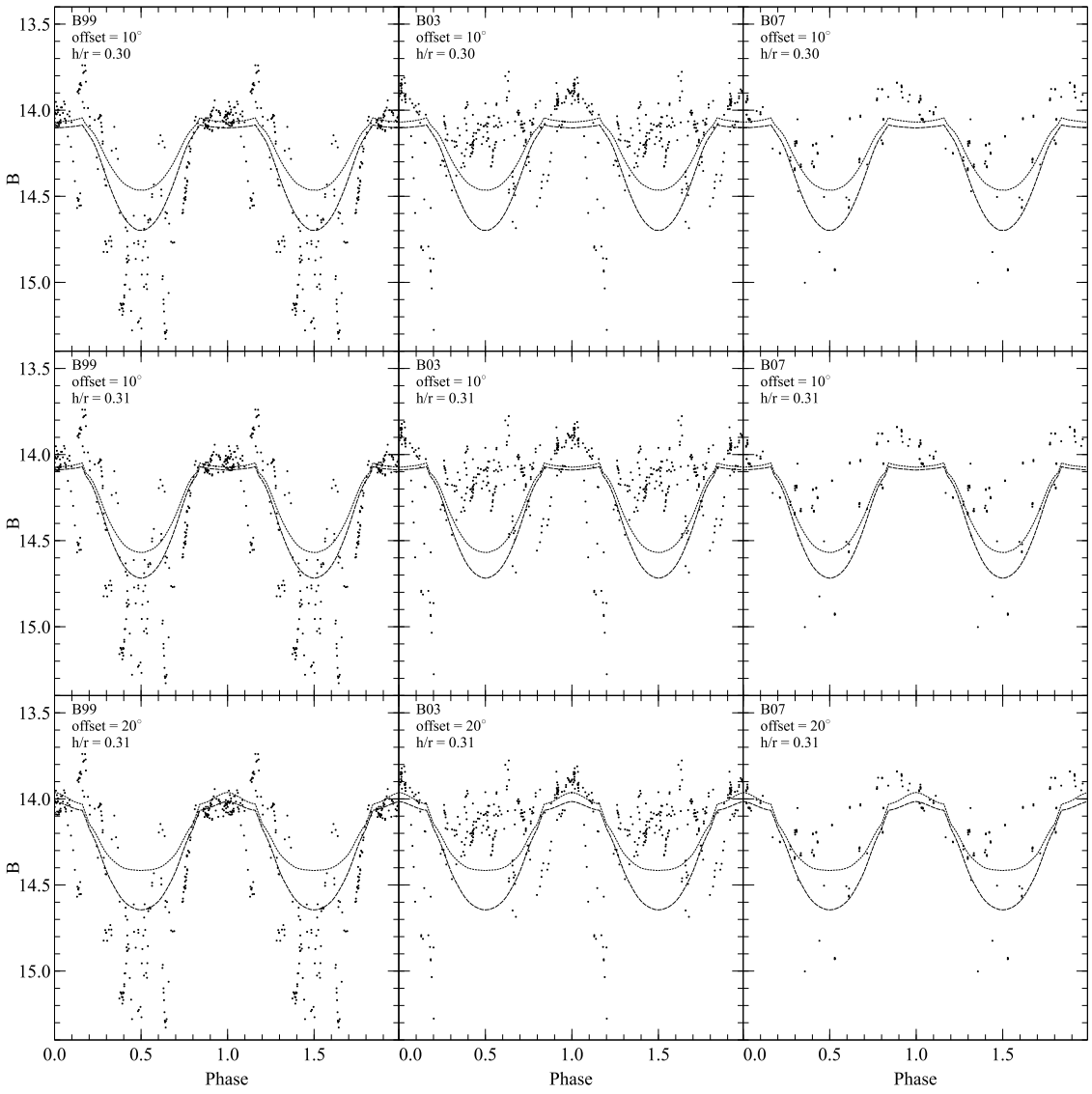

Figure 3.8: Fits to *B*-band photometry. The data source and parameter set are labelled on the top left of each plot. Dashed lines show the largest magnetosphere size, $r_{\rm i} = 5.2$ R$_\star$, and dotted lines show $r_{\rm i} = 6.4$ R$_\star$.

An inner magnetosphere radius of $r_i = 5.2\ R_\star$ has therefore been selected.

The best fits to h_{max}/r_o and θ have been have been chosen using comparisons between models and *ASAS* observations, since the B99 *V*-band data has a significant systematic offset, the B03 data contains two minima either side of $\varphi = 0.5$, and the B07 data was obtained at the same time as *ASAS 3*. The remaining parameter sets are shown in Figure 3.9. While models with $h_{max}/r_o = 0.29$ fit *ASAS 6* well, and *ASAS 2* when accounting for a slight *V*-band offset, they do not have a sufficient amplitude to fit the majority of epochs. Either of the remaining wall heights are acceptable, but $h_{max}/r_o = 0.31$ has been selected since it is the deeper of the two, better suiting *ASAS 3* and *ASAS 5* – two of the cleanest light curves. There is very little difference in models with $\theta = 10°$ and $\theta = 20°$. These best fits are shown with the cumulative data of all observations in Figure 3.10. We have selected $\theta = 10°$ in preference to $\theta = 20°$ on the basis of results from spectral line modelling (see Chapter 4).

The choice of a high aspect ratio of $h_{max}/r_o = 0.31$ produces light curves that are rather deep in the averaged *B*− and *R*-band data. The best consistent fits across the averaged data in all bands are given by two parameter sets: $\theta = 10°$, $h_{max}/r_o = 0.29$, and $r_i = 5.2$; and $\theta = 20°$, $h_{max}/r_o = 0.30$, and $r_i = 5.2$ (Figure 3.11). However, the purpose of this study is to find the best fitting geometric and physical parameters that best describe AA Tau during its accreting phase, and since these averaged data plots include a significant amount of data during AA Tau's 'quieter' phases, the mean amplitude of the light curves is reduced accordingly. The average observational results were therefore most useful only for placing initial restrictions on the parameter space, with our chosen parameter set selected on the basis that it is the most consistent with the photometric data obtained during the deeper occultation events.

3.8 Summary

While initially periodic dips in the light curves of CTTs were thought to be rare, such features have been shown to be present in at least 28 per cent of light curves (Alencar et al.

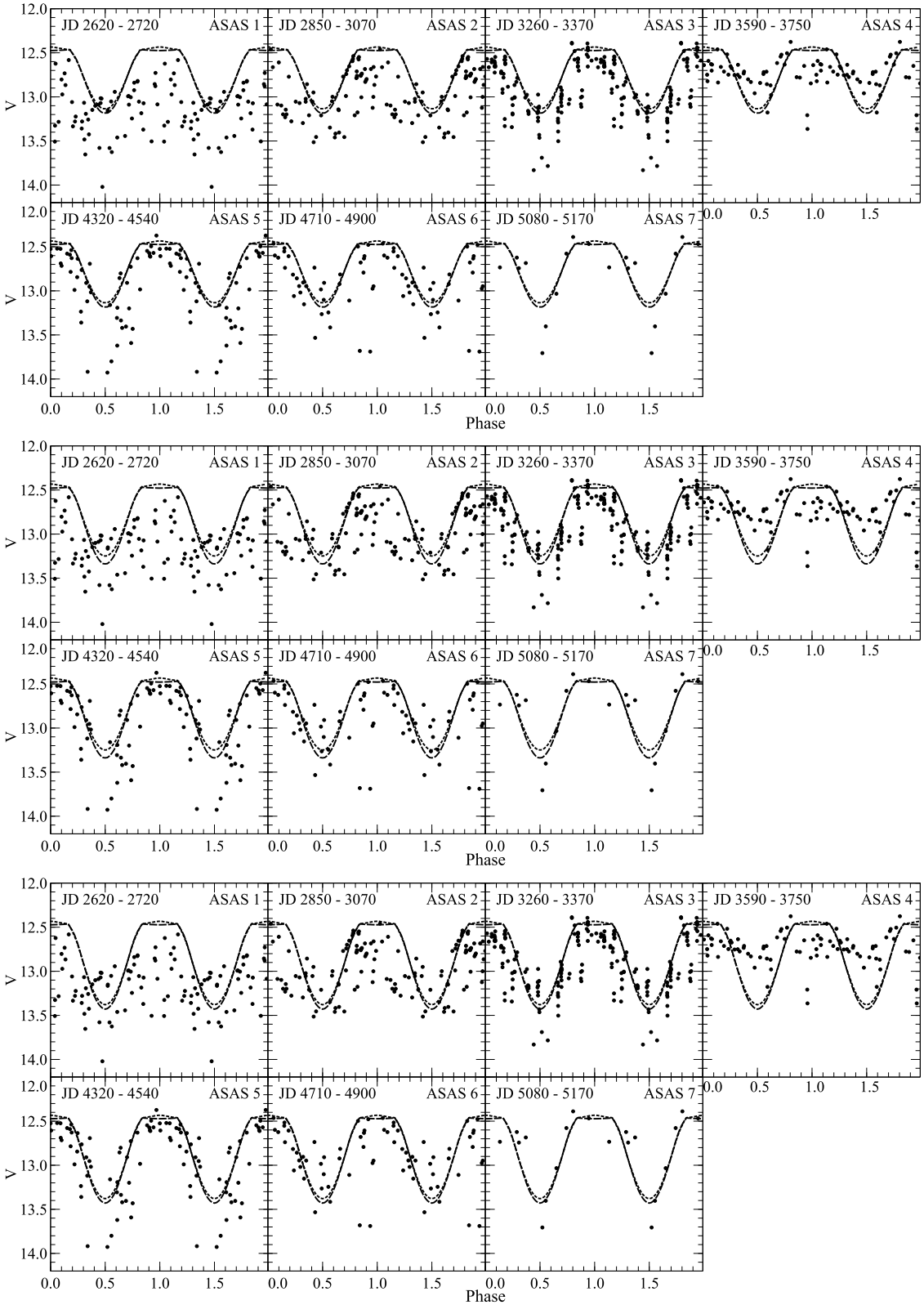

Figure 3.9: Fits to *ASAS* data for $h_{\rm max}/r_{\rm o} = 0.29$ (top), 0.30 (middle), and 0.31 (bottom), with $\theta = 10°$ (dashed) and $\theta = 20°$ (dotted), and $r_{\rm i} = 5.2\ {\rm R}_\star$. The date of each epoch is labelled on the top left of each plot.

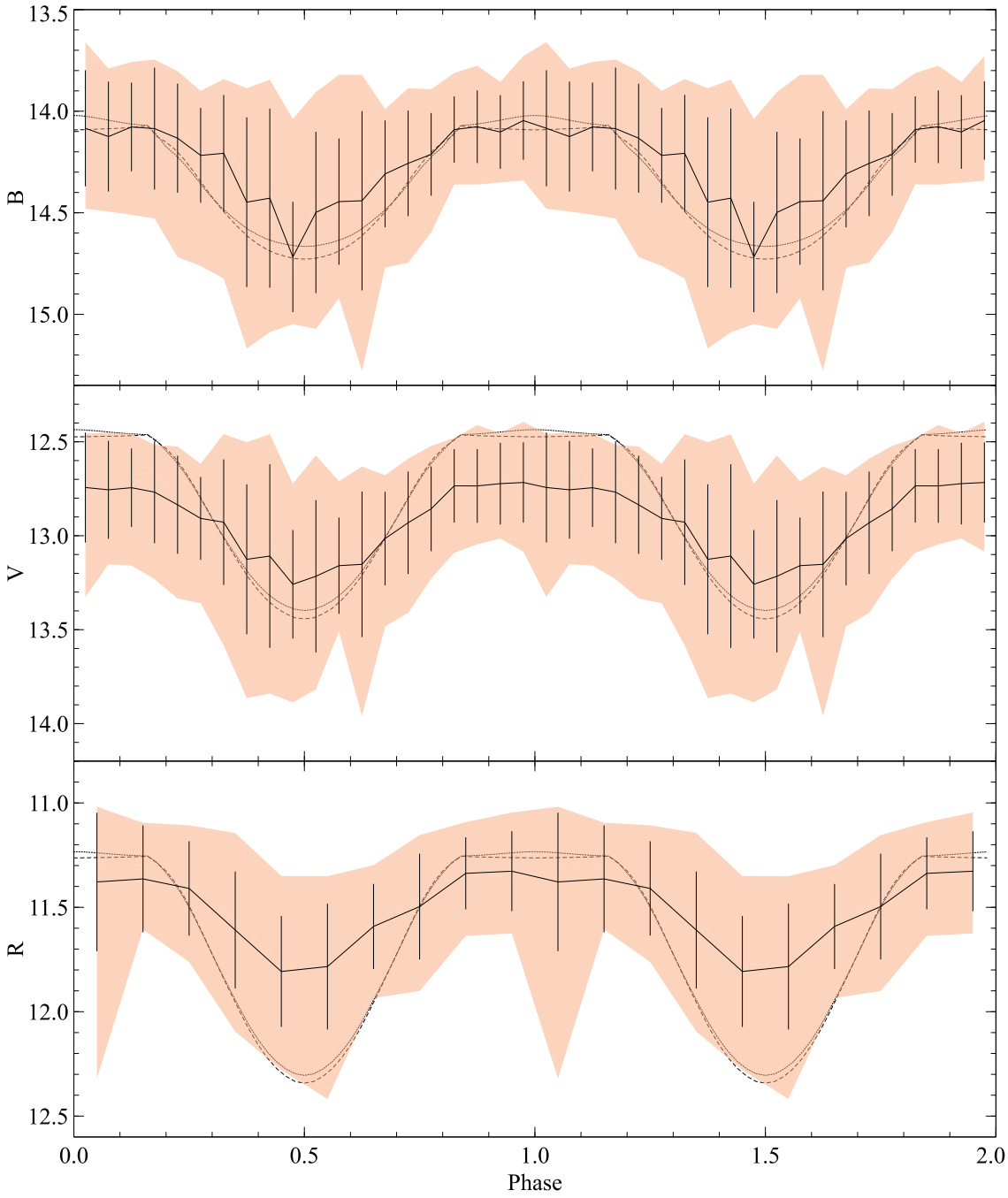

Figure 3.10: Best fits plotted against averaged photometric data from B99, B03, B07, G07, and *ASAS*, determined using individual data sets. As with Figure 3.7, the solid line shows the mean brightness at each phase with the standard deviation given by the error bars. We found observations were best fitted by models with $\dot{M}_{\rm acc} = 5 \times 10^{-9}$ M$_\odot$ yr^{-1}, $r_{\rm i} = 5.2$ R$_\star$ and $h_{\rm max}/r_{\rm o} = 0.31$. The dashed line shows a dipole offset of $\theta = 10°$ and the dotted line shows $\theta = 20°$.

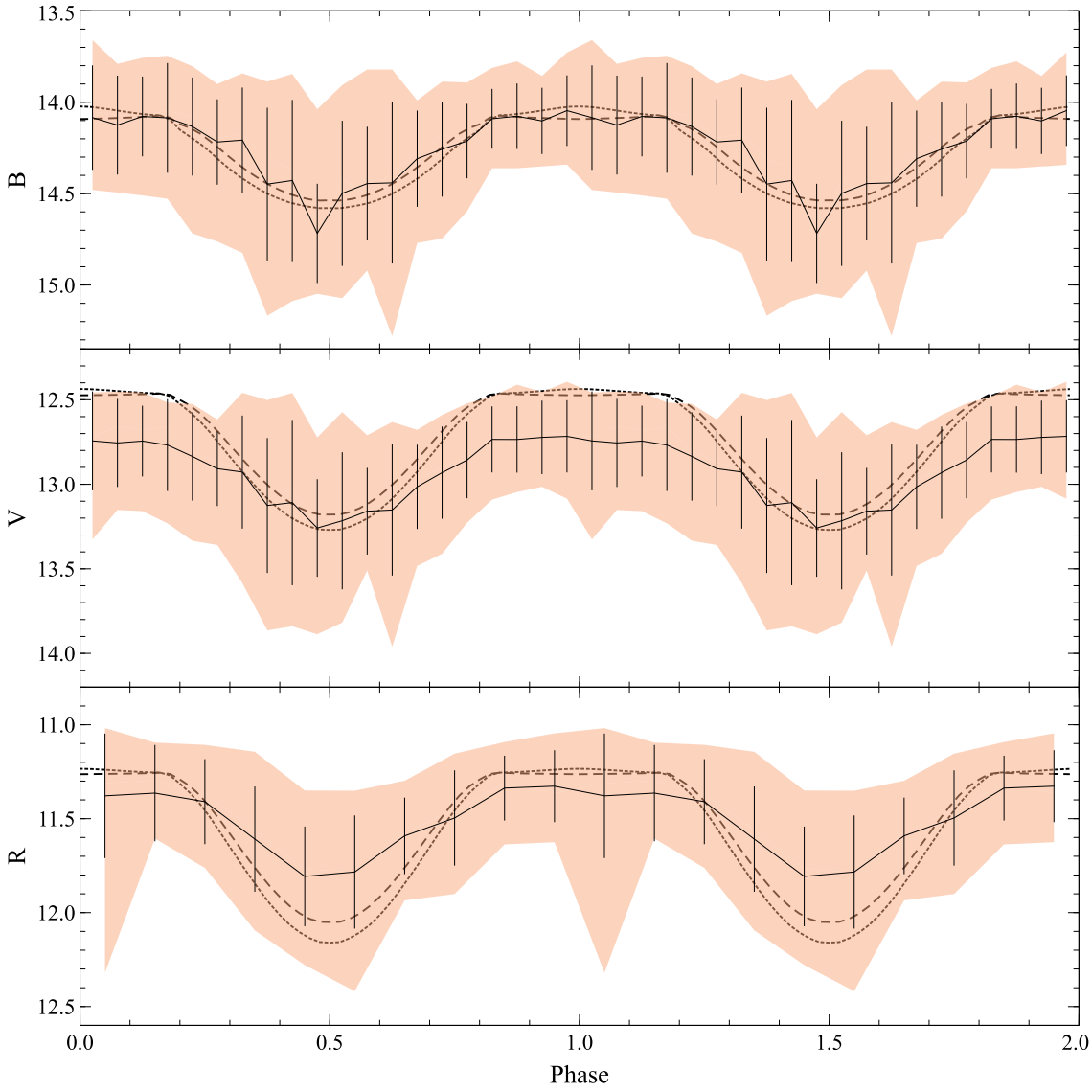

Figure 3.11: Best fits to average photometric data from B99, B03, B07, G07, and *ASAS*, determined using solely this averaged data. The mean brightness at each phase is shown by the solid line with the standard deviation given by the error bars. There are two best fitting models for these averaged observational data, each with $\dot{M}_{\rm acc} = 5 \times 10^{-9}$ M$_\odot$ yr^{-1} and $r_{\rm i} = 5.2$ R$_\star$. The dashed line shows the model with $\theta = 10°$ and $h_{\rm max}/r_{\rm o} = 0.29$, and the dotted line gives $\theta = 20°$ and $h_{\rm max}/r_{\rm o} = 0.30$.

2010). AA Tau was the first CTT observed to exhibit such photometric variations, and has been included in, and the subject of, many observational campaigns since (e.g. Gullbring et al. 1998; Bouvier et al. 1999, 2007, 2013; Grankin et al. 2007; Johns-Krull 2007; Donati et al. 2010). Using the radiative transfer code TORUS we have produced synthetic photometry which was compared to photometric observations from B99, B03 and B07, as well as surveys by *ASAS* and G07, to constrain geometric and physical parameters for AA Tau.

The geometry of AA Tau is fairly well constrained by photometric modelling, despite variations in the observed light curves between individual rotations. While both the aspect ratio and dipole offset affect the photometric amplitude, there does not appear to be any degeneracy between these two parameters; the out-of-occultation brightness is strongly dependent on the dipole offset, where larger offsets yield brighter maxima, enabling us to restrict the range of suitable dipole offsets, easily ruling out the larger values considered here. The aspect ratio could then be varied to achieve a suitable depth in the light curve during occultation. This was the parameter best-constrained by photometry (after the initial elimination of high dipole offset angles), with acceptable fits given by $h_{\rm max}/r_{\rm o} = 0.29 - 0.31$. A best fit of $h_{\rm max}/r_{\rm o} = 0.31$ was determined on the basis of comparison with individual data sets which show AA Tau with a significant disc warp, implying active magnetospheric accretion. The inner magnetosphere radius and dipole offset were less well constrained. The size of the inner magnetosphere radius has a negligible effect on V-band photometry; B-band data have a much stronger dependence on this value, particularly for larger aspect ratios. Using B-band data, we found $r_{\rm i} \sim 5.2 - 6.4$ R$_\star$, with 5.2 R$_\star$ selected on the basis that it gives a deeper minimum during occultation, better fitting some of the individual data sets. Dipole offset values of $\theta < 30^\circ$ provide the best fits, but θ cannot be constrained beyond this with photometry alone.

These results are in good agreement with previously determined values. Our dipole offset of $\theta \sim 10^\circ - 20^\circ$ is consistent with Donati et al. (2010) who found that the magnetic field of AA Tau is best described by a dipole inclined at $\theta \simeq 20^\circ$. Valenti & Johns-Krull

(2004) derived an offset of $\theta = 12^\circ$ from spectropolarimetric measurements, although they assumed a smaller inclination angle of $i = 66^\circ$. Our best-fitting aspect ratio, parameterising the size of the disc warp, is given by $h_{\rm max}/r_{\rm o} = 0.31$. The result from Alencar et al. showing photometric variations similar to that of AA Tau were present in 28 per cent of their sample can be used to independently determine the approximate aspect ratio of these discs; assuming a uniform sinusoidal distribution of system inclinations, a minimum inclination for which variations can be observed is found to be 73.7°. This corresponds to a maximum wall height of 16.3°, yielding a value of $h_{\rm max}/r_{\rm o} \sim 0.3$, as stated by Alencar et al.. The best fitting aspect ratio determined in the models presented in this chapter is therefore in very good agreement with observations.

The next chapter explores the effect that magnetospheric accretion and disc winds have on the Balmer line profiles of AA Tau. The results of line profile modelling are combined with the results obtained here from photometric modelling in order to to ascertain the geometry of the AA Tau star-magnetosphere-wind structure as a whole.

Chapter 4

Spectroscopic modelling of AA Tau

Parts of the work described in this chapter have been published in Esau, Harries & Bouvier, Monthly Notices of the Royal Astronomical Society, 443:1022 (2014).

4.1 Introduction

Spectroscopic studies of Classical T Tauri stars (CTTs) show high-velocity redshifted absorption components in their recombination lines, providing evidence of accretion from the circumstellar disc (e.g. Edwards et al. 1994; Muzerolle et al. 1998). Spectra also show the presence of excess ultraviolet (UV) emission. These observations can be explained by a magnetospheric accretion model (Bertout et al. 1988; Königl 1991; Hartmann et al. 1994, and references therein) . Circumstellar material accretes onto the star via magnetic field lines, travelling ballistically, and kinetic energy is liberated as thermal radiation on impact with the photosphere, producing hotspots near the magnetosphere poles. These hotspots are the source of the excess UV emission. Typical accretion rates of CTTs range between 10^{-7} and 10^{-9} $M_{\odot}$ yr^{-1} (e.g. Basri & Bertout 1989).

Spectra of CTTs also show evidence of outflows on different scales, with blueshifted absorption components and blueshifted forbidden line emission present at high velocities (Mundt 1984; Edwards et al. 1987). These signatures are thought to be due to stellar winds, disc winds, and jets. Stellar winds are understood to be powered by a fraction of

the energy released at the base of the accretion streams, causing material to escape along open magnetic field lines from the stellar surface (e.g. Matt & Pudritz 2005a). Disc winds emanate from open field lines threading the accretion disc (e.g. Camenzind 1990) in a bipolar conical outflow (Konigl & Pudritz 2000). This paradigm was first proposed by Blandford & Payne (1982) to explain observations of jets emanating from the accretion discs of black holes, and was extended by Pudritz & Norman (1983) to explain bipolar outflows associated with embedded protostars. Highly collimated high-velocity jets, emanating from closer to the star than less collimated disc winds, have also been observed in association with young stellar objects (e.g. Burrows et al. 1996; Appenzeller et al. 2005). The correlation between mass accretion diagnostics and wind signatures imply that winds are powered by the accretion process (Cabrit et al. 1990). Additionally, there is no evidence for mass-loss in the spectra of weak-line T Tauri stars, i.e. when there is no accretion occurring. While stellar winds do appear to contribute to mass-loss, disc winds seem to dominate (Cabrit 2007). However, there are numerous possible mechanisms for disc wind formation and the precise origin, or the relative contributions from disc winds of different origins, is still debated (see Ferreira, Dougados, & Cabrit 2006 for a review).

The magnetospheric accretion paradigm is supported by the results of line models. Hartmann et al. (1994) reproduced observed redshifted absorption components and blueshifted emission peaks of Balmer lines using a simple radiative transfer model of magnetospheric infall. This model was extended by Muzerolle et al. (1998), replacing the two-level atom approximation with a multilevel hydrogen atom in statistical equilibrium, followed by a further extension (Muzerolle, Calvet, & Hartmann 2001) which included line broadening and sodium line calculations. Muzerolle et al. (2001) presented a grid of models across a range of parameter space, varying magnetosphere temperature, line-of-sight inclination, accretion rate, and magnetosphere size. They found Hα lines which included Stark broadening were more consistent with observations than previous results. They also found instances where line profiles peaked near zero velocity, allowing for natural interpretation of observed CTT spectra that do not show the blueward emission peaks

calculated in previous models. While a number of lines were included in the study, Hβ was the focus of a detailed examination of profile shapes. A similar study focusing on Hα was carried out by Kurosawa et al. (2006), hereafter K06, using the radiative transfer code TORUS. This used the same accretion flow model and broadening mechanisms as Muzerolle et al. but the model was extended to include a self-consistent calculation for the hotspot temperature. A disc wind was also included using the parameterisation of Knigge, Woods, & Drew (1995, see also Long & Knigge 2002) where a biconical wind emerges from a rotating disc. K06 compared results with a classification scheme for Hα lines proposed by Reipurth, Pedrosa, & Lago (1996), in which seven classes of line shape were defined depending on the relative strength of the secondary peak to the primary peak (in the case of double-peaked emission lines), and whether the secondary falls blueward or redward of the primary. While some individual profiles were reproducible using models consisting solely of either a disc wind or a magnetospheric accretion flow, K06 found that all classes were readily explained using a hybrid wind-accretion model by varying the angle of inclination to the line of sight, the ratio of mass accretion to loss rates, the wind acceleration rate, and magnetosphere temperature (although one class was better explained using a bipolar outflow or spherical wind, rather than the disc-wind model).

The motivation for this study is to test the observed line formation using line profile data from AA Tau. As with the photometric study presented in Chapter 3, I used the radiative transfer code TORUS to produce synthetic observations which are then compared with data in order to constrain various physical and geometric parameters of the components of the AA Tau system. While the model used in the photometric study simply involved constructing the continuum source and wall height, and performing a ray tracing algorithm to calculate the brightness of the object in various wavebands at different viewing angles, the spectroscopic calculations are far more involved; once the grid is constructed, the solution to the equation of statistical equilibrium from Klein & Castor (1978) is computed for pure hydrogen under the Sobolev approximation, using the method described in Section 2.2.3 (see also Rybicki & Hummer 1978; Hartmann et al. 1994).

I present a description of the disc wind geometry used in TORUS in Section 4.2 followed by a comparison of line profiles from magnetosphere and wind models with those calculated by K06 in Section 4.3. Observational Balmer line profiles from AA Tau obtained by Bouvier et al. (2007) are presented in Section 4.4. In section 4.5 I present the synthetic line profiles calculated for AA Tau along with a discussion of the parameter space that was able to be constrained. Finally, in Section 4.7 I summarise the results of this study and, combining these results with the work presented in Chapter 3, I draw comparisons with the results of other work that has sought to constrain the geometries of CTTS under the magnetospheric accretion and outflow paradigm.

4.2 Disc wind geometry

The central absorption frequently observed in the line profiles of CTTS implies the presence of some form of outflow. A disc wind is used in the models presented here, which takes a biconical geometry in the configuration used by Knigge et al. (1995). This wind is parameterised by the mass-loss rate, the degree of collimation, the velocity gradient, and the wind temperature. The azimuthal velocity component of the wind, v_ϕ, is calculated simply from the the Keplerian rotational velocity at the launching point w_i of a wind element, where $v_\phi(w_\mathrm{i}, z = 0) = (GM_\star/w_\mathrm{i})^{1/2}$. Assuming conservation of angular momentum, the azimuthal velocity component is

$$v_\phi(w, z) = v_\phi(w_\mathrm{i}, 0)(w_\mathrm{i}/w), \tag{4.1}$$

where w is the distance from the rotation axis, $w = (x^2 + y^2)^{1/2}$. The model for radiatively driven winds developed by (Castor, Abbott, & Klein 1975) yields a β velocity law where the radial velocity component v_r can be described by the equation

$$v_r(w_\mathrm{i}) = v_\infty\left(1 - \frac{R_\star}{r}\right)^\beta, \tag{4.2}$$

(e.g. Lamers & Rogerson 1978; Haberl et al. 1989), where v_∞ is the terminal velocity,

and r is some radial distance from the star. β is an acceleration parameter where smaller values of β yield greater acceleration. For disc winds, the material at the point of ejection has non-zero velocity. If material at the base of the wind has a velocity v_0, v_r is instead given by $v_0 + (v_\infty - v_0)(1 - R_\star/r)^\beta$. The disc wind in TORUS uses the parameterisation of Knigge et al. (1995), in which the velocity of material at the streamline footprint of the wind is given by the sound speed, c_s, and v_∞ scales with the escape velocity v_{esc} with some scaling factor f. $v(r)$ now takes the form of

$$v_r(w_i) = c_s(w_i) + [f\, v_{esc} - c_s(w_i)]\left(1 - \frac{R_s}{l + R_s}\right)^\beta, \tag{4.3}$$

where l is the distance from the disc surface along the streamlines.

It is assumed that the local mass-loss rate per unit area, $\dot{m}$, is proportional to the local flux F. Since this itself is proportional to the fourth power of temperature, the local mass-loss rate is described by the power law

$$\dot{m}(w) \propto T(w)^{4\alpha}, \tag{4.4}$$

where uniform mass loss is given by $\alpha = 0$. It is assumed that that the mid-plane temperature of the disc takes a radial form, where the temperature and the radius w are related by a power law of the form $T_d \propto w^\gamma$ (e.g. Kenyon et al. 1993), the mass loss rate is related to the radius by

$$\dot{m}(w) \propto w^p, \tag{4.5}$$

where $p = 4\alpha \times \gamma$ and the constant of proportionality is found by integrating the local mass loss rate across the radial extent of the disc wind launching points, normalising to the total mass loss rate. I followed K06 in their choices of $p = -7/2$ for a Keplerian disc (Krasnopolsky et al. 2003) and $\gamma = -1.15$ (Whitney et al. 2003, who found this value describes the temperature profiles of the inner ∼AU of accretion discs). These values yield an α-value of 0.76.

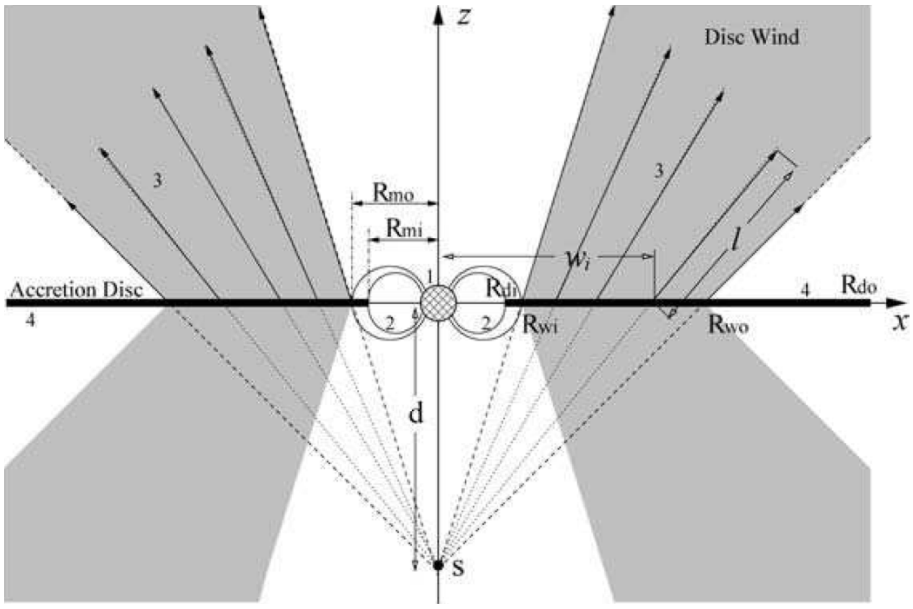

Figure 4.1: The basic geometry of the magnetospheric accretion models used here (note that this figure shows a system with no magnetic dipole offset). The disc wind geometry is parameterised by the distance d to the imaginary wind source point S, and inner and outer wind radii. Reproduced from Kurosawa et al. (2006).

As stated in Chapter 2, a radiative equilibrium calculation is not made for these simulations. The temperature structure of the magnetosphere is defined using a maximum temperature and a cooling rate given in Equation 2.23, since the heating mechanisms are unknown.The disc wind is assumed to be isothermal, the temperature of which is set to a user-defined value.

The collimation of the disc wind is parameterised by the distance to the wind source point; rather than using launching angles, the disc wind launching points are traced back to an imaginary point S on the opposite side of the disc at a distance d from the star. The geometry of the entire star-magnetosphere-wind system is shown in Figure 4.1.

4.3 Hα emission from classical T Tauri stars

Radiative transfer modelling of Hα line emission in CTTS has previously been published by K06. Those models have been re-evaluated here using a more recent version of TORUS as a first step in studying the effects that different wind parameters have on the

Table 4.1: Reference CTTS parameters, used in the models of Kurosawa et al. (2006). $\dot{M}_{\rm wind}$ is the mass loss rate from the wind and r_{di} is the inner disc radius. All other parameters are as described in Table 3.2.

$R_\star$ ($R_\odot$)	$M_\star$ ($M_\odot$)	$T_{\rm eff}$ (K)	$\dot{M}_{\rm acc}$ ($M_\odot\,{\rm yr}^{-1}$)	$r_{\rm i}$ ($R_\star$)	$r_{\rm o}$ ($R_\star$)	$\dot{M}_{\rm wind}$ ($M_\odot\,{\rm yr}^{-1}$)	r_{di} ($r_{\rm o}$)	i
2.0	0.5	4000	10^{-7}	2.2	3.0	10^{-8}	1.0	55°

morphologies of Hα profiles. The stellar parameters used here are representative of a general CTTS, with no particular object in mind. Stellar, magnetosphere, and disc wind parameters are presented in Table 4.1.

Rather than use the value of $\alpha = 0.76$ derived above, I opted for $\alpha = 0.5$ which is the value used in the published figures of K06. Broadening is included for Hα using the method presented by Muzerolle et al. (2001); the ordinary Doppler profile for a line, broadened by the thermal motion of the gas, is defined by the Doppler linewidth

$$\Delta\nu = \frac{\nu_0}{c}\sqrt{\frac{2k_{\rm B}T}{\mu}}, \tag{4.6}$$

where μ is the mass of a hydrogen atom and ν_0 is the central frequency of the line. When additional broadening mechanisms are present, the profile morphology is instead given by the Voigt function $H(a, y)$,

$$H(a,y) = \frac{a}{\pi}\int_{-\infty}^{\infty}\frac{{\rm e}^{-y^2}}{(u-y)^2+a^2}\,{\rm d}y, \tag{4.7}$$

(Mihalas 1978), where $a = \Gamma/4\pi\Delta\nu_D$. y gives the contribution from the Doppler profile, where $y = \Delta\nu/\Delta\nu_D$, and $u - y$ gives the contribution of additional broadening mechanisms, where $u = (\nu - \nu_0/\Delta\nu_D)$. In addition to thermal broadening, natural broadening, van der Waals broadening (due to dipole interactions between neutral atoms), and Stark broadening (due to electron-induced dipoles in neutral atoms) are considered. Γ is the damping constant, which gives the additional broadening contributions from natural, van der Waals, and Stark broadening, where

$$\Gamma = C_{\rm rad} + C_{\rm vdW}\left(\frac{n_{\rm H\,I}}{10^{16}\,{\rm cm}^{-3}}\right)\left(\frac{T}{5000\,{\rm K}}\right)^{0.3} + C_{\rm Stark}\left(\frac{n_{\rm e}}{10^{12}\,{\rm cm}^{-3}}\right)^{2/3}. \quad (4.8)$$

The values for the natural broadening constant $C_{\rm rad}$, the van der Waals broadening constant $C_{\rm vdW}$, and the Stark broadening constant $C_{\rm Stark}$ for Hα are taken from Luttermoser & Johnson (1992) and are given in Table 4.2.

Many changes have been made in various different areas of TORUS since the work of K06 was published. The underlying algorithm that solves the atomic physics has changed, and the line rate equations have been updated with more modern values. The gridding and the ray tracing method have also been improved upon, so signification portions of the code are quite different from this earlier work. The line profiles produced are therefore expected to differ at least a little from the results of K06. To confirm that TORUS still produces consistent line profiles, despite all of the changes that have been implemented, the magnetosphere, disc wind, and hybrid models of K06 have been reproduced and the resulting comparisons are presented in the next three sections.

4.3.1 Magnetosphere contribution to Hα profiles

The magnetosphere contribution to Hα profiles was explored as a function of $\dot{M}_{\rm acc}$ and the maximum temperature in the magnetosphere, $T_{\rm mag}$. The resulting Hα profiles for models with $\dot{M}_{\rm acc} = 10^{-7}$, 10^{-8}, and 10^{-9} $M_\odot$ yr^{-1} and $T_{\rm mag} = 6500$, 7500, 8500, and 9500 K are presented by the solid lines in Figure 4.2. The dotted lines give the results found by K06. The method of calculating the temperature profile in the magnetosphere has been updated since the work of K06; in their models, the temperature was calculated by digitising the temperature profile along the field lines plotted by Hartmann et al. (1994), whereas now the maximum temperature in the magnetosphere is manually defined and heating and cooling laws are applied to self-consistently solve the temperature structure. There are slight differences in intensity between the profiles of the two models, but the profile morphologies are in good agreement. The inverse P Cygni morphology, present due to the infalling material along the accretion stream, is strongest for lower accretion

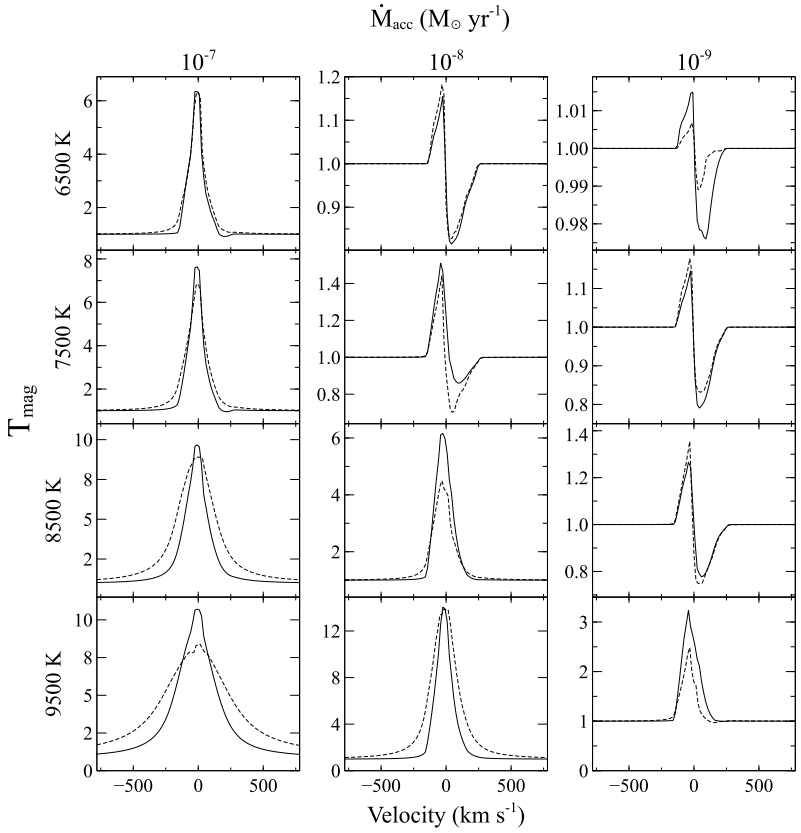

Figure 4.2: Hα profiles from magnetospheric accretion models with no outflow for various magnetosphere temperatures and inflow rates. Solid lines show the models described above, and dotted lines show the profiles computed by Kurosawa et al. (2006). While there are slight differences in intensity between the models, the profile morphologies agree well.

rates and cooler temperatures. Since the damping constant is dependent on particle number density and temperature (see Equation 4.8), higher temperatures and accretion rates lead to progressively stronger emission from the line wings, eventually eliminating the absorption component resulting in a pure symmetric emission line.

4.3.2 Disc wind contribution to Hα profiles

A disc wind as described in Section 4.2 was modelled without the magnetospheric infall in order to examine the contribution of a disc wind to Hα profiles. The resulting profiles for a wind with a mass loss rate of $\dot{M}_{\rm wind} = 10^{-8}$ $M_\odot$ yr^{-1} with various combinations of $T_{\rm wind}$ and β are given in Figure 4.3. The newly calculated profiles reproduce the classical P Cygni profile morphology, particularly at low β, with the position of the absorption fea-

ture consistent between all models. The amount by which the absorption component is blueshifted is dependent on the acceleration parameter β, where profiles with lower values of β, i.e. wind with a high acceleration rate, are blueshifted much more than the virtually central absorption present for the slowest accelerating wind. However, there are obvious differences between these newer models and the previously published results, most notably due to the triple-peaked structure that frequently appears in these newer models, compared with a double-peaked morphology with a central absorption component from K06. One likely reason behind this discrepancy is the way in which the models were calculated; K06 used the grid calculated for their hybrid model (see Section 4.3.3) for these disc wind models, with the cells containing the magnetospheric contribution disabled. Hot spot radiation was also removed by setting a low accretion rate of $\dot{M}_{\rm acc} = 10^{-10}$ M$_\odot$ yr^{-1}, although the continuum radiation used to compute the line emissivities and opacities for the statistical equilibrium calculation still included the continuum contribution from the original higher accretion rate of $\dot{M}_{\rm acc} = 10^{-7}$ M$_\odot$ yr^{-1}. Conversely, the latest models presented here were computed by generating an entirely new grid with absolutely no contribution from magnetospheric infall anywhere in the grid. For this reason, this is not a like-for-like comparison. The central peak at low velocities originates from emission by low-velocity gas at the very base of the wind. The redshifted peak comes from the wind material on the far side of the object, and the blueshifted peak comes from the wind material on the near side. The finer details of the global line profiles come from a complex interplay between the emission from the wind, particularly at the wind base, and absorption from the wind, and also depend on the density and velocity of the gas, so pinpointing the processes that produce specific parts of a profile is not trivial.

4.3.3 Hα profiles from magnetosphere-plus-wind hybrid models

Hybrid models including both a magnetosphere and disc wind were run over the same parameter space as used in the disc wind models of Section 4.3.2. The magnetosphere parameters are those laid out in Table 4.1 with a maximum temperature in the magneto-

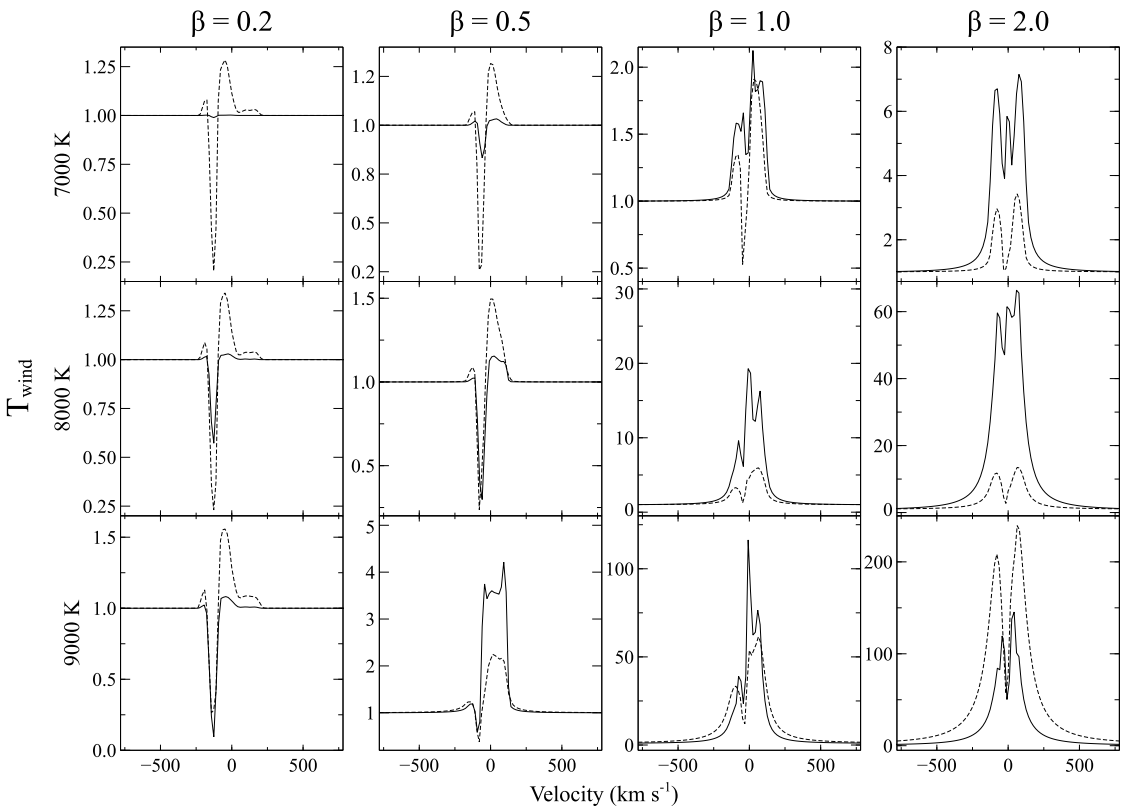

Figure 4.3: Hα profiles from disc wind models with no accretion for various wind temperatures and acceleration rates. Solid lines show the models described above, and dotted lines show the profiles computed by Kurosawa et al. (2006). The newer models frequently produce a triple-peaked structure where results from K06 produce a double-peaked profile with central absorption. Possible causes for this discrepancy are discussed in the text.

sphere of 7500 K. There is generally much better agreement between the newly calculated line profiles and those presented by K06 compared with the wind-only profiles presented in Figure 4.3, particularly for magnetosphere-dominated profiles at $\beta = 0.2$ (i.e. a highly accelerating and thus low-density wind) where just a small blueshifted absorption feature present from the wind. For most other models the morphology is reproduced well with only a difference in intensity between the models. The notable exceptions are for wind temperatures of $T_{\rm wind} = 8000$ and 9000 K with $\beta = 1.0$, although the triple-peaked structure is beginning to come through in the profile for the $T_{\rm wind} = 8000$ K, $\beta = 1.0$ model of K06. Similar patterns from 4.3 are reproduced, with the blushifted absorption feature approaching the centre with decreasing wind acceleration, and with increased line profile intensities for the most wind-dominated profiles at high β and $T_{\rm wind}$.

In summary, these newly calculated results reproduce the work of K06 very well considering the changes that have been made to the code in important and complex areas such as the statistical equilibrium method, the ray tracing, and so on. The intensities of line profiles produced from solely a magnetosphere are in good agreement, and the trends in the profile shapes are also reproduced well, with inverse P Cygni profiles and Gaussian-like profiles each being reproduced in accordance with the original calculations. The profiles produced using solely a disc wind do not agree so well due to the entirely different method of calculating these profiles used originally, as discussed in Section 4.3.2, resulting in a comparison between the results of two methods that are not like-for-like. However, there are broad similarities in the line shapes, such as the strong absorption presence at higher wind temperatures, producing the P Cygni profile, and the broadness of the line agrees well until $\beta = 2.0$. The method that K06 used to produce these profiles of taking a hybrid model and disabling the cells containing the magnetospheric contribution cannot be easily repeated in the current version of TORUS. Despite the poor agreement in the disc wind models, the comparison between the full calculation where both the magnetosphere and wind are present is significantly improved, as discussed above. The sources of disagreement between the two models are well understood and a number of these are due to updates that have been made to improve TORUS. The comparisons presented here were produced to test the newer version of the code, and the results are satisfactory in demonstrating that the code is working solidly.

4.4 Observational spectroscopy for AA Tau

Emission line profiles for Hα, Hβ and Hγ, from Bouvier et al. (2007), were taken between October and December 2004 (JD 2453288 – 341) at the ESO La Silla 3.6 m telescope with the HARPS high-resolution echelle spectrograph. 22 spectra for each line were obtained in total, covering the 3800 – 6900 Å spectral domain at a spectral resolution of $\lambda/\Delta\lambda \approx 115\,000$ with a signal-to-noise ratio between 10 and 30 at 600 nm. The line profiles have been phased over an 8.22 day period, as with the photometry.

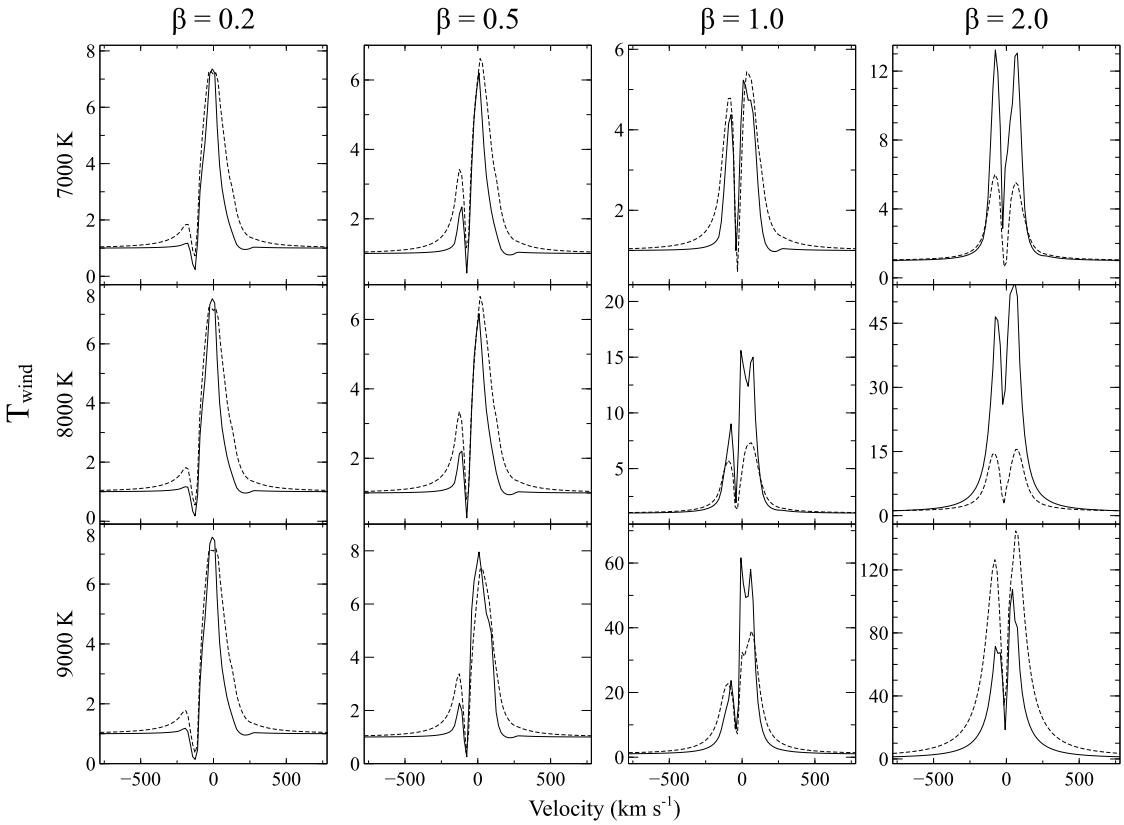

Figure 4.4: Hα profiles from hybrid models including both magnetospheric infall and a disc wind. Solid lines show the models described here, and dotted lines show the profiles computed by Kurosawa et al. (2006). There is generally much better agreement between the two sets of models than for the wind-only models presented in Figure 4.3 with the exception of the triple-peaked structure coming through at higher temperatures with β = 1.0.

The profiles were rectified using Starlink DIPSO (Howarth et al. 2004) by summing together all line profiles for each transition and manually defining line-free continuum bins. Cosmic rays were removed manually from each individual profile. A first-order polynomial fit was performed on the continuum level and each line profile was divided by the resulting continuum. This process is shown in Figure 4.5.

All rectified line profiles for each transition are shown in Figure 4.6 and are ordered by phase. I have focussed on fitting Hβ which, at some phases, displays the inverse P Cygni morphology that is a consequence of the magnetospheric accretion paradigm.

As with photometry, the shape and intensity of emission line profiles vary over short timescales, with variations often apparent between profiles separated by just one or two

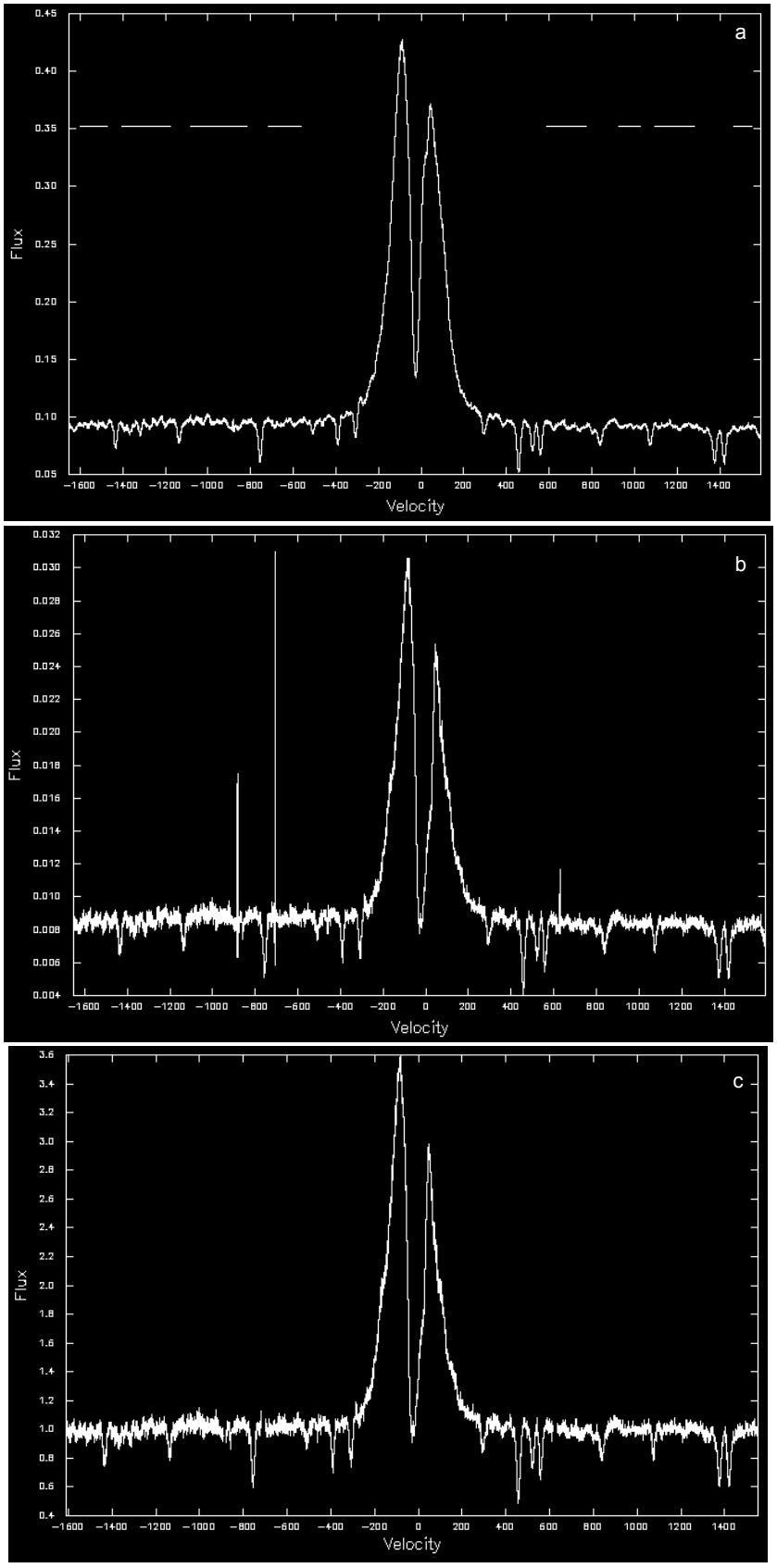

Figure 4.5: The rectification process for Hα. Summed spectra are shown in *a* with the manual continuum selection given by the top dashes. *b* shows a profile plotted from raw data, and *c* shows the same profile with cosmic rays removed and having been normalised.

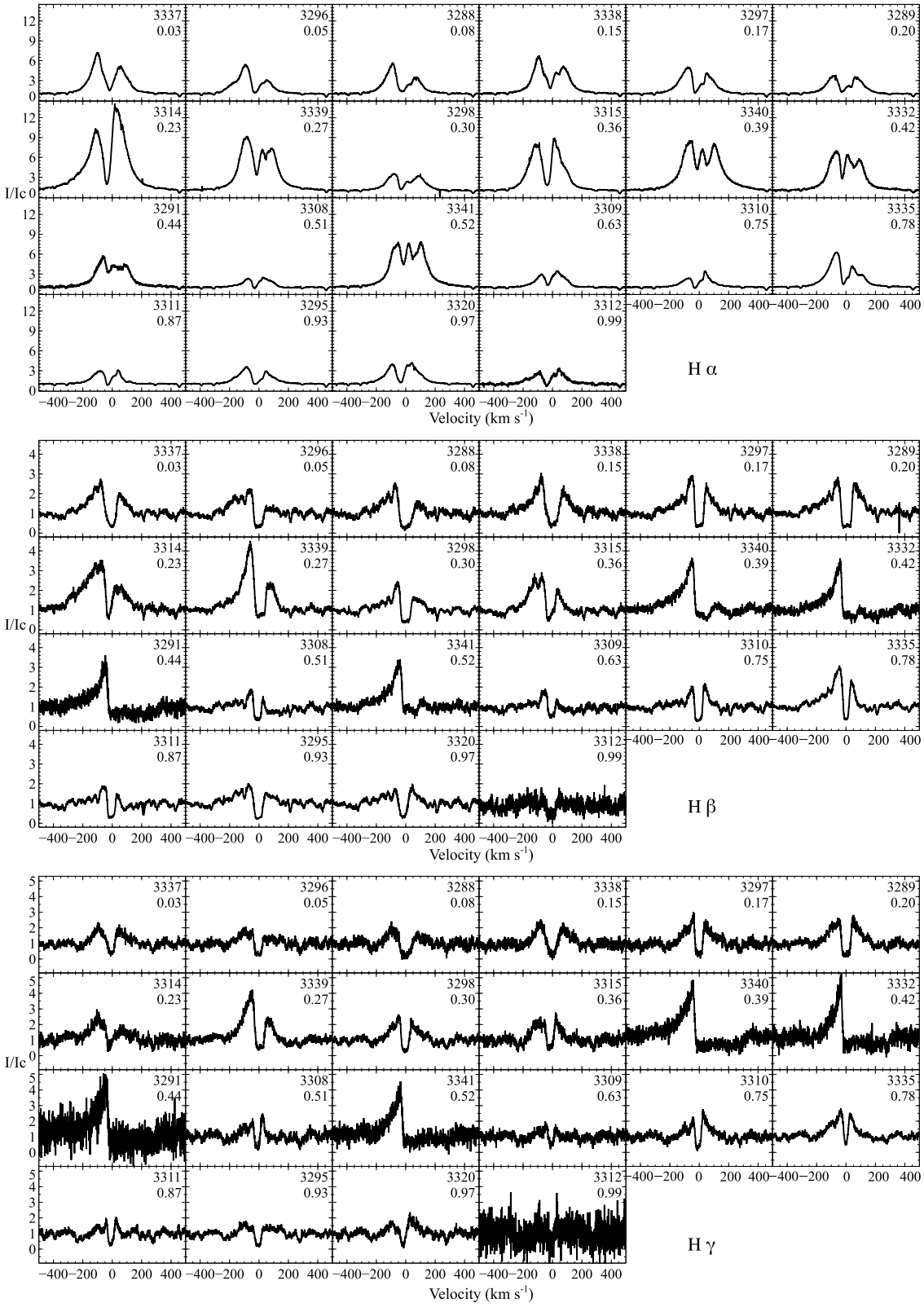

Figure 4.6: Emission line profiles for Hα (top), Hβ (middle), and Hγ (bottom), from Bouvier et al. (2007). Profiles are ordered by rotational phase. JD − 2 450 000 is given on the top right of each profile. The phase is given underneath, where a phase of 0 corresponds to no occultation and a phase of 0.5 corresponds to maximum occultation by the disc warp.

rotations. The phase ordered spectra will therefore appear to vary somewhat erratically from one phase to the next. However, when ordered by date and grouped into individual rotations, variations between adjacent spectra are reduced and more of a trend is apparent during an individual rotation (e.g. see Figure 4.7 for Hβ). An interpretation of the spectral features seen in these profiles is given in B07, but in summary:

– A deep, blueshifted central absorption is always present, consistent with an outflow;

– High-velocity redshifted absorption is present for phases around $\varphi = 0.5$, i.e. during photometric minimum, with the consequence that Hα profiles have a triple-peaked appearance around this phase, whereas in Hβ and Hγ profiles the red wing is suppressed completely. In some instances the absorption falls below the continuum level in an inverse P Cygni (IPC) profile morphology. This redward absorption is consistent with a line of sight down the main accretion funnel flow;

– The redshifted absorption component is not as pronounced in cycles with a shallow photometric minimum (e.g. JD 2 453 308), consistent with a low accretion rate and thus a small (perhaps negligible) disc warp.

Each of these features has been found in numerous observations of other CTTs to varying degrees, with Hα typically demonstrating blueshifted central absorption more so than higher lines, but with higher lines typically showing IPC morphologies (e.g. Edwards et al. 1994; Alencar & Basri 2000; Folha & Emerson 2001).

4.5 AA Tau synthetic spectra

As with photometry, different parameter sets will give the best fits at different times due to the variability of AA Tau's magnetic field. As a starting point I ran numerous two-dimensional models, with no dipole offset, to find the approximate region of $\dot{M}_{\rm wind}$ and $T_{\rm wind}$ values that could describe the three-dimensional system, using the hybrid magnetosphere-plus-wind geometry.

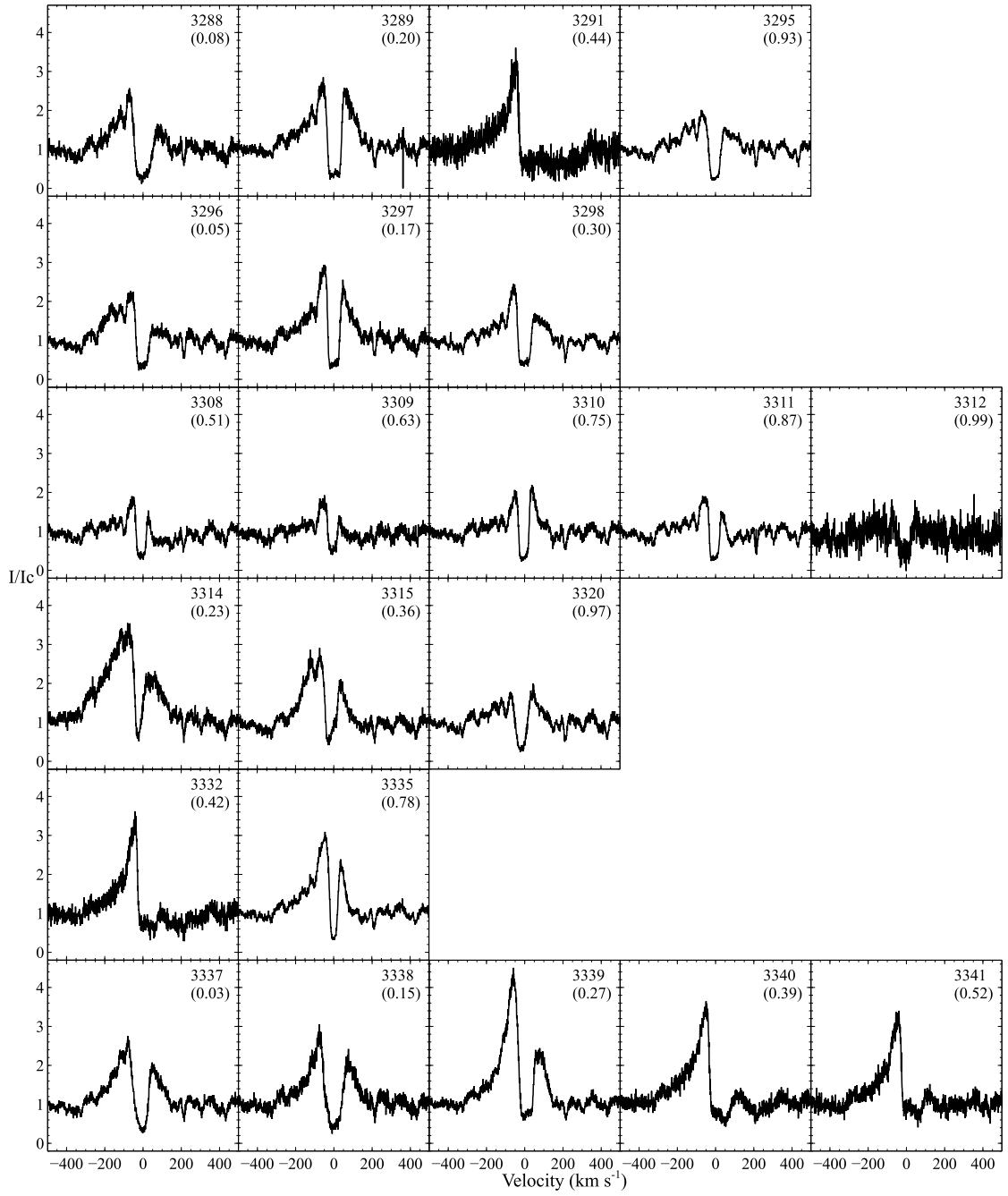

Figure 4.7: Observational spectra for Hβ ordered by date. Spectra obtained during one rotation are plotted in each row. JD − 2 450 000 is given in the top right and phase is given underneath. Change in morphology with phase is much more apparent when dividing into individual rotations, with low-intensity profiles, indicative of less active accretion, showing little variation between phases (e.g. row 3). Stronger profiles show much more variation, with redward emission decreasing or even becoming eliminated towards φ = 0.5, and increasing again towards φ = 1.0 (e.g. top and bottom row).

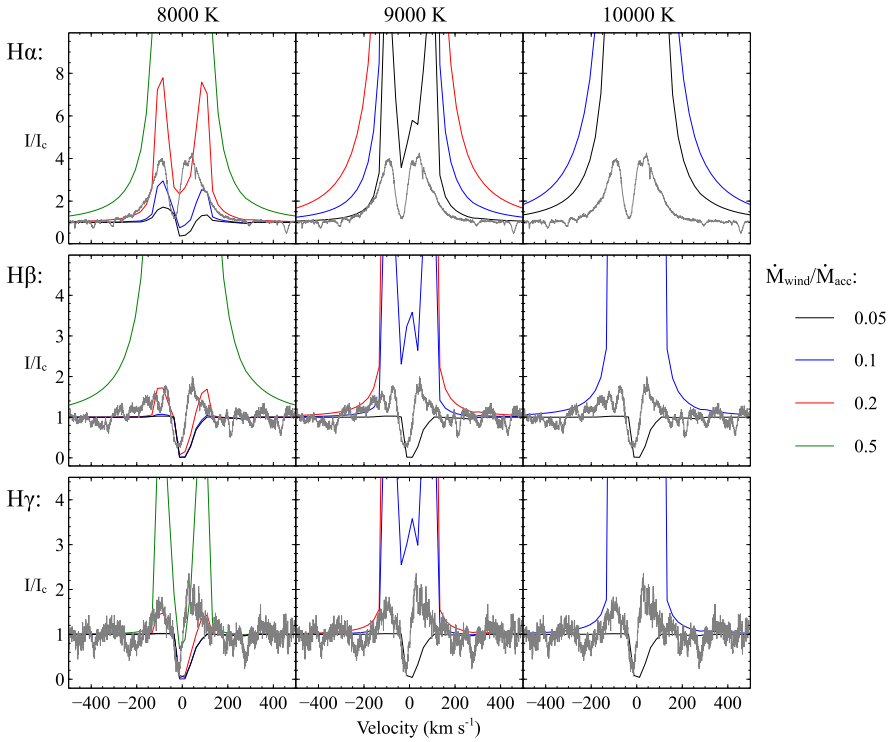

Figure 4.8: Line profiles for Hα, Hβ, and Hγ from two-dimensional models for different values of $\dot{M}_{\rm wind}/\dot{M}_{\rm acc}$ and $T_{\rm wind}$. $T_{\rm mag}$ and β were fixed at 8500 K and 2.0, respectively. Mass loss rates of 0.5 produce only central absorption. Higher ratios produce excessive emission in all line profiles with $T_{\rm wind} \geq 9000$ K. Best fits are given by $\dot{M}_{\rm wind}/\dot{M}_{\rm acc} = 0.1$ for Hα and $\dot{M}_{\rm wind}/\dot{M}_{\rm acc} = 0.2$ for Hβ and Hγ, all with $T_{\rm wind} = 8000$ K

4.5.1 2D models

I covered a wide range of parameter space for these variables, starting with values on the more extreme end of the parameter space and working back from this. The grid of parameters used for this 2D study covered wind temperatures of 8000, 9000 and 10000 K, and $\dot{M}_{\rm wind}/\dot{M}_{\rm acc}$ ratios of 0.05, 0.1, 0.2, and 0.5.

Initial models were run at $T_{\rm wind} = 10000$ K with a low $\dot{M}_{\rm wind}/\dot{M}_{\rm acc}$ of 0.05 to compensate for the excess emission expected for such a high outflow temperature. The canonical value of $\dot{M}_{\rm wind}/\dot{M}_{\rm acc}$ was also included in all models. Figure 4.8 shows the results of this initial parameter search. In every case, models for Hβ and Hγ with $\dot{M}_{\rm wind}/\dot{M}_{\rm acc} = 0.05$ give only central absorption, with no emission component. These lines show excessive emission for $\dot{M}_{\rm wind}/\dot{M}_{\rm acc} \geq 0.1$ for wind temperatures of 9000 and 10000 K. For 8000 K winds emission only becomes important in the higher Balmer lines

for $\dot{M}_{\rm wind}/\dot{M}_{\rm acc} = 0.2$, with values as high as 0.5 again showing excess emission. Hα lines show excessive emission even for $\dot{M}_{\rm wind}/\dot{M}_{\rm acc} = 0.05$ at the higher wind temperatures. At 8000 K, a ratio of 0.1 begins to approach the observed intensity, whereas doubling this to $\dot{M}_{\rm wind}/\dot{M}_{\rm acc} = 0.2$ provides too much excess. Given the sensitivity of emission to $\dot{M}_{\rm wind}/\dot{M}_{\rm acc}$, values in the 3D study were varied in increments of 0.01, maintaining the focus on values around 0.1 where $0.05 \leq \dot{M}_{\rm wind}/\dot{M}_{\rm acc} < 0.2$. Wind temperature was varied in increments of 100 K with $7500 \leq T_{\rm wind} \leq 8500$ K, as well as two models with $T_{\rm wind} = 8000$ and 9000 K. The profiles in Figure 4.8 were modelled with a maximum magnetosphere temperature of $T_{\rm mag} = 8500$ K; this was increased, again in increments of 100 K, in order to produce a more significant emission contribution in the Hβ and Hγ profiles for $\dot{M}_{\rm wind}/\dot{M}_{\rm acc} \simeq 0.1, T_{\rm wind} \simeq 8000$ K.

4.5.2 3D models

Line profiles from 20 different rotational phases were calculated for each parameter set. Natural, van der Waals, and Stark broadening for Hα were included using the parameters listed in Table 4.2. No broadening was included for Hβ and Hγ lines since broadening is less important here and the effects of infall and outflow on the line morphology are the primary areas of interest. The best fitting parameters obtained in the photometric study ($\dot{M}_{\rm acc} = 5 \times 10^{-9}$ M$_\odot$ yr^{-1}, $r_i = 5.2$ R$_\star$, $h_{\rm max}/r_{\rm o} = 0.31$) have been maintained. The maximum temperature in the magnetosphere $T_{\rm mag}$, wind acceleration parameter β, rate of mass loss from the disc wind $\dot{M}_{\rm wind}$, and wind temperature $T_{\rm wind}$ were varied over dipole offsets of $\theta = 10°$ and 20°. β values were modelled at 0.5, 1.0 and 2.0. The minimum value of $T_{\rm mag}$ was reduced to 8000 K in order to investigate the effect of temperatures lower than the value of 8500 K used in Figure 4.8. The full range of parameter space is presented in Table 4.2.

Line profiles for magnetosphere-only models were calculated to address the question of whether observed profiles can be fitted by a model with no outflow. While the study of Hα profiles by Kurosawa et al. (2006) found that magnetosphere-only models were not

Table 4.2: Parameters used for the spectroscopic study, in addition to the stellar parameters given in Table 3.2. The disc wind parameters r_{wi} to f are taken from Kurosawa et al. (2006). The broadening parameters are taken from Luttermoser & Johnson (1992) and are for Hα only. Model parameters $T_{\rm mag}$, β, $\dot{M}_{\rm wind}$ and $T_{\rm wind}$ have been fitted using the values listed below.

Parameter	Description	Value
r_{wi}	Inner disc wind radius	1.0 $r_{\rm o}$
r_{wo}	Outer disc wind radius	35.6 $r_{\rm o}$
d	Position of wind source points	7.33 r_{wi}
α	Exponent in mass loss rate per unit area	0.76
γ	Exponent in disc temperature power law	-1.15
$R_{\rm s}$	Effective acceleration length	8.8 r_{wi}
f	Scaling on the terminal velocity	2.0
$C_{\rm rad}$	Natural broadening parameter	6.4×10^{-4} Å
$C_{\rm vdW}$	van der Waals broadening parameter	4.4×10^{-4} Å
$C_{\rm Stark}$	Stark broadening parameter	1.17×10^{-3} Å
$\lambda_{\rm H\alpha}$	Hα wavelength	6562.8 Å
$\lambda_{\rm H\beta}$	Hβ wavelength	4860.9 Å
$\lambda_{\rm H\gamma}$	Hγ wavelength	4340.0 Å
$T_{\rm mag}$	Maximum magnetosphere temperature	8000 – 9000 K
β	Wind acceleration parameter	0.5, 1.0, 2.0
$\dot{M}_{\rm wind}/\dot{M}_{\rm acc}$	Ratio of mass loss rate to mass accretion rates	0.05 – 0.20
$T_{\rm wind}$	Disc wind temperature	7000 – 9000 K

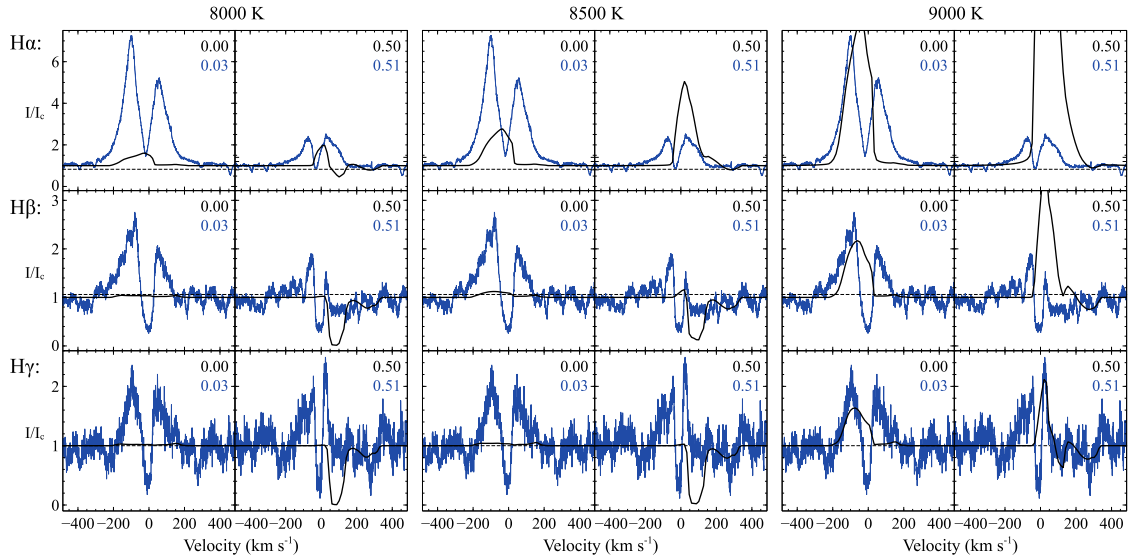

Figure 4.9: Magnetosphere-only models for Hα, Hβ and Hγ at a range of temperatures for $\varphi = 0.0$ and $\varphi = 0.5$. Observed profiles and the phase at which they were taken are given in blue and synthetic profiles in black. The continuum level is shown by the dashed line.

able to reproduce all of the properties observed in CTT profiles, the accretion in their model was axisymmetric with no dipole offset. Here, non-axisymmetric magnetosphere-only models are used with the inclusion of an optically thick disc warp to draw comparisons between observations and synthetic spectra for AA Tau. A selection of line profiles are presented in Figure 4.9 for Hα, Hβ and Hγ with $T_{\rm mag} = 8000$, 8500, and 9000 K. Models are shown at phases of 0.0 (out of occultation) and 0.5 (during occultation) with $\theta = 10°$.

There are features of the magnetosphere-only model that are found in observed profiles such as redshifted absorption components at $\varphi = 0.5$, as expected for observations down the accretion stream. Another feature is the blue-shifted emission at $\varphi = 0.0$, when the accretion stream in the observable hemisphere is at the back of the star relative to the line of sight. However, it is quite clear that the slightly blue-shifted deep absorption that is apparent in observations is not reproduced by any of these magnetosphere-only models. I have included a disc wind as described in Section 4.2 in the following models in an attempt to resolve this discrepancy.

I first studied the effect of wind temperature $T_{\rm wind}$ and acceleration parameter β,

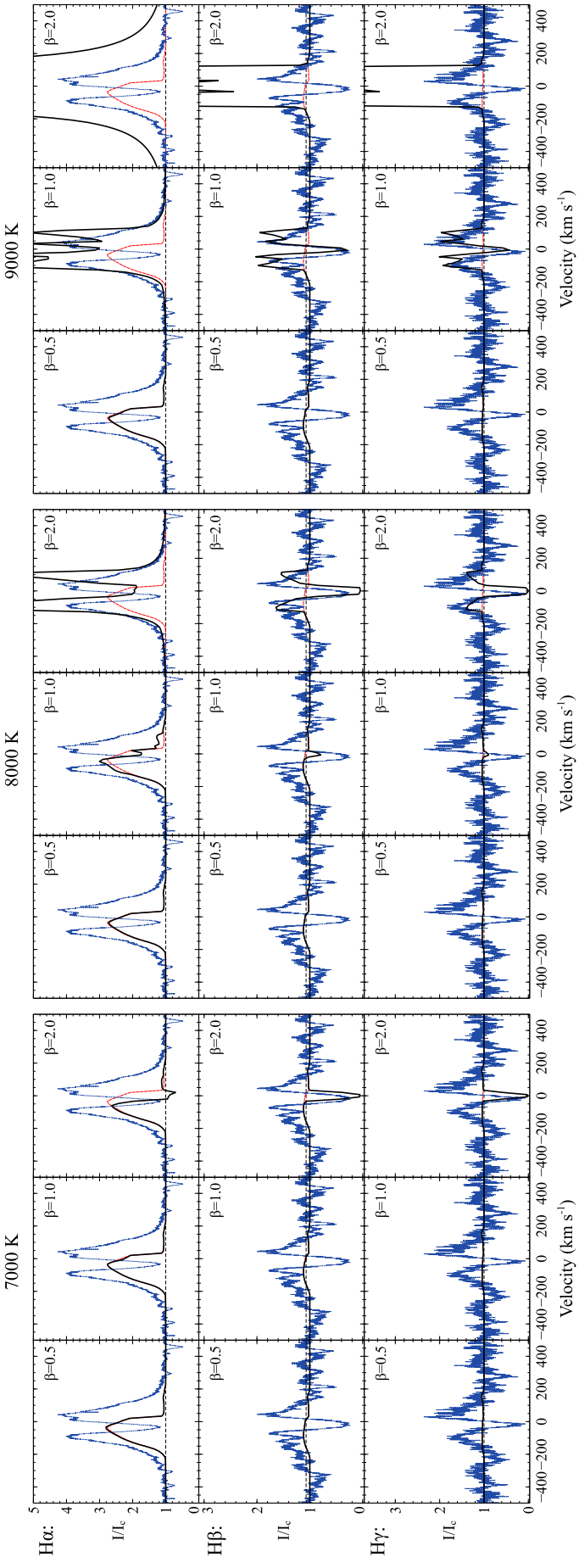

Figure 4.10: Magnetosphere-plus-wind models for Hα, Hβ and Hγ at $\varphi = 0.0$, with $\theta = 10°$. Wind temperature and the acceleration parameter are varied with $T_{\rm wind}$ = 7000, 8000 and 9000 K, and β = 0.5, 1.0 and 2.0. Modelled line profiles are shown in black, observed profiles are shown in blue, and the magnetosphere contribution is given in red.

with results given in Figure 4.10. Synthetic line profiles are given in black with observations in blue. The magnetosphere contribution to each of the profiles is shown in red. The central deep absorption is present in the models for hotter, more slowly accelerating winds when the magnetosphere contributes less to the profile shape relative to the wind. Very little emission is present in Hβ and Hγ for models where $T_{\rm wind}$ = 7000 K although the deep absorption component appears for β = 2.0. For winds at 8000 K the modelled profile shape matches the observed Hβ profile reasonably well with β = 2.0, although the model is a little weak for Hγ and strong for Hα. A similar result is found for $T_{\rm wind}$ = 9000 K with β = 1.0. There is a degeneracy for wind temperatures between 8000 K and 9000 K and acceleration parameters between 1.0 and 2.0 where a number of different values will also provide sufficient fits to the observations. Physically this is a result of the degeneracy between density and temperature. The density of the wind is coupled to the acceleration parameter and the mass loss rate, with temperature contributions defined by $T_{\rm mag}$ and $T_{\rm wind}$. I selected a wind temperature of $T_{\rm wind}$ = 8000 K and β = 2.0 for the disc wind parameter fitting, but even by eliminating β as a free parameter there will still be a degeneracy in density from the mass outflow rate, where the greater intensity in line profiles with an increased mass outflow rate can be reduced again by decreasing one or both of the temperature parameters. For this reason, it is not possible to extract a definitive best fitting parameter set to describe the disc wind, especially since this study is restricted to hydrogen recombination lines. It may be possible to break this degeneracy with additional lines such as He I (e.g. Kwan et al. 2007; Kurosawa et al. 2011).

A more precise dipole offset angle appears to be better constrained by spectroscopy than photometry, having already been restricted to about 10° – 20°. There is very little difference between the two out of occultation, as to be expected, but differences do become apparent during occultation. Models at φ = 0.5 for Hβ are shown in Figure 4.11 to demonstrate this, with $T_{\rm wind}$ and β as above. There is high-velocity redshifted absorption present for both θ = 10° and θ = 20°, but the absorption is stronger for the θ = 20° cases. There is also a difference in the relative emission strengths of the blue and red peaks,

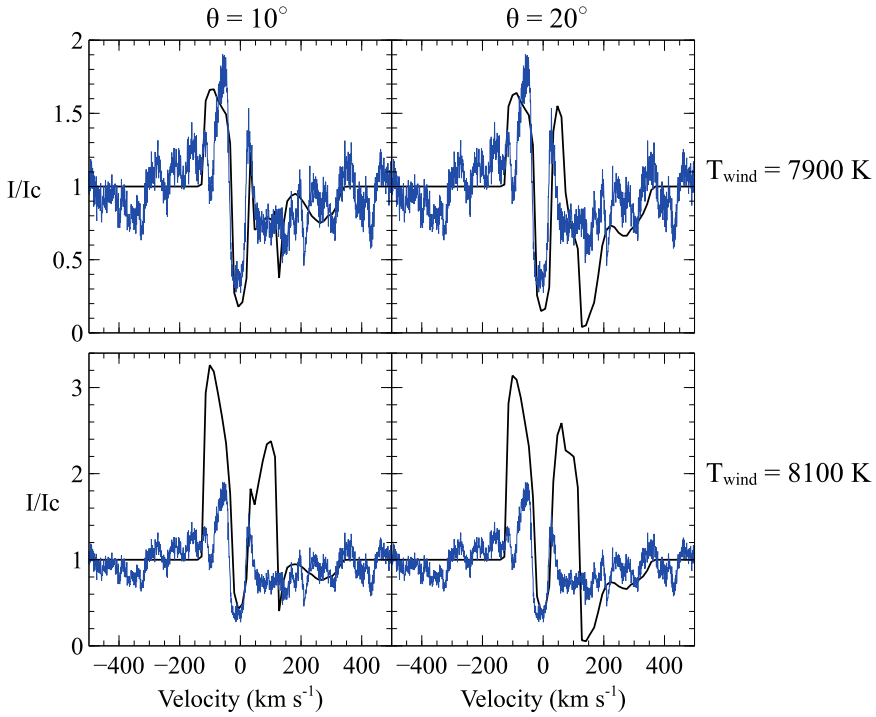

Figure 4.11: Comparisons between observed spectra and models for Hβ with $\theta = 10°$ (left) and $\theta = 20°$ (right). $\dot{M}_{\rm wind}/\dot{M}_{\rm acc} = 0.1$ and $T_{\rm mag} = 8500$ K in each case. $T_{\rm wind}$ is modelled at 7900 K (top) and 8100 K (bottom).

with a greater blue-to-red ratio in the $\theta = 10°$ cases. Since observations show only slight high-velocity redshifted absorption and stronger emission in the blue peak than the red (with the red completely damped in some cases), I selected a dipole offset of $\theta = 10°$.

For the β and $T_{\rm wind}$ values determined above there is very little magnetosphere contribution to the line profile, so I have neglected further study of magnetosphere temperatures below 8400 K. I assigned a maximum magnetosphere temperature of 9000 K, since this produces an Hβ profile of comparable intensity to observations at $\varphi = 0.0$, and exceeds the observed intensity of some of the observed profiles around $\varphi = 0.5$, without any consideration for the addition of a disc wind. The effect of the magnetosphere temperature on Hβ profiles in the range of 8400 K and 9000 K is shown in figure 4.12. The only considerable change between models with different magnetosphere temperatures at $\varphi = 0.0$ is the strength of the blueward emission due to the visibility of part of the accretion stream behind the star. There is also a slight increase in the broadening of the blue wing

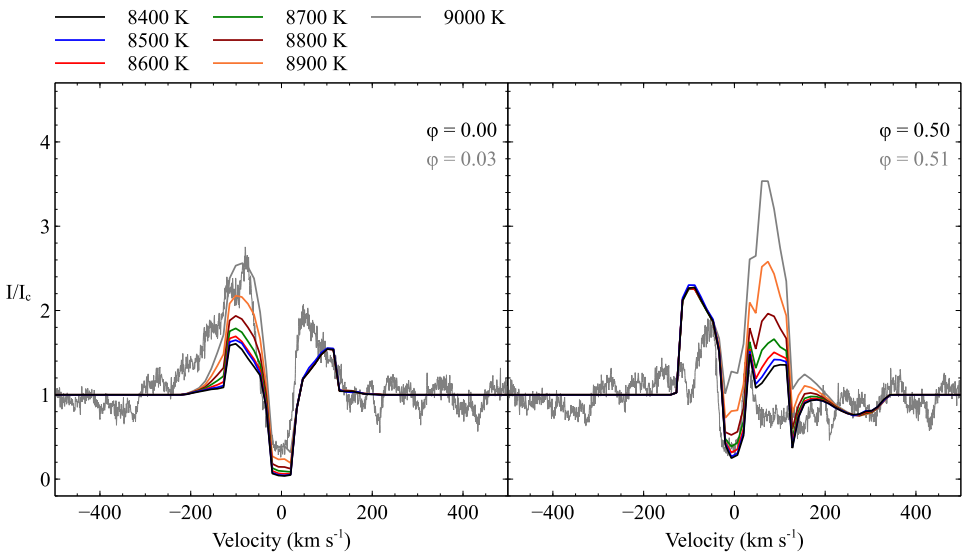

Figure 4.12: Variation of the Hβ profile shape with different $T_{\rm mag}$ values. $\varphi = 0.0$ is shown on the left and $\varphi = 0.5$ on the right. Observed profiles are in grey for comparison. All profiles are calculated with $\dot{M}_{\rm wind}/\dot{M}_{\rm acc} = 0.1$ and $T_{\rm wind} = 8000$ K.

at the highest temperatures. The same variations in intensity occur at $\varphi = 0.5$ for redward emission, where the effect is more pronounced since the entire accretion stream is in view. In general the blue peak is the primary in these observations, pointing towards a magnetosphere temperature of 8500 K which maintains the largest achievable difference in intensity between the primary and secondary peaks.

$T_{\rm wind}$ is restricted to 8000 ± 500 K for $\beta = 2.0$ and $T_{\rm mag} = 8500$ K, and $\dot{M}_{\rm wind}/\dot{M}_{\rm acc}$ has been varied between 0.05 and 0.15, in line with the canonical value of 0.1, by keeping the accretion rate constant at 5×10^{-9} $M_\odot$ yr^{-1} and varying the mass loss rate. The effect of varying $\dot{M}_{\rm wind}/\dot{M}_{\rm acc}$ is shown in Figure 4.13. There is little variation between profiles with ratios separated by 0.01 out of occultation. Variation between profiles is greater during occultation, with the red wing switching from absorption to emission at $\dot{M}_{\rm wind}/\dot{M}_{\rm acc} = 0.09$.

While models with higher mass loss rates fit the observations better out of occultation, ratios around 0.1 fit better during occultation, with higher mass loss rates giving excess emission. The variation in profile shape with different values for $T_{\rm wind}$ is plotted in Figure 4.14. Similarly, different values fit the observed profiles better at different phases,

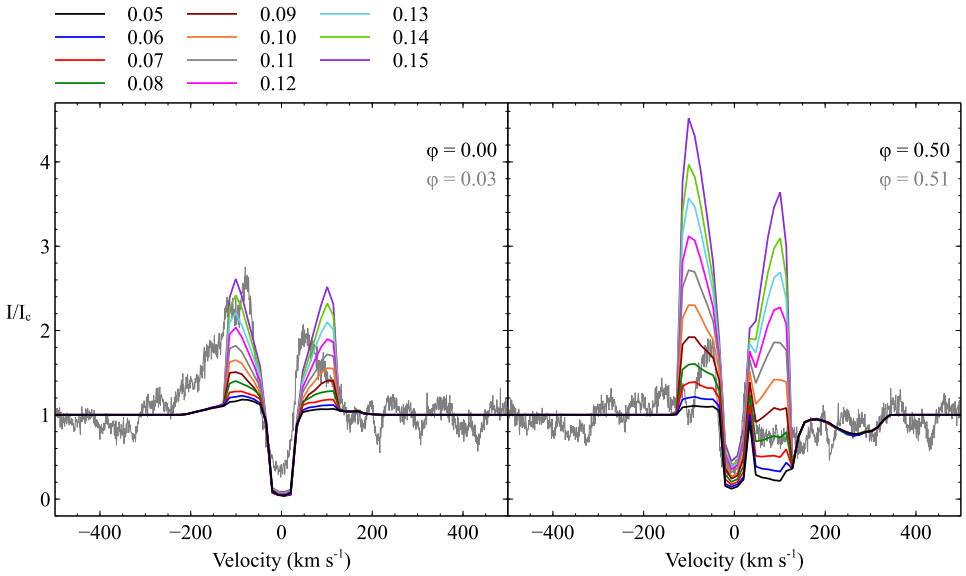

Figure 4.13: Variation of the Hβ profile shape with different $\dot{M}_{\rm wind}/\dot{M}_{\rm acc}$ values. $\varphi = 0.0$ is shown on the left and $\varphi = 0.5$ on the right. Observed profiles are in grey for comparison. All profiles are calculated with $T_{\rm mag} = 8500$ K and $T_{\rm wind} = 8000$ K.

with ∼ 8100–8200 K best describing the profile at $\varphi = 0.0$ and ∼ 7900–8000 K best describing the profile at $\varphi = 0.5$.

Out-of-occultation profiles are well-described by the canonical value of $\dot{M}_{\rm wind}/\dot{M}_{\rm acc} = 0.1$, $T_{\rm mag} = 8900$ K and $T_{\rm wind} = 8000$ K. However, the redward emission was unable to be sufficiently reduced to match observations during occultation. The full grid of profiles for this model is shown in Figure 4.15. During occultation, the line profiles are generally best described by a model with a cooler magnetosphere, where $\dot{M}_{\rm wind}/\dot{M}_{\rm acc} = 0.09$, $T_{\rm mag} = 8500$ K and $T_{\rm wind} = 8000$ K, shown in Figure 4.16. Individual profiles during occultation are also well-matched by $\dot{M}_{\rm wind}/\dot{M}_{\rm acc} = 0.1$, $T_{\rm mag} = 8500$ K and $T_{\rm wind} = 7900$ K ($\varphi = 0.5$, Figure C.3) and $\dot{M}_{\rm wind}/\dot{M}_{\rm acc} = 0.1$, $T_{\rm mag} = 8400$ K and $T_{\rm wind} = 8000$ K (φ =0.40 and 0.55, Figure C.4).

4.6 Discussion

While the spectroscopic models have been used to obtain a best fitting value for β, it is unlikely that spectroscopy places stronger constraints on the dipole offset angle than

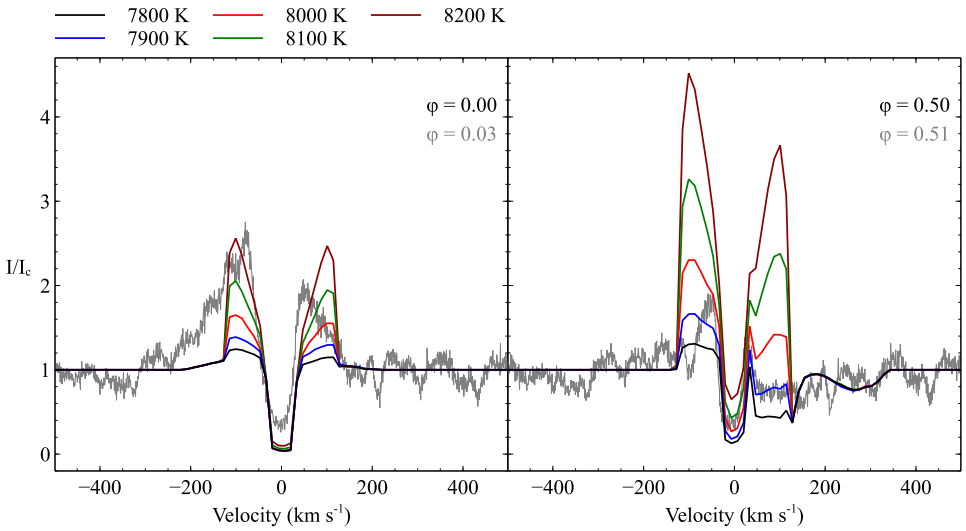

Figure 4.14: Variation of the Hβ profile shape with different $T_{\rm wind}$ values. $\varphi = 0.0$ is shown on the left and $\varphi = 0.5$ on the right. Observed profiles are in grey for comparison. All profiles are calculated with $\dot{M}_{\rm wind}/\dot{M}_{\rm acc} = 0.1$ and $T_{\rm mag} = 8500$ K.

photometry in general due to the degeneracies present in the disc wind model. While I have presented two best fitting parameter sets in the spectroscopic study, there are numerous other acceptable solutions. In general, I have found that for the canonical value of $\dot{M}_{\rm wind}/\dot{M}_{\rm acc} \sim 0.1$ with $T_{\rm mag} = 8500 - 8900$ K, a wind temperature of $T_{\rm wind} = 8000$ K is required. An outflow of some description is certainly necessary to produce the deep central absorption feature seen in observations. It is not clear whether the dominant source of outflow from CTTS is a disc wind, jet, stellar wind, or some combination of these, but the disc wind model used here matches the absorption feature fairly well.

The main issue with these results is the strength of the red emission peak during occultation. I have demonstrated that the red portion of the profile exhibits absorption features for sufficiently low mass loss rates and temperatures, but I have been unable to produce profiles with both sufficient emission at phases out of occultation and sufficient damping on the red side during occultation to match observations. This is particularly noticeable in Hα during occultation, where both the red and blue peaks are significantly stronger than observations, despite providing a reasonable fit out of occultation (see top grids of Figures C.3 and C.4 in Appendix C). There is also a discrepancy between the line

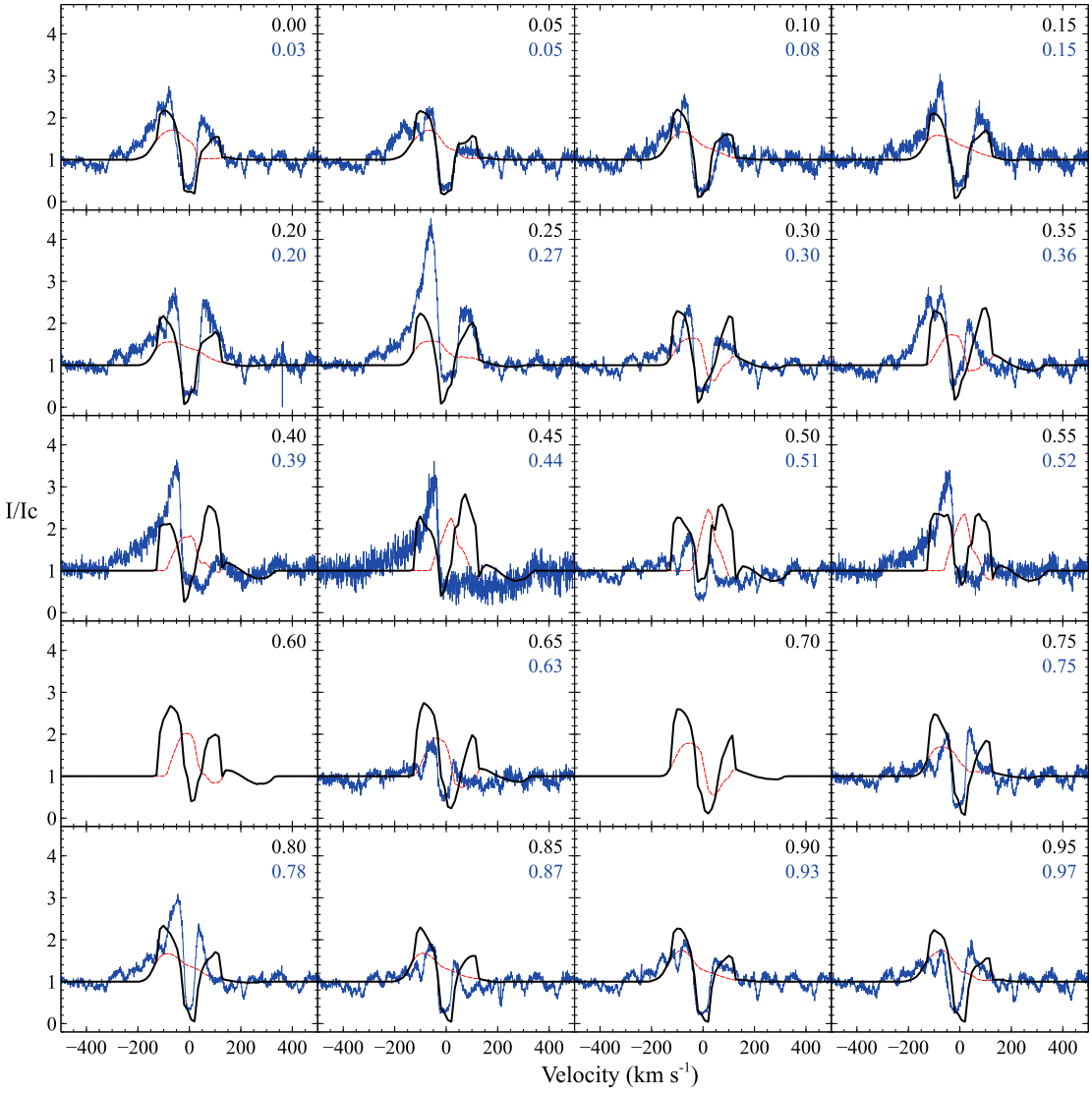

Figure 4.15: Best fitting models for Hβ profiles out of occultation, with $\dot{M}_{\rm wind}/\dot{M}_{\rm acc} = 0.1$, $T_{\rm mag} = 8900$ K and $T_{\rm wind} = 8000$ K. The magnetosphere contribution is shown by the red dotted line, and the magnetosphere-plus-wind profile is shown by the black solid line, with observations in blue.

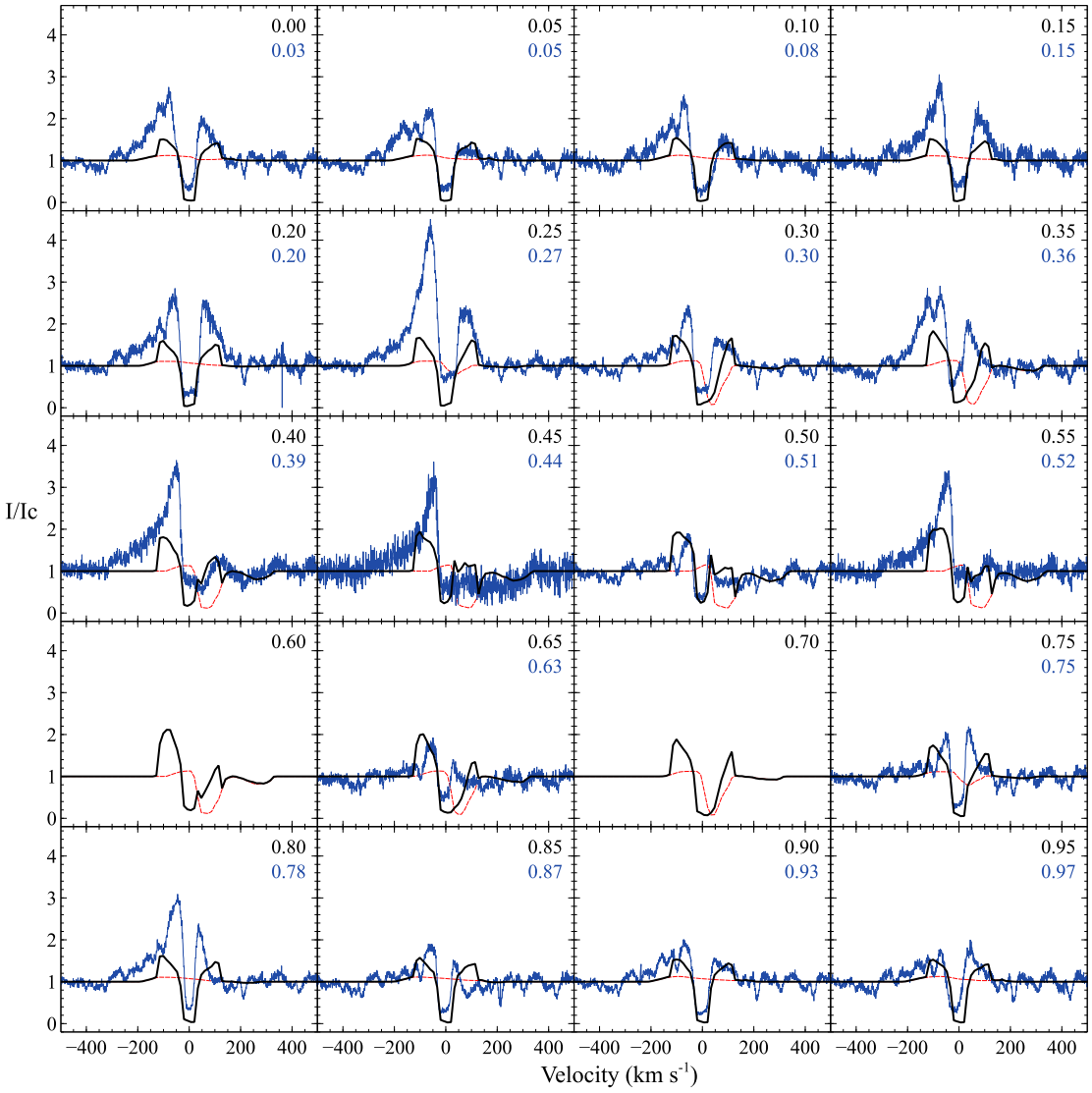

Figure 4.16: Best fitting models for Hβ profiles during occultation, with $\dot{M}_{\rm wind}/\dot{M}_{\rm acc}$ = 0.09, $T_{\rm mag}$ = 8500 K and $T_{\rm wind}$ = 8000 K. The magnetosphere contribution is shown by the red dotted line, and the magnetosphere-plus-wind profile is shown by the black solid line, with observations in blue.

broadening in models and observations for Hβ; while hotter magnetospheres produce more broadening (see Figure 4.12), these temperatures also produce significant redward emission, exacerbating the previous issue with this wind geometry. As with Hα, the Hγ profiles fit observations fairly well out of occultation, but do not provide such a good description during occultation. Examples are given in Appendix C, Figures C.3 and C.4 (bottom grids), where the modelled profiles do not produce such strong emission when the blue side of the profile becomes dominant. This discrepancy may be rectified by using a more complex wind geometry; given the asymmetry of the accretion flow and the evidence for winds being powered by the accretion process, it may be natural to expect a similar asymmetry to be found in the wind geometry. The "eggbeater" model of (Johns & Basri 1995, their Fig. 15) is worth future consideration. This model describes a wind where material is loaded more easily onto the wind flow when there is a large potential to overcome along the funnel flow, i.e. for $\phi = 0$, with the warp on the opposite side of the star to the primary wind source. Accretion and outflow signatures then occur in 180° phases.

4.7 Summary

I have simultaneously fitted photometry and spectroscopy models to AA Tau observations for Hα, Hβ and Hγ spectral lines and have recovered numerous parameters describing the entire system that are consistent with previous studies. I recovered the canonical value of $\dot{M}_{\rm wind}/\dot{M}_{\rm acc} = 0.1$, with values of around 0.05 or lower producing insufficient emission at all rotational phases, and values greater than 0.15 producing excessive emission, particularly at $\varphi = 0.5$. However, I have found that there is a degeneracy between the wind temperature and the acceleration parameter with the consequence that these parameters cannot be constrained using just the Balmer line profiles that were modelled here. One further area of interest is the He I λ10830 line, found to be present for AA Tau in a survey by Edwards et al. (2006). He I λ10830 acts more like a resonance line than the recombination lines that were considered here. With phase-resolved spectroscopy of this line over

AA Tau's 8-day period, this degeneracy could potentially be broken. Further constraints could be placed on the geometry of AA Tau with ground-based high-resolution imaging techniques such as interferometry. Direct imaging of AA Tau has already been achieved using the Hubble Space Telescope clearly showing the disc, as well as showing evidence of jet outflows (Cox et al. 2013). Photopolarimetry is another avenue of study for constraining the disc structure of AA Tau. Polarimetric variations have been observed by Bouvier et al. (1999, 2003) and Ménard et al. (2003), who found polarization is strongest when the system is faint, consistent with the presence of additional disc material enhancing the amount of polarization. Photopolarimetry of the warp modelled by O'Sullivan et al. (2005) yields a warp position slightly interior to the corotation radius, with their warped disc model reproducing observed brightness and polarization variations well.

The geometry of the system varies over time as the magnetic field lines emanating from the star break and reconnect, so while the best fitting parameter sets presented here have been found the best describe the system on average, different values will give superior fits at different specific times. Photometric models were used to constrain the mass accretion rate, the maximum height of the inner disc warp, the dipole offset, and the inner radius of the magnetosphere. Spectroscopic models were then used to further constrain the dipole offset, and to investigate the mass loss rate from a disc wind, the temperature of the wind, and the temperature of the magnetosphere. I have found that models with a mass accretion rate of $\sim 5 \times 10^{-9}$ $M_\odot$ yr^{-1} yielded an accretion luminosity of up to 6.1×10^{-2} $L_\odot$, consistent with the value of 6.5×10^{-2} $L_\odot$ calculated by B99. This accretion rate is consistent with the range of $2 - 7 \times 10^{-9}$ $M_\odot$ yr^{-1} calculated from Hα and Hβ line fluxes in Bouvier et al. (2013). I collated all publicly available *B*- and *V*-band photometry and found that average light curves are best described by $h_{\rm max}/r_{\rm o} \sim 0.31$ and $\theta = 10°$–$20°$, consistent with B99 who also derived $h_{\rm max}/r_{\rm o} = 0.3$ (see also Terquem & Papaloizou 2000), and Alencar et al. (2010) who found $h_{\rm max}/r_{\rm o} \sim 0.3$ for AA Tau-like light curves. The range in dipole offsets is consistent with Donati et al. (2010) who found $\theta = 20°$, although our spectroscopic models favour $\theta = 10°$. A disc wind is required to

recover the line shapes observed, although degeneracies between density and temperature in the disc wind prevent the determination of absolute values. However, I have found that the canonical value for mass loss rate to mass accretion rate of 0.1 best describes the observed line profiles. Disc wind and magnetosphere temperatures of $T_{\rm wind} \sim 7900$–8000 K and $T_{\rm mag} \sim 8400$–8500 K have been established, although there is the possibility of constraining these further by considering additional lines and alternative outflow geometries, possibly including stellar jets and a non-axisymmetric disc wind.

Chapter 5

Modelling the inner discs of Herbig Ae stars

While the paradigm of magnetospheric accretion fits observations of classical T Tauri stars well, there is little evidence of this accretion mechanism applying to Herbig Ae/Be stars. The boundary between CTTs and HAeBe stars is not so clean cut as to say that the properties of these objects diverge at this point; while there are certainly differences between these low- and intermediate-mass progenitors, similarities have also been found, in particular between CTTs and HAes (e.g. Vink et al. 2005; Mottram et al. 2007, discussed in more detail below). Generally similarities between CTTs and HAeBes include the presence of an IR excess in their SEDs indicating the presence of circumstellar material, UV/optical excess (in the case of some HAeBes) indicating accretion, and line emission (see Cauley & Johns-Krull 2014, and references therein). In a study probing the outflow mechanisms inherent in HAeBes using the He I λ10830 line, Cauley & Johns-Krull (2014) found that instances of forbidden blue-shifted line emission in CTTs which indicate large collimated outflows occur much less frequently in HAeBes, leading to the conclusions that outflows in HAeBes are less common. Red-shifted absorption features in the form of IPC profiles, indicating accretion, occur only slightly less frequently in HAes than in CTTs, whereas very few HBes show these signatures. While the sample size of HBes in this study was smaller, resulting in less statistically significant results when attempting to

differentiate between the circumstellar properties of HAe and HBe stars, these results do indicate that HBes may undergo a different accretion mechanism, for instance boundary layer accretion, which naturally explains the reduction in instances of redshifted absorption due to the lack of ballistically infalling material.

As noted in Chapter 1, magnetic fields around HAeBe stars are very weak, and the inner dusty disc does not extend far enough inwards to reach the magnetosphere. Muzerolle et al. (2004) found that observed line profiles of the HAe star UX Ori could be fitted by assuming that there is an inner gaseous disc that extends interior to the dust sublimation radius. It may be either optically thin or optically thick but it is required to be geometrically thin in order for stellar radiation to reach and heat the dusty disc, thus remaining consistent with the excess IR emission observed for these objects (e.g. Hillenbrand et al. 1992; Natta et al. 2001; Dullemond et al. 2001). In a spectropolarimetric study of HAeBe stars, Vink et al. (2005) found that there are similarities in the Hα line polarimetry of CTTs and HAes which indicate the presence of some compact Hα source whose photons are scattered off a rotating disc, which could potentially be due to some sort of magnetospheric accretion process occurring in late-type HAes. HBes, on the other hand, demonstrate a geometrically flat undisrupted disc. A similar conclusion was later reached by Mottram et al. (2007) who found that the behaviour of the line-polarimetry observed for HAe stars is consistent with the presence of an inner hole, similar to the geometry of CTTs. Observations of HBe stars, however, were more consistent with a simple disc accretion mode. This difference was attributed to the fact that while HBe stars lack the convective dynamo that produces the magnetic field, HAe stars may have been sufficiently cool at an earlier stage of their evolution to have produced a convective dynamo which they have been able to maintain during their evolution (Muzerolle et al. 2004). The alternative explanation for the origin of magnetic fields in HAeBes is that they originate from fossil fields, in which part of the magnetic field from within the star forming region is swept up during the process of star formation (Alecian et al. 2007).

Unfortunately the situation is not as simple as separating HAeBe objects into two

categories of HAe (and possibly late HBe) stars whose geometry consists of a magnetospherically accreting inner gaseous disc which transitions into a dusty disc at larger radii, and HBe stars which undergo disc accretion. In addition to the accretion disc geometry, observed SEDs and interferometric visibilities have also been able to be reproduced using geometries which consist of an extended halo in addition to the disc (e.g. Vinković et al. 2006; Weigelt et al. 2011) and a single spherical envelope (e.g. Miroshnichenko et al. 1997; Millan-Gabet et al. 2001).

The nature of the material interior to the dust sublimation radius in disc geometries is also highly debated. Some form of inner material is certainly required in order to explain observations that show excess emission, pointing to the presence of a region interior to the dust sublimation radius of the circumstellar disc in which additional material is found (Tannirkulam et al. 2008a,b). Three frequently suggested sources of this excess are: emission from an optically thick interior gaseous portion of the disc; dust which is able to survive closer to the star due to the absorption of stellar flux by an interior gas disc; and dust emission from refractory grains which are able to survive closer to the star, without the need for additional flux absorption, due to their higher sublimation temperatures (Benisty et al. 2010, hereafter B10).

Self-consistent models of gas and dust are currently very difficult to get right. They require incredibly detailed line lists and we do not currently have the means to produce sufficiently accurate models in order to test the first two of these hypotheses. In this chapter I explore the feasibility of the third of these options by producing self-consistent models of dust sublimation. I have performed numerous SED fits to data from the *Spitzer Infrared Spectrograph* (IRS), supplemented by additional data from the literature, and visibility fits to data from the *PIONIER* instrument on the VLT and the *CHARA* interferometric array for the HAe stars MWC 275 (also known as HD 163296) and AB Aurigae (AB Aur) with the aim of constraining the temperature required for refractory grains to survive far enough in to provide sufficient filling-in of the inner circumstellar disc. I begin by giving a brief overview of the technique of interferometry in Section 5.1 and follow

with a description of the work carried out by B10 in Section 5.2 which led them to propose the source of excess near-IR (NIR) emission as refractory dust. I present the physical parameters of the two objects on which I am focussing in Section 5.3, followed by a discussion of the free parameters that I explore in my models. The numerical method previously described in Chapter 2 is expanded upon in Section 5.4, and results are presented in Section 5.5. The implications of these results are discussed in Section 5.6. Finally in Section 5.7 I present the hypothesis of grain coupling as an alternative source of excess NIR emission.

5.1 Interferometry

Here, I briefly cover the basics of interferometry. A thorough review is given by Monnier (2003, and references therein).

The technique of interferometry exploits the wave properties of light in order to resolve much smaller spatial details than would otherwise be achievable by standard imaging with a single dish. It can be understood in terms of the famous *Young's double-slit experiment*, in which monochromatic light emitted from a point source is shown to produce a series of bright and dark fringes after passing through an opaque panel containing two slits. Fringes are produced as a result of constructive and destructive interference; the beam of light from the initial point source is split into two separate beams on passing through the slits, with the consequence that the path length of each beam is different at any given point on the screen displaying the fringes. A schematic of this is shown in Figure 5.1. Points of constructive interference occur when the two beams arrive at the screen in phase with one another, i.e. each beam has traversed a distance equal to an integer number n of wavelengths, whereas destructive interference occurs when the path lengths of the beams are out of phase, i.e. the path lengths differ by $(0.5 + n)\lambda$.

Adding a second point source at a projected distance of half the fringe spacing, $\lambda/(2b)$, from the first point source will result in a second diffraction pattern shifted in phase by 180° with respect to the first, causing destructive interference at all points on the

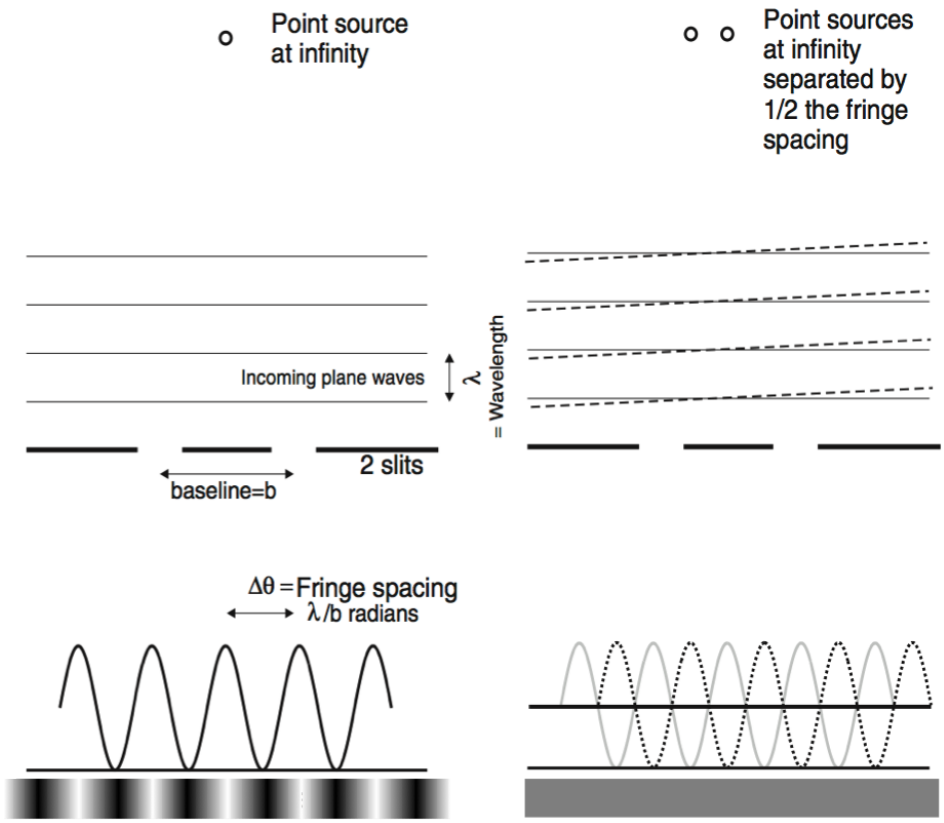

Figure 5.1: A schematic of Young's two-slit experiment (adapted from Monnier 2003). *Left:* A monochromatic point source at infinity passes through two slits separated by a distance b and produces an interference pattern of light and dark fringes. *Right:* A second point source located at a distance of half the fringe spacing from the initial source causes a second sine wave which destructively interferes with the first at all points, resulting in a uniformly illuminated screen.

screen. The result is a uniformly illuminated screen. This demonstrates how measuring fringe contrast, or interference, can be used to ascertain the geometric distribution of light sources.

Interferometric systems consist of a number of telescopes separated by various baselines, where the projected baseline between two telescopes is the apparent separation between them as if viewed from the source. A beam combiner is used to produce the fringes, analogous to the screen in the above two-slit experiment. A schematic of this setup is shown in Figure 5.2. Since there is a delay between the light reaching the first telescope and the light reaching the second telescope, a delay line is also used to ensure the light is in phase at the point of beam combination. Arrays of telescopes such as ALMA, the VLTI, and the CHARA array can be used to make simultaneous interferometric observations at a number of different baselines.

Interference is quantified by the *visibility*, V, which is a measure of the contrast between interference fringes. Specifically, it is the Fourier transform of the brightness distribution across the plane of the sky (with coordinates (l, m)) as a function of baseline coordinates (u, v), also known as the uv-plane. For instance, a point source on the plane of the sky will produce a uniform visibility in the uv-plane. Each pair of telescopes enables one point on the uv-plane to be sampled, so the greater the number of telescopes, i.e. the greater the number of different baselines available, the more the uv-plane can be sampled. Additional uv-coverage is provided naturally from the rotation of the sky. Mathematically, visibility is given by

$$V(u, v) = \int \int I(l, m)\, e^{-2\pi \mathrm{i}(ul+vm)} dl\, dm, \tag{5.1}$$

where $V(u, v)$ is the visibility at any given point on the uv-plane, $I(l, m)$ is the intensity at any given point on the plane of the sky, and u, v, l, and m are the individual coordinates of the two planes being considered. This relationship between the visibility function and the intensity of the incoming radiation is given by the van Cittert-Zernike theorem (Monnier 2003), which states that radiation which is incoherent at source appears coherent

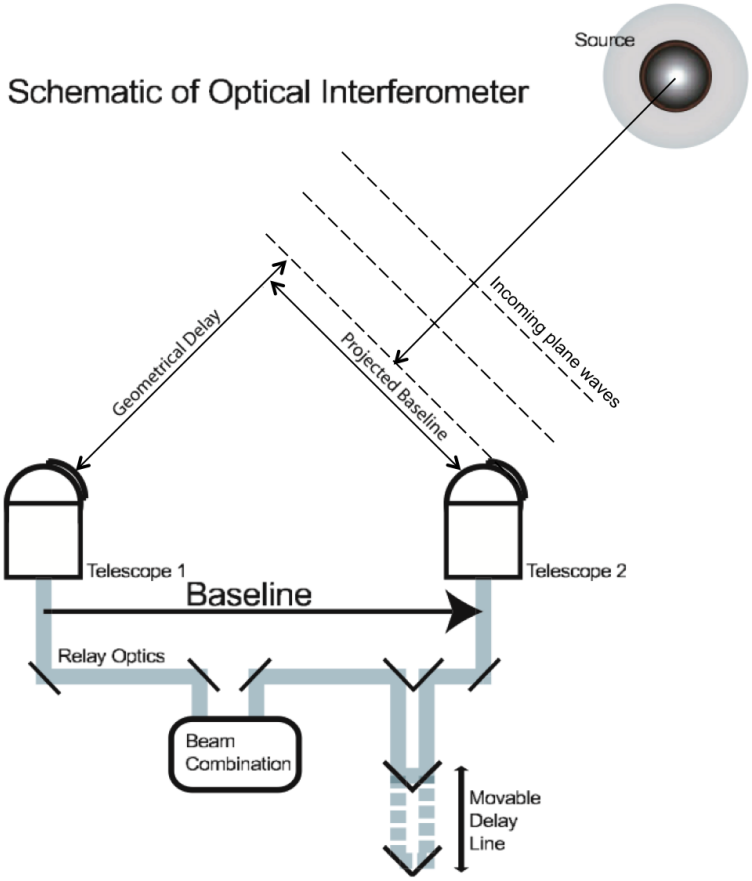

Figure 5.2: A schematic of the main components of an interferometer. Light is intercepted by two telescopes, with the two beams combined to measure the interference. A delay line is included to ensure the light reaches the beam combiner in phase (adapted from Monnier 2003).

at sufficiently large distances.

5.1.1 Visibility curves for different source morphologies

The visibilities derived for the objects presented in this chapter indicate the presence of some form of material interior to the classical silicate dust sublimation radius. The visibility is a Fourier transform of the intensity distribution, for instance Gaussian visibility curves tell us that the object observed must have a Gaussian intensity distribution on the sky. Example intensity distributions for common morphologies are given in Figure 5.3 to demonstrate how different intensity distributions affect the resulting visibilities. For a given spatial frequency, the visibility amplitude is lower for more extended objects. High spatial frequency information is therefore available from more compact objects; the top panel of Figure 5.3 clearly demonstrates this, with a point source producing a uniform visibility at all spatial frequencies. While the Gaussian distribution in the middle panel describes a resolved source, the intensity distribution is still fairly compact so the associated visibility curve is broad, tending to zero at high spatial frequencies. The intensity distribution in the bottom panel gives a bright, unresolved point source surrounded by an extended structure. The central peak in the visibility curve indicates that only short baselines are required to resolve this region, so an extended structure must be present in order for it to be so easily resolved. The non-zero visibility at high spatial frequencies indicates that that there is some object contributing a small fraction of the flux which is unresolved.

Sharp cut-offs present in intensity distributions produce lobes in the visibility curves, where sharper the image, the more significant the lobes beyond the first null. This effect is shown in Figure 5.4, with one-dimensional intensity distributions given in the top panel and the visibility curve produced by each morphology given in the bottom panel. The solid line shows a Gaussian intensity distribution which produces a Gaussian visibility curve, as discussed above. The dotted line shows a limb darkened model in which the intensity initially drops off gradually until reaching the edge of the disc. The solid line gives a uniform disc, in which the intensity is constant across the structure and zero beyond. The

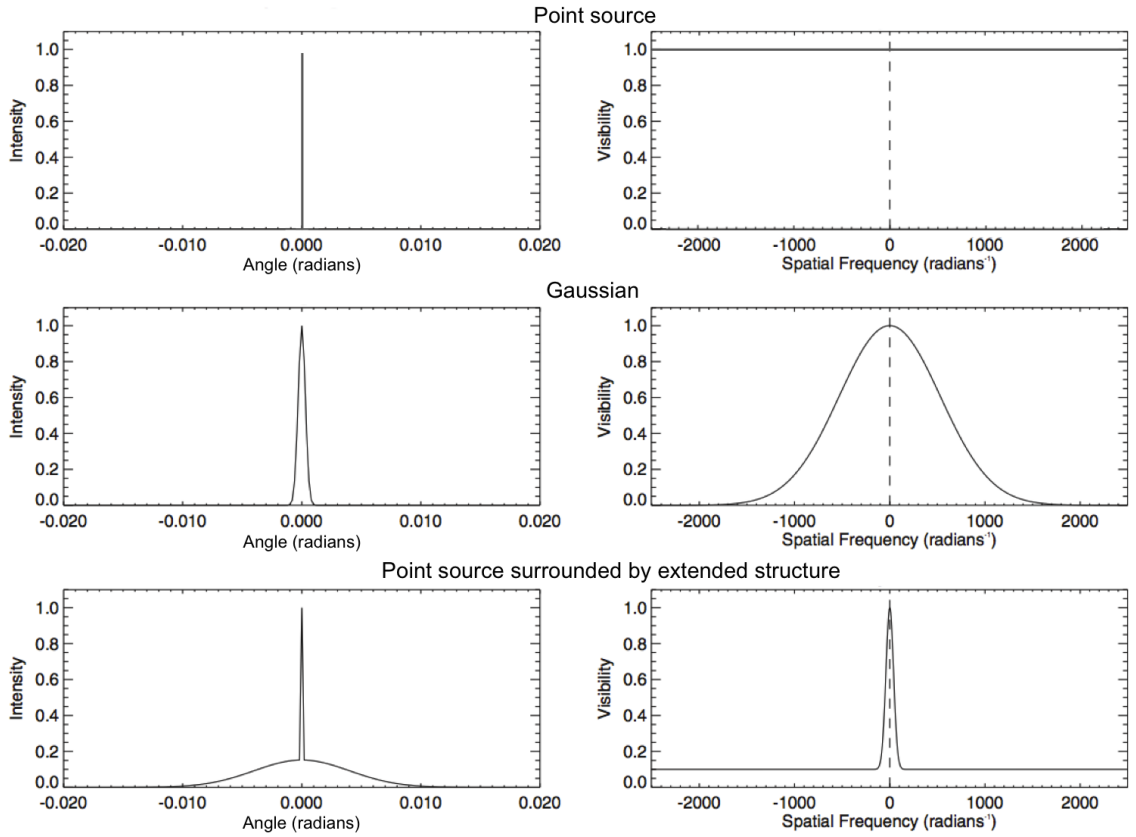

Figure 5.3: Common source morphologies presented in one-dimensional intensity distributions (left) and their associated visibilities (right). The top panels depict a point source, the middle panels depict a Gaussian, and the bottom panels depict an unresolved central point surrounded by an extended structure. Compact objects provide high spatial frequency information, resulting in non-zero visibilities at long baselines (adapted from Monnier 2003).

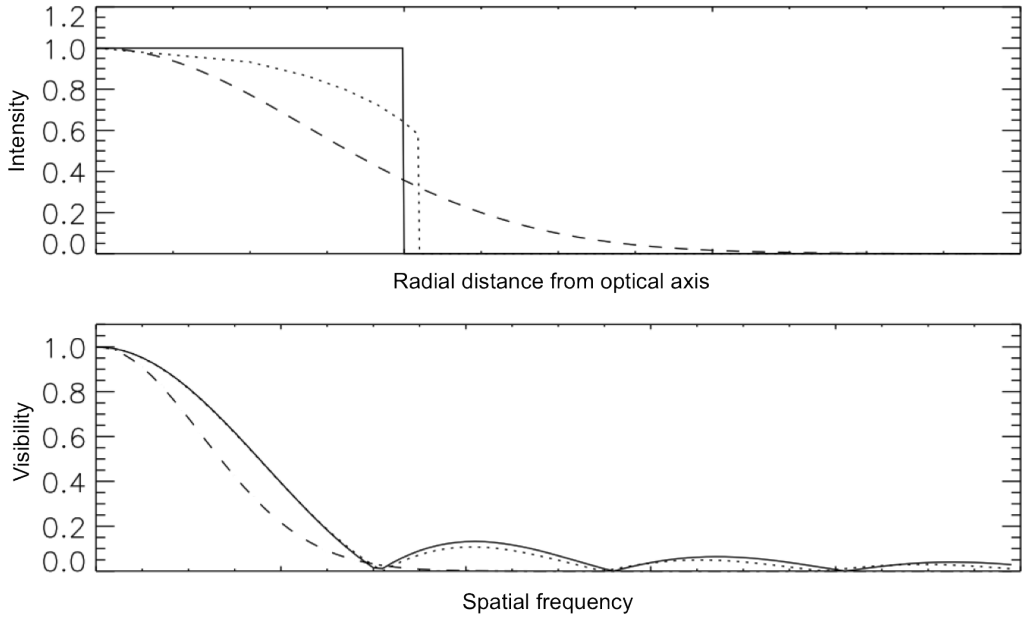

Figure 5.4: Intensity distributions (top) and associated visibility curves (bottom). The solid line shows a uniform disc with an instantaneous decrease in intensity to zero, the dotted line shows an object with some limb darkening, and the dashed line shows a Gaussian intensity distribution. The first lobe of the uniform and limb darkened models are identical since the radial size of the object on the sky is roughly the same in each case. The first lobe of the Gaussian distribution is more compact since its intensity distribution is more extended. Beyond the first null, the uniform disc produces slightly larger lobes since the intensity drops off instantly, with more gradual intensity decreases producing smaller lobes. The Gaussian intensity distribution produces a Gaussian visibility curve. (adapted from Verhoelst 2005).

shape of the first lobe provides information on the size of the structure observed on the sky. Since the uniform disc and limb darkened models are similar in radial extent, the first lobe of their visibilities is identical. However, since the intensity of the Gaussian profile drops off gradually, it produces a more extended intensity distribution and consequently the first lobe of its visibility curve is more narrow. Information on the intensity gradient is given beyond the first null, with the uniform disc producing lobes reaching slightly higher visibilities compared to the limb darkened model. The Gaussian distribution produces an entirely Gaussian visibility curve, approaching zero shortly after the first null of the other two geometries.

5.2 Refractory grains as a source of inner disc emission

Early studies of the distribution of material around HAeBes found that observed SEDs could be reproduced by a circumstellar disc with an inner hole (Hillenbrand et al. 1992). This inner hole was required due to the lack of emission from warm inner circumstellar regions. Excess NIR emission observed in the SEDs was said to be produced by rapidly-accreting material. However, Hartmann et al. showed that inner discs would be optically thick at the required accretion rates, thus favouring dusty circumstellar envelopes as the source of excess NIR emission.

A solution to the problem of a NIR excess in disc models was suggested by Dullemond et al. (2001) in which the presence of an optically thin interior region to the disc, where temperatures exceed that at which dust sublimes, produces an inner disc rim that is directly exposed to stellar radiation. As a consequence, this rim is much hotter than the rest of the disc material and emits in the NIR, reproducing the observed 3 μm bump. The material at the inner rim also 'puffs up' relative to the rest of the disc due to the increased temperature, producing a significant increase in vertical scale height, casting a shadow over significant portions of the disc. The shadowed portion of the disc thus has a reduced temperature since it is no longer illuminated by stellar radiation and radiates at longer wavelengths than an unshadowed disc. A vertical inner rim produces an SED that varies with inclination angle; face-on inclinations produce a less significant NIR excess but produce a stronger far-IR (FIR) contribution. The reverse is true for high inclinations to an extent, since the projected surface area of the heated rim structure is equatorial and so its contribution is more significant for high inclinations. Discs observed entirely edge-on will show no rim emission since the emission is obscured by the opposite edge of the rim. Observations show that the NIR excess observed in HAe SEDs does not depend strongly on the inclination angle of the system (e.g. Natta et al. 2001; Dominik et al. 2003). This motivated Isella & Natta (2005) to model an inner rim with a curved geometry, where they take the dependence of dust sublimation temperature on gas density into account.

The disc density decreases in the vertical direction and so the dust sublimation temperature will decrease with increasing vertical distance from the disc midplane, producing a rim that curves away from the star. Synthetic images computed by Isella & Natta (2005) found that, unlike the vertical disc rim model, the near-IR excess produced by curved rims has little dependence on disc inclination, in agreement with observations of discs at various inclinations. The curved nature of the rim enables inner rim emission to occur over a range of angles, producing a more constant contribution over various inclination angles.

However, more recent work over the last decade has found that the puffed-up rim model is not always sufficient in explaining observations. SEDs of early-type HBe stars, in particular, have been found to be best fitted by geometrically flat disc models, with NIR visibilities being completely inconsistent with puffed-up rim models with silicate dust (Eisner et al. 2004). Conversely, these authors found that the SEDs of HAe and late-type HBe stars were consistent with a puffed-up inner disc wall. This same conclusion was reached by Monnier et al. (2005) from the results of their K-band survey of HAeBes; they found that the inner rims of early HBe stars were closer in to the star than predicted by the puffed-up rim model, and could instead be fitted by the classical flat disc model where an optically thick inner gas disc shields the dust sufficiently for it to survive at smaller radii. The survey carried out by Monnier et al. found that the dust-free inner cavities of the very brightest HBe stars, with spectral types B0–B3, were undersized compared to predictions. Individual less luminous objects have also been found to require an additional inner source of emission to explain observations. In a spectrointerferometric study of the B6 star MWC 147, Kraus et al. (2008) found that an additional emission component from an inner gaseous disc was required in order to agree with observations. The A0 star AB Aurigae was found by Isella et al. (2006) to be the only object in their survey of six HAe stars whose inner dust rim was found to be closer in to the star than that calculated from models assuming a puffed-up rim with silicate dust. Again, they suggested absorption by gas interior to the dust disc was likely to be responsible, shielding and thus cooling the

dust grains so that they may survive further in. Isella et al. also suggest the possibility that more refractory grains than the silicates used in their model may be responsible for the emission, but rule this out due to the high sublimation temperatures (~2800 K) at the required radii. Similarly, Eisner et al. (2007) found that model fits to their observations of 11 HAeBe stars required two rings of different temperatures. Since the temperature required by the inner emission source one again was found to exceed the dust sublimation temperature, Eisner et al. also suggested its origin was from inner gas emission. They found the temperature of the cooler outer ring was comparable to the dust sublimation radius, and thus overall the structure was consistent with a two-component inner gas and outer dust disc, each radiating at different temperatures.

While these authors have generally excluded dust as the source of this inner emission, B10 have suggested that refractory grains may be able to survive at higher temperatures inside the silicate rim and could therefore be a viable alternative to gas emission. In their study of MWC 275, gas was tentatively ruled out as the source of this excess emission; models of optically thick gas in LTE (previously computed by Muzerolle et al. 2004) were shown to produce sufficiently strong NIR emission but also produce strong molecular lines which are not present in the observed SEDs of this object, and models with optically thin gas, in non-LTE, did not reproduce the observed wavelength dependence of the emission.

B10 considered three different refractory grain types – graphite, iron, and corundum (aluminium oxides) – which were modelled assuming that each grain is heated directly by stellar radiation and attenuated by some constant optical depth. The temperature of the silicate rim was set by assuming a luminosity of 75 per cent $L_\star$ to account for shielding by the inner refractory grains. The resulting SED was found to be a good fit for observations. This has been reproduced in Figure 5.5 along with the SEDs computed by B10 for various gaseous contributions. There are limitations in this model in that the calculations were not done self-consistently. By assuming the temperature of the inner silicate rim, the models were not required to involve a self-consistent calculation of the dust temperature. This

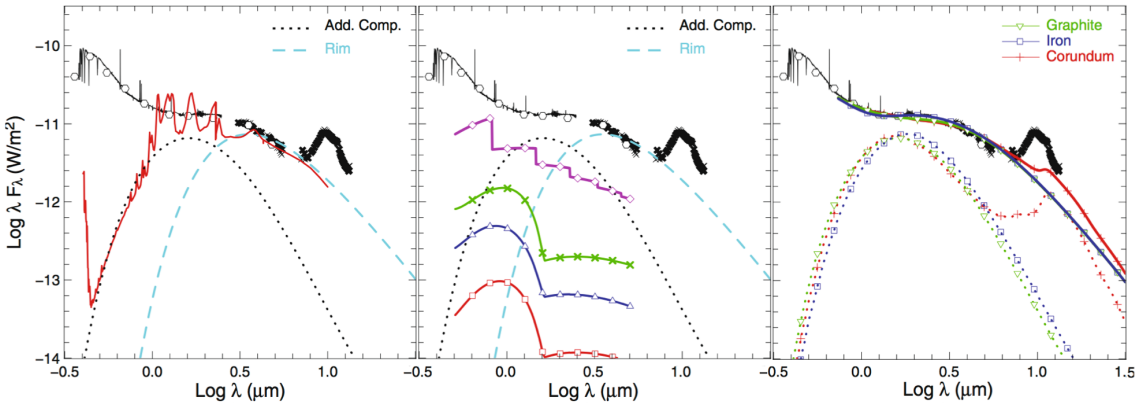

Figure 5.5: SEDs for inner discs composed of optically thick gas (left), optically thin gas (centre), and refractory grains (right). The strength of the emission produced by an optically thick gaseous component (red line) compares well with observations although the strong molecular line emission from the model is not observed. Optically thin gas is shown not to reproduce the correct wavelength dependence (the bottom three lines here show atomic gas heated by the star at various surface densities, and the magenta line with circles shows ionised gas heated by some other source). Refractory grains are found to fit the observed SED well. Their individual contributions are shown by the dotted lines, with the total flux given by the solid lines. Reproduced from Benisty et al. (2010), figs. 8–9.

has the knock-on effect that the position and shape of the inner rim are also not calculated self-consistently. Instead, the location of the inner part of the silicate rim is assumed to be at 0.45 AU from the star, and a simple curved geometry is assumed.

Using TORUS, I have computed SEDs and visibilities for two HAe stars, MWC 275 and AB Aur, using iron grains as the refractory grain type. The purpose here is to fully examine the suggestion that refractory grains may produce the additional NIR emission, improving on the work of B10 by computing fully self-consistent models. TORUS enables dust temperatures and inner disc radii for different dust populations to be calculated self-consistently as well as calculating results for numerous refractory and non-refractory grains simultaneously. The aim is to closely examine the properties of the inner rims of these two objects, with a view to determining whether refractory grains surviving at the temperature required by the best fitting models is physically plausible. B10 found refractory grain temperatures of 2100–2300 K were reached in their models and noted that while graphite may survive at these temperatures, iron and corundum are not expected to survive using the parameters assumed in their models. However, the additional emis-

sion contributed by refractory grains is extremely sensitive to grain fraction; only a very small fraction is required to produce this effect. Since B10 presented their results for iron grains, I focussed on this grain species as well.

5.3 MWC 275 and AB Aur

An interferometric observing campaign targeting MWC 275 and AB Aur carried out by Tannirkulam et al. (2008b) used the CHARA array to obtain interferometric data at baselines up to 325 m. In the years since these data were obtained, no additional data with baselines beyond 130 m has been published, making these CHARA data unique in enabling the study of these disc geometries. These observations produced the surprising result that the visibility curves of these objects show no second lobe and are instead rather flat. This points to the presence of NIR emission interior to the silicate sublimation radius in each of these objects. Tannirkulam et al. (2008a,b) discussed this excess emission in the context of gas emission. They showed that models containing solely a dust rim produced visibility profiles which show significant alternating lobes and nulls at long baselines which are not present in observational data. As a toy model they included Gaussian emission to simulate the spatial distribution of a potential molecular gas emission component, and found that the lobes in the visibility curve were eliminated when this inner Gaussian emission component was introduced. The resulting models fitted both observed visibilities and SEDs well. Comparisons between visibilities calculated with and without this inner emission component are shown in Figure 5.6, and images depicting a disc with and without this central emission are shown in Figure 5.7. Since observations of MWC 275 and AB Aur appear to be consistent with models representative of inner gas emission, it is of interest to see whether it is also possible to obtain good fits to data from these objects using emission from refractory dust as an alternative.

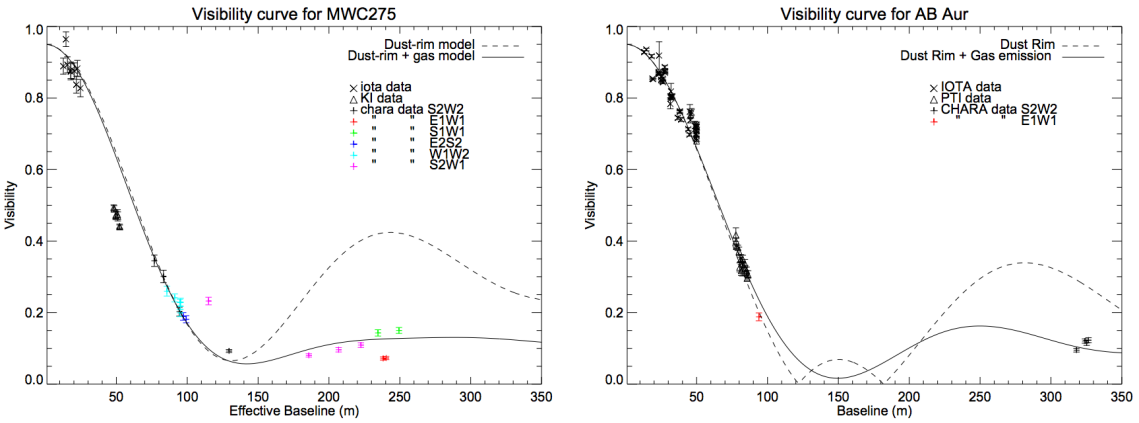

Figure 5.6: Visibilities for MWC 275 and AB Aur using an additional Gaussian emissivity to produce the inner emission (solid line). Visibilities without this inner gas component are given by the dotted line. An inner gas component clearly produces a good fit to observed visibilities; some form of inner emission is certainly necessary. Reproduced from Tannirkulam et al. (2008b).

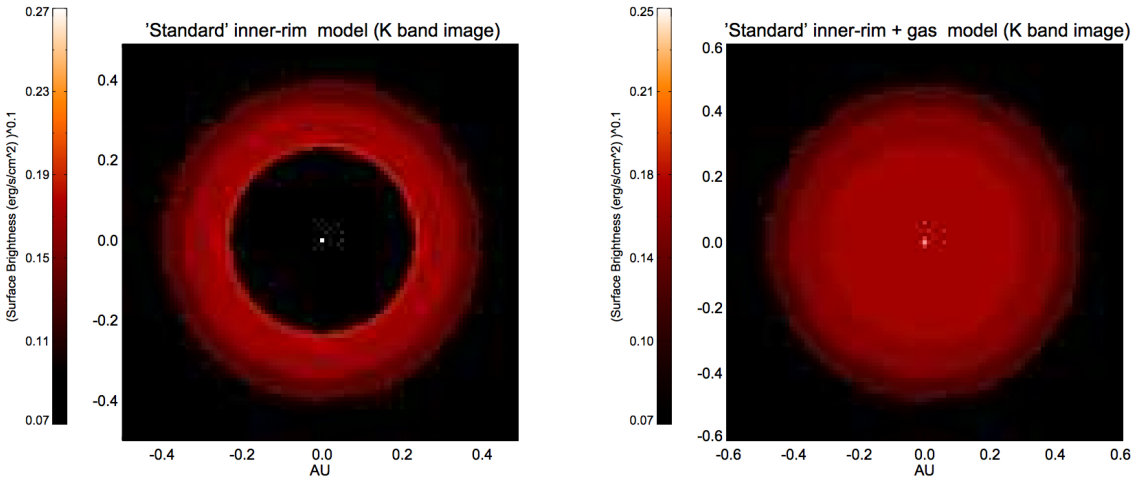

Figure 5.7: Images produced by models of near-IR emission from a general HAe star. The standard dust rim model is shown on the left, which produces visibilities with significant nulls as shown by the dashed line in Figure 5.6. The right-hand image shows a disc which has been filled in centrally by a smooth emission component, producing a much smoother visibility curve. Reproduced from Tannirkulam et al. (2008b).

5.3.1 Observational data

Interferometric data for each of these objects were obtained using two different interferometers. H-band (central wavelength 1.65 µm, $\Delta\lambda$=0.35) observations were made using PIONIER and K-band (central wavelength 2.13 µm) observations were made using the CHARA array.

PIONIER (the Precision Integrated-Optics Near-infrared Imaging ExpeRiment) is an instrument which enables the combination of four beams from either the four 8 m unit telescopes or the four 1.8 m auxilliary telescopes on the VLT Interferometer. The instrument combines the light from the four telescopes using a ABCD pair-wise beam combination scheme, where the optical path delay is modulated using piezo scanners. The integrated optics combiner produces interference patterns for all 6 baseline combinations, which are recorded on a PICNIC detector. Technical details about the instrument itself as well as operation and data reduction are described in Le Bouquin et al. (2011). The data reduction was performed using the standard PIONIER pipeline, which estimates visibility amplitudes from the power spectrum. The observations of the target star are interlaid with observations on calibrator stars of known diameter, which allow the monitoring of the instrumental and atmospheric transfer function and to calibrate the visibilities reliably.

PIONIER data for AB Aur and MWC 275 were taken as part of the Herbig Large Programme (190.C-0963). A PRISM was used to spectrally disperse the H-band and to measure the visibility in 3 spectral channels. The calibrated data are publicly available and were retrieved from the OIDB database[1]. The data will also be presented in the upcoming paper by the PIONIER team (Lazareff et al., A&A submitted). These data were taken on 19–20/08/2012 and 02/07/2013 (MWC 275), and 19/12/2012 and 21/12/2012 (AB Aur).

The CHARA (Center for High Angular Resolution Astronomy) array is an array of six 1 m telescopes which provide 15 baselines between 34–331 m. MWC 275 and AB Aur were observed in 2008 with the CLASSIC beam combiner instrument that can combine arbitrary pairs of the 6 CHARA telescopes. The data were recorded without spectral

[1] http://oidb.jmmc.fr/index.html

dispersion using a K-band filter. Details about the optical design of the instrument and the array as well as the data reduction strategy are presented in ten Brummelaar et al. (2005). In summary, data acquisition typically involves alternating scans of the target object and a calibrator object, where the visibility of the latter is well-known. Detector, scintillation and photon noise in the signal are removed by taking scans with the shutters of each or both telescopes closed for a given baseline. Scans with both shutters closed contain only the detector noise, and scans with one shutter closed contain both detector noise and half the scintillation and photon noise. After correcting for background and detector cosmetics, the visibility is estimated by integrating over the fringe peak in the power spectrum. The visibility measurements on the calibrators are used to estimate the visibility transfer function and to calibrate the target observations both for instrumental and atmospheric influences.

CHARA data were taken over eight runs between June 2004 and June 2007, with data obtained for various orientations and baselines. The longest baselines observed were 325 m for MWC 275 and 320 m for AB Aur (corresponding to resolutions of 0.67 mas and 0.68 mas, respectively, where resolution is defined as $\lambda/2B$ where B is the baseline length). HD 164031, HD 166295, and HD 156365 were used as calibrator stars, and the results from the CHARA reduction software were cross-checked with an independently developed code. The CHARA data are also available on OIDB, and are presented in Tannirkulam et al. (2008b). The visibility profiles of AB Aur and MWC 275 are shown in Figure 5.8 (right), with the wavelength dependence of the visibility profiles shown in the top right panel of this figure.

SED data are compiled from various sources. Continuous SED data for each object are taken from van den Ancker et al. (2000) who, using the Infrared Space Observatory (ISO), obtained spectra for MWC 275 and AB Aur in the wavelength range 2.4–45 μm. These data are supplemented with individual photometric data points from various publications which are presented in Table 5.1 for both objects. Additional SED data are included for MWC 275, which were taken from the Spitzer archive[2]. The AORKEY

[2]http://sha.ipac.caltech.edu/applications/Spitzer/SHA/

Table 5.1: Photometric data for MWC 275 (left) and AB Aur (right). The references listed are: ESA97, ESA (1997); C03, Cutri et al. (2003); W82, Wesselius et al. (1982); H92, Hillenbrand et al. (1992). All data for AB Aur are taken from Hillenbrand et al. (1992)

MWC 275:

Wavelength (μm)	Mag	Ref
0.429	6.994	ESA97
0.554	6.881	ESA97
1.25	6.195	C03
1.65	5.531	C03
2.18	4.779	C03
0.1545	8.382	W82
0.1799	7.200	W82
0.2200	7.181	W82
0.2493	7.339	W82
0.3294	6.989	W82
0.366	6.96	H92
0.429	6.92	H92
0.554	6.83	H92
0.657	6.77	H92
0.768	6.72	H92
1.25	6.25	H92
1.65	5.57	H92
2.18	4.72	H92
3.55	3.51	H92
4.770	3.13	H92
10.47	0.69	H92

AB Aur:

Wavelength (μm)	Mag
0.366	7.21
0.429	7.21
0.554	7.07
0.657	6.82
0.768	6.69
1.25	5.935
1.65	5.061
2.18	4.230
3.55	3.30
4.77	2.90
10.47	0.36
20.10	−1.12

(a unique identification number used in the archive) for this observation sequence is 5650944, and the data were taken as part of the programme 'From Molecular Cores to Planets, continued'. The ISO data are shown in grey in the left-hand plots in 5.8, the photometric data points are shown in red, and the Spitzer data is shown in blue in the MWC 275 SED (the top-left of this figure).

5.3.2 Physical and geometric parameters

While these objects are of similar mass, with MWC 275 at 2.3 $M_\odot$ and AB Aur at 2.4 $M_\odot$ (van den Ancker et al. 1998), their respective disc properties differ. The SED of AB Aur has more infrared excess than that of MWC 275 at wavelengths around 100 μm,

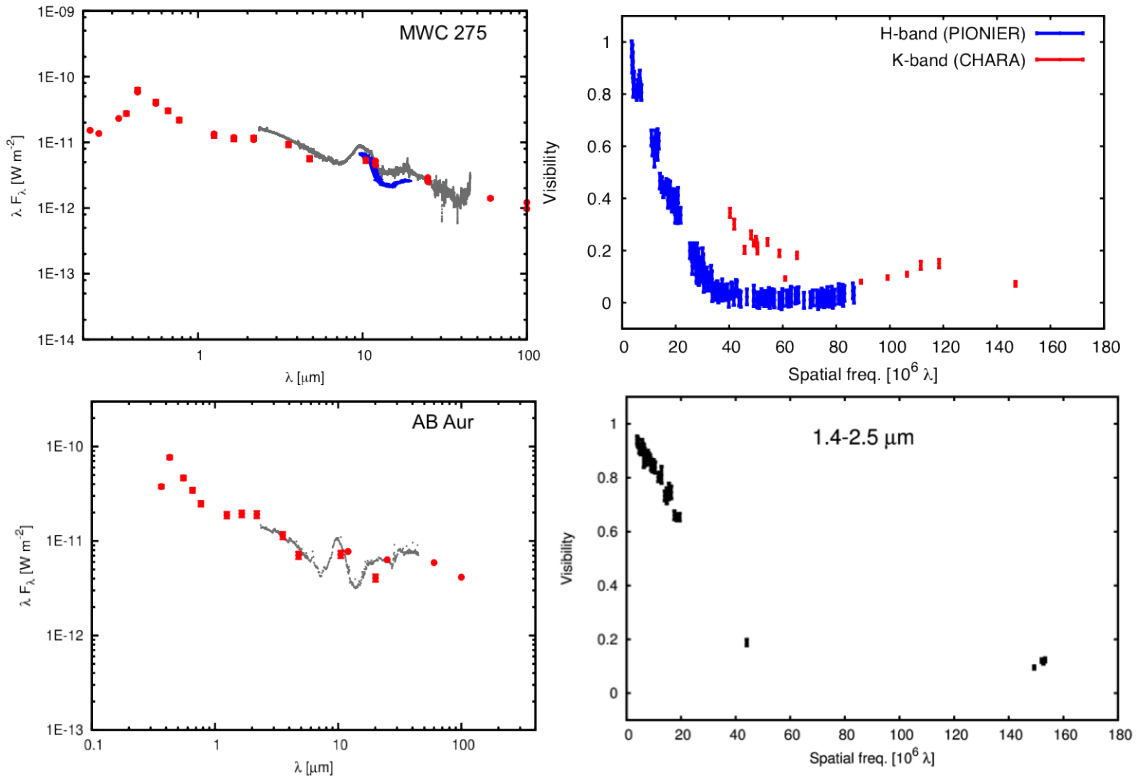

Figure 5.8: Observational data for MWC 275 (top) and AB Aur (bottom). SED data are from *ISO* (grey), *Spitzer-IRS* (blue) and photometric observations from various sources (red; see Table 5.1). The visibilities are from *CHARA* and *PIONIER*, with each data source presented independently for MWC 275 to demonstrate the wavelength dependence on the visibilities.

indicative of a larger emitting surface enabling emission at cooler temperatures which could be a consequence of more significant disc flaring (Meeus et al. 2001). The outer disc radius of the dust component of AB Aur is consistently found to be $\gtrsim$ 300 AU, with values of $\leq$ 300 AU (Grady et al. 1999), ~350 AU (Piétu et al. 2005; Lin et al. 2006), and ~360 AU (Eisner et al. 2004) having been reported. Observations in CO have revealed a much more extended gas disc, reaching ~615 AU (Lin et al. 2006), and an even greater envelope structure has been observed up to ~1300 AU (Grady et al. 1999). The dust disc of MWC 275 is consistently found to be smaller, with the radius of the dust component found to be $\leq$ 200 AU by Isella et al. (2007) and 240 AU by de Gregorio-Monsalvo et al. (2013). CO data tracing the outer gas disc radius by these authors find outer radii of 540 AU and 575 AU, respectively. A larger dusty disc has been found to reach ~540 AU from observations of scattered light by Tilling et al. (2012), matching the radius of the entire disc found by Isella et al. They were able to reconcile this difference by adopting a surface density profile with an exponentially tapered edge (see Hughes et al. 2008), and found emission dominating the inner 200–300 AU of the disc was consistent with their observations.

The most striking difference between the circumstellar discs of these two objects is the presence of a spiral structure in the disc of AB Aur (e.g. Corder et al. 2005; Piétu et al. 2005). The resulting non-homogeneous structure, compounded by the presence of an extended envelope, has made parameterisation of the disc geometry difficult. Disc inclinations have been reported at various values between 17° (Semenov et al. 2005) and 76° (Mannings & Sargent 1997). An inclination of $i < 45°$ was established by Grady et al. (1999) using scattered-light images which is consistent with the value of 39° derived by Piétu et al. (2005) from an interferometric study of AB Aur similar to that performed by Mannings & Sargent. Piétu et al. suggested the difference in inclination angle derived from their study and that of Mannings & Sargent was because emission from the continuum spiral in the disc dominates the total flux in their CO data, biasing the derived inclination towards higher values due to the spiral taking a non circularly-symmetric curved

structure. Piétu et al. note that due to this asymmetry inclinations down to ∼25° cannot be ruled out. Inclinations are still fairly uncertain but in general have been constrained to i ∼20°–30° (e.g. Eisner et al. 2003; Blake & Boogert 2004; Fukagawa et al. 2004), with some reports of ∼15° (e.g. Eisner et al. 2004; Semenov et al. 2005), particularly when considering the minimum values within the uncertainties. A higher inclination of 45°–65° was derived by Liu et al. (2005) from MIR interferometric observations taken at the MMT Observatory with the MIRAC-BLINC instrument. They attributed this inclination to the complex circumstellar structure of AB Aur rather than a true representation of the disc inclination.

The disc of MWC 275 is more inclined on the plane of the sky than that of AB Aur, and much better constrained. MWC 275 was included in the same sample as AB Aur by Mannings & Sargent (1997). Using the same method, they derived an inclination of 58°. Blake & Boogert (2004) found a consistent inclination of 60° ± 10° using direct imaging. More recent determinations have decreased slightly but are still consistent, e.g. $51^{\circ}{}^{+11^{\circ}}_{-9^{\circ}}$ (Wassell et al. 2006); 46° ± 4° (Isella et al. 2007); 48° ± 2° (T08a); 40° ± 10° (Benisty et al. 2010). We have maintained the disc inclinations used by Tannirkulam et al. (2008a, hereafter T08a) for MWC 275 and AB Aur of 48° and 21°, respectively, since the former is well-constrained as discussed above and the latter is a good compromise between values derived at ≳15° (e.g. Blake & Boogert 2004; Eisner et al. 2004; Semenov et al. 2005) and 20°–30° (e.g. Eisner et al. 2003; Fukagawa et al. 2004).

The disc mass $m_{\rm d}$ is the total mass of gas and dust in the disc. For AB Aur disc masses range between 0.007 $M_{\odot}$ (Lin et al. 2006) and 0.016 $M_{\odot}$ (Piétu et al. 2005). Intermediate values of 0.009 $M_{\odot}$ (Corder et al. 2005), 0.01 $M_{\odot}$ (Mannings & Sargent 1997), and 0.013 $M_{\odot}$ (Semenov et al. 2005) have also been derived. On the face of it the consistency of these values indicates that the determination of the disc mass is fairly robust; however, these assume a canonical gas-to-dust ratio of 100 in mass. Derived disc masses would be systematically offset if this assumption is untrue, and it certainly might not be the same for every object. For MWC 275, disc masses range between 0.028 $M_{\odot}$

Table 5.2: Stellar and disc parameters used in this study. References: (1) Natta et al. (2004); (2) Hillenbrand et al. (1992); (3) van den Ancker et al. (1998); (4) Tannirkulam et al. (2008a, see also the discussion in Section 5.3.2 for inclinations). Stellar radii were calculated using $T_{\rm eff}$ and $L_\star$. Disc masses were briefly examined using the models presented in Section 5.4, centred on values from the literature which are discussed in Section 5.3.2.

Parameter	MWC 275	AB Aur	Ref
$T_{\rm eff}$	9500 K	9772 K	(1) MWC 275; (2) AB Aur
$L_\star$	36 $L_\odot$	47 $L_\odot$	(1) MWC 275; (3) AB Aur
d	122 pc	144 pc	(3)
A_V	0.25	0.5	(3)
$M_\star$	2.3 $M_\odot$	2.4 $M_\odot$	(3)
$R_\star$	2.2 $R_\odot$	2.4 $R_\odot$	
i	48°	21°	(4)
$r_{\rm d}$	200 AU	300 AU	(4)
$m_{\rm d}$	0.03–0.10	0.007–0.016	Fitted

(Mannings & Sargent 1997) and 0.089 $M_\odot$ (Qi et al. 2011), i.e. up to an order of magnitude greater than AB Aur. Other determinations include 0.05 $M_\odot$ (Natta et al. 2004) and 0.07 $M_\odot$ (Tilling et al. 2012).

The stellar parameters that I have adopted for each of these objects are presented in Table 5.2. There appears to be some ambiguity in the temperature and thus radius of MWC 275, with a value of $T_{\rm eff} = 10,500$ K (corresponding to a radius of $\sim 1.7\,R_\odot$) given by Meeus et al. (2001). This value was also used in a study by Doucet et al. (2006). A much lower temperature of 9250 K was found from SED fitting by Montesinos et al. (2009) which, along with a luminosity calculated at 34.5 $L_\odot$, gives a radius of 2.3 $R_\odot$. I have maintained the value of 2.2 $R_\odot$ used by T08a. While SEDs at numerous inclinations are calculated by my models, I have used these only to comment broadly on the validity of the values in T08a given the range of values presented in the literature. The results to the visibility fitting are presented in Section 5.4.

5.4 Modelling refractory grain emission

The iterative procedure described in Section 2.2.4 is adopted for modelling the dust. Using this method, the dust is gradually added inwards starting from the outer regions of the disc.

The alternative method of sublimating the dust from the inner disc outwards is far more computationally expensive since the dust is very efficient at shielding stellar radiation, meaning that dust in an annulus outside of the inner rim is sufficiently cool to survive an the initial iteration, but as soon as the inner dust is sublimated the dust in this outer annulus becomes extremely hot and so also sublimates. The annuli in which the iterative sublimation process occurs are very thin, resulting in a considerably greater number of iterations to reach convergence.

The density structure of the disc is described using the α-disc formalism of Shakura & Sunyaev (1973). This describes a flared disc where the density ρ at some radial distance r and height z relative to the disc midplane is given by

$$\rho(r, z) = \rho_0 \left(\frac{r}{r_0} \right)^{-\alpha} \exp\left[-\frac{1}{2} \frac{z^2}{h(r)^2} \right]. \tag{5.2}$$

where $r_0 = 100$ AU. The scale height is given by

$$h(r) = h_0 \left(\frac{r}{r_0} \right)^{\beta}, \tag{5.3}$$

where α and β are fixed such that the surface density has a radial distribution of $\Sigma(r) \propto r^{-1.0}$. The effect that different α and β have on the density structure is discussed briefly in Section 5.5.1.

The disc is primarily composed of silicate grains, with an additional refractory component consisting of iron grains. The grain opacities are calculated under Mie theory, where the absorption coefficient of a given material is related to the complex refractive index. The real and imaginary parts of the refractive index for "astronomical silicate" grain sizes between 10^{-3} and $10^{3}\,\mu$m were taken from Laor & Draine (1993, see also Draine & Lee 1984). The complex refractive indices for iron grains between 10^{-1} and $10^{5}\,\mu$m were taken from Henning & Stognienko (1996).

An example density structure for MWC 275 is given in the top panel of Figure 5.9. The bottom panel shows a plot of silicate dust distribution on the left and the temperature gradient of the inner dust rim on the right.

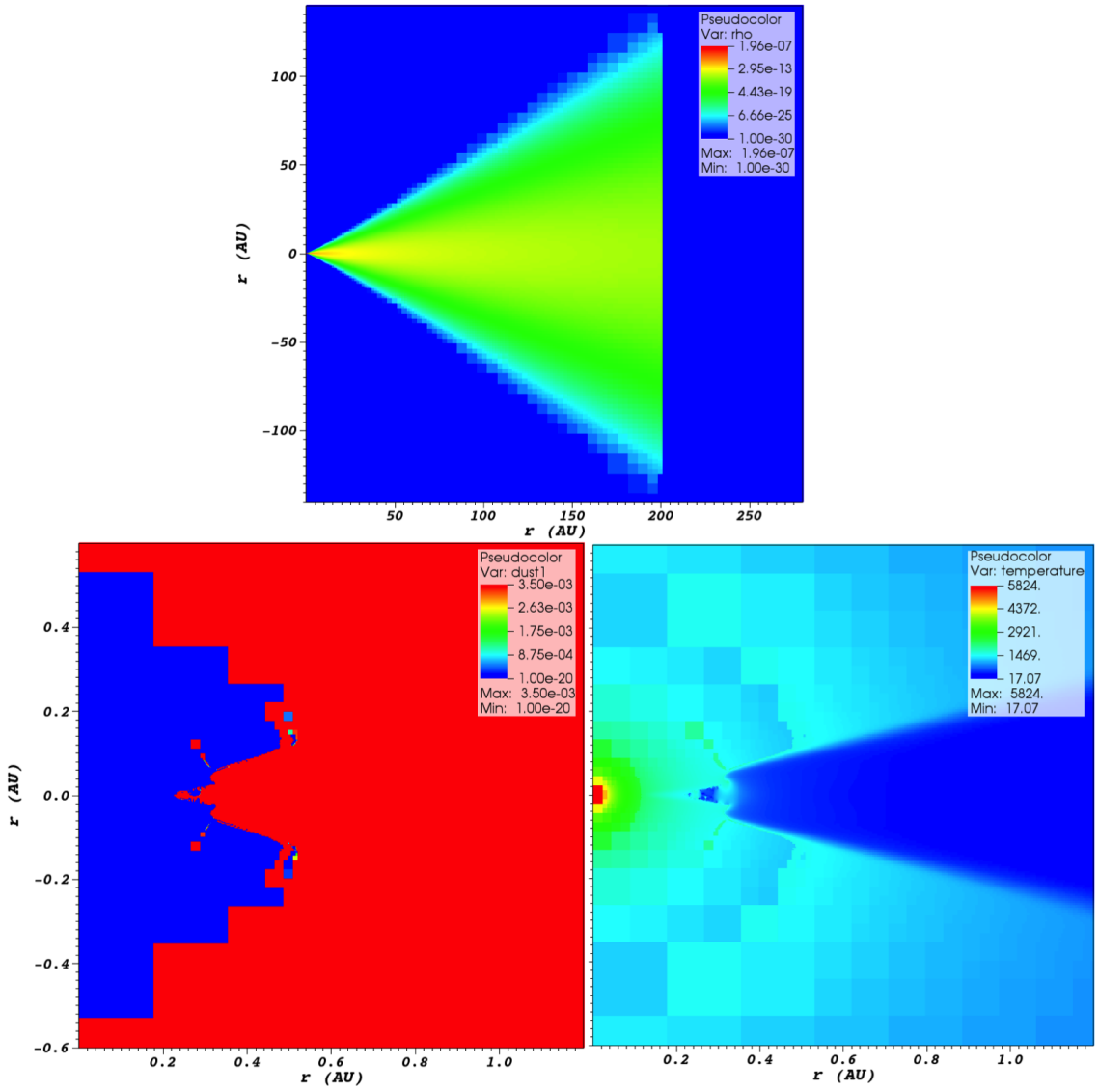

Figure 5.9: Distributions of various data sets from an edge-on view of the MWC 275 disc. Top: The density distribution of the disc material. Bottom left: The silicate dust distribution. Bottom right: The temperature structure of the inner part of the disc. Density and temperature scales are shown to the right of each plot.

5.4.1 Computing the visibilities

Visibilities are calculated by a pipeline (constructed by S. Kraus) which uses the images computed by TORUS at various wavelengths to convert the brightness distribution of the structure in the images to visibility as a function of spatial frequency. The pipeline first converts the pixel-scale information, in AU per pixel, in the images to an angular pixel scale, in milliarcseconds per pixel, using the distance from the observer to the object. Next it computes the visibility amplitude at the specific uv points that were sampled by interferometric observations, which are then plotted against the measured visibility amplitudes. A plot of measured visibility against modelled visibility at a given wavelength is produced to depict the amount of correlation between the observations and the model; the pipeline assumes that the disc plane is orientated along position angles taken from the literature for the objects being modelled to produce this plot. The visibility profile as a function of spatial frequency is computed along a number of different position angles, and the profile in the North-South direction is plotted against observational data for a broad comparison. For the objects presented here, visibility profiles at two different wavelengths are plotted in order to demonstrate the variation in the brightness distribution for observations made using different wavebands.

In addition to visibility profiles, the pipeline also produces plots of the SEDs calculated by TORUS at numerous inclinations along with the observational data collated from the various sources presented in Section 5.3.1

5.5 Results

Here I present the results of SED and visibility modelling for MWC 275 and AB Aur. I begin with a study of the effects that macroscopic disc parameters have on the SEDs, such as flaring and scale height, using these examples to fit the SED for MWC 275. I then present the best fitting disc parameters for AB Aur using the same method. This is followed by visibility fitting in order to constrain the properties of refractory grains in the

inner disc and to determine whether the sublimation temperatures required are sufficiently low for these grains to be a physically plausible source of inner emission.

5.5.1 SED fitting

The overall density structure of the discs modelled here are parameterised by the amount of flaring, defined by the β parameter given in equation 5.3, the scale height of the disc, h, and the disc mass, $m_{\rm d}$. These parameters describe the general geometry of the disc and can be fit using SEDs.

All of the models presented here assume a dust-to-gas mass ratio of 0.01, with $m_{\rm d}$ describing the total disc mass of gas and dust. A dust mass of $0.007\,{\rm M}_{\odot}$ is thus equivalent to a total disc mass of $m_{\rm d} = 0.7\,{\rm M}_{\odot}$; this distinction is explicitly drawn here since the literature varies between discussing disc masses and dust masses. The sensitivity of SEDs on dust mass is presented in Figure 5.10. All other parameters are constant across the models presented in this figure, with a scale height of 6, and a flaring parameter of 1.125. These parameters are discussed below. Increasing the dust mass causes the emission of thermal radiation to become more pronounced at long wavelengths. This effect becomes noticeable at wavelengths greater than $\sim 10\,\mu{\rm m}$.

Increasing the scale height of the disc affects the SED fairly uniformly across the entire dust-dominated part of the SED, as seen in Figure 5.11 (top). Increasing the flaring, however, results in more incident radiation intercepting the disc at larger radii relative to smaller radii, resulting in more emission from the colder dust. As a consequence of increased disc flaring, stellar radiation is more easily intercepted by the colder outer regions of the disc. This produces additional emission at longer wavelengths, as demonstrated in the SEDs presented in Figure 5.12. The top plot gives a direct comparison between discs with $\beta = 1.10$ and $\beta = 1.13$, showing the total SEDs produced by each model (solid lines), as well as the contributions of direct thermal emission from the dust (dashed lines) and scattered thermal emission (dotted lines). The differences between these two models are put into context in the bottom panel of Figure 5.12, where observational data for

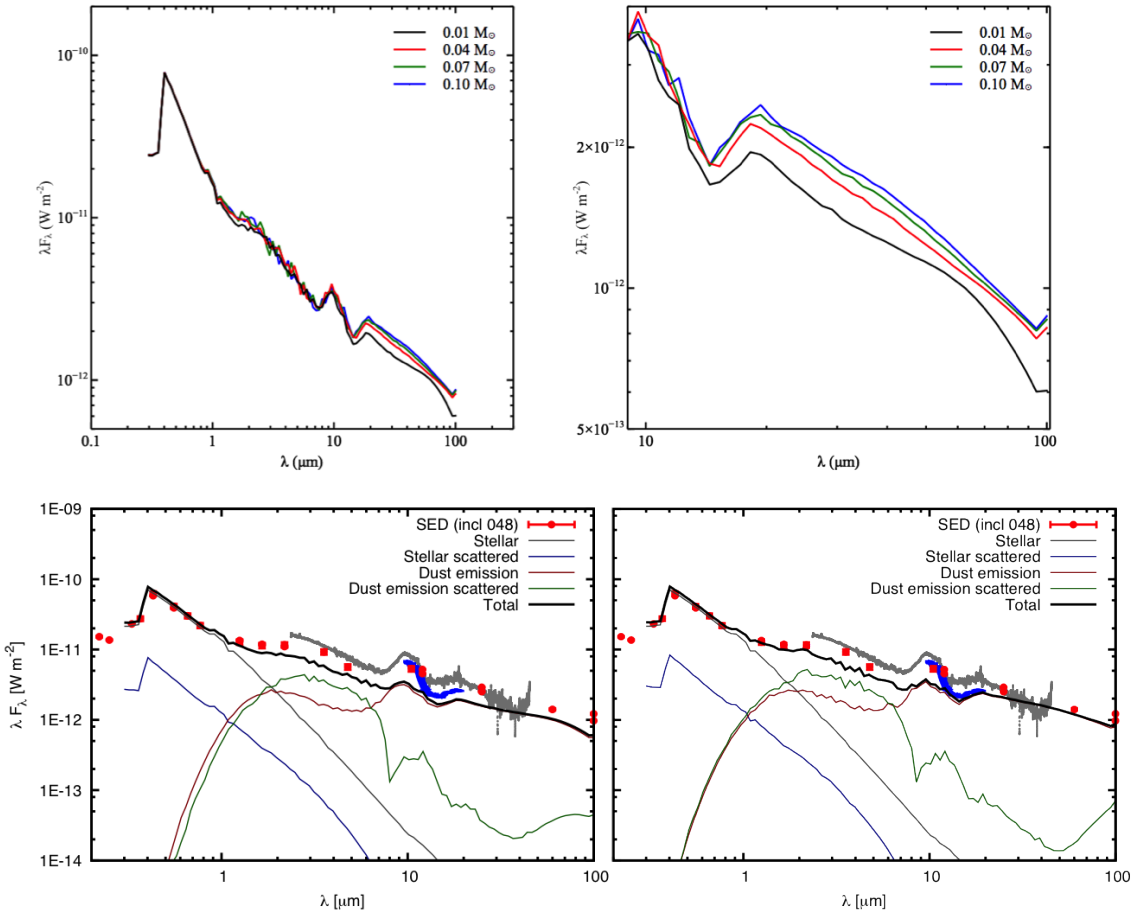

Figure 5.10: The effect of disc mass $m_{\rm d}$ on SEDs for MWC 275. Top: the total SEDs for various disc masses between 0.01 $M_\odot$ and 0.1 $M_\odot$ (left), with a close-up of the mid- to far-IR portion (right). Bottom: comparisons between models and data for $m_{\rm d} = 0.01\,M_\odot$ (low-mass, left) and $m_{\rm d} = 0.1\,M_\odot$ (high-mass, right), with the solid black line denoting the total SED. Coloured lines give the contribution of individual sources of emission to the total spectrum, as indicated in the key. 'Stellar' is the contribution from stellar radiation received directly by the observer, 'stellar scattered' is stellar radiation that has been scattered by the disc towards the observer, 'dust emission' is thermal dust emission from the disc, and 'dust emission scattered' thermal dust emission from the disc that has been scattered towards the observer. Disc mass affects the SED beyond ~10 μm, with larger disc masses producing more emission.

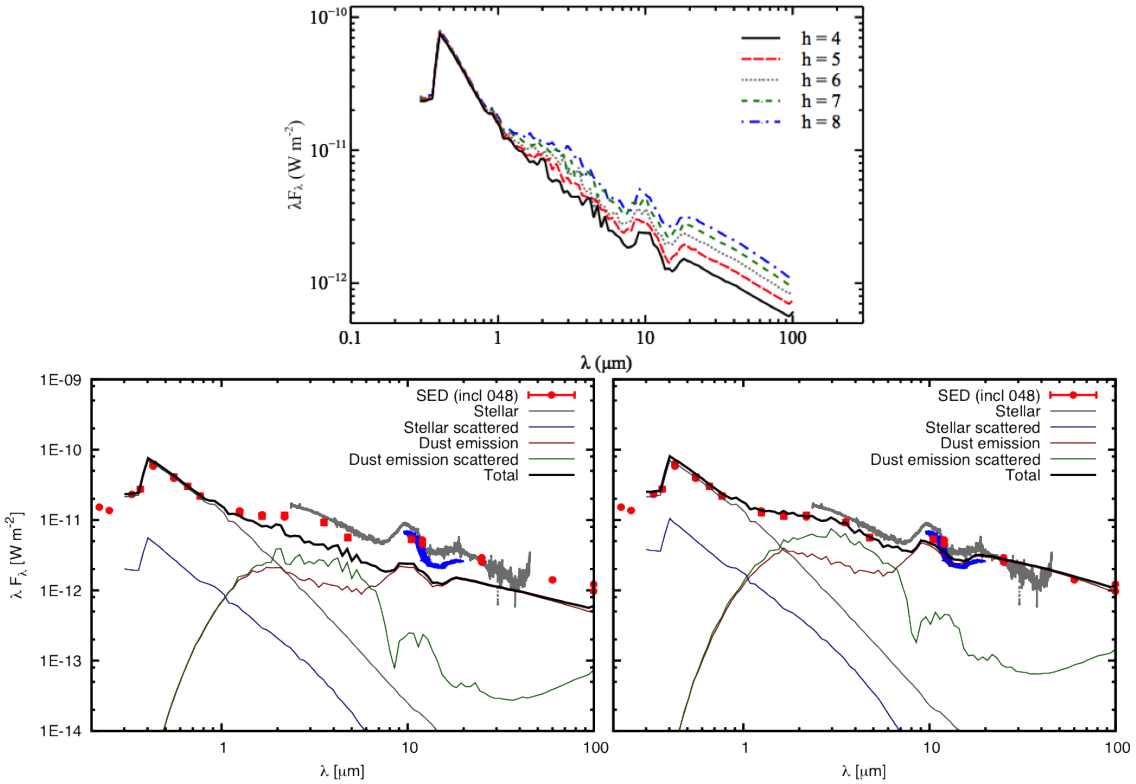

Figure 5.11: The effect of scale height h on SEDs. The scale height is shown to affect the SED right across the dust-dominated part of the SED, beyond ∼1 µm, with larger scale heights increasing the flux observed from the dust. Top: the total SEDs for scale heights of 0.4, 0.5, 0.6, 0.7, and 0.8 AU. Bottom: comparisons between models and data for h = 0.4 AU (the smallest of the modelled scale heights, left) and h = 0.8 AU (the largest scale height, right). The coloured lines in the bottom plots demonstrate the contributions from different sources of emission as described in 5.10.

MWC 275 is plotted with the β = 1.10 model on the left, and the β = 1.13 model on the right. The flux at $\gtrsim$ 100 µm is clearly underestimated in the β = 1.10 model when compared with the data, although the reverse is true at around ∼3 µm, where the flux calculated by the β = 1.13 model is underestimated. The reason for this is demonstrated by the density plots in Figure 5.13 which show the physical effect of β on the disc structure. A variation in the scale height affects the disc height uniformly across the structure, whereas the flaring parameter reduces the height in the inner regions while increasing it at large radii, resulting in a non-uniform change across the dust-dominated parts of the SED. Consequently, an increase in scale height causes the entire dust-dominated part of the SED to increase, but only the FIR region of the SED increases for increased flaring. The NIR region decreases due to the more concentrated dust distribution as a function of

height in the innermost regions of the disc for increased flaring.

The best fitting parameter set for the SED of MWC 275 using the parameters discussed above is one with $m_{\rm d} = 0.07\,{\rm M}_{\odot}$, $h = 8\,{\rm AU}$, and $\beta = 1.125$. SEDs with these parameters are plotted for various inclinations in Figure 5.14. The best fit across the SED has a whole is given by $i = 48°$, which has been plotted on the right-hand side of Figure 5.14.

The SED of AB Aur was found to be much harder to fit. The trend of the observations which showed a levelling-off at $\sim$ 1–2 µm was found to be reproduced for a model with $m_{\rm d} = 0.01\,{\rm M}_{\odot}$, $h = 6\,{\rm AU}$, and $\beta = 1.125$, shown in Figure 5.15 (right). However, the longer-wavelength portion above 20 µm is significantly underestimated in this model, and no other models in the present study have been found to provide a significant improvement. Since this is primarily a study on refractory grain emission, this discrepancy is not a cause for concern as the shorter-wavelength portions at which this interior material emits give a reasonable fit. As with MWC 275, these best fitting parameters are plotted over numerous inclinations in Figure 5.15 (left), yielding a best fitting inclination of $\sim$27°.

5.5.2 Visibility fitting

Using the models for MWC 275 and AB Aur that were adjusted to fit the SEDs, I computed the visibility profiles for these objects. The resulting profiles are plotted in Figure 5.16 (left) for a silicate sublimation temperature of 1500 K (e.g. Pollack et al. 1994; Chiang et al. 2001; Dullemond et al. 2001). The modelled visibilities produce strong lobes, indicating a sharp drop-off which is not consistent with the data. This sharp density cut-off is shown clearly in the images plotted on the right of this figure. In order for modelled visibilities to match observations, some form of additional emission interior to the silicate disc is required.

Iron is chosen to be the representative refractory grain here to enable direct comparisons where appropriate to the work of B10. The approach I have taken in this study is to see how high the iron sublimation temperature needs to be in order to produce the

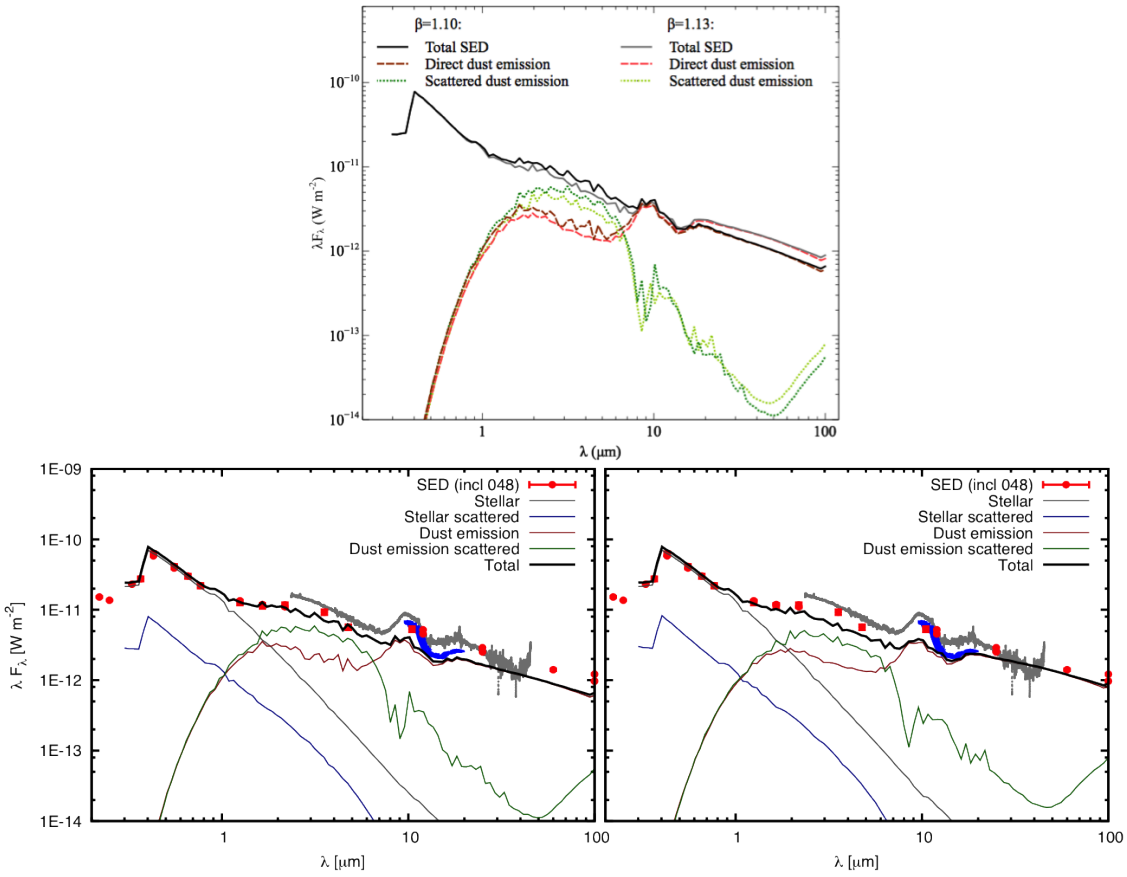

Figure 5.12: Direct comparison between SEDs for MWC 275 with $\beta = 1.10$ and $\beta = 1.13$ (top), including contributions to the SED from direct thermal emission from dust (dashed lines) and scattered thermal emission (dotted lines). Increasing the flaring has the physical effect of increasing the height of the disc at the outermost radii. A more flared disc is shown here to emit more strongly at long wavelengths, beyond $\sim$10 µm, compared to a less flared disc, since a more flared disc results in more stellar emission being intercepted by colder dust. The bottom left plot shows data compared with the $\beta = 1.10$ model (less flaring), and the bottom right plot shows a comparison between the data the $\beta = 1.13$ model (more flaring). The coloured lines in the bottom plots demonstrate the contributions from different sources of emission as described in 5.10.

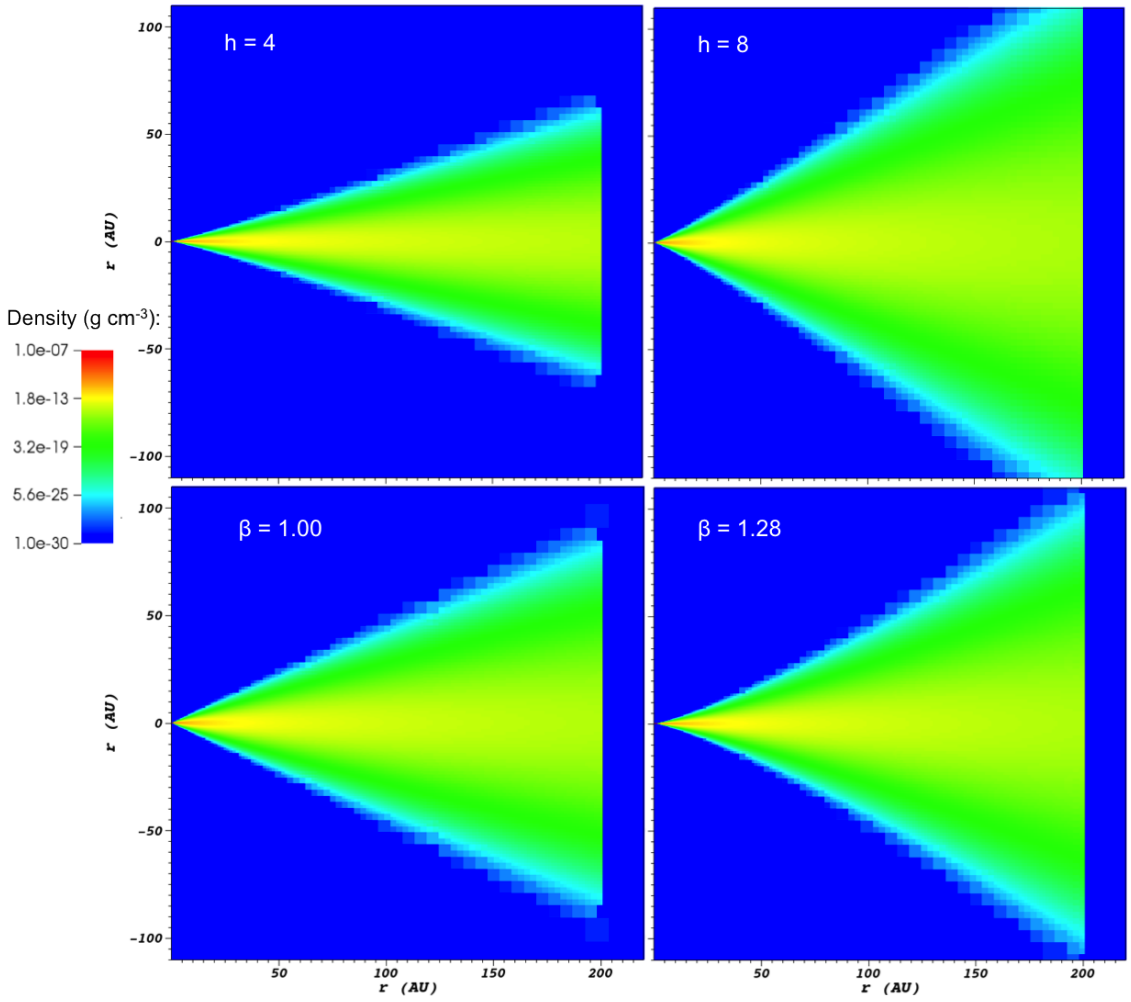

Figure 5.13: Density plots demonstrating the different effects on the disc structure when changing the scale height of the disc and flaring parameter β. The top panel shows the variation with scale height, with $h = 4$ AU on the left and $h = 8$ AU on the right, keeping β constant. The bottom panel shows $\beta = 1.00$ (left) and $\beta = 1.20$ (right), with constant h. The reason behind the different effects on SEDs is clear; there is a constant increase in the disc opening angle at all radii when increasing the scale height, but the inner region of the disc becomes more pinched and the outer reagion more flared when increasing β.

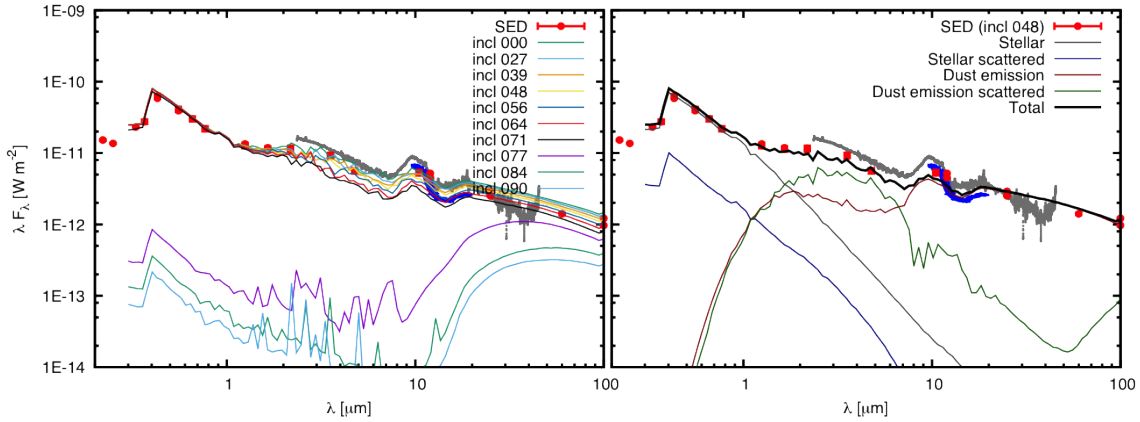

Figure 5.14: SEDs at different inclinations for the best fitting disc parameters of MWC 275 (left) and the overall best fit (right), with an inclination of 48°. The best fitting parameters for disc mass, scale height, and flaring parameter are $m_{\rm d} = 0.07\,{\rm M}_{\odot}$, $h = 8\,{\rm AU}$, and $\beta = 1.125$.

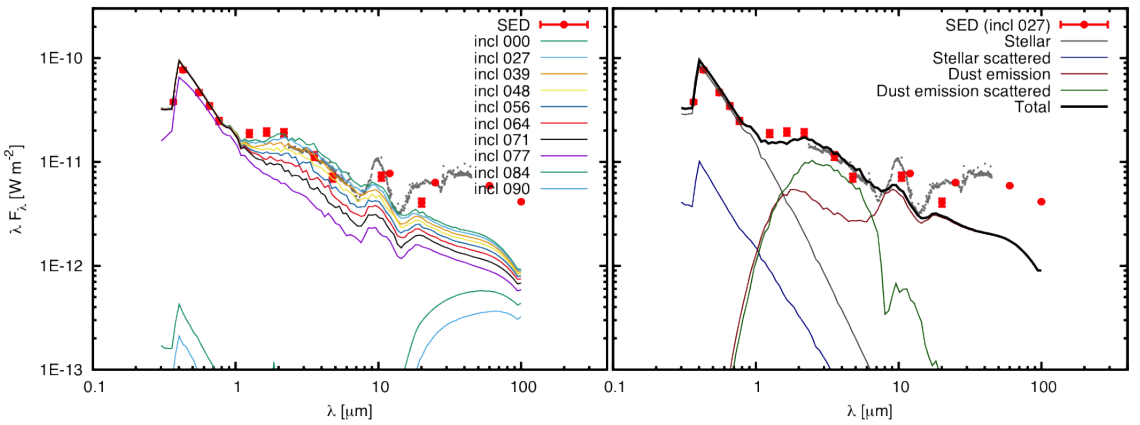

Figure 5.15: SEDs at different inclinations for the best fitting disc parameters of AB Aur (left) and the overall best fit (right), with an inclination of 27°. The best fitting parameters for disc mass, scale height, and flaring parameter are $m_{\rm d} = 0.01\,{\rm M}_{\odot}$, $h = 6\,{\rm AU}$, and $\beta = 1.125$.

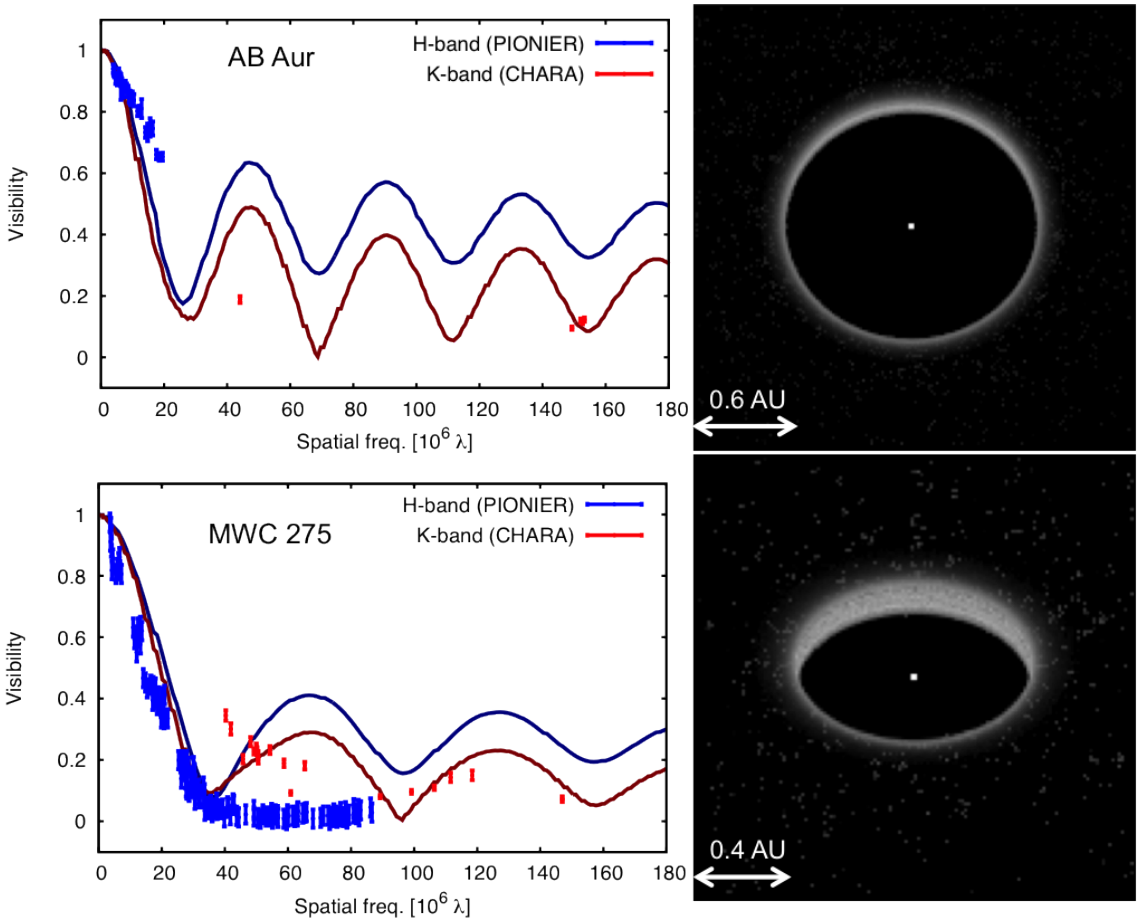

Figure 5.16: Visibilities and images for AB Aur (top) and MWC 275 (bottom). The nulls in the visibility curves demonstrate the need for inner emission, which is lacking in the images. There is evidence of a null in the observational MWC 275 K-band data, although the H-band data is clearly very smooth, representative of a much more Gaussian-like intensity distribution at this wavelength. The images on the right are calculated at 2.45 µm.

result of B10 that refractory dust alone is able to produce sufficient inner rim emission. B10 found that sublimation temperatures as high as 2300 K within 0.1 AU were required to produce sufficient emission, and it was noted that this temperature could be too high for many refractory species. Initial models here were calculated with an extreme iron sublimation temperature of 2500 K with the aim of reducing the temperature down towards a more realistic value.

The ratio of the total dust grain mass to the total mass of material (i.e. gas and dust) in the disc is given by the grain mass fraction. The mass fraction of a specific grain type is denoted by f_{X}, where X is the grain type. The effect that different mass fractions of iron grains have on the visibilities is shown in Figure 5.17. These models are computed with two populations of silicate grains, between 0.001–0.01 µm and 1–2 µm, and one population of iron grains, with sizes between 0.2–2.0 µm. An iron fraction of $f_{\mathrm{Fe}} = 1 \times 10^{-9}$ is not enough to produce sufficient emission to affect the visibilities significantly. How little the iron contributes to the intensity when at this fraction is evident in the images presented in the right-hand column of Figure 5.17; while the inner iron rim is still noticeable, emission between this and the inner silicate rim is lacking. The visibilities improve with increasing iron mass fractions but an inner refractory rim only exists up to mass fractions of around $f_{\mathrm{Fe}} = 1 \times 10^{-8}$. Beyond this value, the refractory grains and silicate grains couple together, and the results are no longer in the paradigm of inner refractory grain emission. Thermal coupling is discussed further in Section 5.7. Significant refractory grain emission is present over just one order of magnitude, with values either side of the range producing either not a high enough number density of iron grains to emit sufficiently, or so much iron that it shields the silicates and they couple together. The fine-tuning required to achieve sufficient emission from iron grains suggests that an inner rim consisting solely of refractory grains is unlikely to explain observations. This same coupling effect occurs for AB Aur for dust fractions beyond $f_{\mathrm{Fe}} = 1 \times 10^{-7}$, with the separate iron emission no longer present for mass fractions of $f_{\mathrm{Fe}} = 5 \times 10^{-7}$. The iron contribution almost disappears when the dust fraction is reduced to $f_{\mathrm{Fe}} = 1 \times 10^{-8}$.

Visibilities and images for $f_{\rm Fe} = 1 \times 10^{-7}$ and $f_{\rm Fe} = 5 \times 10^{-8}$, the two fractions modelled for which the refractory grains were found to cause some filling in of the inner disc, are plotted in Figure 5.18.

Adopting a value of $f_{\rm Fe} = 1 \times 10^{-7}$, additional models were run for AB Aur in order to examine how significant the effect of reducing the sublimation temperature is on the visibility profile. Results are plotted in Figure 5.19. This figure demonstrates that incredibly large increases in temperature are necessary to produce relatively small changes in the visibility profile. An iron sublimation temperature of 2000 K, presented in the top panel of Figure 5.19, produces a refractory grain rim with an inner radius of about 0.45 AU. This is the value that B10 determined for the radius of the silicate rim, with an iron rim four times closer in towards the star. While the visibility profile is a significant improvement on the profile calculated for no refractory emission at all (see Figure 5.16), the lobes are still significant, with four lobes present in the H-band. Increasing the temperature by 200 K begins to smooth the profiles at spatial frequencies beyond 120 m/µm, with the inner refractory grain radius decreasing to 0.35 AU. Further increasing the sublimation temperature to 2600 K (bottom panel of Figure 5.19) produces an inner rim at 0.23 AU, with a smooth visibility profile at spatial frequencies beyond 100 m/µm. These results demonstrate the difficultly in finding a good fit to the visibilities using the refractory grain hypothesis; the sublimation temperature has been increased to values significantly higher than the temperatures found by B10, who found that even the temperature derived from their models were high. Even with increasing the iron sublimation temperature to 2600 K, the resulting inner emission is still not sufficient to smooth the visibility profile entirely.

5.6 Discussion

Past efforts on modelling the inner emission of Herbig Ae/Be circumstellar discs have focussed strongly on gas as either the partial or entire opacity source (e.g. Eisner et al. 2007; Tannirkulam et al. 2008b). While such emission has been found to show potential in providing this opacity, opacity bands for molecules such as CO and H_2O are expected

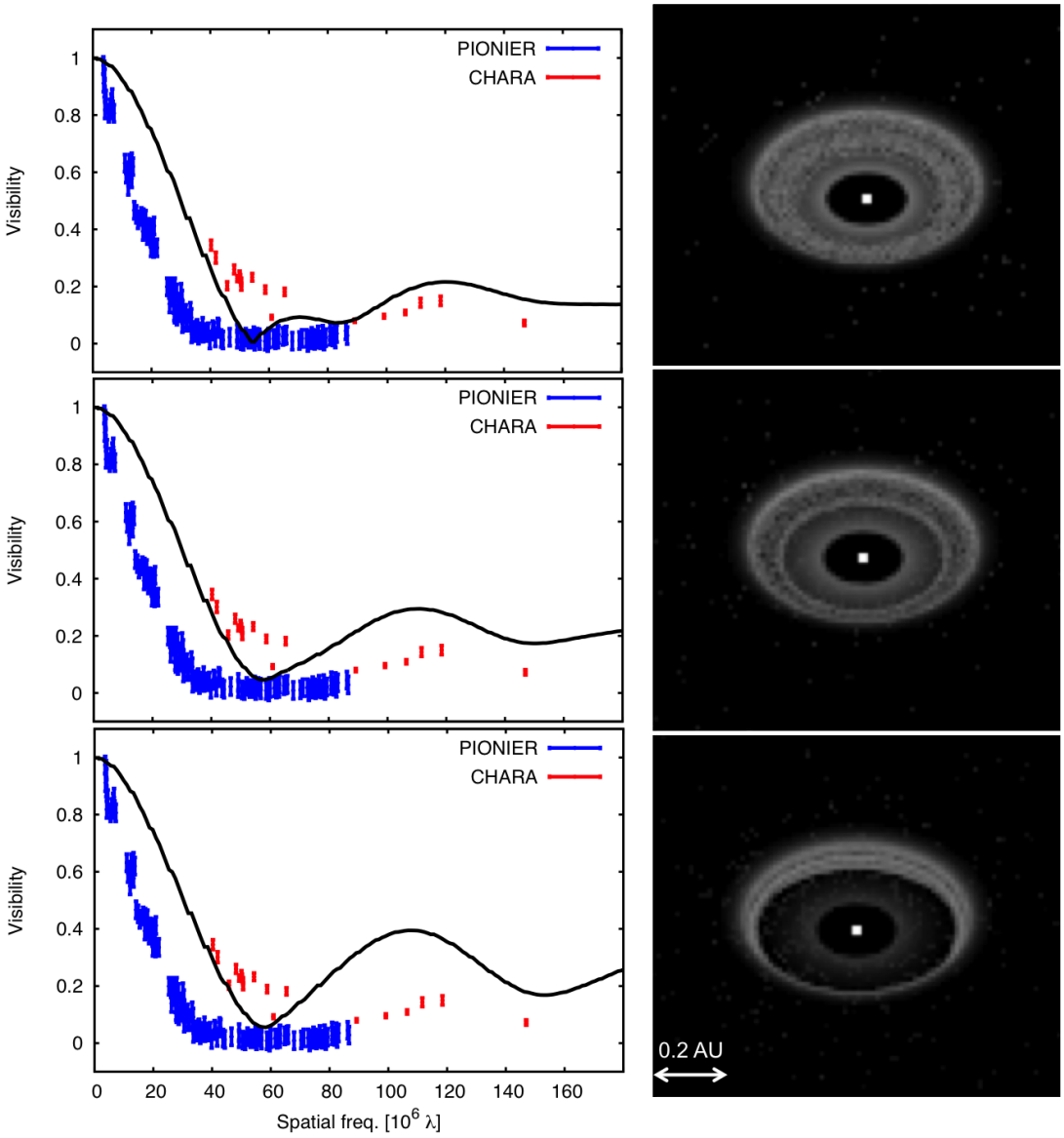

Figure 5.17: Images (calculated at 1.45 µm) and visibilities (calculated at 2 µm, intermediate to the *H*- and *K*-bands) of MWC 275 demonstrating the effect that various iron mass fractions have on the visibility curves. $f_{\rm Fe} = 1 \times 10^{-8}$ is shown on the top, decreasing downw ito 5×10^{-9} (middle) and 1×10^{-9} (bottom). This lowest value is clearly unable to produce enough emission to fill in the inner disc. The best fit is therefore given by the $f_{\rm Fe} = 1 \times 10^{-8}$ model, for which a significant iron rim is present in the image.

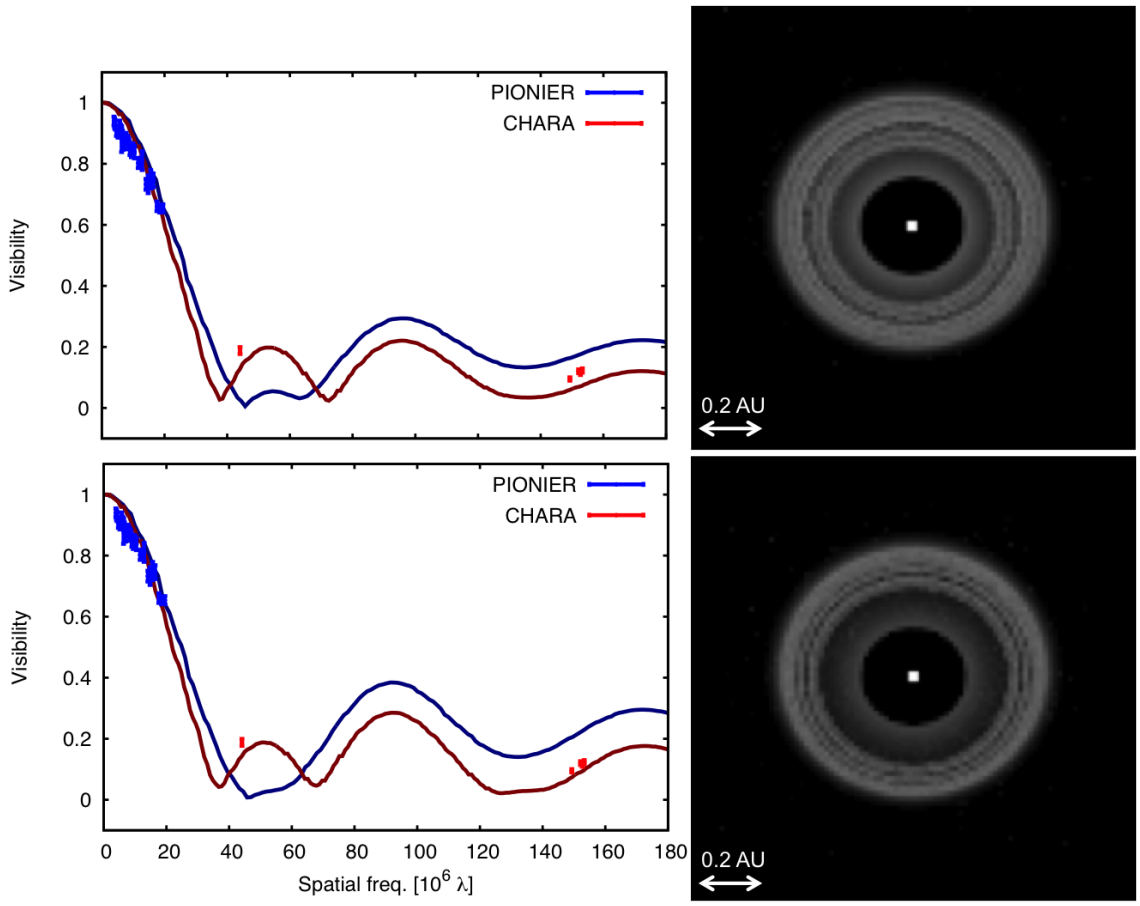

Figure 5.18: Visibilities and images for AB Aur with $f_{\rm Fe} = 1{\times}10^{-7}$ and $f_{\rm Fe} = 5{\times}10^{-8}$. The visibilities in particular are very similar between these models. Visibilities are calculated at 1.54 µm (blue) and 2.4 µm (red). Images are calculated at 1.45 µm.

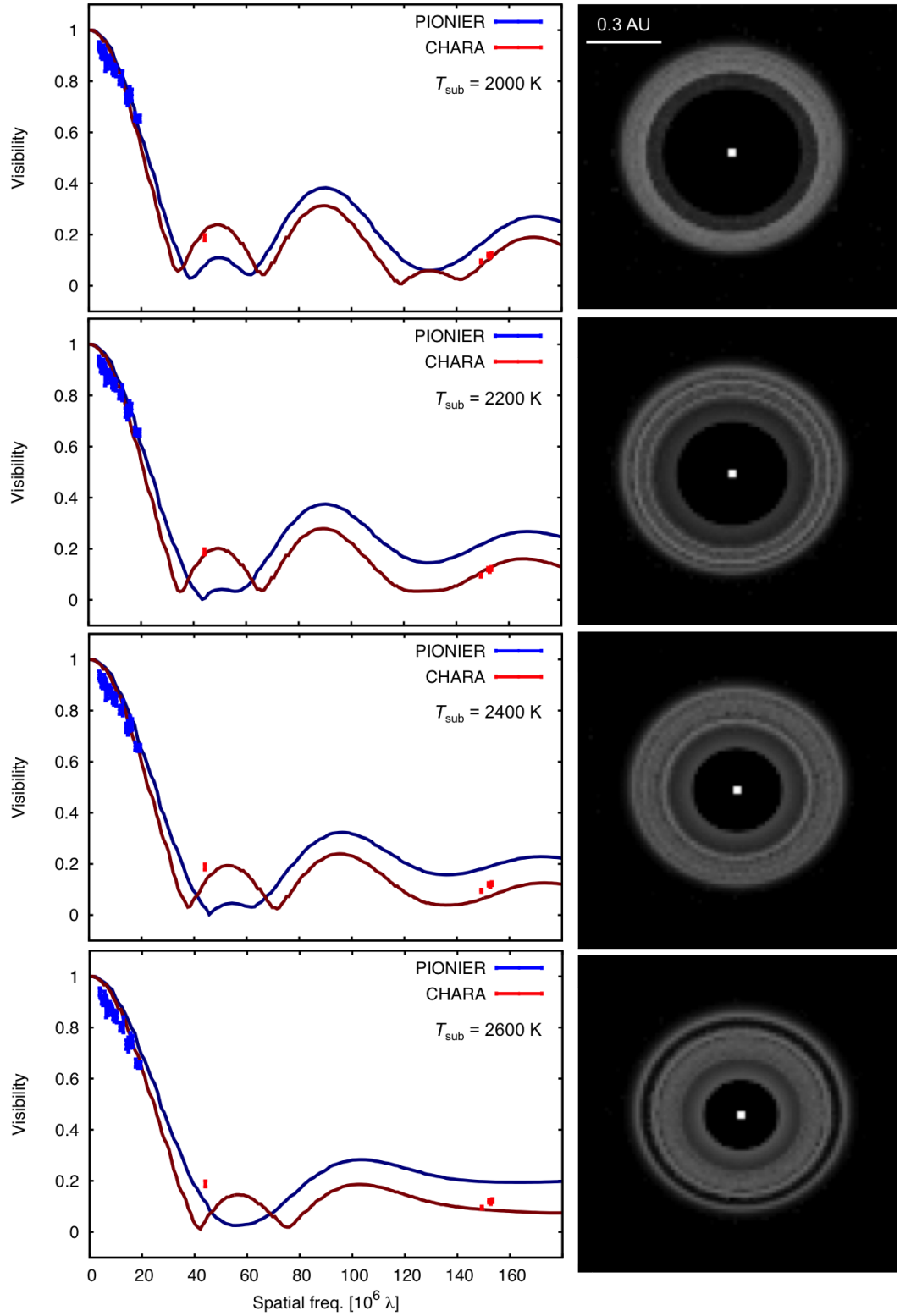

Figure 5.19: The effect of sublimation temperature on inner disc structure for AB Aur. An inner iron ring is observable at $T_{sub} = 2000$ but the inner portion of the disc is too large for sufficient filling in to occur. The inner hole decreases between each model, although three lobes are still prominent in the visibilities at both wavelengths up to $T_{sub} = 2400$. Visibilities are calculated at 1.54 µm (blue) and 2.4 µm (red). Images are calculated at 1.45 µm.

to be present in the SEDs, which are not observed. The idea that the smooth inner emission observed could be produced by refractory grains, as proposed by B10 in a study on MWC 275, is attractive since the SED will consist of continuum emission, removing the issue of molecular bands. This hypothesis has been investigated further here. B10 found that their model was reasonably successful; for an interior iron rim extending from 0.10–0.45 AU at a temperature of 2100 K, the very inner regions of the circumstellar disc became sufficiently dense to produce an additional source of emission. However, their model relies on numerous assumptions such as the temperature of the dust grains and the shape of the rim. I have used radiative equilibrium models that calculate the sublimation radii of silicates and iron grains self-consistently in an effort to determine the sublimation temperature required to produce sufficient opacity. While significant interior emission may be produced by refractory dust in order to produce smoother visibility profiles compared to instances where no refractory grains are present, the results presented here demonstrate that temperatures in excess of 2600 K are required to smooth the profiles entirely. These models therefore demonstrate that the idea that inner disc emission is produced by refractory grain emission alone is highly unlikely.

I have found that the structure of the inner discs of both MWC 275 and AB Aur are extremely sensitive to the relative mass of refractory grains in the disc, possibly restricting the suitable mass fractions to just one order of magnitude; any more and the silicates become shielded by the refractory grains, any less and the effect is not prominent enough to produce sufficient emission. I obtained a best fitting iron grain mass fraction of $f_{\rm Fe} = 5 \times 10^{-9}$ for MWC 275 and $f_{\rm Fe} = 1 \times 10^{-7}$ for AB Aur. These were calculated with an iron grain sublimation temperature of 2500 K, which is likely to be too high. However, lower temperatures were found to still produce significant lobes in the visibility curves, as demonstrated in Figure 5.19.

Comparisons between the images and visibilities obtained by B10 and in this study for MWC 275 are shown in Figures 5.20 and 5.21, respectively. Figure 5.20 includes a comparison of the extent of the refractory grain contribution to the disc emission between

the two models. The B10 models produce refractory emission over a larger radial extent, which is particularly important in the very innermost region. This discrepancy is even greater when considering the fact that the inner rim of the B10 models has a temperature of 2100 K, whereas the comparison images from this study were calculated with a sublimation temperature of 2500 K, yielding an inner rim radius of ∼0.18 AU; nearly twice that of the previously determined 0.10 AU.

The best fitting visibilities determined here, using a more comprehensive model than done so previously, do not at present fit sufficiently well to add significant weight to the hypothesis that the emission observed interior to the silicate disc in HAeBes is due to refractory grains. The range in which the value of the iron mass fraction falls between having no effect on the visibilities to completely shielding the silicates has taken place across just over one order of magnitude. This raises questions as to the likelihood that the dust properties of circumstellar discs would be sufficiently fine-tuned for the refractory dust to emit at the level needed for this filling-in while remaining decoupled from other species. This conclusion has been independently reached by Kama et al. (2009) who performed Monte Carlo radiative transfer models to study the effect that different grain species and sizes have on the structure of the inner rim in general protoplanetary discs. They found that "sublimation-based differentiation ... is unlikely" due to the fine-tuning of grain properties required and noted that simultaneous fitting of SEDs and visibilities is required in order to study the dependence of the inner rim geometry on grain type further.

5.7 Silicate and refractory grain coupling

It is possible to have a situation where there is a mixture of grains present in which the refractory grains enable the silicate grains to exist at radii closer in to the star than the classical silicate rim radius. Complete shielding occurs when the iron grain mass fraction reaches $f_{\mathrm{Fe}} \sim 5 \times 10^{-8}$, as shown in Figure 5.22 (top), in which a reasonable fit to the CHARA data is achieved. At this point there is no longer a distinction between the inner iron rim and the silicate disc. Shielding changes the temperature distribution so that the

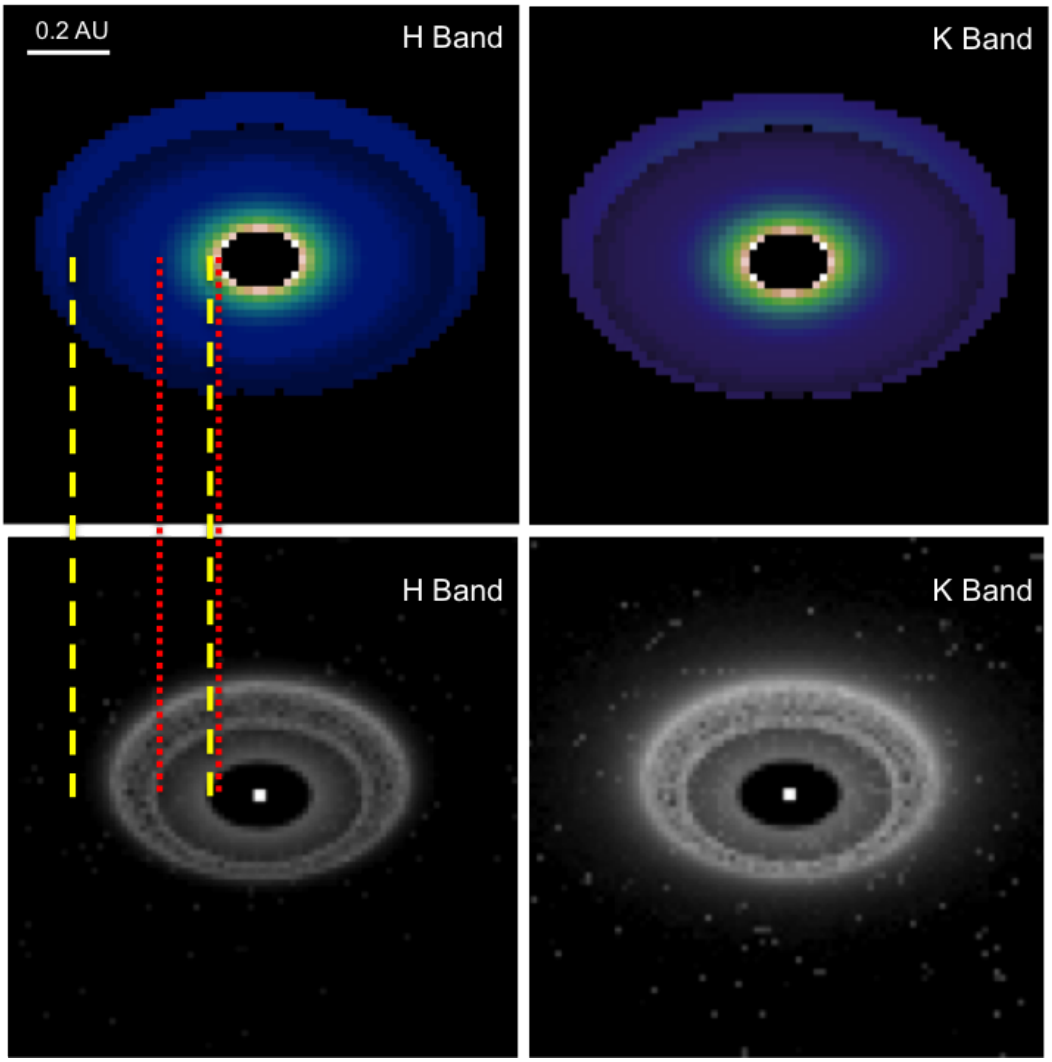

Figure 5.20: A comparison between the images in the *H*- and *K*-bands (left and right, respectively) for MWC 275 produced by B10 (top) and in the study presented in this chapter (bottom). Dotted red lines denote the extent of the refractory grain contribution to the inner disc calculated in this study, and dashed yellow lines denote the extent of the refractory grain contribution in the work of B10.

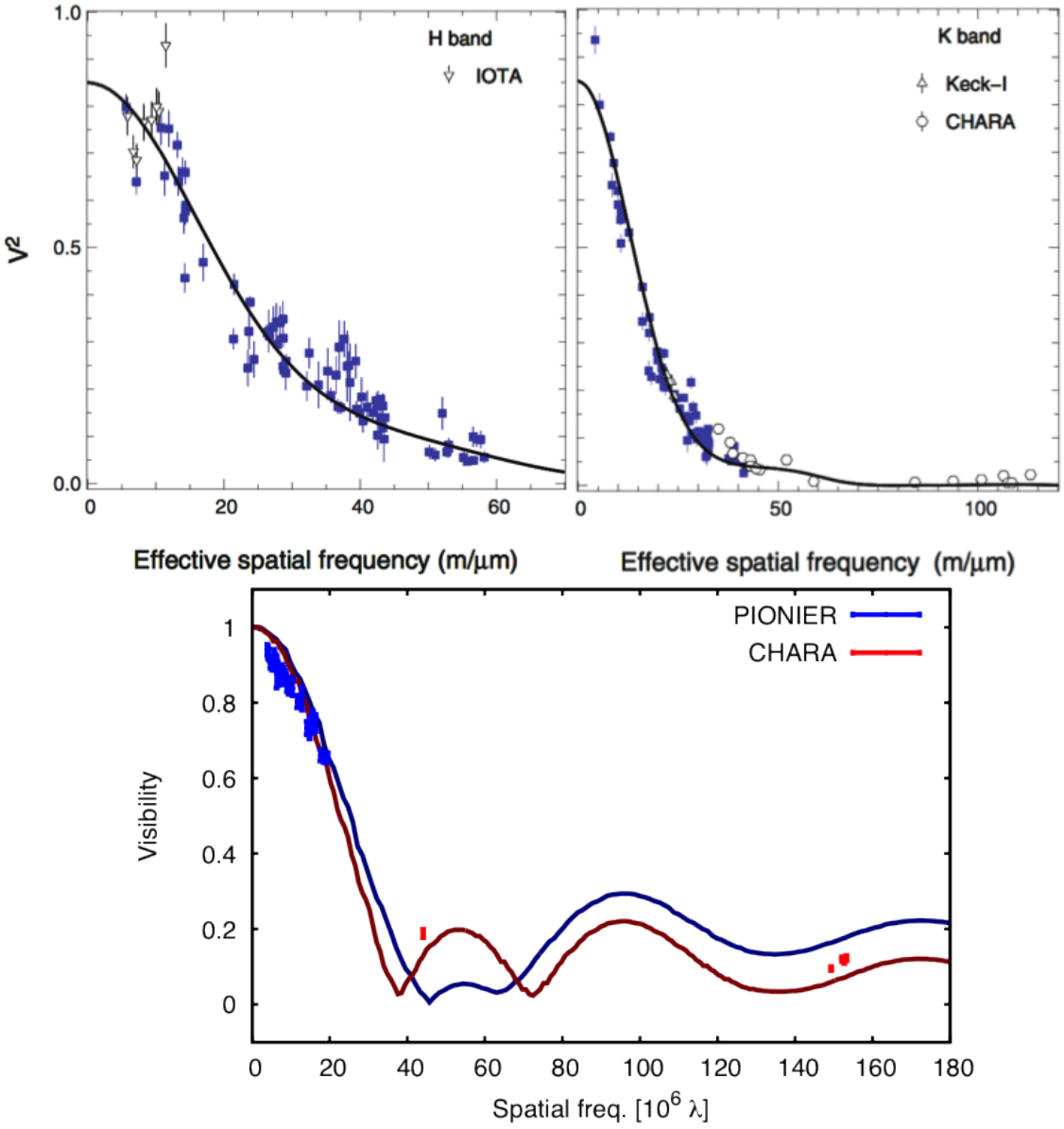

Figure 5.21: A comparison between visibilities in the *H*- and *K*-bands produced by B10 (top left and top right, respectively) for AB Aur and in the study presented in this chapter (bottom). The visibility curves take a much more Gaussian form in the B10 models. While refractory grain emission significantly improves the fit when compared to discs with no refractory grains, they alone have not been found to be sufficient in this study to reproduce observed visibilities.

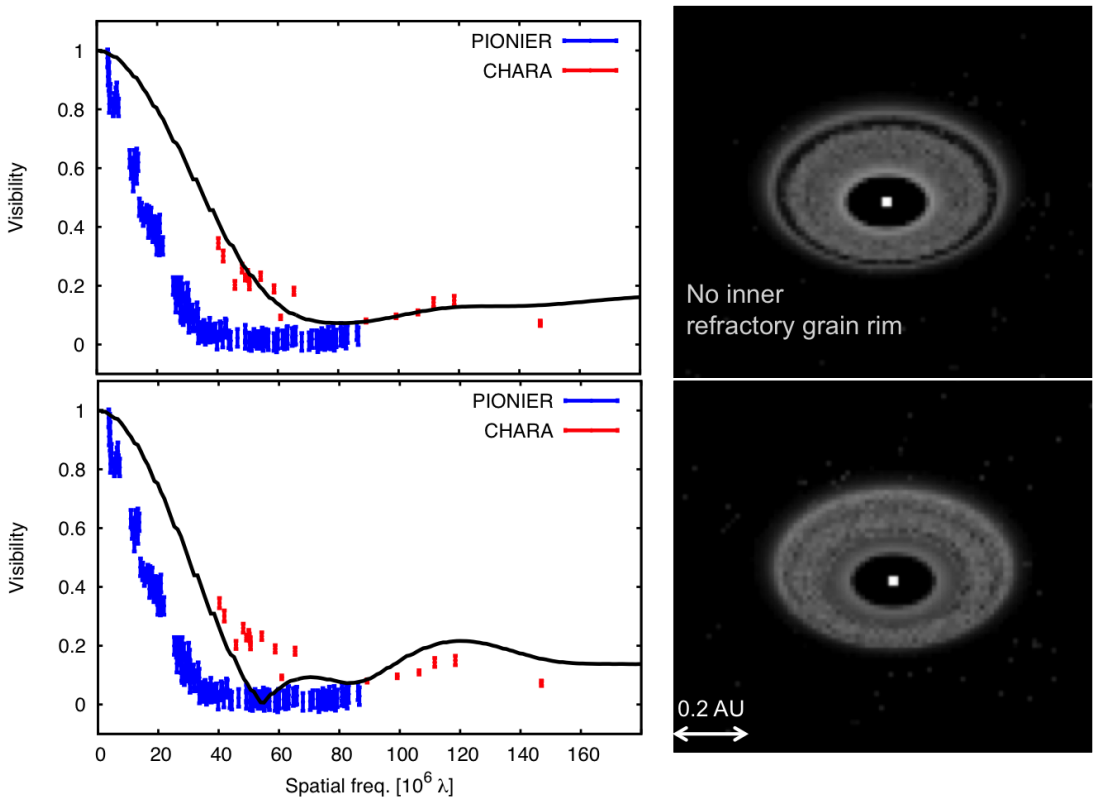

Figure 5.22: Images (calculated at 1.45 µm) and visibilities (calculated at 2 µm, intermediate to the *H*- and *K*-bands) of MWC 275 demonstrating the effect of grain shielding. $f_{\mathrm{Fe}} = 5 \times 10^{-8}$ is shown on top with $f_{\mathrm{Fe}} = 1 \times 10^{-8}$ on the bottom. The visibility curve for $f_{\mathrm{Fe}} = 5 \times 10^{-8}$ fits the CHARA data well, producing a smooth curve across all spatial resolutions. The corresponding image on the right shows there is no iron rim present. The iron and silicate grains have become coupled and so the iron grains are no longer is no longer producing an inner rim.

temperature of the silicate dust is cooler further in towards the star; the silicate dust is able to survive at smaller radii, and the two dust species are entirely coupled together. The effect of refractory grain shielding is shown more clearly in Figure 5.23, in which temperature and dust distributions are plotted for $f_{\mathrm{Fe}} = 5 \times 10^{-8}$ and $f_{\mathrm{Fe}} = 1 \times 10^{-8}$. Higher-temperature material is able to penetrate much further in towards the star in the former model, with no obvious boundary between the inner silicate and iron rims in the right-hand dust plots.

While I have been unable to produce results that support the idea proposed by B10 of refractory grain emission providing the inner disc opacity required to match observations, I have found that dust coupling is likely to be a more plausible scenario. A key

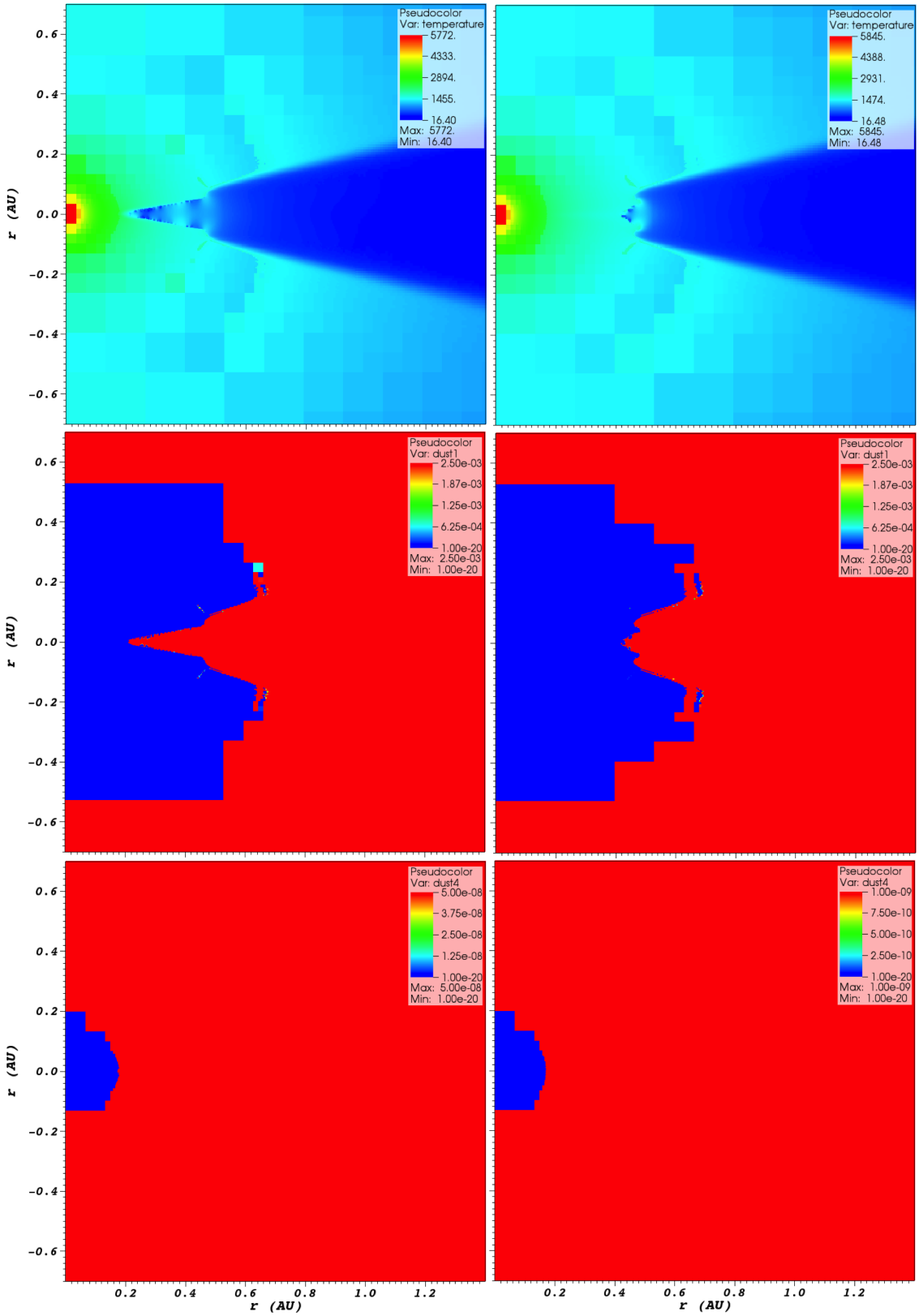

Figure 5.23: The effect of shielding by refractory grains in the circumstellar disc of MWC 275. Temperature (top), silicate grain (middle) and refractory grain (bottom) distributions are plotted for $f_{\rm Fe} = 5 \times 10^{-8}$ (left) and $f_{\rm Fe} = 1 \times 10^{-9}$ (right). The silicate disc of the 5×10^{-8} model reaches much further in towards the star since the silicates are shielded by the iron, removing the inner iron rim observed in the 1×10^{-9} model.

assumption in the work of B10 is that an inner refractory grain rim is present which independent of the silicate grains. In the models presented here, cooling due to the refractory grains is sufficient to bring the temperature of the silicate grains down so that one single rim is produced. This enables dust of different species to couple and fill in the inner region of the disc beyond the classical silicate rim radius, from which sufficient radiation is emitted to reproduce the observed visibility profiles. The results presented in this chapter demonstrate that there is a complex interplay between the shielding effect of the refractory grains and their emission as an individual species, separate from the silicates. This puts tight constraints on the abundance of any refractory grains that are present. The possibility that silicate dust shielded by refractory dust could produce this inner emission is certainly a result worthy of further study.

The best fitting model calculated here requires an iron grain mass fraction of $\sim 5 \times 10^{-8}$ with a sublimation temperature of $\sim$ 2500 K. At the moment it is not clear that this is a physically reasonable set of parameters for refractory grains. There are not currently strong depictions of the abundances, sizes, or temperatures of refractory grains in circumstellar discs in the literature. A focus needs to be brought on dust grain growth for refractory grains along the lines of calculations performed in Zubko (1998), and experimental work on the sublimation temperatures of different grain species (e.g. Pollack et al. 1994; Henning & Stognienko 1996). If the abundances required by the models presented in this chapter can be shown to be reasonable from grain formation models, and if these high sublimation temperatures can be found from experimental work, then silicate shielding by refractory grains could be a plausible alternative to refractory grain emission alone.

Chapter 6

Conclusions and future work

The aim of this thesis has been to test the hypothesis of magnetospheric accretion relating to Classical T Tauri stars, and the source of emission in the inner regions of Herbig Ae circumstellar discs. Specifically, these studies focussed on modelling the Classical T Tauri star AA Tau as a test case for the magnetospheric accretion paradigm, and explored refractory dust as a source of emission in the Herbig Ae objects MWC 275 and AB Aur. These studies have used, but by no means exhausted, the capabilities of the TORUS radiative transfer code to model a wide range of phenomena, from accretion streams to disc winds to thermal dust emission and more. These calculations are incredibly complex, with subtleties that can easily be overlooked and unappreciated by a non-experienced user, for instance methods of AMR refinement for different structures, discussed in Section 3.5, and the outwards-in method for dust sublimation, discussed in Section 5.4.

A summary of my major findings is as follows:

- I have produced a self-consistent magnetospheric accretion model for AA Tau and found that photometric modelling constrains the height of the warp. This will be an important constraint on future MHD modelling on of the star-disc interaction, particularly when taking the warp height alongside magnetic field measurements.

- I have produced the first three-dimensional dipole offset line profile models showing how the simple geometric picture of AA Tau fits with observations. This is the first

attempt at time series fitting, and has demonstrated how line profiles vary depending on the position of the disc warp and accretion shock.

- I have, for the first time, used self-consistent models to test the hypothesis of refractory grain emission as a source of inner disc emission in Herbig Ae stars. I have found that the temperature required is significantly higher than that expected for the refractory grains under consideration here. I have discovered that refractory grains shielding the silicates may be a more plausible method of producing inner disc emission in the objects modelled here.

These key results are expanded upon in the following sections, and I also identify avenues of future work relevant to the ideas that I have explored that are worth investigating further.

6.1 Magnetospheric accretion in classical T Tauri stars

Photometric observations of classical T Tauri stars have now shown that periodic dips occur in the light curves of about 30 per cent of these objects, although this is a relatively recent result Alencar et al. (2010). The archetypal CTTS demonstrating this photometric behaviour is AA Tau. Photometric monitoring by Bouvier et al. (1999) yielded fairly regular light curves across all wavebands, indicating that this variation was to do with material obscuring the photosphere rather than photospheric spots. Spectroscopic observations (e.g. Bouvier et al. 2007) are also variable with a similar periodicity as the photometry, that tend to be described as 'quasi'-periodic due to intermittent 'quiet' phases when not much activity is observed. Line profiles are indicative of both infall and outflow, which when taken with this variability, are consistent with the theory of magnetospheric accretion. In this, a stellar magnetic dipole truncates the circumstellar disc and matter accretes onto the star via the field lines. For stars with dipoles inclined to their rotation axis, a warp will form in the disc of the star, and it is this which obscures the photosphere periodically, as a result of rotation of the disc I have extensively and robustly tested this

theory, performing a broad parameter search in order to examine certain features of this phenomenon thoroughly.

The numerical method that I used is described in detail in Chapter 2. In summary, once the user-defined inputs are read in, the code sets up the required microphysics, adds the geometry of the system being modelled to the grid, begins the AMR refinement process, iteratively solves the equations of radiative transfer and statistical equilibrium and outputs the required data. The focus of Chapter 3 was to use a simplified version of the model, which is calculated under the assumption of local thermodynamic equilibrium, to simulate the geometry of the circumstellar environment of AA Tau required in order to reproduce the observed variations. The disc warp is parameterised by the outer magnetosphere the aspect ratio of the warp, and the angle by with the magnetic dipole is offset from the rotation axis. The properties of the hot spots that occur on the magnetic poles as a result of this accretion mechanism are dependent on the radial extent of the magnetosphere, parameterised by inner and outer magnetosphere radii, and the accretion rate, which directly affects the luminosity of the hotspots. These photometric models self-consistently solve for the hotspot temperature using these parameters. I found that a dipole offset of θ~10–20° and an aspect ratio of $h_{\rm max}/r_0$=0.31, consistent with the above result that ~30 per cent of CTTS systems show this behaviour. The offset angle was also found to be consistent with other determinations, discussed in the text.

This work is continued in Chapter 4, this time using a full non-local thermodynamic equilibrium method to calculate the profiles for various Balmer lines. Before applying this model to AA Tau, I performed some tests on the accretion streams and the disc outflows to determine whether the results had changed significantly from previous work using TORUS. I reproduced the study of Kurosawa et al. (2006) since during this time a significant portion of the code had either been updated or changed. Lines formed in the accretion flow were found to match very well. Wind parameters were not in such good agreement globally, although the general trends were reproduced, such the occurrence of P Cygni versus more Gaussian-like profiles. It was noted that the original method of calculating the line

profiles from the disc wind involved disabling the accretion columns, which may have resulted in the hotspot luminosity being left on in the original models, thus providing an inconsistent result. This certainly seems likely, since the hybrid magnetosphere-plus-wind models were found to be more consistent with the original results than those found from the comparison with the wind alone.

Once the validity of these results had been established, I focussed on modelling the Balmer lines of AA Tau. I first obtained observational spectra, and rectified these in preparation for the analysis of my models. I then produced synthetic line profiles using just the magnetosphere contribution, demonstrating that some form of outflow is absolutely necessary in order to reproduce the observed absorption features. I considered only a disc wind for the outflow contribution since the focus of the study was to reconcile observational evidence of outflows with a magnetospheric accretion model, rather than a study on signatures from different types of outflow. The disc wind geometry was parameterised as initiating from an imaginary source point located at a distance d from the star's rotational axis, with inner and outer wind radii. Physical parameters that were studied as part of the line profile modelling covered the wind and magnetosphere temperatures, the mass loss rate, and the wind acceleration. The results of these simulations recovered the canonical mass-loss to mass-accretion rate ratio of 0.1, a magnetosphere temperature of ~8500 K, and a wind temperature of ~8000 K. However, I found there there is some degeneracy between the wind acceleration, related to the wind density, and the wind temperature. I have used this result to identify further areas of research which are discussed in the following.

6.1.1 Future work

One clear avenue deserving of further research is applying this model to other CTTS. Now that a number of these objects with AA Tau-like variability have been observed, it is natural to apply this model to these additional sources in order to comment on the global validity of this magnetospheric accretion model. This also provides an ideal testing

ground for outflow models; while I have used a stellar wind to parameterise AA Tau's outflow, its outflow mechanism is not certain and the options are not limited to merely stellar and/or disc winds. Of particular interest is the 'egg-beater' model of Johns & Basri (1995), described briefly in Section 4.6. A non-axisymmetric disc wind is perfectly feasible given the non-axisymmetric accretion flow; the wind is expected to be out of phase with the accretion signatures by 180° since it is easiest to load the wind when it is least energetically favourable for material to accrete, and *vice versa*. Having a wealth of targets to observe also means that if a given outflow mechanism is not ubiquitous, and may instead be generated by one or a number of mechanisms, observational signatures of these different types of outflow could be more readily identified given a more varied sample.

Studying different lines, particularly those with different formation mechanisms, is also an area that is definitely worth examining. Given the degeneracies that I found in disc wind parameters when using solely Balmer lines to interpret results, considering different lines would be a potential method of further constraining results. The He I λ10830 line has been detected in AA Tau as well as other numerous CTTS (Edwards et al. 2006). He I and He II has been implemented in TORUS and tested in the context of both disc and stellar winds for archetypal CTTS parameters (Kurosawa et al. 2011). The inclusion of helium lines in models of specific stars for which helium transitions have been observed is therefore a natural choice for progression.

With the ever-increasing resolution available, particularly with interferometric arrays, it will soon be possible to perform spectrally resolved interferometry on objets down to this size. Enabling spatial information to be directly obtained in this way will enable much more robust parameter constraints to be made on these objects in the near future.

6.2 Emission interior to the silicate discs of HAeBes

Moving up the mass range to Herbig Ae stars introduces another phenomenon in the interior regions of circumstellar discs. Evidence for magnetospheric accretion declines in this

mass range due to much hotter circumstellar regions causing dust to sublimate and thus not reach the magnetosphere. For even more massive stars, in the Herbig Be regime, there is evidence that magnetic fields are not prominent or are even non-existent, implying that a disc accretion mechanism is more likely. These objects have significantly more complex environments than CTTS, showing evidence for spirals in their discs (e.g. AB Aur), dust halos in addition to circumstellar discs (e.g. MWC 297), and puffed-up inner rims enabling additional stellar radiation to be intercepted by the disc, casting a shadow over the disc (e.g. MWC 275).

These objects show evidence of inner disc emission interior to the dust sublimation radius of a standard circumstellar disc comprised of silicate grains. Gas is frequently cited as being the cause of this emission (e.g. Eisner et al. 2007; Tannirkulam et al. 2008b; Kraus et al. 2008). It has also been suggested that this may be emission from refractory grains which could survive in the hot inner regions of the disc (Benisty et al. 2010). The presence of an inner source of emission is evident in visibility measurements since visibilities provide a Fourier transform of the intensity of a region on the sky; the Gaussian visibility profiles observed are therefore representative of a Gaussian intensity distribution, rather than the sharp inner rim indicated by solely a silicate sublimation radius with no interior material. In Chapter 5 I examined the possibility that this inner emission could be dominated by refractory grain emission, testing the idea of Benisty et al. (2010) in a much more self-consistent way. Using the HAes AB Aur and MWC 275, I performed parameter searches to determine the disc geometry using SEDs, then using the best fitting results to these I performed visibility modelling. These models were calculated under radiative equilibrium, allowing the dust to sublimate using a given sublimation temperature, producing inner disc radii and rim shapes that are calculated self-consistently. This was a key improvement on the work presented by B10; these authors made numerous assumptions in their model in particularly important areas such as assuming the inner silicate rim is irradiated by an effective stellar luminosity of 75% $L_\star$. This assumption goes on to affect the position of the inner rim, which itself will affect the size of the inner cavity that

must be filled by refractory grains, and the shape of the rim. The models presented in this thesis are the first ones that calculate this refractory emission self-consistently, and simultaneously with silicate grain sublimation.

Free parameters included the disc mass, inclination, scale height, and degree of disc flaring. These were fitted using SEDs, the results of which are presented in Section 5.5.1. A reasonable fit was obtained for MWC 275, although I was unable to reproduce the long-wavelength end of AB Aur at 100 μm. However, as noted in the text, its disc is more difficult to parameterise due to the presence of a spiral structure in its disc as well as an extended envelope. This was not a concern since the prime areas of interest in this study are the H and K bands, within which I produced images and visibilities to test refractory grain emission. To simplify comparisons with existing work, I chose to use iron for the refractory grain contribution since this was the focus of B10. They did suggest that graphite could potentially be more likely to survive at the temperatures required for refractory emission to contribute a significant part of this emission, but they did not rule out iron as a source.

My primary focus was to find the sublimation temperature required in order for iron grains to survive close enough in to the star to produce sufficient rim emission. Firstly, I examined the effect of different refractory grain mass fractions on the visibility profiles. I found that the mass fraction of the grains is an incredibly sensitive parameter; the parameter space for which the grains can provide this emission covers about one order of magnitude. I established mass fractions of $f_{\rm Fe} = 5\times10^{-9}$ for MWC 275 and $f_{\rm Fe} = 1\times10^{-7}$ for AB Aur. I modelled refractory grain sublimation temperatures up to 2600 K, which did produce smooth visibility profiles at baselines greater than ∼100 m/μm but was still not sufficient to produce a wide enough refractory grain rim for Gaussian-like visibility profiles. This value for the iron sublimation temperature is significantly higher than that expected for refractory grains that are present in HAe discs. The extreme sensitivity of the refractory grain mass fraction on the ability to produce refractory emission at all is also a concern for this model. Although the idea that an inner rim made of refractory dust

grains may produce sufficient emission for the filling in of HAe discs is an attractive one, it does not appear to work in practice and the inner emission must be due to some other source. However, as noted in the text, there is still plenty of scope for investigation into the importance of refractory grains, particularly in the context of shielding as discussed in Section 5.7.

6.2.1 Future work

The models presented here are incredibly complex. The free parameters provided by this grain study, such as size distributions and different grain types, make a full and comprehensive parameter search a difficult task. There are a lot of interesting results to come out of this, which will be examined thoroughly and published in due course. Once a full grid of parameters has been analysed, there is scope to include a χ^2 minimisation since, unlike the AA Tau study, these data are not variable. There is little spread in the visibility data making this an ideal target for future work.

A logical way to build on this work is to investigate the possibility that inner disc emission is produced by a mixture of silicate and refractory grains, with the silicates shielded so that they can survive closer in to the star. Kama et al. (2009) have previously found that thermal coupling in the inner rims of circumstellar discs is a more likely outcome than the grains remaining distinct. This shielding does not require fine-tuning of the refractory grain fractions that was found to be necessary to produce a refractory grain rim, which makes this idea attractive.

If these refractory grain models are found to be insufficient in providing the inner emission required, whether or not thermal coupling is included, models including gas should be investigated. Adding molecular opacities provides an additional method of shielding the grains, as well as producing an extra source of inner emission. Rayleigh scattering may also be a considerable factor in these models that should be implemented in the future; due to its $1/\lambda^4$ dependency, the effect is dominant in the UV, resulting in increased removal of the radiation field for hotter stars. Once again, the end result is dust

being shielded from the stellar radiation, enabling a smaller radius for the dusty inner rim.

The presence of refractory grains is undoubtedly plausible in contributing some of the emission. Even if it is not the dominant source, it appears likely that refractory grains may play a role in shielding silicate grains. Implementing additional features such as molecular opacities is a difficult but worthwhile task. This is an area of research that will produce interesting results, wherever this current direction takes us.

Appendix A

Observational photometry of AA Tau

In section 3.2 I presented existing photometric observations of AA Tau. Here, I include figures showing all of the *B*-, *V*- and *R*-band observations, as a function of time, of AA Tau that have been used in this study. Figure A.1 shows the *B*-band data obtained by B99, B03, B07, and G07; Figure A.2 shows the *V*-band data obtained by these authors and *ASAS*; and Figure A.3 shows the *R*-band data obtained by G07.

Short-term changes in photometric behaviour are quite clear, for instance in 1999–2000 where the system shows little variation initially but exhibits deep luminosity dips just a few weeks later. A simular 'quiet' period is evident towards the end of 2005.

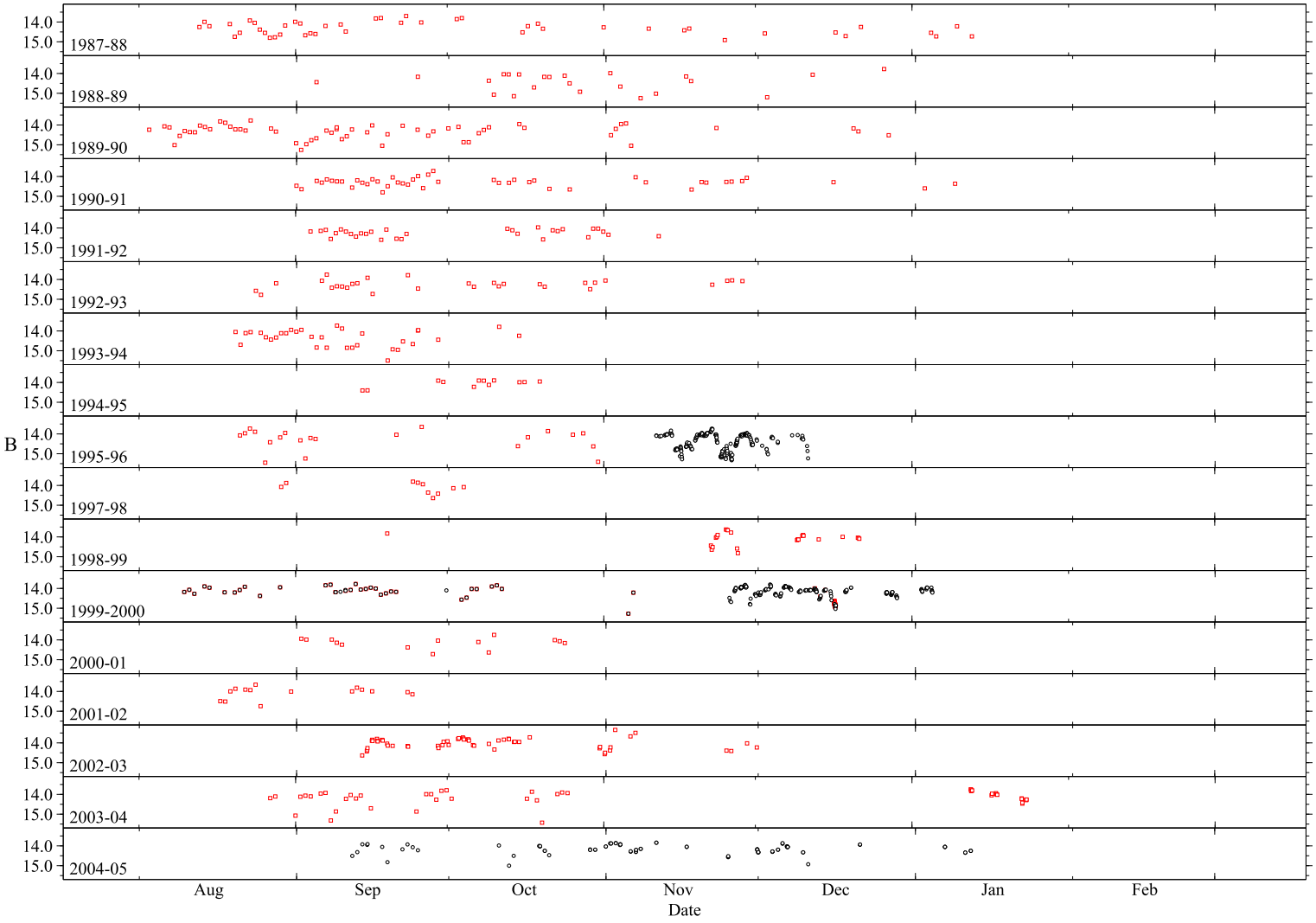

Figure A.1: *B*-band observations of AA Tau from 1987–2005 B99; B03; B07; G07. Data from Bouvier et al. are shown with black circles and data from Grankin et al. are shown with red squares.

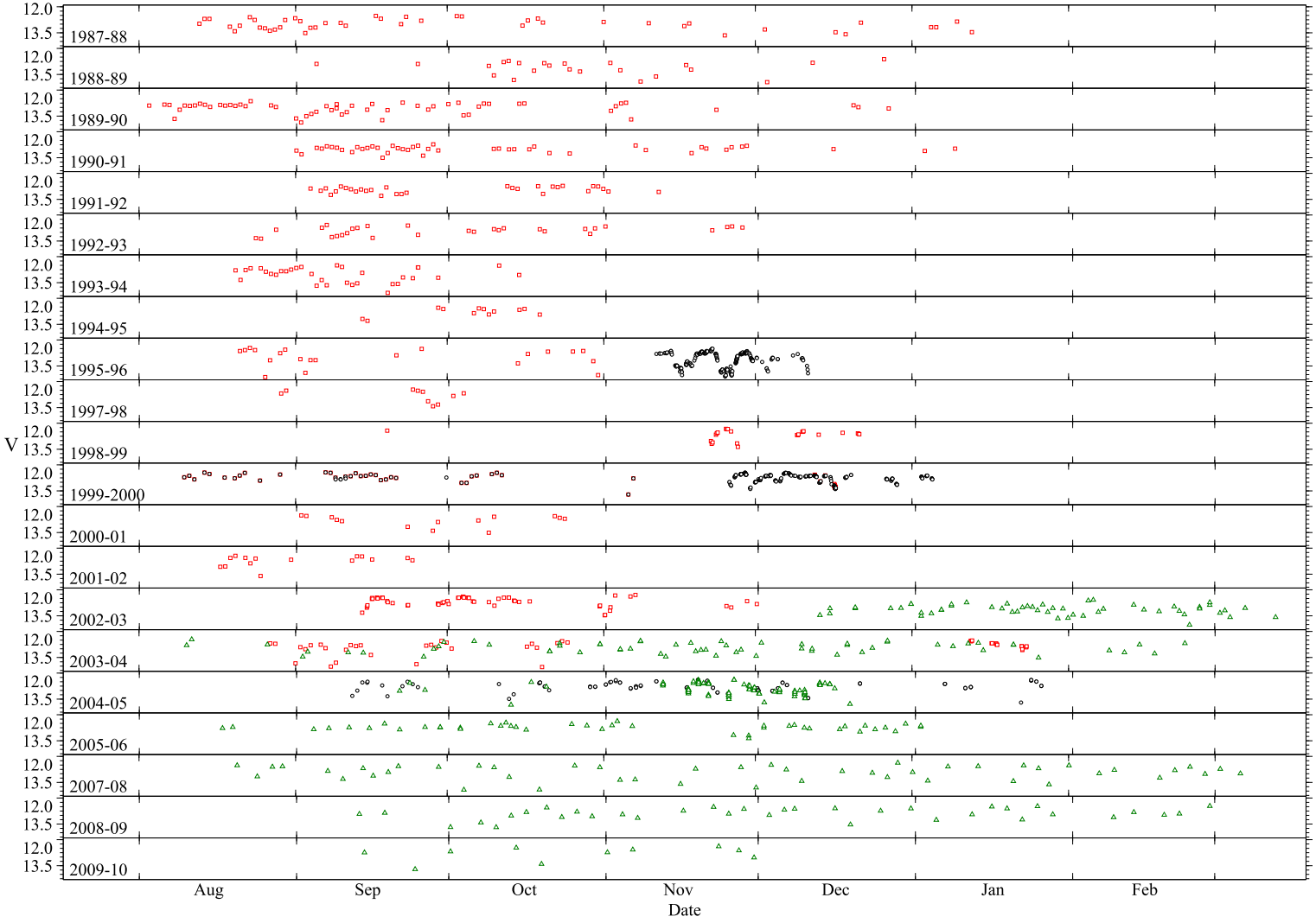

Figure A.2: *V*-band observations of AA Tau from 1987–2010. Data from Bouvier et al. and Grankin et al. are as in Figure A.1. Data from *ASAS* are shown with green triangles.

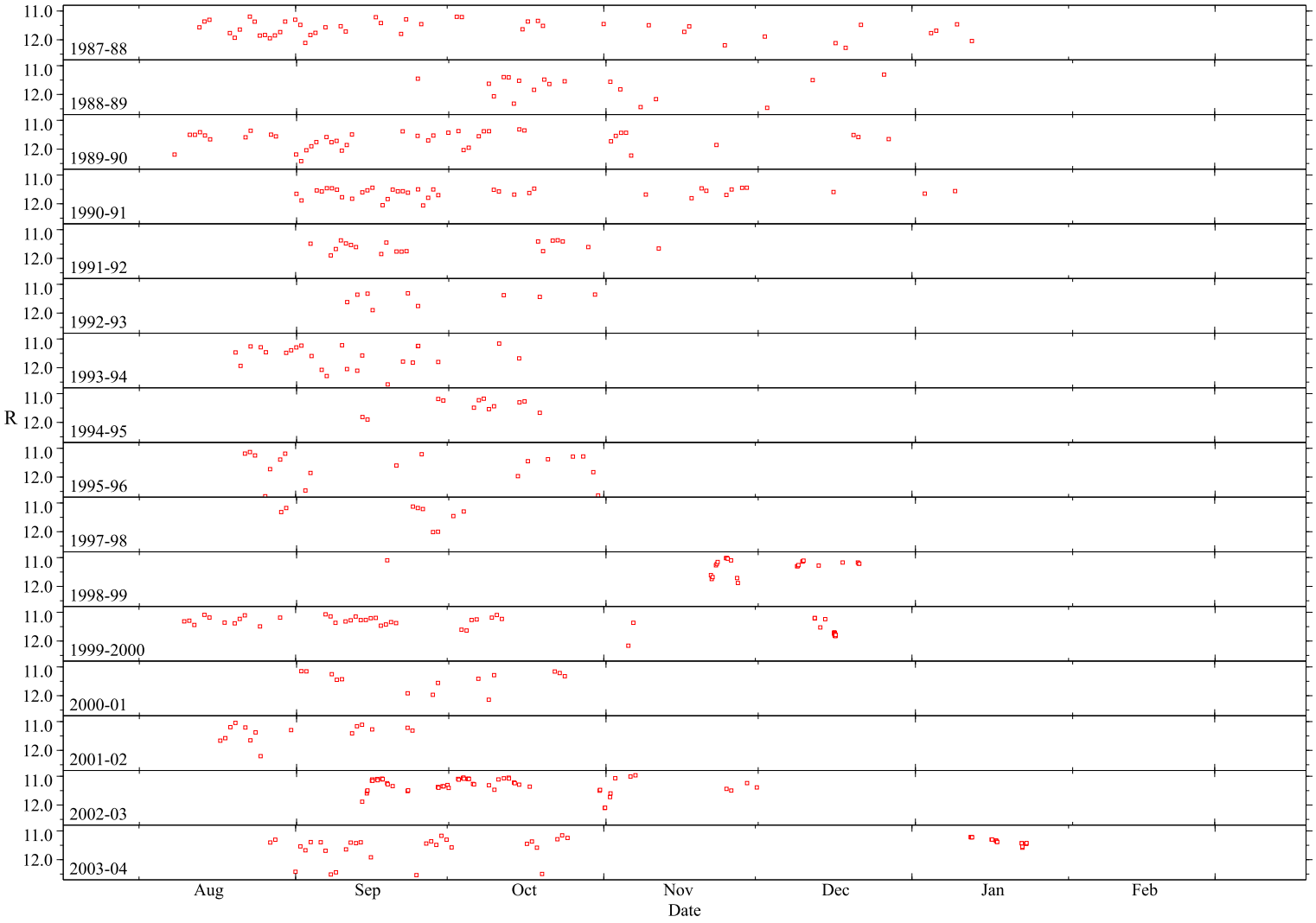

Figure A.3: *R*-band observational photometry for AA Tau from 1987–2004 from Grankin et al. (2007)

Appendix B

Additional computational models for AA Tau

Section 3.2 discussed the process of selecting the best fitting photometric models for AA Tau. Here I present the light curves produced using some of the parameters that can be ruled out with respect to the AA Tau system. These figures take the same form as Figure 3.10, with the mean lightcurves from observational data given by the solid line and the range covered by the median 90 per cent of data given by the shaded region. The top panel of each figure shows *B*-band models with *V*-band models underneath. Different magnetosphere sizes are presented, with $r_i = 5.2$ (dashed line), $r_i = 7.6$ (dotted line), and $r_i = 7.6$ (dash-dot line). Values for the dipole offset and aspect ratio are given in the figure captions. A mass accretion rate of $\dot{M}_{acc} = 5 \times 10^{-9}$ $M_\odot$ yr^{-1} is used for each of these models. All other parameters have been kept constant and are as presented in Table 3.2. These figures are presented in order of increasing dipole offset, with each offset group organised with increasing aspect ratio.

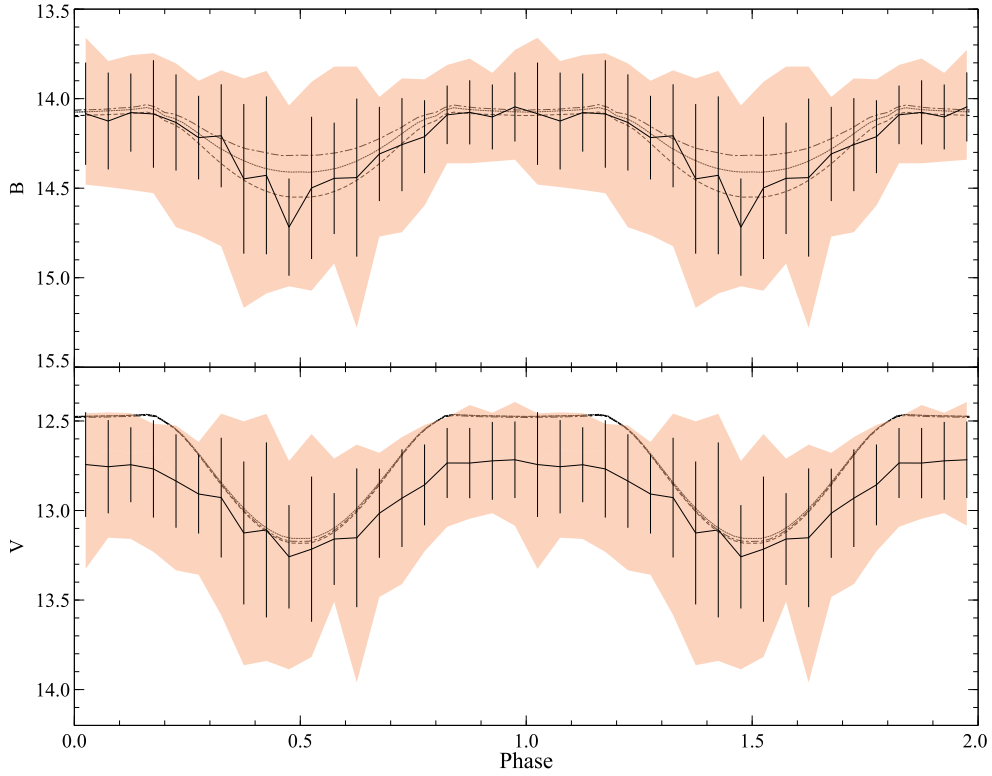

Figure B.1: Comparisons between observations and models with $\theta = 10°$, $h_{\max}/r_{\rm o} = 0.29$.

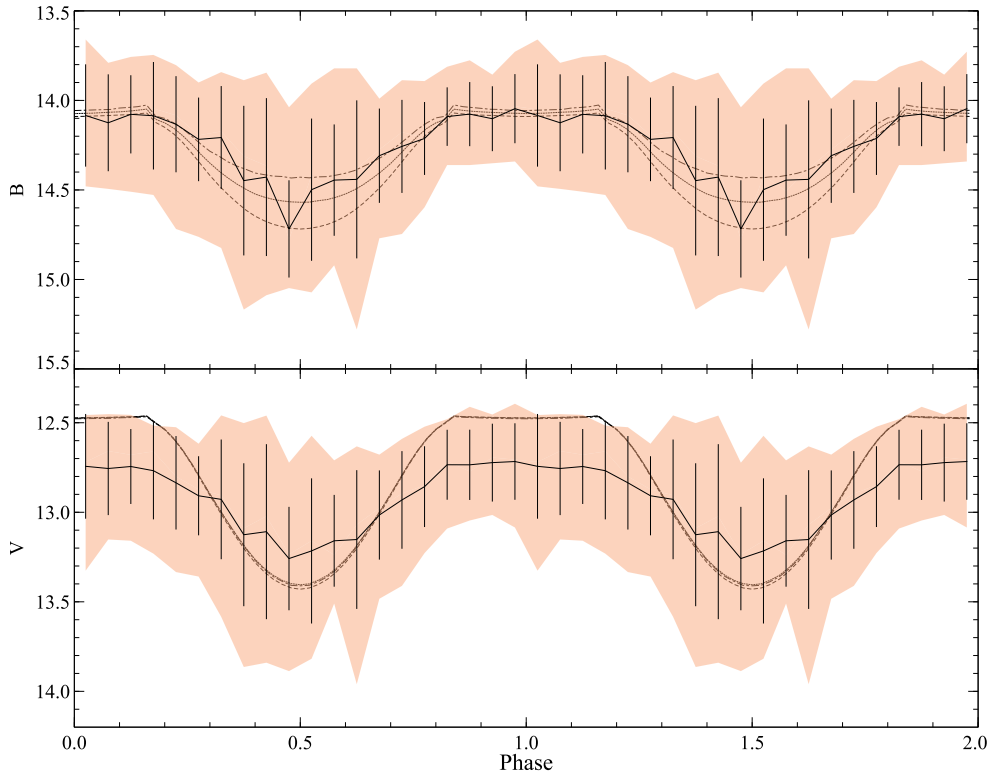

Figure B.2: Comparisons between observations and models with $\theta = 10°$, $h_{\max}/r_{\rm o} = 0.31$.

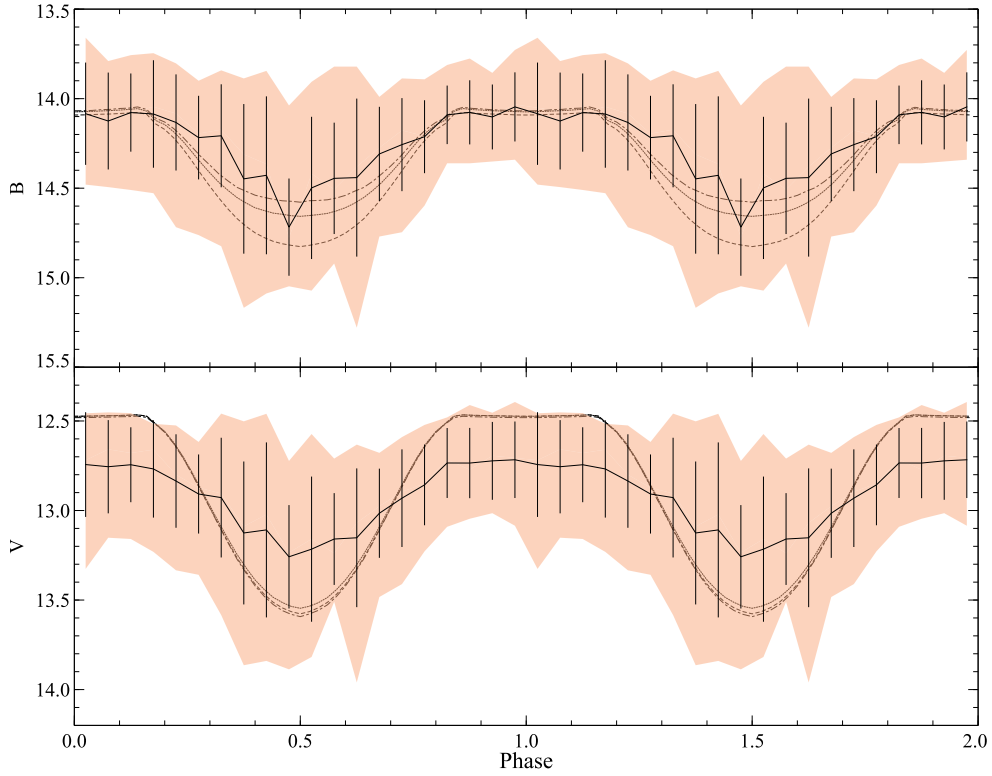

Figure B.3: Comparisons between observations and models with $\theta = 10°$, $h_{max}/r_o = 0.32$.

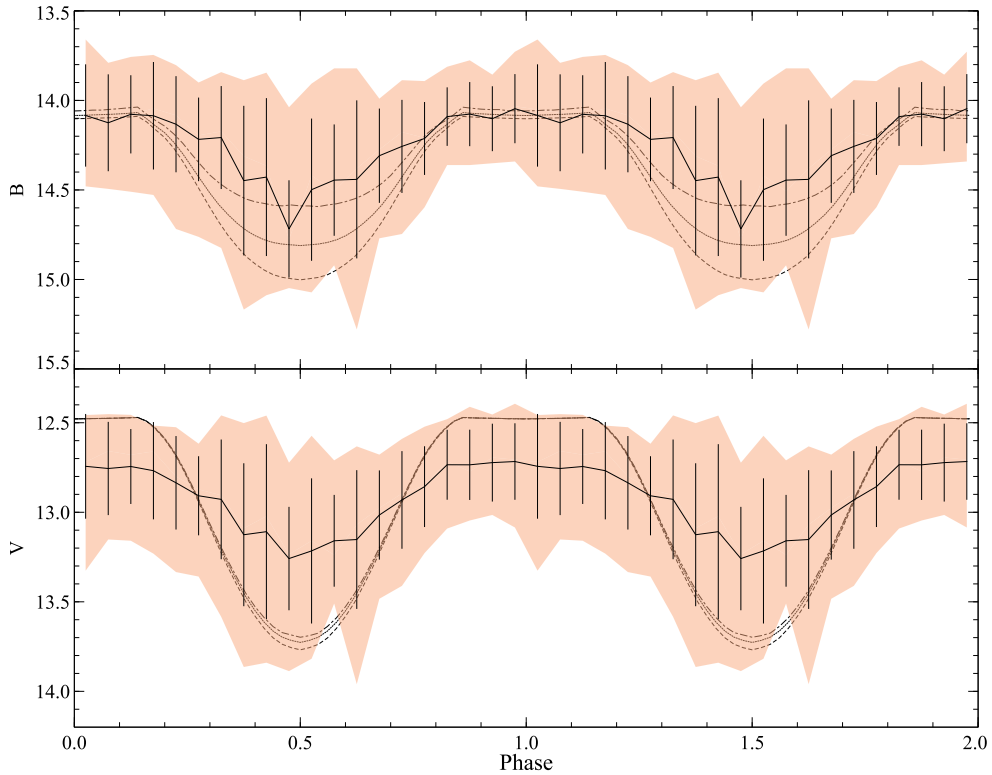

Figure B.4: Comparisons between observations and models with $\theta = 10°$, $h_{max}/r_o = 0.33$.

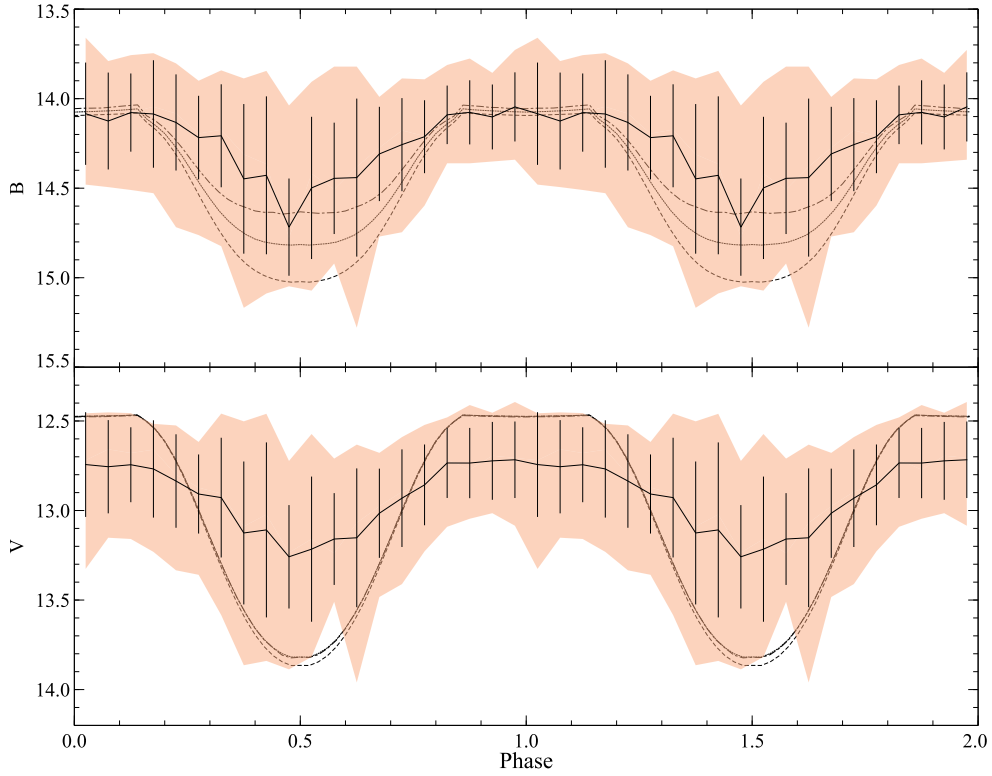

Figure B.5: Comparisons between observations and models with $\theta = 10°$, $h_{max}/r_o = 0.34$.

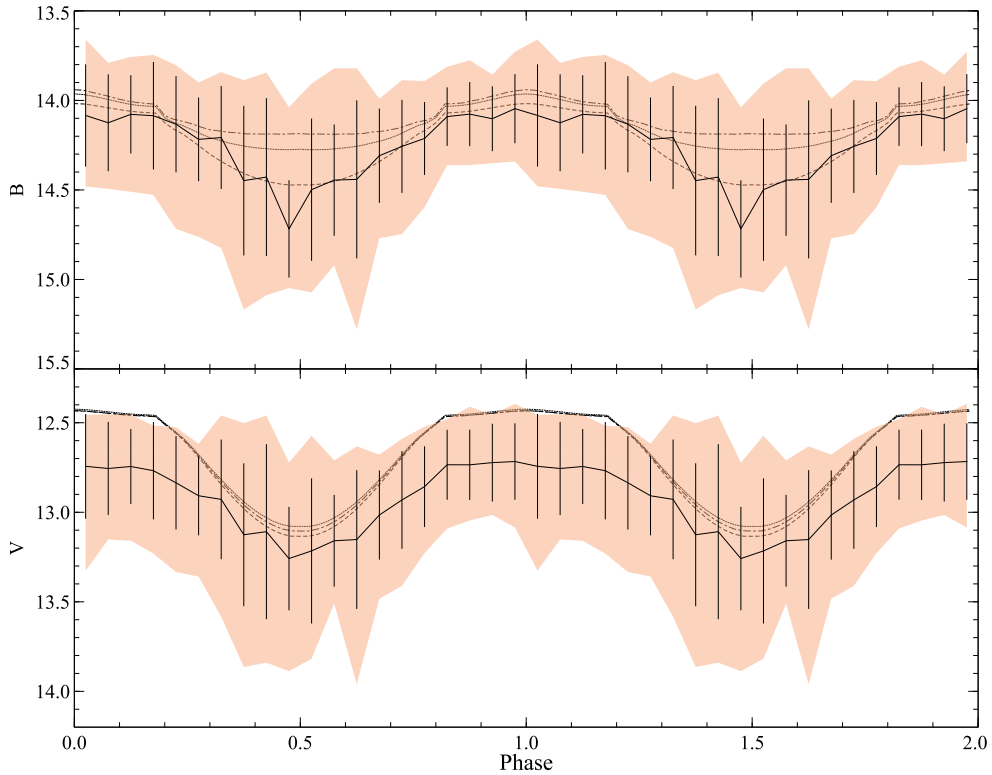

Figure B.6: Comparisons between observations and models with $\theta = 20°$, $h_{max}/r_o = 0.29$.

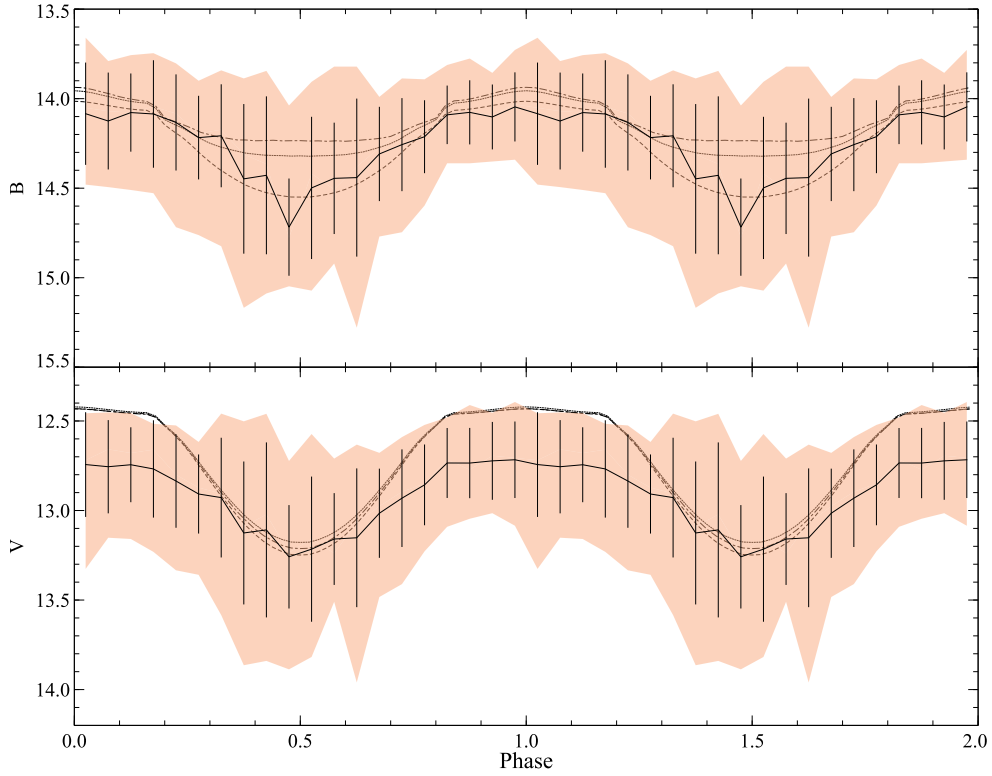

Figure B.7: Comparisons between observations and models with $\theta = 20°$, $h_{max}/r_o = 0.30$.

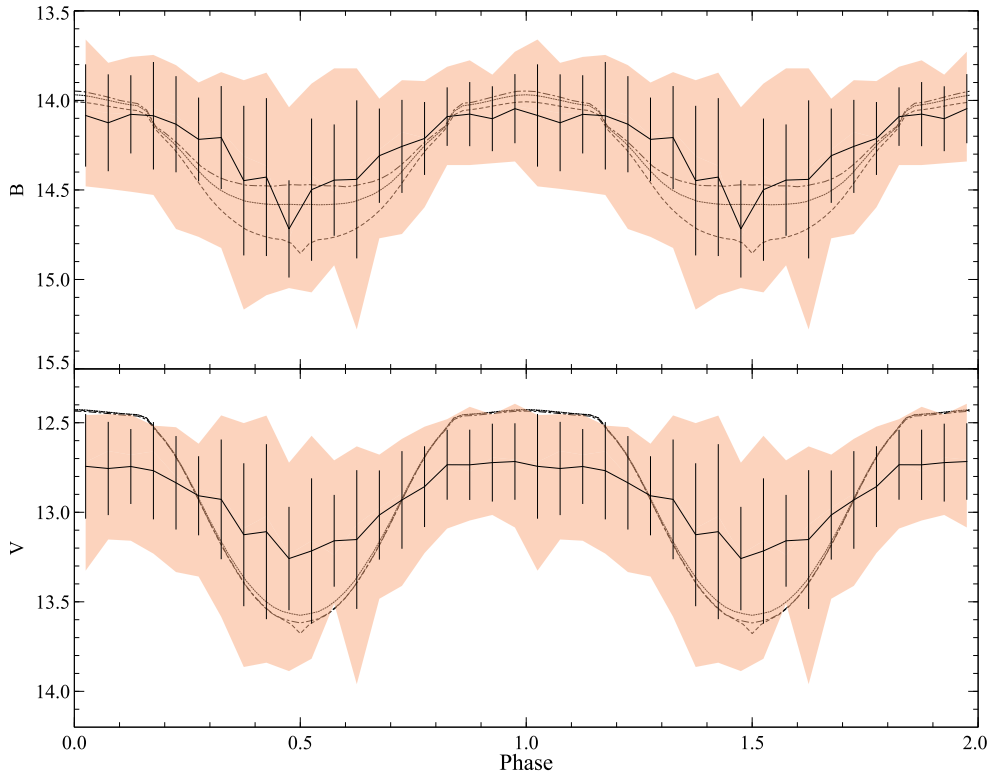

Figure B.8: Comparisons between observations and models with $\theta = 20°$, $h_{max}/r_o = 0.33$.

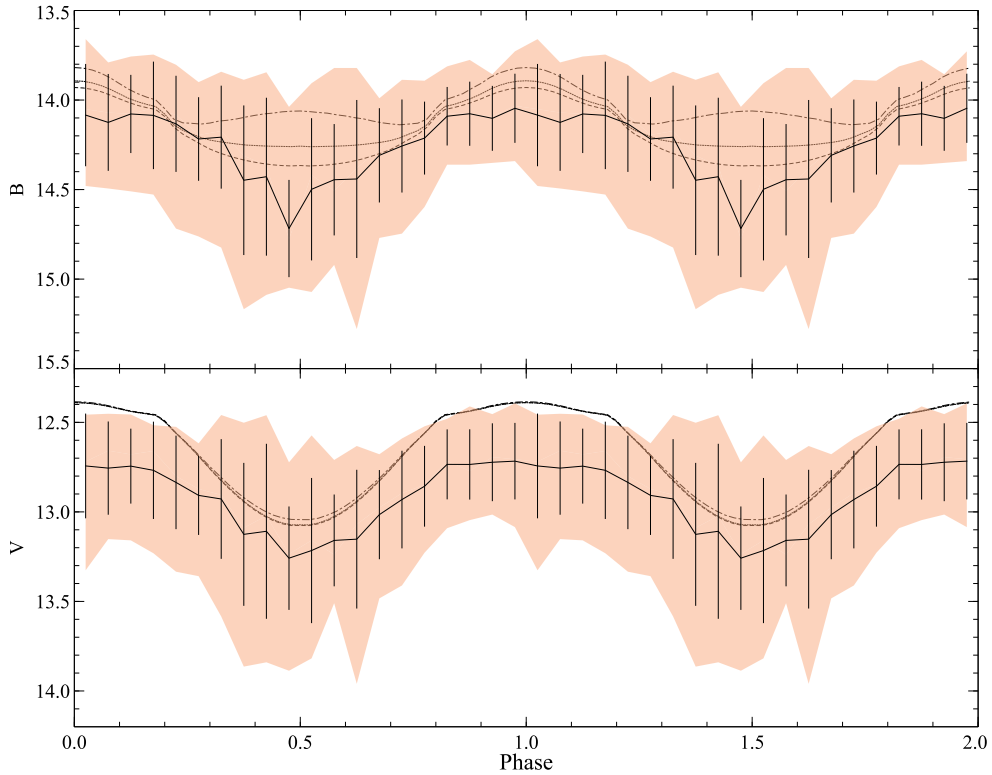

Figure B.9: Comparisons between observations and models with $\theta = 30°$, $h_{\max}/r_{\rm o} = 0.29$.

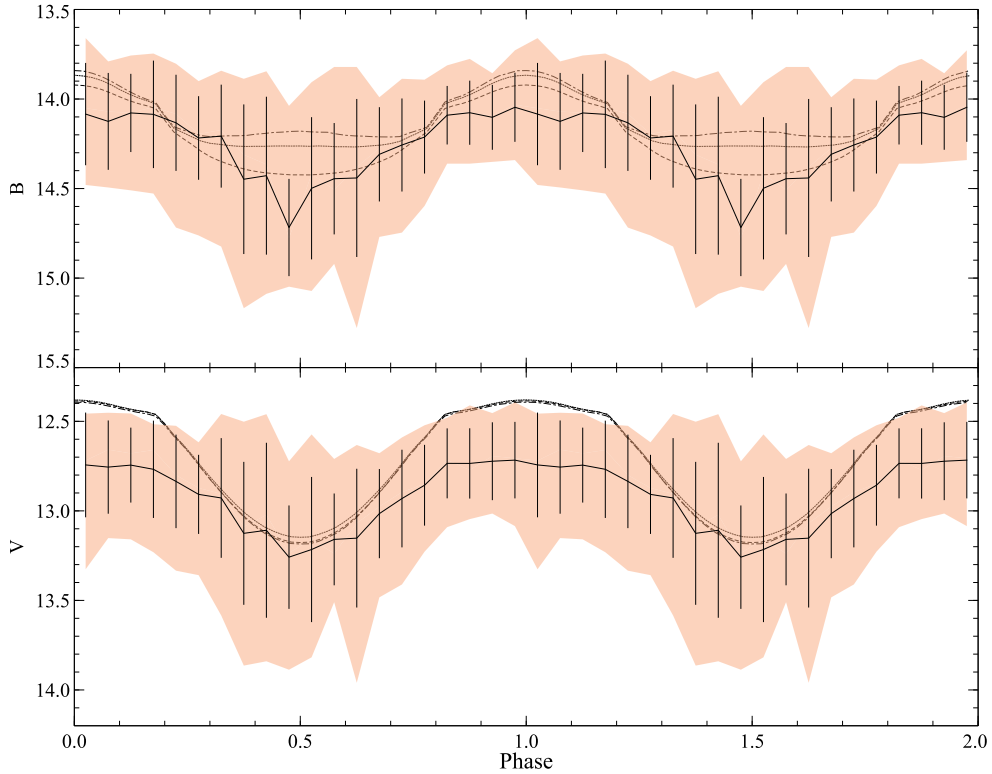

Figure B.10: Comparisons between observations and models with $\theta = 30°$, $h_{max}/r_o = 0.30$.

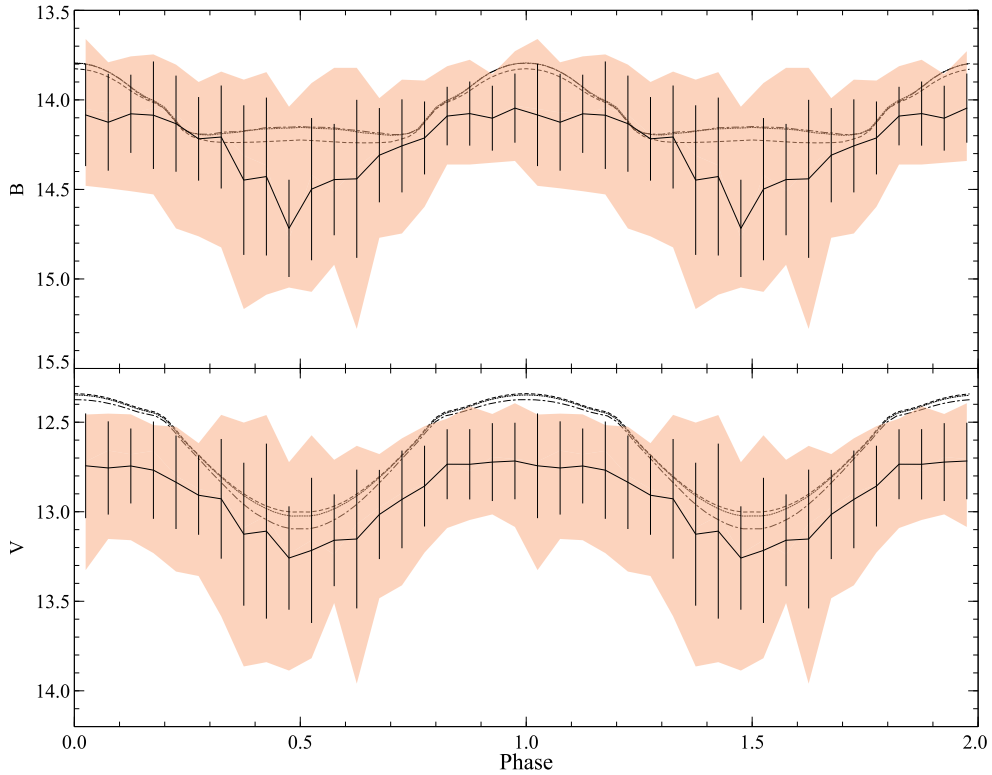

Figure B.11: Comparisons between observations and models with $\theta = 40°$, $h_{max}/r_o = 0.29$.

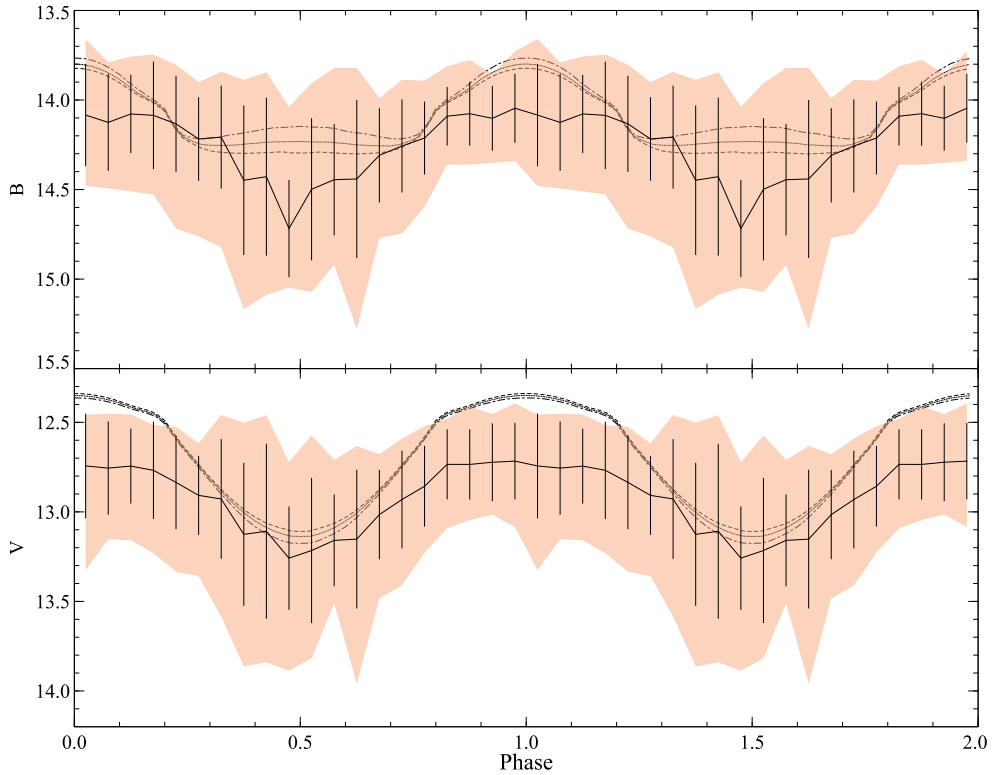

Figure B.12: Comparisons between observations and models with $\theta = 40°$, $h_{max}/r_o = 0.30$.

Appendix C

Additional line profile parameter sets for AA Tau

Section 4.5 discussed the best fitting spectroscopic models for AA Tau. In Figures C.1 and C.2 I present Hα and Hγ line profiles calculated using the best fitting parameter sets determined for Hβ. I also present alternative fits using magnetosphere and wind temperatures that fall within the ranges determined in Section 4.5. Models which included both magnetospheric accretion and a disc wind are given by the black line and the magnetosphere contribution is given in red. Observational profiles are given in blue. The corresponding phase for these data are given to the top right of each profile. Figures C.3 and C.4 give alternative parameter sets that provide good fits to Hα, Hβ, and Hγ profiles out of occultation. All parameters are as defined in Table 4.2 unless stated in the figure captions.

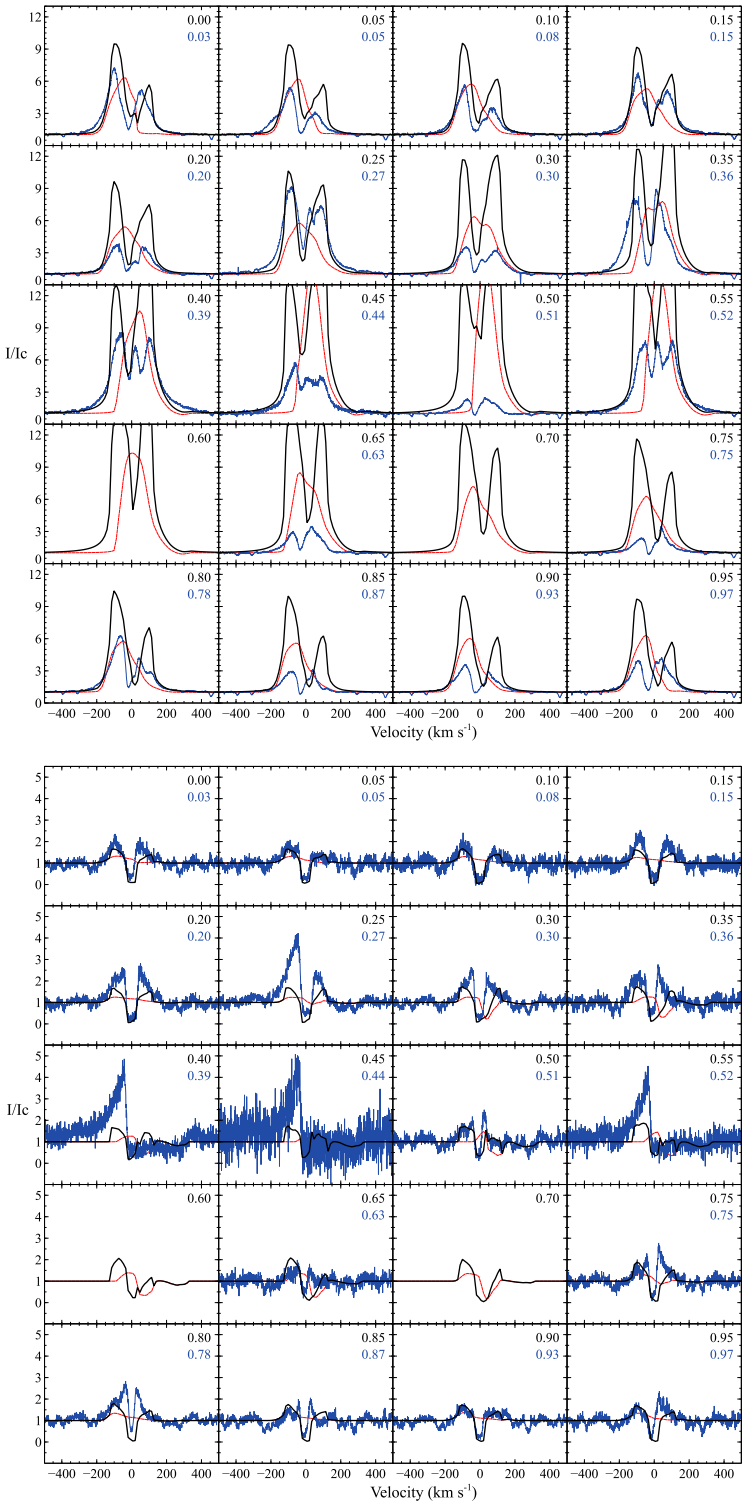

Figure C.1: Hα (top) and Hγ (bottom) profiles calculated using the best fitting parameter set found for Hβ when AA Tau is not being occulted by the disc warp. Here $\dot{M}_{\rm wind}/\dot{M}_{\rm acc}$ = 0.10, $T_{\rm mag}$ = 8900 K, $T_{\rm wind}$ = 8000 K. Models show good agreement with Hα at the lowest and highest phases. There are instances in Hα where the absorption component is too central (e.g. φ = 0.00, 0.95), but at other times observations are reproduced well (e.g. φ = 0.15, 0.25).

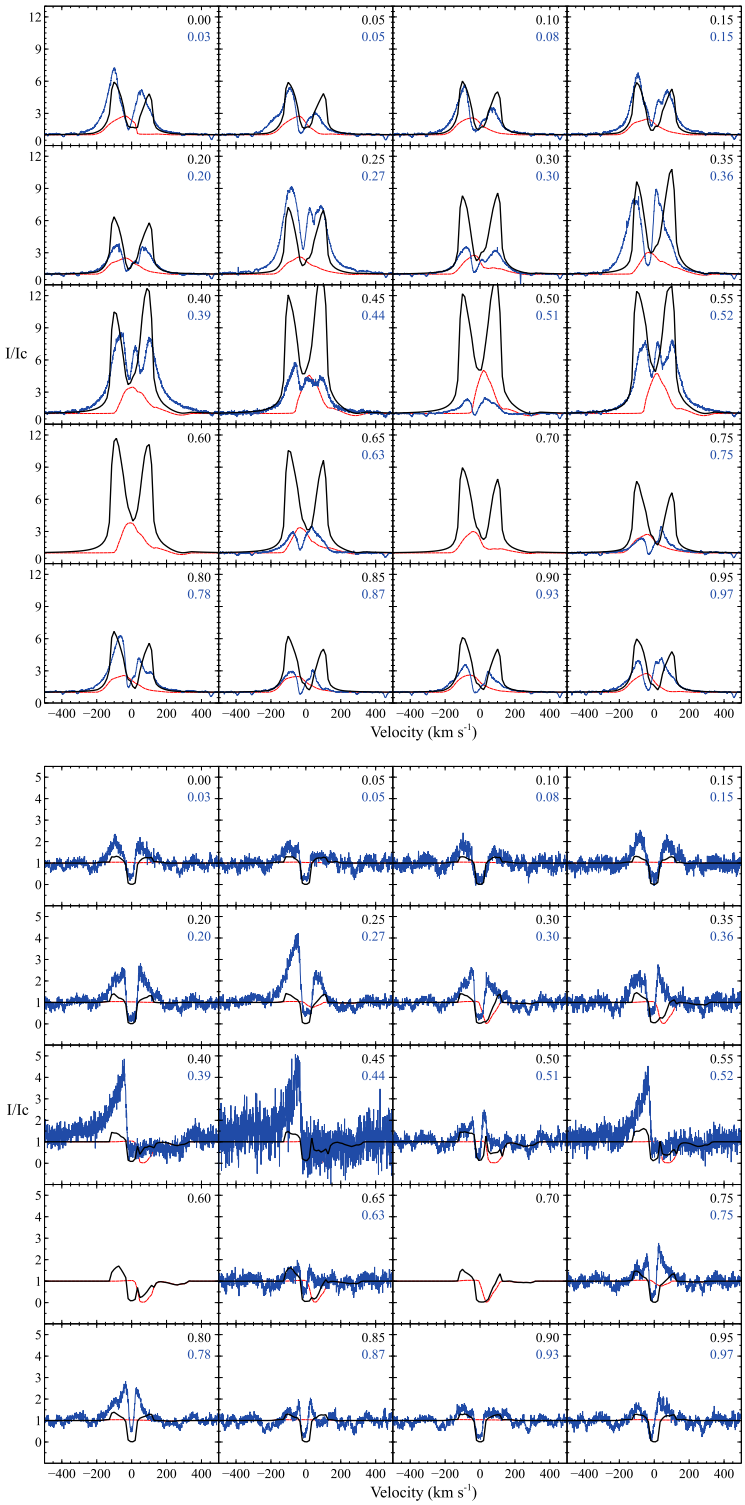

Figure C.2: Hα (top) and Hγ (bottom) profiles calculated using the best fitting parameter set found for Hβ for AA Tau during occultation. Here $\dot{M}_{\rm wind}/\dot{M}_{\rm acc} = 0.09$, $T_{\rm mag} = 8500$ K, $T_{\rm wind} = 8000$ K. While Hβ models reproduce the higher-intensity blue emission peak relative to the red, the opposite it true for Hα. This behaviour occurs at the $\varphi = 0.36$ observation, but most additional observational data taken during occultation display a triple-peaked structure which is not reproduced by the models. Hγ models maintain the stronger blue peak, with the red emission replaced by absorption at the central phases, but the intensity is significantly lower than that given by observations. Models for each of these lines also provide good fits out of occultation.

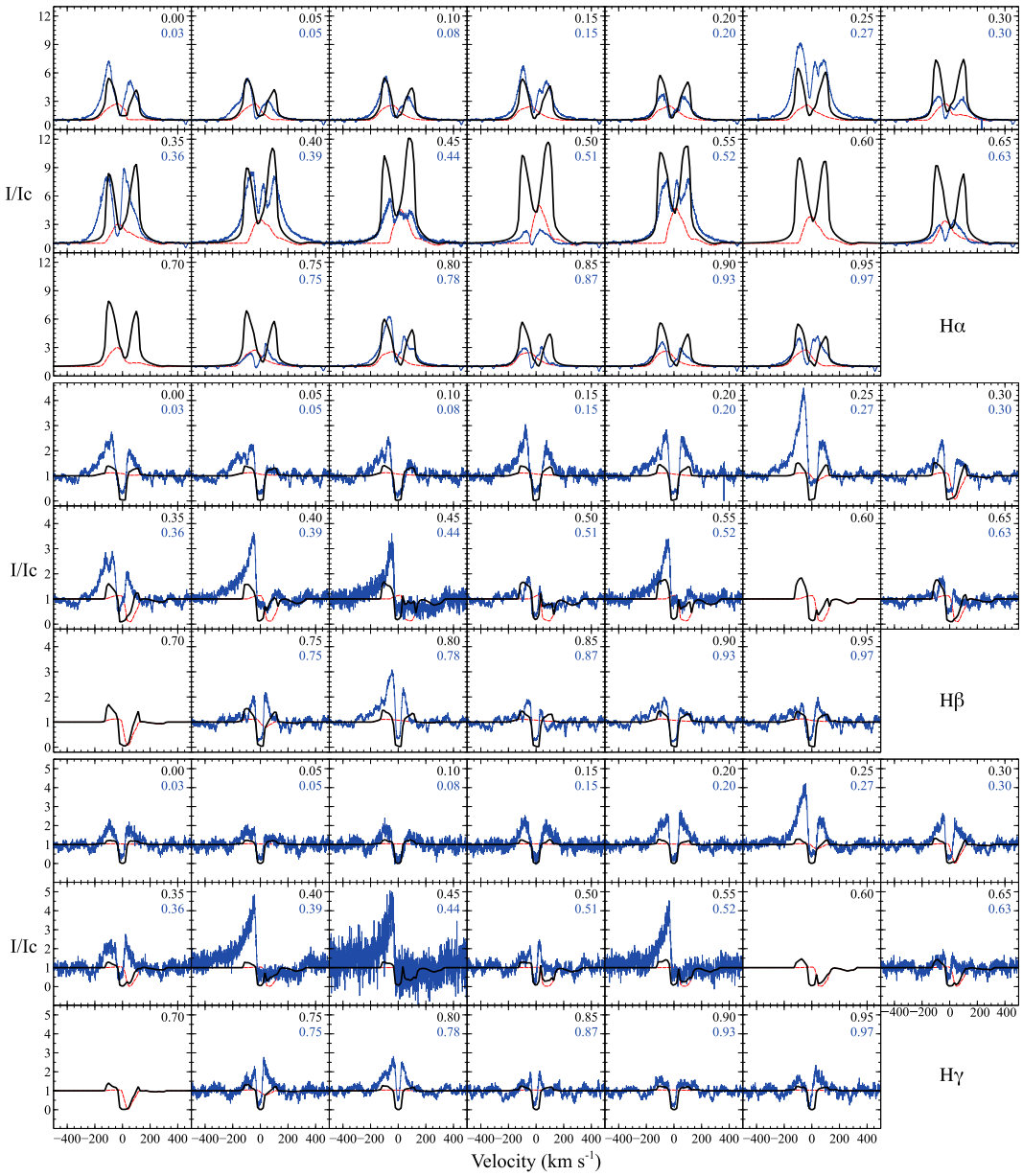

Figure C.3: Observed profiles compared with models where $\dot{M}_{\rm wind}/\dot{M}_{\rm acc} = 0.10$, $T_{\rm mag} = 8500$ K, $T_{\rm wind} = 7900$ K. The line profiles calculated at the lowest and highest inclinations using this model are almost indistinguishable from those presented in C.2 with $\dot{M}_{\rm wind}/\dot{M}_{\rm acc} = 0.09$ and $T_{\rm wind} = 8000$ K, although the line intensities at central inclinations are noticeably weaker here than in the $T_{\rm wind} = 8000$ K model. This dependence of intensity on different wind temperatures as a function of phase is presented in Figure 4.14.

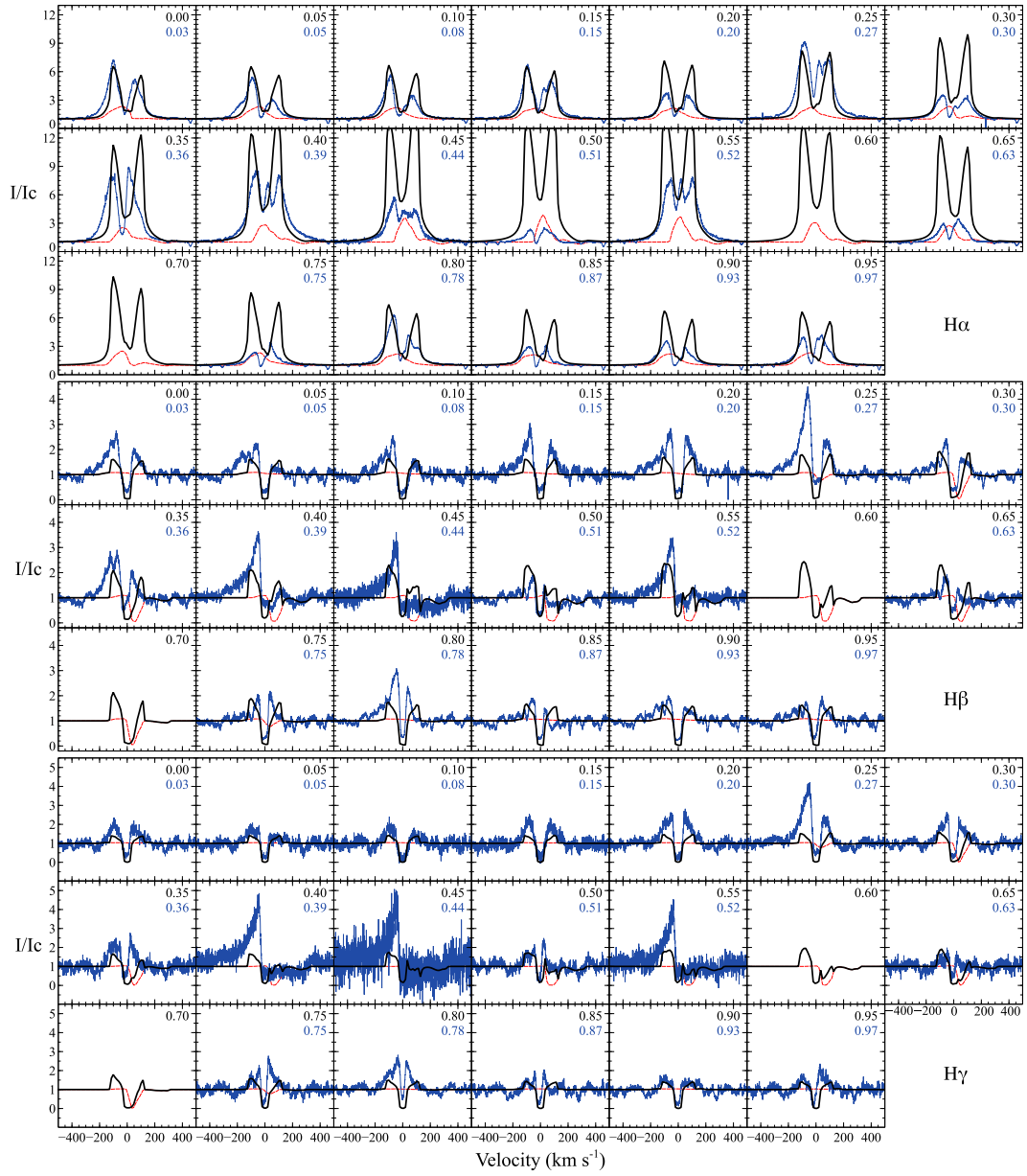

Figure C.4: Observed profiles compared with models for $\dot{M}_{\rm wind}/\dot{M}_{\rm acc} = 0.10$, $T_{\rm mag} = 8400$ K, $T_{\rm wind} = 8000$ K. While the magnetosphere temperature is 100 K lower here than in Figures 4.16 and C.2, the increase in $\dot{M}_{\rm wind}/\dot{M}_{\rm acc}$ from 0.09 to 0.10 results in stronger emission. It is clear from Figure 4.12 that there is very little variation between models with magnetosphere temperatures of 8400 K and 8500 K, whereas the increase in $\dot{M}_{\rm wind}/\dot{M}_{\rm acc}$ from 0.09 to 0.10 provides a more noticeable increase in emission, particularly during occultation (see Figure 4.13).

Bibliography

Alecian, E., Wade, G. A., Catala, C., et al. 2007, in IAU Symposium, Vol. 243, IAU Symposium, ed. J. Bouvier & I. Appenzeller, 43–50

Alencar, S. H. P. & Basri, G. 2000, AJ, 119, 1881

Alencar, S. H. P., Basri, G., Hartmann, L., & Calvet, N. 2005, A&A, 440, 595

Alencar, S. H. P., Teixeira, P. S., Guimarães, M. M., et al. 2010, A&A, 519, A88

Aly, J. J. & Kuijpers, J. 1990, A&A, 227, 473

André, P. 1994, in The Cold Universe, ed. T. Montmerle, C. J. Lada, I. F. Mirabel, & J. Tran Thanh Van, 179

André, P., Ward-Thompson, D., & Barsony, M. 1993, ApJ, 406, 122

Appenzeller, I., Bertout, C., & Stahl, O. 2005, A&A, 434, 1005

Appenzeller, I. & Mundt, R. 1989, A&A Rev., 1, 291

Appenzeller, I., Oestreicher, R., & Jankovics, I. 1984, A&A, 141, 108

Appenzeller, I. & Wolf, B. 1977, A&A, 54, 713

Artemenko, S. A., Grankin, K. N., & Petrov, P. P. 2012, Astronomy Letters, 38, 783

Basri, G. & Bertout, C. 1989, ApJ, 341, 340

Basri, G., Marcy, G. W., & Valenti, J. A. 1992, ApJ, 390, 622

Bastian, U., Finkenzeller, U., Jaschek, C., & Jaschek, M. 1983, A&A, 126, 438

Beckwith, S., Skrutskie, M. F., Zuckerman, B., & Dyck, H. M. 1984, ApJ, 287, 793

Beckwith, S. V. W., Sargent, A. I., Chini, R. S., & Guesten, R. 1990, AJ, 99, 924

Beech, M. & Mitalas, R. 1994, ApJS, 95, 517

Beltrán, M. T., Sánchez-Monge, Á., Cesaroni, R., et al. 2014, A&A, 571, A52

Benisty, M., Natta, A., Isella, A., et al. 2010, A&A, 511, A74

Bergin, E. A. & Tafalla, M. 2007, ARA&A, 45, 339

Bertout, C. 1989, ARA&A, 27, 351

Bertout, C., Basri, G., & Bouvier, J. 1988, ApJ, 330, 350

Bildsten, L., Brown, E. F., Matzner, C. D., & Ushomirsky, G. 1997, ApJ, 482, 442

Blake, G. A. & Boogert, A. C. A. 2004, ApJL, 606, L73

Blandford, R. D. & Payne, D. G. 1982, MNRAS, 199, 883

Blitz, L. 1993, in Protostars and Planets III, ed. E. H. Levy & J. I. Lunine, 125–161

Böhm, T. & Catala, C. 1994, A&A, 290, 167

Bonsack, W. K. & Greenstein, J. L. 1960, ApJ, 131, 83

Boss, A. P. 1988, ApJ, 331, 370

Bouvier, J., Alencar, S. H. P., Boutelier, T., et al. 2007, A&A, 463, 1017

Bouvier, J. & Bertout, C. 1989, A&A, 211, 99

Bouvier, J., Chelli, A., Allain, S., et al. 1999, A&A, 349, 619

Bouvier, J., Covino, E., Kovo, O., et al. 1995, A&A, 299, 89

Bouvier, J., Grankin, K., Ellerbroek, L. E., Bouy, H., & Barrado, D. 2013, A&A, 557, A77

Bouvier, J., Grankin, K. N., Alencar, S. H. P., et al. 2003, A&A, 409, 169

Bouvier, J., Lanzafame, A. C., Venuti, L., et al. 2016, A&A, 590, A78

Burrows, C. J., Stapelfeldt, K. R., Watson, A. M., et al. 1996, ApJ, 473, 437

Cabrit, S. 2007, in IAU Symposium, Vol. 243, IAU Symposium, ed. J. Bouvier & I. Appenzeller, 203–214

Cabrit, S., Edwards, S., Strom, S. E., & Strom, K. M. 1990, ApJ, 354, 687

Calvet, N. & Hartmann, L. 1992, ApJ, 386, 239

Camenzind, M. 1990, in Reviews in Modern Astronomy, Vol. 3, Reviews in Modern Astronomy, ed. G. Klare, 234–265

Castor, J. I. 1970, MNRAS, 149, 111

Castor, J. I., Abbott, D. C., & Klein, R. I. 1975, ApJ, 195, 157

Catala, C., Alecian, E., Donati, J.-F., et al. 2007, A&A, 462, 293

Catala, C., Donati, J. F., Böhm, T., et al. 1999, A&A, 345, 884

Cauley, P. W. & Johns-Krull, C. M. 2014, ApJ, 797, 112

Cesaroni, R., Felli, M., Testi, L., Walmsley, C. M., & Olmi, L. 1997, A&A, 325, 725

Chen, H., Myers, P. C., Ladd, E. F., & Wood, D. O. S. 1995, ApJ, 445, 377

Chiang, E. I., Joung, M. K., Creech-Eakman, M. J., et al. 2001, ApJ, 547, 1077

Cohen, M., Bieging, J. H., & Schwartz, P. R. 1982, ApJ, 253, 707

Cohen, M. & Kuhi, L. V. 1979, ApJS, 41, 743

Cohen, M. & Schmidt, G. D. 1981, AJ, 86, 1228

Collier Cameron, A. & Campbell, C. G. 1993, A&A, 274, 309

Corcoran, M. & Ray, T. P. 1997, A&A, 321, 189

Corder, S., Eisner, J., & Sargent, A. 2005, ApJL, 622, L133

Cotera, A. S., Whitney, B. A., Young, E., et al. 2001, ApJ, 556, 958

Cox, A. N. 2000, Allen's astrophysical quantities (New York: Springer)

Cox, A. W., Grady, C. A., Hammel, H. B., et al. 2013, ApJ, 762, 40

Cutri, R. M., Skrutskie, M. F., van Dyk, S., et al. 2003, VizieR Online Data Catalog, 2246, 0

D'Antona, F. & Mazzitelli, I. 1994, ApJS, 90, 467

de Berg, M., Cheong, O., van Kreveld, M., & Stein, C. 2008, Computational Geometry (Springer-Verlag TELOS)

de Gregorio-Monsalvo, I., Ménard, F., Dent, W., et al. 2013, A&A, 557, A133

di Francesco, J., Evans, II, N. J., Caselli, P., et al. 2007, Protostars and Planets V, 17

Dominik, C., Dullemond, C. P., Waters, L. B. F. M., & Walch, S. 2003, A&A, 398, 607

Donati, J.-F. & Brown, S. F. 1997, A&A, 326, 1135

Donati, J.-F., Jardine, M. M., Gregory, S. G., et al. 2007, MNRAS, 380, 1297

Donati, J.-F., Semel, M., Carter, B. D., Rees, D. E., & Collier Cameron, A. 1997, MNRAS, 291, 658

Donati, J.-F., Skelly, M. B., Bouvier, J., et al. 2010, MNRAS, 409, 1347

Doucet, C., Pantin, E., Lagage, P. O., & Dullemond, C. P. 2006, A&A, 460, 117

Draine, B. T. & Lee, H. M. 1984, ApJ, 285, 89

Dullemond, C. P., Dominik, C., & Natta, A. 2001, ApJ, 560, 957

Duncan, D. K. 1981, ApJ, 248, 651

Edwards, S. 1979, PASP, 91, 329

Edwards, S., Cabrit, S., Strom, S. E., et al. 1987, ApJ, 321, 473

Edwards, S., Fischer, W., Hillenbrand, L., & Kwan, J. 2006, ApJ, 646, 319

Edwards, S., Fischer, W., Kwan, J., Hillenbrand, L., & Dupree, A. K. 2003, ApJL, 599, L41

Edwards, S., Hartigan, P., Ghandour, L., & Andrulis, C. 1994, AJ, 108, 1056

Edwards, S., Ray, T., & Mundt, R. 1993, in Protostars and Planets III, ed. E. H. Levy & J. I. Lunine, 567–602

Eisner, J. A., Chiang, E. I., Lane, B. F., & Akeson, R. L. 2007, ApJ, 657, 347

Eisner, J. A., Lane, B. F., Akeson, R. L., Hillenbrand, L. A., & Sargent, A. I. 2003, ApJ, 588, 360

Eisner, J. A., Lane, B. F., Hillenbrand, L. A., Akeson, R. L., & Sargent, A. I. 2004, ApJ, 613, 1049

ESA. 1997, VizieR Online Data Catalog, 1239, 0

Ferreira, J., Dougados, C., & Cabrit, S. 2006, A&A, 453, 785

Finkenzeller, U. & Mundt, R. 1984, A&AS, 55, 109

Folha, D. F. M. & Emerson, J. P. 2001, A&A, 365, 90

Fukagawa, M., Hayashi, M., Tamura, M., et al. 2004, ApJL, 605, L53

Ghosh, P. & Lamb, F. K. 1979, ApJ, 232, 259

Ghosh, P., Pethick, C. J., & Lamb, F. K. 1977, ApJ, 217, 578

Goldsmith, P. F., Bergin, E. A., & Lis, D. C. 1997, ApJ, 491, 615

Goodson, A. P., Böhm, K.-H., & Winglee, R. M. 1999, ApJ, 524, 142

Goodson, A. P. & Winglee, R. M. 1999, ApJ, 524, 159

Goodson, A. P., Winglee, R. M., & Böhm, K.-H. 1997, ApJ, 489, 199

Grady, C. A., Woodgate, B., Bruhweiler, F. C., et al. 1999, ApJL, 523, L151

Grankin, K. N., Melnikov, S. Y., Bouvier, J., Herbst, W., & Shevchenko, V. S. 2007, A&A, 461, 183

Grasdalen, G. L., Strom, S. E., Strom, K. M., et al. 1984, ApJL, 283, L57

Guenther, E. W., Lehmann, H., Emerson, J. P., & Staude, J. 1999, A&A, 341, 768

Gullbring, E., Hartmann, L., Briceño, C., & Calvet, N. 1998, ApJ, 492, 323

Haberl, F., White, N. E., & Kallman, T. R. 1989, ApJ, 343, 409

Hamann, F. 1994, ApJS, 93, 485

Harries, T. J. 2000, MNRAS, 315, 722

Harries, T. J., Monnier, J. D., Symington, N. H., & Kurosawa, R. 2004, MNRAS, 350, 565

Hartigan, P., Edwards, S., & Ghandour, L. 1995, ApJ, 452, 736

Hartmann, L. 2009, Accretion Processes in Star Formation: Second Edition (Cambridge University Press)

Hartmann, L., Avrett, E., & Edwards, S. 1982, ApJ, 261, 279

Hartmann, L., Hewett, R., & Calvet, N. 1994, ApJ, 426, 669

Hartmann, L., Kenyon, S. J., & Calvet, N. 1993, ApJ, 407, 219

Hartmann, L. & Stauffer, J. R. 1989, AJ, 97, 873

Hayashi, C. 1961, PASJ, 13, 450

Henning, T. & Stognienko, R. 1996, A&A, 311, 291

Henyey, L. G., Lelevier, R., & Levée, R. D. 1955, PASP, 67, 154

Herbig, G. H. 1952, JRASC, 46, 222

Herbig, G. H. 1957, ApJ, 125, 612

Herbig, G. H. 1960, ApJS, 4, 337

Herbig, G. H. 1962, Advances in Astronomy and Astrophysics, 1, 47

Herbig, G. H. & Bell, K. R. 1988, Third Catalog of Emission-Line Stars of the Orion Population (Santa Cruz, CA: Lick Observatory)

Hernández, J., Calvet, N., Hartmann, L., et al. 2005, AJ, 129, 856

Hillenbrand, L. A., Strom, S. E., Vrba, F. J., & Keene, J. 1992, ApJ, 397, 613

Howarth, I. D. 2011, MNRAS, 413, 1515

Howarth, I. D., Murray, J., Mills, D., & Berry, D. S. 2004, Starlink User Note, 50

Hubrig, S., Stelzer, B., Schöller, M., et al. 2009, A&A, 502, 283

Hughes, A. M., Wilner, D. J., Qi, C., & Hogerheijde, M. R. 2008, ApJ, 678, 1119

Isella, A. & Natta, A. 2005, A&A, 438, 899

Isella, A., Testi, L., & Natta, A. 2006, A&A, 451, 951

Isella, A., Testi, L., Natta, A., et al. 2007, A&A, 469, 213

Jeans, J. H. 1902, Royal Society of London Philosophical Transactions Series A, 199, 1

Johns, C. M. & Basri, G. 1995, ApJ, 449, 341

Johns-Krull, C. M. 2007, ApJ, 664, 975

Johns-Krull, C. M. & Basri, G. 1997, ApJ, 474, 433

Johns-Krull, C. M. & Hatzes, A. P. 1997, ApJ, 487, 896

Johns-Krull, C. M., Valenti, J. A., Hatzes, A. P., & Kanaan, A. 1999a, ApJL, 510, L41

Johns-Krull, C. M., Valenti, J. A., & Koresko, C. 1999b, ApJ, 516, 900

Joy, A. H. 1942, PASP, 54, 15

Joy, A. H. 1945, ApJ, 102, 168

Joy, A. H. 1949, ApJ, 110, 424

Kama, M., Min, M., & Dominik, C. 2009, A&A, 506, 1199

Kenyon, S. J., Calvet, N., & Hartmann, L. 1993, ApJ, 414, 676

Kenyon, S. J. & Hartmann, L. 1995, ApJS, 101, 117

Kenyon, S. J., Hartmann, L., Hewett, R., et al. 1994, AJ, 107, 2153

Klein, R. I. & Castor, J. I. 1978, ApJ, 220, 902

Knigge, C., Woods, J. A., & Drew, J. E. 1995, MNRAS, 273, 225

Königl, A. 1991, ApJL, 370, L39

Konigl, A. & Pudritz, R. E. 2000, Protostars and Planets IV, 759

Kopal, Z. 1950, Harvard College Observatory Circular, 454, 1

Krasnopolsky, R., Li, Z.-Y., & Blandford, R. D. 2003, ApJ, 595, 631

Kraus, S., Preibisch, T., & Ohnaka, K. 2008, ApJ, 676, 490

Kuhi, L. V. 1964, ApJ, 140, 1409

Kurosawa, R., Harries, T. J., & Symington, N. H. 2006, MNRAS, 370, 580

Kurosawa, R. & Romanova, M. M. 2012, MNRAS, 426, 2901

Kurosawa, R., Romanova, M. M., & Harries, T. J. 2011, MNRAS, 416, 2623

Kurucz, R. L. 1979, ApJS, 40, 1

Kwan, J. 1997, ApJ, 489, 284

Kwan, J., Edwards, S., & Fischer, W. 2007, ApJ, 657, 897

Lada, C. J. 1985, ARA&A, 23, 267

Lada, C. J. 1987, in IAU Symposium, Vol. 115, Star Forming Regions, ed. M. Peimbert & J. Jugaku, 1–17

Lada, C. J. & Adams, F. C. 1992, ApJ, 393, 278

Lamers, H. J. G. L. M., Cerruti-Sola, M., & Perinotto, M. 1987, ApJ, 314, 726

Lamers, H. J. G. L. M. & Rogerson, Jr., J. B. 1978, A&A, 66, 417

Laor, A. & Draine, B. T. 1993, ApJ, 402, 441

Le Bouquin, J.-B., Berger, J.-P., Lazareff, B., et al. 2011, A&A, 535, A67

Lin, S.-Y., Ohashi, N., Lim, J., et al. 2006, ApJ, 645, 1297

Liu, W. M., Hinz, P. M., Hoffmann, W. F., et al. 2005, ApJL, 618, L133

Long, K. S. & Knigge, C. 2002, ApJ, 579, 725

Lovelace, R. V. E., Romanova, M. M., & Bisnovatyi-Kogan, G. S. 1995, MNRAS, 275, 244

Low, C. & Lynden-Bell, D. 1976, MNRAS, 176, 367

Lucy, L. B. 1999, A&A, 344, 282

Luttermoser, D. G. & Johnson, H. R. 1992, ApJ, 388, 579

Lynden-Bell, D. & Pringle, J. E. 1974, MNRAS, 168, 603

Mac Low, M.-M. & Klessen, R. S. 2004, Reviews of Modern Physics, 76, 125

Mahdavi, A. & Kenyon, S. J. 1998, ApJ, 497, 342

Malfait, K., Bogaert, E., & Waelkens, C. 1998, A&A, 331, 211

Mannings, V. & Sargent, A. I. 1997, ApJ, 490, 792

Martin, S. C. 1996, ApJ, 470, 537

Matt, S. & Pudritz, R. E. 2005a, ApJL, 632, L135

Matt, S. & Pudritz, R. E. 2005b, MNRAS, 356, 167

Meeus, G., Waters, L. B. F. M., Bouwman, J., et al. 2001, A&A, 365, 476

Ménard, F., Bouvier, J., Dougados, C., Mel'nikov, S. Y., & Grankin, K. N. 2003, A&A, 409, 163

Mendoza, E. E. 1968, ApJ, 151, 977

Mihalas, D. 1978, Stellar atmospheres 2nd edn. (San Francisco: W. H. Freeman and Co.)

Millan-Gabet, R., Schloerb, F. P., & Traub, W. A. 2001, ApJ, 546, 358

Miller, K. A. & Stone, J. M. 1997, ApJ, 489, 890

Miroshnichenko, A., Ivezić, Ž., & Elitzur, M. 1997, ApJL, 475, L41

Monnier, J. D. 2003, Reports on Progress in Physics, 66, 789

Monnier, J. D., Millan-Gabet, R., Billmeier, R., et al. 2005, ApJ, 624, 832

Montesinos, B., Eiroa, C., Mora, A., & Merín, B. 2009, A&A, 495, 901

Montmerle, T., Koch-Miramond, L., Falgarone, E., & Grindlay, J. E. 1983, ApJ, 269, 182

Mottram, J. C., Vink, J. S., Oudmaijer, R. D., & Patel, M. 2007, MNRAS, 377, 1363

Mundt, R. 1984, ApJ, 280, 749

Mundt, R. & Fried, J. W. 1983, ApJL, 274, L83

Muzerolle, J., Calvet, N., & Hartmann, L. 1998, ApJ, 492, 743

Muzerolle, J., Calvet, N., & Hartmann, L. 2001, ApJ, 550, 944

Muzerolle, J., D'Alessio, P., Calvet, N., & Hartmann, L. 2004, ApJ, 617, 406

Myers, P. C. & Ladd, E. F. 1993, ApJL, 413, L47

Natta, A., Prusti, T., Neri, R., et al. 2001, A&A, 371, 186

Natta, A., Testi, L., Neri, R., Shepherd, D. S., & Wilner, D. J. 2004, A&A, 416, 179

Oliveira, J. M., Foing, B. H., van Loon, J. T., & Unruh, Y. C. 2000, A&A, 362, 615

O'Sullivan, M., Truss, M., Walker, C., et al. 2005, MNRAS, 358, 632

Palla, F. & Stahler, S. W. 1993, ApJ, 418, 414

Piétu, V., Guilloteau, S., & Dutrey, A. 2005, A&A, 443, 945

Pojmanski, G., Pilecki, B., & Szczygiel, D. 2005, Acta Astronomica, 55, 275

Pollack, J. B., Hollenbach, D., Beckwith, S., et al. 1994, ApJ, 421, 615

Praderie, F., Catala, C., Simon, T., & Boesgaard, A. M. 1986, ApJ, 303, 311

Pudritz, R. E. & Norman, C. A. 1983, ApJ, 274, 677

Qi, C., D'Alessio, P., Öberg, K. I., et al. 2011, ApJ, 740, 84

Reipurth, B., Pedrosa, A., & Lago, M. T. V. T. 1996, A&AS, 120, 229

Romanova, M. M., Ustyugova, G. V., Koldoba, A. V., & Lovelace, R. V. E. 2002, ApJ, 578, 420

Romanova, M. M., Ustyugova, G. V., Koldoba, A. V., & Lovelace, R. V. E. 2004, ApJ, 610, 920

Romanova, M. M., Ustyugova, G. V., Koldoba, A. V., & Lovelace, R. V. E. 2009, MNRAS, 399, 1802

Romanova, M. M., Ustyugova, G. V., Koldoba, A. V., Wick, J. V., & Lovelace, R. V. E. 2003, ApJ, 595, 1009

Rybicki, G. B. & Hummer, D. G. 1978, ApJ, 219, 654

Rydgren, A. E., Schmelz, J. T., & Vrba, F. J. 1982, ApJ, 256, 168

Schultz, G. V. & Wiemer, W. 1975, A&A, 43, 133

Semenov, D., Pavlyuchenkov, Y., Schreyer, K., et al. 2005, ApJ, 621, 853

Shakura, N. I. & Sunyaev, R. A. 1973, A&A, 24, 337

Shu, F., Najita, J., Ostriker, E., et al. 1994, ApJ, 429, 781

Simon, T., Vrba, F. J., & Herbst, W. 1990, AJ, 100, 1957

Skinner, S. L., Brown, A., & Stewart, R. T. 1993, ApJS, 87, 217

Sloan, G. C., Keller, L. D., Forrest, W. J., et al. 2005, ApJ, 632, 956

Smith, K. W., Lewis, G. F., Bonnell, I. A., Bunclark, P. S., & Emerson, J. P. 1999, MNRAS, 304, 367

Sobolev, V. V. 1957, Soviet Ast., 1, 678

Soderblom, D. R. 1983, ApJS, 53, 1

Stahler, S. & Palla, F. 2004, The Formation of Stars (Weinheim: Wiley-VCH)

Stapelfeldt, K. R., Watson, A. M., Krist, J. E., et al. 1999, ApJL, 516, L95

Stone, J. M. & Norman, M. L. 1992, ApJS, 80, 753

Strom, K. M., Strom, S. E., Edwards, S., Cabrit, S., & Skrutskie, M. F. 1989, AJ, 97, 1451

Strom, K. M., Strom, S. E., Wolff, S. C., Morgan, J., & Wenz, M. 1986, ApJS, 62, 39

Strom, S. E., Strom, K. M., & Grasdalen, G. L. 1975, ARA&A, 13, 187

Strom, S. E., Strom, K. M., Yost, J., Carrasco, L., & Grasdalen, G. 1972, ApJ, 173, 353

Symington, N. H. 2006, PhD thesis, University of Exeter, Exeter, Devon, EX4 4QL

Symington, N. H., Harries, T. J., & Kurosawa, R. 2005, MNRAS, 356, 1489

Tannirkulam, A., Monnier, J. D., Harries, T. J., et al. 2008a, ApJ, 689, 513

Tannirkulam, A., Monnier, J. D., Millan-Gabet, R., et al. 2008b, ApJL, 677, L51

ten Brummelaar, T. A., McAlister, H. A., Ridgway, S. T., et al. 2005, ApJ, 628, 453

Terquem, C. & Papaloizou, J. C. B. 2000, A&A, 360, 1031

Thé, P. S., de Winter, D., & Perez, M. R. 1994, A&AS, 104, 315

Tilling, I., Woitke, P., Meeus, G., et al. 2012, A&A, 538, A20

Uzdensky, D. A., Königl, A., & Litwin, C. 2002, ApJ, 565, 1191

Valenti, J. A. & Johns-Krull, C. M. 2004, Ap&SS, 292, 619

van den Ancker, M. E., Bouwman, J., Wesselius, P. R., et al. 2000, A&A, 357, 325

van den Ancker, M. E., de Winter, D., & Tjin A Djie, H. R. E. 1998, A&A, 330, 145

Verhoelst, T. 2005, PhD thesis, KU Leuven

Vink, J. S., Drew, J. E., Harries, T. J., Oudmaijer, R. D., & Unruh, Y. 2005, MNRAS, 359, 1049

Vinković, D., Ivezić, Ž., Jurkić, T., & Elitzur, M. 2006, ApJ, 636, 348

Vrba, F. J., Chugainov, P. F., Weaver, W. B., & Stauffer, J. S. 1993, AJ, 106, 1608

Vrba, F. J., Rydgren, A. E., Chugainov, P. F., Shakovskaia, N. I., & Weaver, W. B. 1989, AJ, 97, 483

Wade, G. A., Bagnulo, S., Drouin, D., Landstreet, J. D., & Monin, D. 2007, MNRAS, 376, 1145

Wade, G. A., Drouin, D., Bagnulo, S., et al. 2005, A&A, 442, L31

Walker, M. F. 1956, ApJS, 2, 365

Walker, M. F. 1972, ApJ, 175, 89

Ward-Thompson, D., André, P., Crutcher, R., et al. 2007, Protostars and Planets V, 33

Wassell, E. J., Grady, C. A., Woodgate, B., Kimble, R. A., & Bruhweiler, F. C. 2006, ApJ, 650, 985

Weigelt, G., Grinin, V. P., Groh, J. H., et al. 2011, A&A, 527, A103

Wesselius, P. R., van Duinen, R. J., de Jonge, A. R. W., et al. 1982, A&AS, 49, 427

White, R. J. & Basri, G. 2003, ApJ, 582, 1109

White, R. J. & Hillenbrand, L. A. 2005, ApJL, 621, L65

Whitney, B. A., Wood, K., Bjorkman, J. E., & Wolff, M. J. 2003, ApJ, 591, 1049

Williams, J. P., Blitz, L., & McKee, C. F. 2000, Protostars and Planets IV, 97

Wood, K., Wolk, S. J., Stanek, K. Z., et al. 2000, ApJL, 542, L21

Yusef-Zadeh, F., Morris, M., & White, R. L. 1984, ApJ, 278, 186

Zubko, V. G. 1998, MNRAS, 295, 109